
Towards many body physics with ultracold NaK molecules

Zhenkai Lu



Fakultät für Physik

Vielteilchenphysik mit ultrakalten NaK Molekülen

Dissertation an der Fakultät für Physik
Ludwig-Maximilians-Universität München
Fakultät für Physik

vorgelegt von

Zhenkai Lu

aus Ningbo, China

München, den 5. Mai 2016

Tag der mündlichen Prüfung: 6. July 2016

Erstgutachter: Prof. Immanuel Bloch

Zweitgutachter: Prof. Georgy V. Shlyapnikov

Weiter Prüfungskommissionsmitglieder: Prof. T. W. Hänsch, Prof. V. F. Mukhanov, Prof. U. Schollwöck, Prof. J. von Delft

Zusammenfassung

Diese Arbeit beschreibt den Aufbau eines neuartigen Experiments zur Produktion eines ultrakalten Gases aus chemisch stabilen $^{23}\text{Na}^{40}\text{K}$ -Molekülen im absoluten Grundzustand. Es ist zu erwarten, dass die langreichweitigen Wechselwirkungen zwischen Grundzustandsmolekülen die Beobachtung neuer Vielteilchen-Quantenzustände und die Simulation prototypischer Spingittermodelle zur Erforschung von Quantenmagnetismus und Hochtemperatursupraleitern ermöglichen.

Unter anderem werden in dieser Arbeit die folgenden experimentellen Prozeduren vorgestellt: Einfangen von $^{23}\text{Na}^{40}\text{K}$ -Atomen und Kühlung diese bis zur Quantenentartung, Assoziation schwach gebundener Feshbach-Moleküle und Transfer der Feshbach-Moleküle in den molekularen Grundzustand mittels STIRAP. Dieser Transfer wurde in unserem Experiment mit einer Effizienz von 60% über den Zwischenzustand $|d^3\Pi, \nu = 5, J = 1, \Omega = 1\rangle$ erfolgreich durchgeführt, wobei die Hyperfeinstruktur des Zwischenzustandes nicht aufgelöst wurde.

Außerdem wird eine störungstheoretische Untersuchung der Eigenschaften eines einkomponentigen, schwach wechselwirkenden, zweidimensionalen Gases von Fermionen mit einem Dipolmoment d , welches senkrecht zur Ebene ihrer Translationsbewegung ausgerichtet ist, präsentiert. Falls die Dipolmomente zu dieser Ebene gekippt werden, wird die Wechselwirkung anisotrop. Kollektive Anregungen im stoßfreien Regime werden in dieser Situation untersucht. Es wird weiterhin die Existenz stabiler supersolider Zustände in einem System von bosonischen Dipolen in zwei Dimensionen vorhergesagt, sofern eine zusätzliche abstoßende Dreikörperkontaktwechselwirkung vorhanden ist. Diese neuartigen Quanteneffekte sollten experimentell zugänglich sein, sobald die NaK-Grundzustandsmoleküle durch weitere evaporative Kühlung die Quantenentartung erreichen.

Abstract

This thesis reports on the construction of a novel experimental apparatus to create an ultracold sample of chemical stable $^{23}\text{Na}^{40}\text{K}$ polar molecules at their absolute ground states. The long range nature of the dipolar interactions between the ground state molecules, is expected to facilitate to observe new quantum many-body states and to simulate prototypical lattice spin models for exploring quantum magnetism and high T_c superconductivity.

The experimental procedures are presented in this thesis including: trapping and cooling ^{23}Na and ^{40}K atoms to quantum degeneracy, associating weakly bound state molecules with Feshbach resonances, and transferring the Feshbach molecules to the rovibrational ground states via stimulated Raman adiabatic passage. As a result, successful transfer has been demonstrated in our experiment with a single-path transfer efficiency $\simeq 60\%$ via a hyperfine non-resolved intermediate state $|d^3\Pi, \nu = 5, J = 1, \Omega = 1\rangle$.

In addition, a perturbative theoretical study on the Fermi liquid properties of a single-component weakly-interacting two dimensional dipolar fermions with dipole moments d oriented perpendicularly to the plane of their translational motion is presented in the thesis. When the dipole moments are tilted with respect to the translational plane, the effect of anisotropic interaction appears, and collective excitations in the collisionless regime are studied in this configuration. Furthermore, stable dilute supersolid states with two-dimensional bosonic dipoles are predicted to exist with an additional three-body repulsive contact interaction. These novel quantum effects should be accessible experimentally once the NaK ground state molecules reach quantum degeneracy by further evaporative cooling.

Contents

Zusammenfassung	v
Abstract	vii
1. Introduction	1
2. Fermi liquid of two-dimensional polar molecules	7
2.1. Introduction	7
2.2. Low-energy scattering of fermionic polar molecules in 2D	9
2.2.1. General relations	10
2.2.2. Low-energy p -wave scattering	12
2.2.3. Scattering with $ l > 1$	15
2.2.4. First order Born approximation and the leading part of the scattering amplitude	17
2.3. Thermodynamical quantities at $T = 0$	18
2.3.1. General relations of Fermi liquid theory	18
2.3.2. Two-body and many-body contributions to the ground state energy	20
2.3.3. Interaction function of quasiparticles	24
2.3.4. Compressibility, ground state energy, and effective mass	26
2.4. Zero sound	28
2.5. Concluding remarks	34
3. Zero sound in a two-dimensional dipolar Fermi gas	37
3.1. Introduction	37
3.2. General relations. Anisotropy of the Fermi surface	39
3.3. Interaction function of quasiparticles	42
3.4. Dynamical structure factor and zero sound modes	44
3.5. Relaxation rate of quasiparticles	49
3.6. Damping of zero sound	52
3.7. Concluding remarks	57

4. Stable dilute supersolid of two-dimensional dipolar bosons	59
4.1. Introduction	59
4.2. Method	60
4.2.1. Hamiltonian	60
4.2.2. Bogoliubov excitation spectrum of a uniform BEC	61
4.2.3. Variational ansatz	61
4.2.4. Energy functionals	62
4.3. Results	64
4.4. Numerical methods	67
4.5. Concluding remarks	70
5. The experimental setup and procedure	71
5.1. Overview	71
5.2. Creating a degenerate $^{23}\text{Na}^{40}\text{K}$ Bose-Fermi mixture	73
5.2.1. Na Zeeman slower and Na laser system	73
5.2.2. K 2D-MOT and K laser system	74
5.2.3. Dual species 3D MOT	75
5.2.4. Plugged magnetic trap and evaporative cooling	75
5.2.5. Optical dipole trap and transport	76
5.2.6. Degenerate Bose-Fermi mixture	77
5.3. RF association of Feshbach molecules	78
5.3.1. Introduction	78
5.3.2. Experimental setup	79
5.3.3. Experimental steps	80
5.3.4. Experimental results	81
5.3.5. Summary	82
5.4. Creating rovibrational ground states of $^{23}\text{Na}^{40}\text{K}$ molecules	83
5.4.1. Theoretical background	83
5.4.2. Molecular structure of the intermediate manifold	85
5.4.3. Raman laser system	89
5.4.4. Identification of the rovibrational ground state $ X^1\Sigma, \nu = 0, J = 0\rangle$	90
5.4.5. Preliminary result of STIRAP transfer	92
5.4.6. Summary and Outlook	92
6. Asymptotic-bound-state model for Feshbach resonances	95
6.1. Introduction	95
6.2. Basics of Asymptotic Bound-state Model	96
6.3. Spin basis and Hamiltonian	97
6.3.1. Relative Hamiltonian	98

6.3.2.	Internal energy	98
6.3.3.	Angular momentum conservation	98
6.4.	The standard ABM	99
6.4.1.	Entrance channel energy	99
6.4.2.	Closed channel energy	99
6.5.	The dressed ABM	100
6.5.1.	The contribution of the continuum states	100
6.5.2.	Implementation the dressed ABM	101
6.5.3.	Transformation of spin basis in the dressed ABM	102
6.6.	Open/Closed channel fraction	104
6.7.	Application in $^{23}\text{Na}^{40}\text{K}$ system	105
6.7.1.	Modification of the model	105
6.7.2.	Free parameters of $^{23}\text{Na}^{40}\text{K}$ system	105
6.8.	$^{23}\text{Na} F = 1, m_F = 1\rangle + ^{40}\text{K} F = 9/2, m_F = -9/2\rangle$ channel	106
6.8.1.	Resonance position and width	106
6.8.2.	Spin components of Feshbach molecules	107
6.8.3.	Close channel fraction	108
6.9.	Discussion and outlook	108
7.	Bose polaron	111
7.1.	Introduction	111
7.2.	Inverse radio-frequency (rf) spectroscopy	112
7.2.1.	Theoretical framework	112
7.2.2.	Theoretical prediction	114
7.3.	Experimental details	117
7.3.1.	Experimental sequence	117
7.3.2.	Experimental calibration	118
7.4.	Experimental results: rf spectral response across the FB resonance	121
7.5.	Discussion	121
7.5.1.	Discrepancies between experiments and theory	121
7.5.2.	Possible reasons	121
7.6.	Outlook	124
8.	Conclusion and outlook	127
A.	Calculation of integrals for the thermodynamical quantities	129
A.1.	Direct calculation of the first order contribution to the interaction energy	129
A.2.	Calculation of the interaction function $\tilde{F}_1^{(2)}$	131
A.3.	Calculation of the interaction function $\tilde{F}_2^{(2)}$	133

B. Calculation of the integral for the relaxation rate of quasiparticles	137
References	141
List of Figures	155
List of Tables	161
Acknowledgements	163

Introduction

After the first creation of Bose-Einstein condensate with atomic gases[1, 2], dilute ultracold atomic system has become a versatile and useful platform for simulating standard condensed matter models, discovering novel quantum phases, and advancing our knowledge of nature over the last two decades[3, 4].

Several landmark experiments have been realized with ultra cold atomic gases, for example superfluid - Mott insulator transition in optical lattices [5], vortices and superfluidity in both Bose[6] and Fermi gases[7], and BEC-BCS crossover with two-component Fermi gas [8, 9]. These achievements benefit from the experimental techniques being developed recently which allow to control the experimental parameters with high precision. One powerful tool is to control the interaction of atoms via Feshbach resonances[10]. By tuning magnetic fields, an ultracold atomic system can be made repulsive interacting ($a > 0$), attractive interacting ($a < 0$), non interacting ($a = 0$) or strongly interacting ($|a| \rightarrow \infty$) in a continuous manner. Secondly, the dimensions of the systems can be controlled experimentally by using optical lattices[11], ranging from 0D to 3D. Ultracold atoms in an optical lattice can be used to test and simulate various properties of Hubbard models that has been extensively studied in theoretical condensed matter physics[12, 13, 14].

However, ultracold atomic systems are governed by *van der Waals* interaction, $\sim 1/r^6$, which is a “short-range” interaction in 3D. At the ultracold limit, the interactions between atoms can be well described by a single parameter *s-wave scattering length*, a [15]. It simplifies theoretical descriptions of the system, nevertheless, limits the scope of physics that can be investigated. For some models such as Heisenberg model [16] and t-J model [17] that describing quantum magnetism and high T_c superconductivity, *long range* interactions over few lattice sites are required.

Therefore, it is timely to synthesis experimental techniques developed from ultracold experiments, to construct a setup aiming to create a quantum system governed by long range interactions. Ultracold polar molecular systems have been considered to be a nice candidate: compared to ultracold Rydberg atomic systems[18], polar molecules are expected to have longer lifetime hence are more feasible to investigate dynamical properties. Polar molecular systems also have tunable dipole moments compared to magnetic atoms [19, 20], so the interaction between the molecules can be controlled by an external polarizing field.

The interaction between polar molecules at large separation r is [21]:

$$U(r) = \frac{d^2}{r^3}(1 - 3\cos^2\theta), \quad (1.1)$$

where d is the dipole moment of molecules and θ is the angle between \mathbf{r} and the dipole orientation. $r_* = md^2/\hbar^2$ is called dipole length characterizing the interaction strength between the molecules. The $1/r^3$ character and anisotropy of the dipole-dipole interaction give rise to realizing novel quantum states, such as quantum magnetism[22], exotic superfluidity[23, 24], and topological phases[25]. Besides quantum many-body effects, cold and ultracold polar molecules have the applications for precise measurement[26], quantum information process[27, 28], etc.

To date, direct cooling of chemically inert polar molecules is still not sufficient to reach ultracold temperatures due to its complex molecular structures [26]. A breakthrough experiment accomplished in JILA provides an alternative way to create polar molecules near quantum degeneracy [29]. In that experiment, a weakly bound Feshbach molecules were associated from an ultracold ^{40}K ^{87}Rb mixture first. These weakly bound molecules are transferred to rovibrational ground state by using the technique called *stimulated Raman adiabatic passage* (STIRAP). STIRAP is an adiabatic process, therefore the phase space density of the sample is conserved.

The surprising discovery of chemical reactions of ^{40}K ^{87}Rb at ultralow temperatures [30, 31] appeared to be a major challenge of performing further evaporation towards quantum degeneracy. Some other bi-alkali-metal molecules like KCs, NaK, NaCs and RbCs were predicted to be chemical stable [32].

We have chosen NaK molecules in our experiments for the following reasons,

1. Laser cooling of Na and K atoms are now standard techniques.
2. NaK ground state molecules are chemical stable, so further evaporation is possible.
3. Potassium atoms have both bosonic (^{39}K and ^{41}K) and fermionic (^{40}K) isotopes, therefore NaK molecules can either be Bosons or Fermions.

This thesis reports the theoretical studies of ultracold polar molecular systems and the experimental effort of creating an ultracold sample of fermionic $^{23}\text{Na}^{40}\text{K}$ ground state molecules.

As to the theoretical part, I investigate *weakly interacting* dilute dipolar bosonic and fermionic gases in two dimensions. In the dilute limit, $nr_*^2 \ll 1$ ($k_F r_* \ll 1$ for fermions), analytical results can be obtained perturbatively. In addition, it is more feasible to perform experiments in the dilute limit given the fact that most of ultracold atomic experiments were done in this regime. In particular, I have studied the Fermi liquid properties of dipolar fermions in 2D and obtained ‘‘Lee-Huang-Yang’’ type coefficients for the equation of state. These beyond-mean-field coefficients could be measured via *in-situ* imaging techniques [33, 34]. Collective excitations in the *collisionless* regime, ‘‘zero sounds’’, are predicted to exist in this system.

The studies of ultracold dipolar bosonic gases may open perspective for the observation of *supersolid* states. This remarkable quantum phenomenon combining superfluidity with a crystalline order has been discussed over the last half century without a solid experimental evidence. We propose that, stable continuous space supersolid states exist in a dilute two-dimensional dipolar bosonic system.

I further present details of the experimental apparatus we built over the last few years. The implementation of specific experimental techniques for making degenerated Bose-Fermi $^{23}\text{Na}^{40}\text{K}$ mixture, associating weakly bound Feshbach molecules and adiabatically transferring towards to the ground states, is a major part of the work reported herein.

Our apparatus can also be used to investigate Bose polaron physics where impurity atoms strongly interact with a Bose-Einstein condensate. Preliminary experimental results are included in this thesis.

Outline

- In Chapter 2 Fermi liquid properties of a weakly interacting 2D gas of single-component fermionic polar molecules with dipole moments d oriented perpendicularly to the plane of their translational motion was studied. The low-energy scattering problem with dipole-dipole interactions is solved and a perturbation theory up to the second order of the small parameter k_{Fr_*} is developed. Equation of states and thermodynamic quantities are obtained analytically. This chapter is based on the publication: *Fermi liquid of two-dimensional polar molecules*, Phys. Rev. A **85**, 023614 (2012), which was written originally by myself (first authorship).
- Chapter 3 focuses on the zero sound in systems where the fermionic dipoles are tilted with respect to the plane of their translational motion (which can be realized in our experimental apparatus). It is shown that the propagation of zero sound is provided by both mean field and beyond mean field effects, and the anisotropy of the sound velocity is the same as the one of the Fermi velocity. Dynamical structure factor is calculated and the damping rate of the zero sound is estimated to be smaller than the relaxation rate of incoherent quasiparticle excitations. This chapter is based on the publication: *Zero sound in a two-dimensional dipolar Fermi gas*, Phys. Rev. A **88**, 033625 (2013), which was written originally by myself (first authorship).
- Chapter 4 considers two-dimensional bosonic dipoles oriented perpendicularly to the plane. It is shown that continuous space supersolid states can be stabilized with a three-body repulsive contact interaction in the dilute regime. The phase diagram of the system over the whole parameter space is obtained. This chapter is based on the publication: *Stable Dilute Supersolid of Two-Dimensional Dipolar Bosons*, Phys. Rev. Lett. **115**, 075303 (2015), which was

written originally by myself (first authorship).

- Chapter 5 is dedicated to the details of the experimental apparatus and the experimental procedures of creating ground state molecules. It is divided into three sections detailing three major steps: making a degenerated Bose-Fermi mixture, associating weakly bound Feshbach molecules and STIRAP transfer.

This chapter summarizes my major experimental contribution during my PhD period. There is no result published from this experimental setup as the time of writing this thesis. Being the first generation of this experiment, Dr. Nikolaus W. Buchheim and I have constructed the setup together since 2011 to 2016. The similarities between the thesis of Dr. Buchheim [123] and this thesis are due to the great overlapping of our experimental works, which can not be identified individually. Dr. Buchheim has agreed the rights of citing and quoting the figures and texts appeared in this chapter from Dr. Buchheim's thesis [123].

- Chapter 6 presents the implementation of asymptotic-bound-state (ABM) model for $^{23}\text{Na}^{40}\text{K}$ system. This model has been used for analyzing spin characters of the Feshbach molecules.
- Chapter 7 starts with a short background introduction of quantum impurity problems with an emphasis on Bose polarons that fermionic ^{40}K impurity atoms strongly interact with a Bose-Einstein condensate. Preliminary results of inverse rf spectroscopy of Bose polarons are included.
- I conclude the thesis in Chapter 8, with an outlook of future experiments.

Publications

The following articles have been published in refereed journals in the context of this thesis:

1. *Stable Dilute Supersolid of Two-Dimensional Dipolar Bosons*
Zhen-Kai Lu, Yun Li, D.S. Petrov, and G. V. Shlyapnikov
Phys. Rev. Lett. **115**, 075303 (2015)
2. *Zero sound in a two-dimensional dipolar Fermi gas*
Zhen-Kai Lu, S. I. Matveenko, and G. V. Shlyapnikov
Phys. Rev. A **88**, 033625 (2013)
3. *Fermi liquid of two-dimensional polar molecules*
Zhen-Kai Lu and G. V. Shlyapnikov
Phys. Rev. A **85**, 023614 (2012)

In addition, I have contributed the following paper during the course of my PhD:

1. *All-optical control of superradiance and matter waves using a dispersive cavity*
Shih-Wei Su, **Zhen-Kai Lu**, Shih-Chuan Gou, Wen-Te Liao
arXiv:1508.04878, submitted to Phys. Rev. Lett.

Fermi liquid of two-dimensional polar molecules

In this Chapter, we study Fermi liquid properties of a weakly interacting 2D gas of single-component fermionic polar molecules with dipole moments d oriented perpendicularly to the plane of their translational motion. This geometry allows the minimization of inelastic losses due to chemical reactions for reactive molecules and, at the same time, provides a possibility of a clear description of many-body (beyond mean field) effects. The long-range character of the dipole-dipole repulsive interaction between the molecules, which scales as $1/r^3$ at large distances r , makes the problem drastically different from the well-known problem of the two-species Fermi gas with repulsive contact interspecies interaction. We solve the low-energy scattering problem and develop a many-body perturbation theory beyond the mean field. The theory relies on the presence of a small parameter $k_F r_*$, where k_F is the Fermi momentum, and $r_* = md^2/\hbar^2$ is the dipole-dipole length, with m being the molecule mass. We obtain thermodynamic quantities as a series of expansion up to the second order in $k_F r_*$ and argue that many-body corrections to the ground-state energy can be identified in experiments with ultracold molecules, like it has been recently done for ultracold fermionic atoms. Moreover, we show that only many-body effects provide the existence of zero sound and calculate the sound velocity.

Note1: This chapter is based on the publication: *Fermi liquid of two-dimensional polar molecules*, Phys. Rev. A **85**, 023614 (2012), which was written originally by myself (first authorship).

Note2: In this chapter, “we” refers to Zhenkai Lu and G. V. Shlyapnikov.

2.1. Introduction

The recent breakthrough in creating ultracold diatomic polar molecules in the ground ro-vibrational state [29, 35, 36, 37] and cooling them towards quantum degeneracy [29] has opened fascinating prospects for the observation of novel quantum phases [38, 26, 39, 40, 41, 42, 43, 44, 45, 46, 47, 48, 49, 23, 50, 51, 52, 53, 54, 55]. A serious problem in this direction is related to ultracold chemical reactions, such as $\text{KRb} + \text{KRb} \Rightarrow \text{K}_2 + \text{Rb}_2$ observed in the JILA experiments with KRb molecules [56, 30], which places severe limitations on the achievable density in three-dimensional

samples. In order to suppress chemical reactions and perform evaporative cooling, it has been proposed to induce a strong dipole-dipole repulsion between the molecules by confining them to a (quasi)two-dimensional (2D) geometry and orienting their dipole moments (by a strong electric field) perpendicularly to the plane of the 2D translational motion [57, 58]. The suppression of chemical reactions by nearly two orders of magnitude in the quasi 2D geometry has been demonstrated in the recent JILA experiment [31]. At the same time, not all polar molecules of alkali atoms, on which experimental efforts are presently focused, may undergo these chemical reactions [32]. In particular, they are energetically unfavorable for RbCs bosonic molecules obtained in Innsbruck [37], or for NaK and KCs molecules which are now being actively studied by several experimental groups (see, e.g. [59]). It is thus expected that future experimental studies of many-body physics will deal with non-reactive polar molecules or with molecules strongly confined to the 2D regime.

Therefore, the 2D system of fermionic polar molecules attracts a great deal of interest, in particular when they are in the same internal state. Various aspects have been discussed regarding this system in literature, in particular the emergence and beyond mean field description of the topological $p_x + ip_y$ phase for microwave-dressed polar molecules [43, 23], interlayer superfluids in bilayer and multilayer systems [44, 50, 46, 60], the emergence of density-wave phases for tilted dipoles [48, 49, 52, 53, 54]. The case of superfluid pairing for tilted dipoles in the quasi 2D geometry beyond the simple BCS approach has been discussed in Ref. [54]. The Fermi liquid behavior of this system has been addressed by using the Fourier transform of the dipole-dipole interaction potential [61, 62, 49, 42, 63, 64, 54] and then employing various types of mean field approaches, such as the Hartree-Fock approximation [49] or variational approaches [42, 63]. It should be noted, however, that the short-range physics can become important for the interaction between such polar molecules, since in combination with the long-range behavior it introduces a peculiar momentum dependence of the scattering amplitude [23].

On the other hand, this is a subtle question of many-body (beyond mean field) effects in the Fermi liquid behavior of 2D polar molecules, and it can be examined in ultracold molecule experiments. For the case of atomic fermions, a milestone in this direction is the recent result at ENS, where the experiment demonstrated the many-body correction to the ground state energy of a short-range interacting two-species fermionic dilute gas [33, 34]. This correction was originally calculated by Huang, Lee, and Yang [65, 66] by using a rather tedious procedure. Later, it was found by Abrikosov and Khalatnikov [67] in an elegant way based on the Landau Fermi liquid theory [68].

In this chapter, we study a weakly interacting 2D gas of fermionic polar molecules which are all in the same internal state. It is assumed that each molecule has an average dipole moment d which is perpendicular to the plane of the translational motion, so that the molecule-molecule interaction at large separations r is

$$U(r) = \frac{d^2}{r^3} = \frac{\hbar^2 r_*}{mr^3}, \quad (2.1)$$

where $r_* = md^2/\hbar^2$ is the characteristic dipole-dipole distance, and m is the molecule mass. The value of d depends on the external electric field. At ultralow temperatures that are much smaller than the Fermi energy, characteristic momenta of particles are of the order of the Fermi momentum k_F , and the criterion of the weakly interacting regime is:

$$k_F r_* \ll 1. \quad (2.2)$$

In this regime, the Fermi liquid properties of this system, such as the ground state energy, compressibility, effective mass, can be written as a series of expansion in the small parameter $k_F r_*$. We obtain explicit expressions of these quantities up to the second order in $k_F r_*$, which requires us to reveal the role of the short-range physics in the scattering properties and develop a theory beyond the mean field. Our analysis shows that only many-body (beyond mean field) effects provide the existence of undamped zero sound in the collisionless regime.

The chapter is organized as follows. In Section 2.2 we analyze the low-energy 2D scattering of the polar molecules due to the dipole-dipole interaction. We obtain the scattering amplitude for all scattering channels with odd orbital angular momenta. The leading part of the amplitude comes from the so-called anomalous scattering, that is the scattering related to the interaction between particles at distances of the order of their de Broglie wavelength. This part of the amplitude corresponds to the first Born approximation and, due to the long-range $1/r^3$ character of the dipole-dipole interaction, it is proportional to the relative momentum k of colliding particles for any orbital angular momentum l . We then take into account the second Born correction, which gives a contribution proportional to k^2 . For the p -wave scattering channel it is necessary to include the short-range contribution, which together with the second Born correction leads to the term behaving as $k^2 \ln k$. In Section 2.3, after reviewing the Landau Fermi liquid theory for 2D systems, we specify two-body (mean field) and many-body (beyond mean field) contributions to the ground state energy for 2D fermionic polar molecules in the weakly interacting regime. We then calculate the interaction function of quasiparticles on the Fermi surface and, following the idea of Abrikosov-Khalatnikov [67], obtain the compressibility, ground state energy, and effective mass of quasiparticles. In Section 2.4 we calculate the zero sound velocity and stress that the many-body contribution to the interaction function of quasiparticles is necessary for finding the undamped zero sound. In Section 2.5, we conclude and emphasize that the 2D gas of fermionic polar molecules represents a novel Fermi liquid, which is promising for revealing many-body effects. Moreover, we show that with present facilities it is feasible to obtain this system in both collisionless and hydrodynamic regimes. We also summarize some recent development of this subject based on various theoretical tools, such as quantum Monte-Carlo, variational methods, etc.

2.2. Low-energy scattering of fermionic polar molecules in 2D

2.2.1. General relations

We first discuss low-energy two-body scattering of identical fermionic polar molecules undergoing the 2D translational motion and interacting with each other at large separations via the potential $U(r)$ (2.1). The term “low-energy” means that their relative momenta satisfy the inequality $kr_* \ll 1$. In order to develop many-body theory for a weakly interacting gas of such molecules, we need to know the off-shell scattering amplitude defined as [15],

$$f(\mathbf{k}', \mathbf{k}) = \int \exp(-i\mathbf{k}'\mathbf{r})U(r)\tilde{\psi}_{\mathbf{k}}(\mathbf{r})d^2\mathbf{r}, \quad (2.3)$$

where $\tilde{\psi}_{\mathbf{k}}(\mathbf{r})$ is the true wavefunction of the relative motion with momentum \mathbf{k} . It is governed by the Schrödinger equation [15],

$$\left(-\frac{\hbar^2}{m}\Delta + U(r)\right)\tilde{\psi}_{\mathbf{k}}(\mathbf{r}) = \frac{\hbar^2 k^2}{m}\tilde{\psi}_{\mathbf{k}}(\mathbf{r}). \quad (2.4)$$

For $|\mathbf{k}'| = |\mathbf{k}|$ we have the on-shell amplitude which enters an asymptotic expression for $\tilde{\psi}_{\mathbf{k}}(\mathbf{r})$ at $r \rightarrow \infty$ [15, 23]:

$$\tilde{\psi}_{\mathbf{k}}(\mathbf{r}) = \exp(i\mathbf{k}\mathbf{r}) - \frac{m}{\hbar^2} \sqrt{\frac{i}{8\pi kr}} f(k, \varphi) \exp(ikr), \quad (2.5)$$

with φ being the scattering angle, i.e. the angle between the vectors \mathbf{k}' and \mathbf{k} .

The wavefunction $\tilde{\psi}_{\mathbf{k}}(\mathbf{r})$ can be represented as a sum of partial waves $\tilde{\psi}_l(k, r)$ corresponding to the motion with a given value of the orbital angular momentum l :

$$\tilde{\psi}_{\mathbf{k}}(\mathbf{r}) = \sum_{l=-\infty}^{\infty} \tilde{\psi}_l(k, r) i^l \exp(il\varphi). \quad (2.6)$$

Using the relation

$$\exp(i\mathbf{k}\mathbf{r}) = \sum_{l=-\infty}^{\infty} i^l J_l(kr) \exp[il(\varphi_k - \varphi_r)], \quad (2.7)$$

where J_l is the Bessel function, and φ_k and φ_r are the angles of the vectors \mathbf{k} and \mathbf{r} with respect to the quantization axis. Eqs. (2.6) and (2.7) allow one to express the scattering amplitude as a sum of partial-wave contributions:

$$f(\mathbf{k}', \mathbf{k}) = \sum_{l=-\infty}^{\infty} \exp(il\varphi) f_l(k', k), \quad (2.8)$$

with the off-shell l -wave amplitude given by

$$f_l(k', k) = \int_0^\infty J_l(k'r)U(r)\tilde{\psi}_l(k, r)2\pi r dr. \quad (2.9)$$

Similar relations can be written for the on-shell scattering amplitude:

$$f(k, \varphi) = \sum_{l=-\infty}^{\infty} \exp(il\varphi)f_l(k), \quad (2.10)$$

$$f_l(k) = \int_0^\infty J_l(k'r)U(r)\tilde{\psi}_l(k, r)2\pi r dr. \quad (2.11)$$

The asymptotic form of the wavefunction of the l -wave relative motion at $r \rightarrow \infty$ may be represented as

$$\tilde{\psi}_l(k, r) \propto \frac{\cos(kr - \pi/4 + \delta_l(k))}{\sqrt{kr}}, \quad (2.12)$$

where $\delta_l(k)$ is the scattering phase shift. This is obvious because in the absence of scattering the l -wave part of the plane wave $\exp(i\mathbf{k}\mathbf{r})$ at $r \rightarrow \infty$ is $(kr)^{-1/2} \cos(kr - \pi/4)$. Comparing Eq. (2.12) with the l -wave part of Eq. (2.5) we obtain a relation between the partial on-shell amplitude and the phase shift:

$$f_l(k) = -\frac{4\hbar^2}{m} \frac{\tan \delta_l(k)}{1 - i \tan \delta_l(k)}. \quad (2.13)$$

Note that away from resonances the scattering phase shift is small in the low-momentum limit $kr_* \ll 1$.

For the solution of the scattering problem it is more convenient to normalize the wavefunction of the radial relative motion with orbital angular momentum l in such a way that it is real, and for $r \rightarrow \infty$ one has:

$$\psi_l(k, r) = [J_l(kr) - \tan \delta_l(k)N_l(kr)] \propto \cos(kr - l\pi/2 - \pi/4 + \delta_l(k)), \quad (2.14)$$

where N_l is the Neumann function. One checks straightforwardly that

$$\tilde{\psi}_l(k, r) = \frac{\psi_l(k, r)}{1 - i \tan \delta_l(k)}.$$

Using this relation the off-shell scattering amplitude (2.9) can be represented as

$$f_l(k', k) = \frac{\bar{f}_l(k', k)}{1 - i \tan \delta_l(k)}, \quad (2.15)$$

where $\bar{f}_l(k', k)$ is real and follows from Eq. (2.9) with $\tilde{\psi}_l(k, r)$ replaced by $\psi_l(k, r)$.

Setting $k' = k$ we then obtain the related on-shell scattering amplitude:

$$\bar{f}_l(k, k) \equiv \bar{f}_l(k) = -\frac{4\hbar^2}{m} \tan \delta_l(k). \quad (2.16)$$

2.2.2. Low-energy p -wave scattering

As we will see, the slow $1/r^3$ decay of the potential $U(r)$ at sufficiently large distances makes the scattering drastically different from that of short-range interacting atoms. For identical fermionic polar molecules, only the scattering with odd orbital angular momenta l is possible. For finding the amplitude of the p -wave scattering in the ultracold limit, $kr_* \ll 1$, we employ the method developed in Ref. [23] and used there for the scattering potential containing an attractive $1/r^3$ dipole-dipole tail. We divide the range of distances into two parts: $r < r_0$ and $r > r_0$, where r_0 is in the interval $r_* \ll r_0 \ll k^{-1}$. In region I where $r < r_0$, the p -wave relative motion of two particles is governed by the Schrödinger equation with zero kinetic energy:

$$-\frac{\hbar^2}{m} \left(\frac{d^2 \psi_I}{dr^2} + \frac{1}{r} \frac{d\psi_I}{dr} - \frac{\psi_I}{r^2} \right) + U(r)\psi_I = 0. \quad (2.17)$$

At distances where the potential $U(r)$ already acquires the form (2.1), the solution of Eq. (2.17) can be expressed in terms of growing and decaying Bessel functions:

$$\psi_I(r) \propto \left[AI_2 \left(2\sqrt{\frac{r_*}{r}} \right) + K_2 \left(2\sqrt{\frac{r_*}{r}} \right) \right]. \quad (2.18)$$

The constant A is determined by the behavior of $U(r)$ at short distances where Eq. (2.1) is no longer valid. If the interaction potential $U(r)$ has the form (2.1) up to very short distances, then $A = 0$, so that for $r \rightarrow 0$ equation (2.18) gives an exponentially decaying wavefunction.

It should be noted here that for the quasi 2D regime obtained by a tight confinement of the translational motion in one direction, we can encounter the situation where $r_* \lesssim l_0$, with l_0 being the confinement length. However, we may always select $r_0 \gg l_0$ if the condition $kl_0 \ll 1$ is satisfied. Therefore, our results for the 2D p -wave scattering obtained below in this section remain applicable for the quasi2D regime. The character of the relative motion of particles at distances $r \lesssim l_0$ is only contained in the value of the coefficient A , and the extra requirement is the inequality $kl_0 \ll 1$.

At large distances, $r > r_0$, the relative motion is practically free and the potential $U(r)$ can be considered as perturbation. To zero order, the relative wavefunction is given by

$$\psi_{II}^{(0)}(r) = J_1(kr) - \tan \delta_I(k) N_1(kr), \quad (2.19)$$

where the phase shift $\delta_I(k)$ is due to the interaction between particles in region I.

Equalizing the logarithmic derivatives of $\psi_I(r)$ and $\psi_{II}^{(0)}$ at $r = r_0$ we obtain:

$$\tan \delta_I = -\frac{\pi k^2 r_0 r_*}{8} \left[1 + \frac{r_*}{r_0} \left(2C - \frac{1}{2} - 2A + \ln \frac{r_*}{r_0} \right) \right], \quad (2.20)$$

with $C = 0.5772$ being the Euler constant.

We now include perturbatively the contribution to the p -wave scattering phase shift from distance $r > r_0$. In this region, to first order in $U(r)$, the relative wavefunction is given by

$$\psi_{II}^{(1)}(r) = \psi_{II}^{(0)}(r) - \int_{r_0}^{\infty} G(r, r') U(r') \psi_{II}^{(0)}(r') 2\pi r' dr', \quad (2.21)$$

where the Green function for the free p -wave motion obeys the radial equation:

$$-\frac{\hbar^2}{m} \left(\frac{d^2}{dr^2} + \frac{1}{r} \frac{d}{dr} - \frac{1}{r^2} + k^2 \right) G(r, r') = \frac{\delta(r - r')}{2\pi r}.$$

For the normalization of the relative wavefunction chosen in Eq. (2.14), we have:

$$G(r, r') = -\frac{m}{4\hbar^2} \begin{cases} \psi_{II}^{(0)}(r') N_1(kr), & r > r' \\ \psi_{II}^{(0)}(r) N_1(kr'). & r < r' \end{cases} \quad (2.22)$$

Substituting this Green function into Eq. (2.21) and taking the limit $r \rightarrow \infty$, for the first order contribution to the phase shift we have:

$$\tan \delta_1^{(1)}(k) = \tan \delta_I(k) - \frac{m}{4\hbar^2} \int_{r_0}^{\infty} [\psi_{II}^{(0)}(r)]^2 U(r) 2\pi r dr. \quad (2.23)$$

Using Eqs. (2.19) and (2.20) we then obtain:

$$\tan \delta_1^{(1)}(k) = -\frac{2kr_*}{3} - \frac{\pi k^2 r_*^2}{8} \left(-2A + 2C + \ln \frac{r_*}{r_0} - \frac{3}{2} \right). \quad (2.24)$$

To second order in $U(r)$, we have the relative wavefunction:

$$\begin{aligned} \psi_{II}^{(2)}(r) &= \psi_{II}^{(1)}(r) + \int_{r_0}^{\infty} G(r, r') U(r') 2\pi r' dr' \\ &\times \int_{r_0}^{\infty} G(r', r'') U(r'') \psi_{II}^{(0)}(r'') 2\pi r'' dr''. \end{aligned} \quad (2.25)$$

Taking the limit $r \rightarrow \infty$ in this equation we see that including the second order

contribution, the scattering phase shift becomes:

$$\begin{aligned}\tan \delta_1(k) &= \tan \delta_1^{(1)}(k) - \frac{m^2}{8\hbar^4} \int_{r_0}^{\infty} \psi_{II}^{(0)}(r)^2 U(r) 2\pi r dr \\ &\times \int_r^{\infty} N_1(kr') U(r') \psi_{II}^{(0)}(r') 2\pi r' dr'.\end{aligned}\quad (2.26)$$

As we are not interested in terms that are proportional to k^3 or higher powers of k , we may omit the term $\tan \delta_I(k) N_1(kr)$ in the expression for $\psi_{II}^{(0)}(r)$. Then the integration over dr' leads to:

$$\begin{aligned}\tan \delta_1(k) &= \tan \delta_1^{(1)}(k) - \frac{(\pi k r_*)^2}{2} \int_{kr_0}^{\infty} \frac{J_1^2(x)}{x^2} dx \\ &\times \left[\frac{2}{3} x (N_0(x) J_2(x) - N_1(x) J_1(x)) - \frac{1}{2} N_0(x) J_1(x) + \frac{1}{6} N_1(x) J_2(x) - \frac{1}{\pi x} \right]\end{aligned}\quad (2.27)$$

For the first four terms in the square brackets, we may put the lower limit of integration equal to zero and use the following relations:

$$\begin{aligned}\int_0^{\infty} J_1^3(x) N_1(x) \frac{dx}{x} &= -\frac{1}{4\pi}, \\ \int_0^{\infty} J_1^2(x) J_2(x) N_0(x) \frac{dx}{x} &= \frac{1}{8\pi}, \\ \int_0^{\infty} J_1^3(x) N_0(x) \frac{dx}{x^2} &= \frac{1}{16\pi}, \\ \int_0^{\infty} J_1^2(x) J_2(x) N_1(x) \frac{dx}{x^2} &= -\frac{1}{16\pi}.\end{aligned}$$

For the last term in the square brackets we have:

$$\int_{kr_0}^{\infty} J_1^2(x) \frac{dx}{x^3} \approx \frac{1}{16} - \frac{C}{4} + \frac{\ln 2}{4} - \frac{1}{4} \ln kr_0.\quad (2.28)$$

We then obtain:

$$\begin{aligned}\tan \delta_1(k) &= \tan \delta_1^{(1)}(k) - \frac{\pi (kr_*)^2}{8} \left[\frac{7}{12} + C - \ln 2 + \ln kr_0 \right] \\ &= -\frac{2kr_*}{3} - \frac{\pi k^2 r_*^2}{8} \ln \xi kr_*,\end{aligned}\quad (2.29)$$

where:

$$\xi = \exp \left(3C - \ln 2 - \frac{11}{12} - 2A \right).\quad (2.30)$$

Using Eqs. (2.16) and (2.29) we represent the on-shell p -wave scattering amplitude

$\bar{f}_1(k)$ in the form:

$$\bar{f}_1(k) = \bar{f}_1^{(1)}(k) + \bar{f}_1^{(2)}(k), \quad (2.31)$$

with

$$\bar{f}_1^{(1)}(k) = \frac{8\hbar^2}{3m} kr_* \quad (2.32)$$

and

$$\bar{f}_1^{(2)}(k) = \frac{\pi\hbar^2}{2m} (kr_*)^2 \ln \xi kr_*. \quad (2.33)$$

The leading term is $\bar{f}_1^{(1)}(k) \propto k$. It appears to first order in $U(r)$ and comes from the scattering at distances $r \sim 1/k$. This term can be called “anomalous scattering” term (see [15]). The term $\bar{f}_1^{(2)}(k) \propto k^2 \ln \xi kr_*$ comes from both large distances $\sim 1/k$ and short distances. Note that the behavior of the wavefunction at short distances where $U(r)$ is no longer given by Eq. (2.1), is contained in Eq. (2.29) only through the coefficient ξ under logarithm.

2.2.3. Scattering with $|l| > 1$

The presence of strong anomalous p -wave scattering, i.e. the scattering from inter-particle distances $\sim 1/k$, originates from the slow $1/r^3$ decay of the potential $U(r)$ at large r . The strong anomalous scattering is also present for partial waves with higher l . In this section we follow the same method as in the case of the p -wave scattering and calculate the amplitude of the l -wave scattering with $|l| > 1$. For simplicity we consider positive l , having in mind that the scattering amplitude and phase shift depend only on $|l|$.

To zero order in $U(r)$, the wavefunction of the l -wave relative motion at large distances $r > r_0$ is written as:

$$\psi_{l(II)}^{(0)}(k, r) = [J_l(kr) - \tan \delta_{l(I)}(k) N_l(kr)], \quad (2.34)$$

where $\delta_{l(I)}(k)$ is the l -wave scattering phase shift coming from the interaction at distances $r < r_0$. We then match $\psi_{l(II)}^{(0)}(k, r)$ at $r = r_0$ with the short-distance wavefunction $\psi_{l(I)}(r)$ which follows from the Schrödinger equation for the l -wave relative motion in the potential $U(r)$ at $k = 0$. This immediately gives a relation:

$$\tan \delta_{l(I)}(k) = \frac{kJ'_l(kr_0) - w_l J_l(kr_0)}{kN'_l(kr_0) - w_l N_l(kr_0)}, \quad (2.35)$$

where the momentum-independent quantity w_l is the logarithmic derivative of $\psi_{l(I)}(r)$ at $r = r_0$. Since we have the inequality $kr_0 \ll 1$, the arguments of the Bessel functions in Eq. (2.35) are small and they reduce to $J_l(x) \sim x^l$, $N_l(x) \sim x^{-l}$. This leads to $\tan \delta_{l(I)}(k) \sim (kr_0)^{2l}$. Thus, the phase shift coming from the interaction at short distances is of the order of $(kr_0)^{2l}$. As we confine ourselves to second order in k , we may put $\tan \delta_{l(I)}(k) = 0$ for the scattering with $|l| > 1$.

Then, like for the p -wave scattering, we calculate the contribution to the phase shift from distances $r > r_0$ by considering the potential $U(r)$ as perturbation. To first and second order in $U(r)$, at $r > r_0$ we have similar expressions as Eq. (2.23), (2.25) for the relative wavefunction of the l -wave motion. Following the same method as in the case of the p -wave scattering and retaining only the terms up to k^2 , for the first order phase shift we have:

$$\begin{aligned}\tan \delta_l^{(1)}(k) &= -\frac{m}{4\hbar^2} \int_{r_0}^{\infty} [\psi_{l(II)}^{(0)}(r)]^2 U(r) 2\pi r dr \\ &\simeq -\frac{\pi k r_*}{2} \int_{k r_0}^{\infty} J_l^2(x) \frac{1}{x^2} dx = -\frac{2k r_*}{4l^2 - 1}.\end{aligned}\quad (2.36)$$

The second order phase shift is:

$$\begin{aligned}\tan \delta_l^{(2)}(k) &= -\frac{m^2}{8\hbar^4} \int_{r_0}^{\infty} \psi_{l(II)}^{(0)}(r)^2 U(r) 2\pi r dr \times \int_r^{\infty} N_l(kr') U(r') \psi_{l(II)}^{(0)}(r') 2\pi r' dr' \\ &\simeq -\frac{(\pi k r_*)^2}{2} \int_{k r_0}^{\infty} \frac{J_l^2(x)}{x^2} dx \int_x^{\infty} \frac{N_l(y) J_l(y)}{y^2} dy,\end{aligned}\quad (2.37)$$

and we may put the lower limit of integration equal to zero. For the integral over dy , we obtain :

$$\begin{aligned}&\int_x^{\infty} \frac{N_l(y) J_l(y)}{y^2} dy \\ &= \frac{1}{2l(2l-1)} J_l(x) N_{l-1}(x) + \frac{1}{2l(2l+1)} J_{l+1}(x) N_l(x) \\ &+ \frac{2x}{4l^2-1} [N_{l-1}(x) J_{l+1}(x) - J_l(x) N_l(x)] - \frac{1}{\pi l x}.\end{aligned}\quad (2.38)$$

Then, using the relations:

$$\begin{aligned}\int_0^{\infty} \frac{J_l^2(x)}{x^3} dx &= \frac{1}{4l(l^2-1)}, \\ \int_0^{\infty} \frac{J_l^2(x)}{x} N_{l-1}(x) J_{l+1}(x) dx &= \frac{1}{4l(l+1)\pi}, \\ \int_0^{\infty} \frac{J_l^3(x)}{x} N_l(x) dx &= -\frac{1}{4l^2\pi}, \\ \int_0^{\infty} \frac{J_l^2(x)}{x^2} J_l(x) N_{l-1}(x) dx &= \frac{1}{8l^2(l+1)\pi}, \\ \int_0^{\infty} \frac{J_l^2(x)}{x^2} J_{l+1}(x) N_l(x) dx &= -\frac{1}{8l^2(l+1)\pi},\end{aligned}$$

we find the following result for the second order phase shift:

$$\tan \delta_l^{(2)}(k) = \frac{3\pi(kr_*)^2}{8} \frac{1}{l(l^2-1)(4l^2-1)}. \quad (2.39)$$

So, the total phase shift is given by

$$\tan \delta_l(k) = \tan \delta_l^{(1)}(k) + \tan \delta_l^{(2)}(k) = -\frac{2kr_*}{4l^2-1} + \frac{3\pi(kr_*)^2}{8l(l^2-1)(4l^2-1)}. \quad (2.40)$$

Then, according to Eq. (2.16) the on-shell scattering amplitude $\bar{f}_l(k)$ is

$$\bar{f}_l(k) = \bar{f}_l^{(1)}(k) + \bar{f}_l^{(2)}(k), \quad (2.41)$$

where

$$\bar{f}_l^{(1)}(k) = \frac{8\hbar^2 kr_*}{m} \frac{1}{4l^2-1}, \quad (2.42)$$

$$\bar{f}_l^{(2)}(k) = -\frac{3\pi\hbar^2}{2m} (kr_*)^2 \frac{1}{|l|(l^2-1)(4l^2-1)}. \quad (2.43)$$

Note that Eqs. (2.42) and (2.43) do not contain short-range contributions as those are proportional to $k^{2|l|}$ and can be omitted for $|l| > 1$.

2.2.4. First order Born approximation and the leading part of the scattering amplitude

As we already said above, in the low-momentum limit for both $|l| = 1$ and $|l| > 1$ the leading part of the on-shell scattering amplitude $\bar{f}_l(k)$ is $\bar{f}_l^{(1)}(k)$ and it is contained in the first order contribution from distances $r > r_0$. For $|l| > 1$ it is given by Eq. (2.42) and follows from Eq. (2.36) with $\psi_{l(II)}^{(0)} = J_l(kr)$. In the case of $|l| = 1$ this leading part is given by Eq. (2.32) and follows from the integral term of Eq. (2.23) in which one keeps only $J_1(kr)$ in the expression for $\psi_{II}^{(0)}(r)$. This means that $\bar{f}_l^{(1)}(k)$ actually follows from the first order Born approximation.

The off-shell scattering amplitude can also be represented as $\bar{f}_l(k', k) = \bar{f}_l^{(1)}(k', k) + \bar{f}_l^{(2)}(k', k)$, and the leading contribution $\bar{f}_l^{(1)}(k', k)$ follows from the first Born approximation. It is given by Eq. (2.9) in which one should replace $\tilde{\psi}_l(k, r)$ by $J_l(kr)$:

$$\bar{f}_l^{(1)}(k', k) = \int_0^\infty J_l(kr) J_l(kr') U(r) 2\pi r dr. \quad (2.44)$$

Note that it is not important that we put zero for the lower limit of the integration, since this can only give a correction which behaves as k^2 or a higher power of k .

Then, putting $U(r) = \hbar^2 r_* / mr^3$ in Eq. (2.44), we obtain:

$$\bar{f}_l^{(1)}(k', k) = \frac{\pi \hbar^2 \Gamma(l - 1/2)}{m \sqrt{\pi}} \frac{k^l r_*}{(k')^{l-1}} F\left(-\frac{1}{2}, -\frac{1}{2} + l, 1 + l, \frac{k^2}{k'^2}\right), \quad (2.45)$$

where F is the hypergeometric function. The result of Eq. (2.45) corresponds to $k < k'$, and for $k > k'$ one should interchange k and k' .

For identical fermions the full scattering amplitude contains only partial amplitudes with odd l . Since the scattered waves with relative momenta \mathbf{k}' and $-\mathbf{k}'$ correspond to interchanging the identical fermions, the scattering amplitude can be written as (see, e.g. [15]):

$$\tilde{f}(\mathbf{k}', \mathbf{k}) = f(\mathbf{k}', \mathbf{k}) - f(-\mathbf{k}', \mathbf{k}). \quad (2.46)$$

Then, according to equation (2.10) one can write:

$$\tilde{f}(\mathbf{k}', \mathbf{k}) = 2 \sum_{l \text{ odd}} f_l(k', k) \exp(il\varphi). \quad (2.47)$$

In the first Born approximation there is no difference between $f_l(k', k)$ and $\bar{f}_l(k', k)$ because $\tan \delta_l(k)$ in the denominator of Eq. (2.15) is proportional to k and can be disregarded. Therefore, one may use $\bar{f}_l^{(1)}(k', k)$ of Eq. (2.45) for $f_l(k', k)$ in Eq. (2.47). One can represent $\tilde{f}(\mathbf{k}', \mathbf{k})$ in a different form recalling that in the first Born approximation we have:

$$f(\mathbf{k}', \mathbf{k}) = \int U(r) \exp[i(\mathbf{k} - \mathbf{k}')\mathbf{r}] d^2r. \quad (2.48)$$

Performing the integration in this equation, with $U(r)$ given by Eq. (2.1), and using Eq. (2.46) we obtain:

$$\tilde{f}(\mathbf{k}', \mathbf{k}) = \frac{2\pi \hbar^2 r_*}{m} \{|\mathbf{k} + \mathbf{k}'| - |\mathbf{k} - \mathbf{k}'|\}. \quad (2.49)$$

Equation (2.49) is also obtained by a direct summation over odd l in Eq. (2.47), with $f_l(k', k)$ following from Eq. (2.45).

2.3. Thermodynamical quantities at $T = 0$

2.3.1. General relations of Fermi liquid theory

Identical fermionic polar molecules undergoing a two-dimensional translational motion and repulsively interacting with each other via the potential (2.1) represent a 2D Fermi liquid. General relations of the Landau Fermi liquid theory remain similar to those in 3D (see, e.g. [68]). The number of “dressed” particles, or quasiparticles, is the same as the total number of particles N , and the (quasi)particle Fermi momentum is

$$k_F = \sqrt{\frac{4\pi N}{S}}, \quad (2.50)$$

where S is the surface area. At $T = 0$ the momentum distribution of free quasiparticles is the step function

$$n(\mathbf{k}) = \theta(k_F - k), \quad (2.51)$$

i.e. $n(\mathbf{k}) = 1$ for $k < k_F$ and zero otherwise. The chemical potential is equal to the boundary energy at the Fermi circle, $\mu = \epsilon_F \equiv \epsilon(k_F)$.

The quasiparticle energy $\epsilon(\mathbf{k})$ is a variational derivative of the total energy with respect to the distribution function $n(\mathbf{k})$. Due to the interaction between quasiparticles, the deviation δn of this distribution from the step function (3.5) results in the change of the quasiparticle energy:

$$\delta\epsilon(\mathbf{k}) = \int F(\mathbf{k}, \mathbf{k}') \delta n(\mathbf{k}') \frac{d^2 k'}{(2\pi)^2}. \quad (2.52)$$

The interaction function of quasiparticles $F(\mathbf{k}, \mathbf{k}')$ is thus the second variational derivative of the total energy with regard to $n(\mathbf{k})$. The quantity $\delta n(\mathbf{k})$ is significantly different from zero only near the Fermi surface, so that one may put $\mathbf{k} = k_F \mathbf{n}$ and $\mathbf{k}' = k_F \mathbf{n}'$ in the arguments of F in Eq. (3.6), where \mathbf{n} and \mathbf{n}' are unit vectors in the directions of \mathbf{k} and \mathbf{k}' . The quasiparticle energy near the Fermi surface can be written as:

$$\epsilon(\mathbf{k}) = \epsilon_F + \hbar v_F (k - k_F) + \int F(\mathbf{k}, \mathbf{k}') \delta n(\mathbf{k}') \frac{d^2 k'}{(2\pi)^2}. \quad (2.53)$$

The quantity $v_F = \partial\epsilon(\mathbf{k})/\hbar\partial k|_{k=k_F}$ is the Fermi velocity, and the effective mass of a quasiparticle is defined as $m^* = \hbar k_F/v_F$. It can be obtained from the relation (see [68]):

$$\frac{1}{m} = \frac{1}{m^*} + \frac{1}{(2\pi\hbar)^2} \int_0^{2\pi} F(\theta) \cos\theta d\theta, \quad (2.54)$$

where θ is the angle between the vectors \mathbf{n} and \mathbf{n}' , and $F(\theta) = F(k_F \mathbf{n}, k_F \mathbf{n}')$.

The compressibility κ at $T = 0$ is given by [68]:

$$\kappa^{-1} = \frac{N^2}{S} \frac{\partial\mu}{\partial N}. \quad (2.55)$$

The chemical potential is $\mu = \epsilon_F$, and the variation of μ due to a change in the number of particles can be expressed as

$$\delta\mu = \int F(k_F \mathbf{n}, \mathbf{k}') \delta n(\mathbf{k}') \frac{d^2 k'}{(2\pi)^2} + \frac{\partial\epsilon_F}{\partial k_F} \delta k_F. \quad (2.56)$$

The quantity $\delta n(\mathbf{k}')$ is appreciably different from zero only when \mathbf{k}' is near the Fermi surface, so that we can replace the interaction function F by its value on the Fermi

surface. Then the first term of Eq. (2.56) becomes

$$\int F(\theta) \frac{d\theta}{2\pi} \int \delta n(\mathbf{k}') \frac{d^2 k'}{(2\pi)^2} = \frac{\delta N}{2\pi S} \int F(\theta) d\theta.$$

The second term of Eq. (2.56) reduces to

$$\frac{\partial \epsilon_F}{\partial k_F} \delta k_F = \frac{\hbar^2 k_F}{m^*} \delta k_F = \frac{2\pi \hbar^2}{m^*} \frac{\delta N}{S}. \quad (2.57)$$

We thus have (see [68]):

$$\frac{\partial \mu}{\partial N} = \frac{1}{2\pi S} \int_0^{2\pi} F(\theta) d\theta + \frac{2\pi \hbar^2}{m^* S} = \frac{2\pi \hbar^2}{m S} + \frac{1}{2\pi S} \int_0^{2\pi} (1 - \cos \theta) F(\theta) d\theta. \quad (2.58)$$

Equation (2.58) shows that the knowledge of the interaction function of quasiparticles on the Fermi surface, $F(\theta)$, allows one to calculate $\partial \mu / \partial N$ and, hence, the chemical potential $\mu = \partial E / \partial N$ and the ground state energy E . This elegant way of finding the ground state energy has been proposed by Abrikosov and Khalatnikov [67]. It was implemented in Ref. [67] for a two-component 3D Fermi gas with a weak repulsive contact (short-range) interspecies interaction.

We develop a theory beyond the mean field for calculating the interaction function of quasiparticles for a single-component 2D gas of fermionic polar molecules in the weakly interacting regime. We obtain the ground state energy as a series of expansion in the small parameter $k_F r_*$ and confine ourselves to the second order. In this sense our work represents a sort of Lee-Huang-Yang [65, 66] and Abrikosov-Khalatnikov [67] calculation for this dipolar system. As we will see, the long-range character of the dipole-dipole interaction makes the result quite different from that in the case of short-range interactions.

2.3.2. Two-body and many-body contributions to the ground state energy

We first write down the expression for the kinetic energy and specify two-body (mean field) and many-body (beyond mean field) contributions to the interaction energy. The Hamiltonian of the system reads:

$$\hat{\mathcal{H}} = \sum_{\mathbf{k}} \frac{\hbar^2 k^2}{2m} \hat{a}_{\mathbf{k}}^\dagger \hat{a}_{\mathbf{k}} + \frac{1}{2S} \sum_{\mathbf{k}_1, \mathbf{k}_2, \mathbf{q}} U(\mathbf{q}) \hat{a}_{\mathbf{k}_1 + \mathbf{q}}^\dagger \hat{a}_{\mathbf{k}_2 - \mathbf{q}}^\dagger \hat{a}_{\mathbf{k}_2} \hat{a}_{\mathbf{k}_1}, \quad (2.59)$$

where $\hat{a}_{\mathbf{k}}^\dagger$ and $\hat{a}_{\mathbf{k}}$ are creation and annihilation operators of fermionic polar molecules, and $U(\mathbf{q})$ is the Fourier transform of the interaction potential $U(r)$:

$$U(\mathbf{q}) = \int d^2 \mathbf{r} U(r) e^{-i\mathbf{q} \cdot \mathbf{r}}, \quad (2.60)$$

The first term of Eq. (2.59) represents the kinetic energy and it gives the main contribution to the total energy E of the system. This term has only diagonal matrix elements, and using the momentum distribution (3.5) at $T = 0$ we have:

$$\frac{E_{kin}}{S} = \int_0^{k_F} \frac{\hbar^2 k^2}{2m} \frac{2\pi k dk}{(2\pi)^2} = \frac{\hbar^2 k_F^4}{16m}. \quad (2.61)$$

The interaction between the fermionic molecules is described by the second term in Eq. (2.59) and compared to the kinetic energy it provides a correction to the total energy E . The first order correction is given by the diagonal matrix element of the interaction term of the Hamiltonian:

$$E^{(1)} = \frac{1}{2S} \sum_{\mathbf{k}_1, \mathbf{k}_2, \mathbf{q}} U(\mathbf{q}) \langle \hat{a}_{\mathbf{k}_1+\mathbf{q}}^\dagger \hat{a}_{\mathbf{k}_2-\mathbf{q}}^\dagger \hat{a}_{\mathbf{k}_2} \hat{a}_{\mathbf{k}_1} \rangle = \frac{1}{2S} \sum_{\mathbf{k}_1, \mathbf{k}_2} [U(0) - U(\mathbf{k}_2 - \mathbf{k}_1)] n_{\mathbf{k}_1} n_{\mathbf{k}_2}. \quad (2.62)$$

The second order correction to the energy of the state $|j\rangle$ of a non-interacting system can be expressed as:

$$E_j^{(2)} = \sum_{m \neq j} \frac{V_{jm} V_{mj}}{E_j - E_m}, \quad (2.63)$$

where the summation is over eigenstates $|m\rangle$ of the non-interacting system, and V_{jm} is the non-diagonal matrix element. In our case the symbol j corresponds to the ground state and the symbol m to excited states. The non-diagonal matrix element is

$$V_{jm} = \frac{1}{2S} \left\langle m \left| \sum_{\mathbf{k}_1, \mathbf{k}_2, \mathbf{q}} U(\mathbf{q}) \hat{a}_{\mathbf{k}_1+\mathbf{q}}^\dagger \hat{a}_{\mathbf{k}_2-\mathbf{q}}^\dagger \hat{a}_{\mathbf{k}_2} \hat{a}_{\mathbf{k}_1} \right| j \right\rangle. \quad (2.64)$$

This matrix element corresponds to the scattering of two particles from the initial state $\mathbf{k}_1, \mathbf{k}_2$ to an intermediate state $\mathbf{k}'_1, \mathbf{k}'_2$, and the matrix element V_{mj} describes the reversed process in which the two particles return from the intermediate to initial state. Taking into account the momentum conservation law $\mathbf{k}_1 + \mathbf{k}_2 = \mathbf{k}'_1 + \mathbf{k}'_2$ the quantity $V_{jm} V_{mj} = |V_{jm}|^2$ is given by

$$|V_{jm}|^2 = \frac{1}{(2S)^2} n_{\mathbf{k}_1} n_{\mathbf{k}_2} (1 - n_{\mathbf{k}'_1}) (1 - n_{\mathbf{k}'_2}) \times |U(\mathbf{k}'_1 - \mathbf{k}_1) - U(\mathbf{k}'_2 - \mathbf{k}_1)|^2, \quad (2.65)$$

and the second order correction to the ground state energy takes the form:

$$E^{(2)} = \frac{1}{(2S)^2} \sum_{\mathbf{k}_1, \mathbf{k}_2, \mathbf{k}'_1} \left[|U(\mathbf{k}'_1 - \mathbf{k}_1) - U(\mathbf{k}'_2 - \mathbf{k}_1)|^2 \times \frac{n_{\mathbf{k}_1} n_{\mathbf{k}_2} (1 - n_{\mathbf{k}'_1}) (1 - n_{\mathbf{k}'_2})}{\hbar^2 (\mathbf{k}_1^2 + \mathbf{k}_2^2 - \mathbf{k}'_1{}^2 - \mathbf{k}'_2{}^2) / 2m} \right]. \quad (2.66)$$

From Eq. (2.66) we see that the second order correction diverges because of the term proportional to $n_{\mathbf{k}_1} n_{\mathbf{k}_2}$, which is divergent at large k'_1 . This artificial divergence is

eliminated by expressing the energy correction in terms of a real physical quantity, the scattering amplitude. The relation between the Fourier component of the interaction potential and the off-shell scattering amplitude is given by [15]:

$$f(\mathbf{k}', \mathbf{k}) = U(\mathbf{k}' - \mathbf{k}) + \frac{1}{S} \sum_{\mathbf{k}''} \frac{U(\mathbf{k}' - \mathbf{k}'')f(\mathbf{k}'', \mathbf{k})}{(E_{\mathbf{k}} - E_{\mathbf{k}''} - i0)}, \quad (2.67)$$

where $E_{\mathbf{k}} = \hbar^2 \mathbf{k}^2/m$ and $E_{\mathbf{k}''} = \hbar^2 \mathbf{k}''^2/m$ are relative collision energies. Obviously, we have: $E_{\mathbf{k}} - E_{\mathbf{k}''} = \hbar^2(\mathbf{k}_1^2 + \mathbf{k}_2^2 - \mathbf{k}_1''^2 - \mathbf{k}_2''^2)/2m$, with $\mathbf{k}_1, \mathbf{k}_2$ ($\mathbf{k}_1'', \mathbf{k}_2''$) being the momenta of colliding particles in the initial (intermediate) state, as the relative momenta are given by $\mathbf{k} = (\mathbf{k}_1 - \mathbf{k}_2)/2$, $\mathbf{k}'' = (\mathbf{k}_1'' - \mathbf{k}_2'')/2$. We thus can write:

$$U(\mathbf{k}' - \mathbf{k}) = f(\mathbf{k}', \mathbf{k}) - \frac{2m}{\hbar^2 S} \sum_{\mathbf{k}_1''} \frac{U(\mathbf{k}' - \mathbf{k}'')f(\mathbf{k}'', \mathbf{k})}{\mathbf{k}_1^2 + \mathbf{k}_2^2 - \mathbf{k}_1''^2 - \mathbf{k}_2''^2 - i0}. \quad (2.68)$$

Then, putting $\mathbf{k}' = \mathbf{k}$ we have

$$U(0) = f(\mathbf{k}, \mathbf{k}) - \frac{2m}{\hbar^2 S} \sum_{\mathbf{k}_1''} \frac{U(\mathbf{k} - \mathbf{k}'')f(\mathbf{k}'', \mathbf{k})}{\mathbf{k}_1^2 + \mathbf{k}_2^2 - \mathbf{k}_1''^2 - \mathbf{k}_2''^2 - i0},$$

and setting $\mathbf{k}' = -\mathbf{k}$ we obtain

$$U(\mathbf{k}_2 - \mathbf{k}_1) = f(-\mathbf{k}, \mathbf{k}) - \frac{2m}{\hbar^2 S} \sum_{\mathbf{k}_1''} \frac{U(-\mathbf{k} - \mathbf{k}'')f(\mathbf{k}'', \mathbf{k})}{\mathbf{k}_1^2 + \mathbf{k}_2^2 - \mathbf{k}_1''^2 - \mathbf{k}_2''^2 - i0}.$$

Using these relations the first order correction (2.62) takes the form:

$$\begin{aligned} E^{(1)} &= \frac{1}{2S} \sum_{\mathbf{k}_1, \mathbf{k}_2} [f(\mathbf{k}, \mathbf{k}) - f(-\mathbf{k}, \mathbf{k})] n_{\mathbf{k}_1} n_{\mathbf{k}_2} \\ &- \frac{1}{2S^2} \sum_{\mathbf{k}_1, \mathbf{k}_2, \mathbf{k}_1''} \frac{[U(\mathbf{k} - \mathbf{k}') - U(-\mathbf{k} - \mathbf{k}')]f(\mathbf{k}', \mathbf{k})}{\hbar^2(\mathbf{k}_1^2 + \mathbf{k}_2^2 - \mathbf{k}_1''^2 - \mathbf{k}_2''^2 - i0)/2m} n_{\mathbf{k}_1} n_{\mathbf{k}_2}. \end{aligned} \quad (2.69)$$

The quantity $[U(\mathbf{k} - \mathbf{k}') - U(-\mathbf{k} - \mathbf{k}')] in the second term of Eq. (2.69), being expanded in circular harmonics $\exp(il\varphi)$ contains terms with odd l . Therefore, partial amplitudes with even l in the expansion of the multiple $f(\mathbf{k}', \mathbf{k})$ vanish after the integration over d^2k' . Hence, this amplitude can be replaced by $[f(\mathbf{k}', \mathbf{k}) - f(\mathbf{k}', -\mathbf{k})]/2$. As we are interested only in the terms that behave themselves as $\sim k$ or $\sim k^2$, the amplitudes in the second term of Eq. (2.69) are the ones that follow from the first Born approximation and are proportional to k . Therefore, we may put $[U(\mathbf{k} - \mathbf{k}') - U(-\mathbf{k} - \mathbf{k}')] = [f(\mathbf{k}, \mathbf{k}') - f(-\mathbf{k}, \mathbf{k}')] and $f(\mathbf{k}', \mathbf{k}) = f^*(\mathbf{k}, \mathbf{k}')$. Then the$$

first order correction takes the form:

$$E^{(1)} = \frac{1}{2S} \sum_{\mathbf{k}_1, \mathbf{k}_2} [f(\mathbf{k}, \mathbf{k}) - f(-\mathbf{k}, \mathbf{k})] n_{\mathbf{k}_1} n_{\mathbf{k}_2} - \frac{1}{(2S)^2} \times \sum_{\mathbf{k}_1, \mathbf{k}_2, \mathbf{k}'_1} \frac{|f(\mathbf{k}', \mathbf{k}) - f(\mathbf{k}', -\mathbf{k})|^2}{\hbar^2(\mathbf{k}_1^2 + \mathbf{k}_2^2 - \mathbf{k}'_1{}^2 - \mathbf{k}'_2{}^2 - i0)/2m} n_{\mathbf{k}_1} n_{\mathbf{k}_2}. \quad (2.70)$$

Using the expansion of the full scattering amplitude in terms of partial amplitudes as given by Eq. (2.47) we represent the first order correction as

$$E^{(1)} = \frac{1}{S} \sum_{\mathbf{k}_1, \mathbf{k}_2} \sum_{l \text{ odd}} f_l(k) n_{\mathbf{k}_1} n_{\mathbf{k}_2} - \frac{1}{S^2} \sum_{\mathbf{k}_1, \mathbf{k}_2} \sum_{l \text{ odd}} \times \int \frac{d^2 k'}{(2\pi)^2} \frac{f_l^2(k)}{\hbar^2(\mathbf{k}_1^2 + \mathbf{k}_2^2 - \mathbf{k}'_1{}^2 - \mathbf{k}'_2{}^2 - i0)/2m} n_{\mathbf{k}_1} n_{\mathbf{k}_2}. \quad (2.71)$$

The contribution of the pole in the integration over $d^2 k'$ in the second term of Eq. (2.71) gives $imf_l^2(k)/4\hbar^2$ for each term in the sum over \mathbf{k}_1 , \mathbf{k}_2 , and l , and we may use here the amplitude $\bar{f}_l^{(1)}(k)$. In the first term of Eq. (2.71) we should use $f_l(k) = f_l^{(1)}(k) + f_l^{(2)}(k)$. However, we may replace $f_l^{(2)}$ by $\bar{f}_l^{(2)}$ because the account of $\tan \delta(k)$ in the denominator of Eq. (2.15) leads to k^3 terms and terms containing higher powers of k . For the amplitude $f_l^{(1)}(k)$, we use the expression:

$$f_l^{(1)}(k) = \bar{f}_l^{(1)} + i \tan \delta(k) \bar{f}_l^{(1)} = \bar{f}_l^{(1)} - im[\bar{f}_l^{(1)}]^2/4\hbar^2,$$

which assumes a small scattering phase shift. The second term of this expression, being substituted into the first line of Eq. (2.71), exactly cancels the contribution of the pole in the second term of (2.71). Thus, we may use the amplitude \bar{f}_l in the first term of equation (2.71) and take the principal value of the integral in the second term. The resulting expression for the first order correction reads:

$$E^{(1)} = \frac{1}{S} \sum_{\mathbf{k}_1, \mathbf{k}_2} \bar{f}(\mathbf{k}) n_{\mathbf{k}_1} n_{\mathbf{k}_2} - \frac{1}{(2S)^2} \times \sum_{\mathbf{k}_1, \mathbf{k}_2, \mathbf{k}'_1} \frac{2m|f(\mathbf{k}, \mathbf{k}') - f(-\mathbf{k}, \mathbf{k}')|^2}{\hbar^2(\mathbf{k}_1^2 + \mathbf{k}_2^2 - \mathbf{k}'_1{}^2 - \mathbf{k}'_2{}^2)} n_{\mathbf{k}_1} n_{\mathbf{k}_2}, \quad (2.72)$$

where $\bar{f}(\mathbf{k}) = \sum_{l \text{ odd}} \bar{f}_l(k)$.

The second order correction (2.66) can also be expressed in terms of the scattering amplitude by using Eq.(2.67). Replacing $U(\mathbf{k}_1 - \mathbf{k}'_1) = U(\mathbf{k} - \mathbf{k}')$ and $U(\mathbf{k}'_2 - \mathbf{k}_1) = U(-\mathbf{k} - \mathbf{k}')$ by $f(\mathbf{k}', \mathbf{k})$ and $f(-\mathbf{k}, \mathbf{k}')$, respectively, we have:

$$E^{(2)} = \frac{1}{(2S)^2} \sum_{\mathbf{k}_1, \mathbf{k}_2, \mathbf{k}'_1} \left[\frac{|f(\mathbf{k}', \mathbf{k}) - f(\mathbf{k}', -\mathbf{k})|^2}{\hbar^2(\mathbf{k}_1^2 + \mathbf{k}_2^2 - \mathbf{k}'_1{}^2 - \mathbf{k}'_2{}^2)/2m} \times n_{\mathbf{k}_1} n_{\mathbf{k}_2} (1 - n_{\mathbf{k}'_1})(1 - n_{\mathbf{k}'_2}) \right]. \quad (2.73)$$

Note that the divergent term proportional to $n_{\mathbf{k}_1} n_{\mathbf{k}_2}$ in Eq. (2.73) and the (diver-

gent) second term of Eq. (2.72) exactly cancel each other, and the sum of the first and second order corrections can be represented as $E^{(1)} + E^{(2)} = \tilde{E}^{(1)} + \tilde{E}^{(2)}$, where

$$\tilde{E}^{(1)} = \frac{1}{S} \sum_{\mathbf{k}_1, \mathbf{k}_2} \bar{f}(\mathbf{k}) n_{\mathbf{k}_1} n_{\mathbf{k}_2}, \quad (2.74)$$

and

$$\tilde{E}^{(2)} = \frac{1}{(2S)^2} \sum_{\mathbf{k}_1, \mathbf{k}_2, \mathbf{k}'_1} \left\{ \frac{|f(\mathbf{k}', \mathbf{k}) - f(\mathbf{k}', -\mathbf{k})|^2}{\hbar^2(\mathbf{k}_1^2 + \mathbf{k}_2^2 - \mathbf{k}'_1{}^2 - \mathbf{k}'_2{}^2)/2m} \times n_{\mathbf{k}_1} n_{\mathbf{k}_2} [(1 - n_{\mathbf{k}'_1})(1 - n_{\mathbf{k}'_2}) - 1] \right\}. \quad (2.75)$$

The term $\tilde{E}^{(1)}$ originates from the two-body contributions to the interaction energy and can be quoted as the mean field term. The term $\tilde{E}^{(2)}$ is the many-body contribution, which is beyond mean field.

It is worth noting that the term proportional to the product of four occupation numbers vanishes because its numerator is symmetrical and the denominator is anti-symmetrical with respect to an interchange of $\mathbf{k}_1, \mathbf{k}_2$ and $\mathbf{k}'_1, \mathbf{k}'_2$. The terms containing a product of three occupation numbers, $n_{\mathbf{k}_1} n_{\mathbf{k}_2} n_{\mathbf{k}'_1}$ and $n_{\mathbf{k}_1} n_{\mathbf{k}_2} n_{\mathbf{k}'_2}$ are equal to each other because the denominator is symmetrical with respect to an interchange of \mathbf{k}'_1 and \mathbf{k}'_2 . We thus reduce Eq. (2.75) to

$$\tilde{E}^{(2)} = -\frac{1}{2S^2} \sum_{\mathbf{k}_1, \mathbf{k}_2, \mathbf{k}'_1} \frac{2m|f(\mathbf{k}', \mathbf{k}) - f(\mathbf{k}', -\mathbf{k})|^2}{\hbar^2(\mathbf{k}_1^2 + \mathbf{k}_2^2 - \mathbf{k}'_1{}^2 - \mathbf{k}'_2{}^2)} n_{\mathbf{k}_1} n_{\mathbf{k}_2} n_{\mathbf{k}'_1}. \quad (2.76)$$

Equations (2.74) and (2.76) allow a direct calculation of the ground state energy. With respect to the mean field term $\tilde{E}^{(1)}$ this is done in Appendix A.1. However, a direct calculation of the many-body correction $\tilde{E}^{(2)}$ is even a more tedious task than in the case of two-component fermions with a contact interaction. We therefore turn to the Abrikosov-Khalatnikov idea of calculating the ground state energy (and other thermodynamic quantities) through the interaction function of quasiparticles on the Fermi surface.

2.3.3. Interaction function of quasiparticles

The interaction function of quasiparticles $F(\mathbf{k}, \mathbf{k}')$ is the second variational derivative of the total energy with respect to the distribution $n_{\mathbf{k}}$. The kinetic energy of our system is linear in $n_{\mathbf{k}}$ (see Eq. (2.59)), and the second variational derivative is related to the variation of the interaction energy \tilde{E} . We have [68]:

$$\delta \tilde{E} = \frac{1}{2S} \sum_{\mathbf{k}, \mathbf{k}'} F(\mathbf{k}, \mathbf{k}') \delta n_{\mathbf{k}} \delta n_{\mathbf{k}'}, \quad (2.77)$$

where $\tilde{E} = \tilde{E}^{(1)} + \tilde{E}^{(2)}$, and the quantities $\tilde{E}^{(1)}$ and $\tilde{E}^{(2)}$ are given by equations (2.74) and (2.76). On the Fermi surface we should put $|\mathbf{k}| = |\mathbf{k}'| = k_F$, so that the

interaction function will depend only on the angle θ between \mathbf{k} and \mathbf{k}' . Hereinafter it will be denoted as $\tilde{F}(\theta)$.

The contribution $\tilde{F}^{(1)}(\theta) = 2S\delta\tilde{E}^{(1)}/\delta n_{\mathbf{k}}\delta n_{\mathbf{k}'}$ is given by

$$\tilde{F}^{(1)}(\theta) = 2f\left(\frac{|\mathbf{k} - \mathbf{k}'|}{2}\right) = 2\sum_{l \text{ odd}} \bar{f}_l\left(k_F|\sin\frac{\theta}{2}|\right), \quad (2.78)$$

where $\bar{f}_l = \bar{f}_l^{(1)} + \bar{f}_l^{(2)}$, and the amplitudes $\bar{f}_l^{(1)}$ and $\bar{f}_l^{(2)}$ follow from Eqs. (2.32) and (2.33) at $|l| = 1$, and from Eqs. (2.42), (2.43) at $|l| > 1$. We thus may write equation (2.42),

$$\bar{f}_l^{(1)}(k) = \frac{8\hbar^2}{m} \frac{1}{4l^2 - 1} kr_*,$$

for any odd l , and

$$\bar{f}_l^{(2)}(k) = \frac{\pi\hbar^2}{2m} (kr_*)^2 \times \begin{cases} \ln(\xi kr_*); & |l| = 1 \\ -\frac{3}{|l|(l^2-1)(4l^2-1)}; & |l| > 1 \end{cases}$$

with ξ from Eq. (2.30). Making a summation over all odd l we obtain:

$$\bar{f}^{(1)}(k) = \sum_{l \text{ odd}} \bar{f}_l^{(1)}(k) = \frac{2\pi\hbar^2}{m} kr_*, \quad (2.79)$$

$$\bar{f}^{(2)}(k) = \sum_{l \text{ odd}} \bar{f}_l^{(2)}(k) = \frac{\pi\hbar^2}{m} (kr_*)^2 \left[\ln(\xi kr_*) - \frac{25}{12} + 3\ln 2 \right]. \quad (2.80)$$

Putting $k = k_F|\sin(\theta/2)|$ and substituting the results of equations (2.79) and (2.80) into Eq. (2.78) we find:

$$\begin{aligned} \tilde{F}^{(1)}(\theta) &= \frac{4\pi\hbar^2 k_F r_*}{m} |\sin\frac{\theta}{2}| + \frac{2\hbar^2}{m} (k_F r_*)^2 \\ &\times \pi \sin^2\frac{\theta}{2} \left[\ln|\xi r_* k_F \sin\frac{\theta}{2}| - \frac{25}{12} + 3\ln 2 \right]. \end{aligned} \quad (2.81)$$

The many-body correction (2.76) we represent as $\tilde{E}^{(2)} = \tilde{E}_1^{(2)} + \tilde{E}_2^{(2)}$, where

$$\tilde{E}_1^{(2)} = -\frac{8(\pi\hbar r_*)^2}{mS^2} \sum_{\mathbf{k}_1, \mathbf{k}_2, \mathbf{k}'_1} \frac{|\mathbf{k}'_1 - \mathbf{k}_1|^2}{\mathbf{k}_1^2 + \mathbf{k}_2^2 - \mathbf{k}'_1{}^2 - \mathbf{k}'_2{}^2} n_{\mathbf{k}_1} n_{\mathbf{k}_2} n_{\mathbf{k}'_1}, \quad (2.82)$$

$$\tilde{E}_2^{(2)} = \frac{8(\pi\hbar r_*)^2}{mS^2} \sum_{\mathbf{k}_1, \mathbf{k}_2, \mathbf{k}'_1} \frac{|\mathbf{k}_1 - \mathbf{k}'_1| \cdot |\mathbf{k}_2 - \mathbf{k}'_1|}{\mathbf{k}_1^2 + \mathbf{k}_2^2 - \mathbf{k}'_1{}^2 - \mathbf{k}'_2{}^2} n_{\mathbf{k}_1} n_{\mathbf{k}_2} n_{\mathbf{k}'_1}, \quad (2.83)$$

and we used Eqs (2.46) and (2.49) for the scattering amplitudes. The contribution

to the interaction function from $\tilde{E}_1^{(2)}$ is calculated in Appendix A.2 and it reads:

$$\tilde{F}_1^{(2)}(\theta) = \frac{2\hbar^2(k_F r_*)^2}{m} \left[3\pi + 2\pi \sin^2 \frac{\theta}{2} \left(\frac{4}{3} - \ln \left| \tan \frac{\theta}{2} \right| \right) \right]. \quad (2.84)$$

The contribution from $\tilde{E}_2^{(2)}$ is calculated in Appendix A.3. It is given by

$$\begin{aligned} \tilde{F}_2^{(2)}(\theta) = & \frac{2\hbar^2 k_F^2 r_*^2}{m} \left\{ -\sin^2 \frac{\theta}{2} \left\{ \pi \ln 2 + \frac{\pi}{2} - \pi \ln \left| \sin \frac{\theta}{2} \right| + 4 \ln \left| \cos \frac{\theta}{2} \right| - 4 \ln(1 + \left| \sin \frac{\theta}{2} \right|) \right. \right. \\ & + \mathcal{G}(\theta) + \frac{4 \arcsin \left| \sin \frac{\theta}{2} \right| - 2\pi}{\left| \cos \frac{\theta}{2} \right|} \left. \right\} - \frac{1}{\left| \cos \frac{\theta}{2} \right|} \left(\pi - 2 \arcsin \left| \sin \frac{\theta}{2} \right| + \left| \sin \theta \right| \right) \\ & - 4 \left[\cos^2 \frac{\theta}{2} \ln \frac{1 + \left| \sin(\theta/2) \right|}{1 - \left| \sin(\theta/2) \right|} + 2 \left| \sin \frac{\theta}{2} \right| \right] \left. \right\}, \end{aligned} \quad (2.85)$$

where

$$\mathcal{G}(\theta) = \int_0^\pi 2 \sin^2 \varphi \ln \left(\sin \varphi + \sqrt{\sin^2 \frac{\theta}{2} + \cos^2 \frac{\theta}{2} \sin^2 \varphi} \right) d\varphi,$$

so that

$$\frac{d\mathcal{G}(\theta)}{d\theta} = \frac{\pi}{2} \cot \frac{\theta}{2} - \frac{\left| \sin(\theta/2) \right|}{\sin(\theta/2)} \frac{1}{\cos(\theta/2)} + \frac{\arcsin \left| \cos(\theta/2) \right|}{\left| \cos(\theta/2) \right|} \left(\tan \frac{\theta}{2} - \cot \frac{\theta}{2} \right). \quad (2.86)$$

We thus have $\tilde{F}(\theta) = \tilde{F}^{(1)}(\theta) + \tilde{F}_1^{(2)}(\theta) + \tilde{F}_2^{(2)}(\theta)$, where $\tilde{F}^{(1)}$, $\tilde{F}_1^{(2)}$, $\tilde{F}_2^{(2)}$ follow from Eqs. (3.20), (2.84), and (2.85). This allows us to proceed with the calculation of thermodynamic quantities.

2.3.4. Compressibility, ground state energy, and effective mass

We first calculate the compressibility at $T = 0$. On the basis of Eq. (2.58) we obtain:

$$\begin{aligned} \frac{\partial \mu}{\partial N} &= \frac{2\pi\hbar^2}{mS} + \frac{1}{2\pi S} \int (1 - \cos \theta) \left[\tilde{F}^{(1)}(\theta) + \tilde{F}_1^{(2)}(\theta) + \tilde{F}_2^{(2)}(\theta) \right] d\theta \\ &= \frac{2\pi\hbar^2}{mS} + \frac{32\hbar^2}{3mS} k_F r_* + \frac{3\pi\hbar^2}{2mS} (k_F r_*)^2 \left(\ln[4\xi k_F r_*] - \frac{3}{2} \right) \\ &+ \frac{6\pi\hbar^2}{mS} (k_F r_*)^2 - \frac{\hbar^2}{\pi mS} (k_F r_*)^2 (30 - 8G + 21\zeta(3)), \end{aligned} \quad (2.87)$$

where $G = 0.915966$ is the Catalan constant, and $\zeta(3) = 1.20206$ is the Riemann zeta function. Calculating coefficients and recalling that $k_F = \sqrt{4\pi N/S}$ we represent the inverse compressibility following from Eq. (2.55) in a compact form:

$$\kappa^{-1} = \frac{\hbar^2 k_F^2 N}{2m S} \left(1 + \frac{16}{3\pi} k_F r_* + \frac{3}{4} (k_F r_*)^2 \ln(\zeta_1 k_F r_*) \right), \quad (2.88)$$

where we obtain the coefficient $\zeta_1 = 2.16 \exp(-2A)$ by using Eq. (2.30) for the coefficient ξ which depends on the short-range behavior through the constant A (see Eq. (2.18)). For the chemical potential and ground state energy we obtain:

$$\begin{aligned} \mu &= \frac{2\pi\hbar^2 N}{mS} + \frac{64\hbar^2 N}{9mS} k_{Fr_*} + \frac{3\pi\hbar^2 N}{4mS} (k_{Fr_*})^2 \left(\ln[4\xi k_{Fr_*}] - \frac{7}{4} \right) \\ &+ \frac{3\pi\hbar^2 N}{mS} (k_{Fr_*})^2 - \frac{\hbar^2 N}{2\pi mS} (k_{Fr_*})^2 (30 - 8G + 21\zeta(3)) \\ &= \frac{\hbar^2 k_F^2}{2m} \left(1 + \frac{32}{9\pi} k_{Fr_*} + \frac{3}{8} (k_{Fr_*})^2 \ln(\zeta_2 k_{Fr_*}) \right). \end{aligned} \quad (2.89)$$

$$\begin{aligned} \frac{E}{N} &= \frac{\pi\hbar^2 N}{mS} + \frac{128\hbar^2 N}{45mS} k_{Fr_*} + \frac{\pi\hbar^2 N}{4mS} (k_{Fr_*})^2 \left(\ln[4\xi k_{Fr_*}] - \frac{23}{12} \right) \\ &+ \frac{\pi\hbar^2 N}{mS} - \frac{\hbar^2 N}{6\pi mS} (30 - 8G + 21\zeta(3)) \\ &= \frac{\hbar^2 k_F^2}{4m} \left(1 + \frac{128}{45\pi} k_{Fr_*} + \frac{1}{4} (k_{Fr_*})^2 \ln(\zeta_3 k_{Fr_*}) \right), \end{aligned} \quad (2.90)$$

with numerical coefficients $\zeta_2 = 1.68 \exp(-2A)$ and $\zeta_3 = 1.43 \exp(-2A)$. Note that the first term in the second line of Eq. (2.87) and the first terms in the first lines of Eqs. (2.89) and (2.90) represent the contributions of the kinetic energy, the second and third terms correspond to the contributions of the mean field part of the interaction energy, and the last two terms are the contributions of the many-body effects.

The effective mass is calculated in a similar way by using Eq. (2.54):

$$\begin{aligned} \frac{1}{m^*} &= \frac{1}{m} - \frac{1}{(2\pi\hbar)^2} \int_0^{2\pi} (F^{(1)}(\theta) + F_1^{(2)}(\theta) + F_2^{(2)}(\theta)) \cos \theta d\theta \\ &= \frac{1}{m} \left[1 + \frac{4k_{Fr_*}}{3\pi} + \frac{(k_{Fr_*})^2}{4} \left(\ln[4k_{Fr_*}\xi] - \frac{8}{3} + \frac{48G - 20 - 14\zeta(3)}{\pi^2} \right) \right] \\ &= \frac{1}{m} \left[1 + \frac{4}{3\pi} k_{Fr_*} + \frac{1}{4} (k_{Fr_*})^2 \ln(\zeta_4 k_{Fr_*}) \right], \end{aligned} \quad (2.91)$$

where the numerical coefficient $\zeta_4 = 0.65 \exp(-2A)$. Note that if the potential $U(r)$ has the dipole-dipole form (2.1) up to very short distances, we have to put $A = 0$ in the expressions for the coefficients $\zeta_1, \zeta_2, \zeta_3, \zeta_4$. Considering the quasi2D regime, this will be the case for r_* greatly exceeding the length of the sample in the tightly confined direction, l_0 . Then, as one can see from equations (2.88), (2.89), (2.90), and (2.91), the terms proportional to $(k_{Fr_*})^2$ are always negative in the considered limit $k_{Fr_*} \ll 1$. These terms may become significant for $k_{Fr_*} > 0.3$.

2.4. Zero sound

In the collisionless regime of the Fermi liquid at very low temperatures, where the frequency of variations of the momentum distribution function greatly exceeds the relaxation rate of quasiparticles, one has zero sound waves. For these waves, variations $\delta n(\mathbf{q}, \mathbf{r}, t)$ of the momentum distribution are related to deformations of the Fermi surface, which remains a sharp boundary between filled and empty quasiparticle states. At $T \rightarrow 0$ the equilibrium distribution $n_{\mathbf{q}}$ is the step function (3.5), so that $\partial n_{\mathbf{q}}/\partial \mathbf{q} = -\mathbf{n}\delta(q - k_F) = -\hbar\mathbf{v}\delta(\epsilon_q - \epsilon_F)$, where $\mathbf{v} = v_F\mathbf{n}$, with \mathbf{n} being a unit vector in the direction of \mathbf{q} . Then, searching for the variations δn in the form:

$$\delta n(\mathbf{q}, \mathbf{r}, t) = \delta(\epsilon_q - \epsilon_F)\nu(\mathbf{n}) \exp i(\mathbf{k}\mathbf{r} - \omega t)$$

and using Eq. (3.6), from the kinetic equation in the collisionless regime:

$$\frac{\partial \delta n}{\partial t} + \mathbf{v} \cdot \frac{\partial \delta n}{\partial \mathbf{r}} - \frac{\partial n_{\mathbf{q}}}{\partial \mathbf{q}} \cdot \frac{\partial \delta \epsilon_q}{\hbar \partial \mathbf{r}} = 0,$$

one obtains an integral equation for the function $\nu(\mathbf{n})$ representing displacements of the Fermi surface in the direction of \mathbf{n} [68]:

$$(\omega - v_F \mathbf{n} \cdot \mathbf{k})\nu(\mathbf{n}) = \frac{k_F}{(2\pi)^2 \hbar} \mathbf{n} \cdot \mathbf{k} \int F(k_F \mathbf{n}, k_F \mathbf{n}')\nu(\mathbf{n}') d\mathbf{n}'.$$

Introducing the velocity of zero sound $u_0 = \omega/k$ and dividing both sides of this equation by $v_F k$ we have:

$$(s - \cos \theta)\nu(\theta) = \frac{m^* \cos \theta}{(2\pi \hbar)^2} \int_0^{2\pi} \tilde{F}(\theta - \theta')\nu(\theta') d\theta', \quad (2.92)$$

where $s = u_0/v_F$, and θ, θ' are the angles between \mathbf{k} and \mathbf{n}, \mathbf{n}' , so that $\theta - \theta'$ is the angle between \mathbf{n} and \mathbf{n}' . The dependence of the interaction function of quasiparticles $\tilde{F} = \tilde{F}^{(1)} + \tilde{F}_1^{(2)} + \tilde{F}_2^{(2)}$ on $(\theta - \theta')$ follows from Eqs. (3.20), (2.84), and (2.85) in which one has to replace θ by $(\theta - \theta')$.

The solution of equation (2.92) gives the function $\nu(\theta)$ and the velocity of zero sound u_0 , and in principle one may obtain several types of solutions. It is important to emphasize that undamped zero sound requires the condition $s > 1$, i.e. the sound velocity should exceed the Fermi velocity [68]. We will discuss this issue below.

For solving Eq. (2.92) we represent the interaction function \tilde{F} as a sum of the part proportional to $k_F r_*$ and the part proportional to $(k_F r_*)^2$. As follows from Eqs. (3.20), (2.84), and (2.85), we have:

$$\tilde{F}(\theta - \theta') = \frac{4\pi \hbar^2}{m} k_F r_* \left| \sin \frac{\theta - \theta'}{2} \right| + \frac{2\hbar^2}{m} (k_F r_*)^2 \Phi(\theta - \theta'), \quad (2.93)$$

where the function $\Phi(\theta - \theta')$ is given by the sum of three terms. The first one is the

term in the second line of Eq. (3.20), the second term is the expression in the square brackets in Eq. (2.84), the third term is the one in curly brackets in Eq. (2.85), and we should replace θ by $(\theta - \theta')$ in all these terms. It is important that the function $\Phi(\theta - \theta')$ does not have singularities and $\Phi(0) = \Phi(\pm 2\pi) = 2\pi$. Using Eq. (2.93) the integral equation (2.92) is reduced to the form:

$$(s - \cos \theta)\nu(\theta) = \beta \cos \theta \int_0^{2\pi} \nu(\theta') \left| \sin \frac{\theta - \theta'}{2} \right| d\theta' + \frac{\beta^2 m}{2m^*} \cos \theta \int_0^{2\pi} \nu(\theta') \Phi(\theta - \theta') d\theta', \quad (2.94)$$

where $\beta = (m^*/\pi m)k_F r_* \ll 1$.

We now represent the function $\nu(\theta)$ as

$$\nu(\theta) = \sum_{p=0}^{\infty} C_p \cos p\theta. \quad (2.95)$$

Then, integrating over $d\theta'$ in Eq. (2.94), multiplying both sides of this equation by $\cos j\theta$ and integrating over $d\theta$, we obtain a system of linear equations for the coefficients C_j . We write this system for the coefficients $\eta_j = C_j(1 - \beta/(j^2 - 1/4))$, so that $C_j = \eta_j(1 + \beta U_j)$, where $U_j = (j^2 - 1/4 - \beta)^{-1}$. The system reads:

$$(s - 1)(1 + \beta U_0)\eta_0 + [\eta_0 - \frac{1}{2}\eta_1] + \beta U_0\eta_0 = \frac{\beta^2}{2}\bar{\Phi}_0; \quad (2.96)$$

$$(s - 1)(1 + \beta U_1)\eta_1 + [\eta_1 - \eta_0 - \frac{1}{2}\eta_2] + \beta U_1\eta_1 = \frac{\beta^2}{2}\bar{\Phi}_1; \quad (2.97)$$

$$(s - 1)(1 + \beta U_j)\eta_j + [\eta_j - \frac{1}{2}(\eta_{j-1} + \eta_{j+1})] + \beta U_j\eta_j = \frac{\beta^2}{2}\bar{\Phi}_j; \quad j \geq 2, \quad (2.98)$$

where

$$\bar{\Phi}_j = \frac{\tilde{C}_j}{\pi} \int_0^{2\pi} \cos \theta \cos j\theta d\theta \int_0^{2\pi} \sum_{p=0}^{\infty} C_p \cos p\theta' \Phi(\theta - \theta') d\theta', \quad (2.99)$$

with $\tilde{C}_j = 1$ for $j \geq 1$ and $\tilde{C}_0 = 1/2$, and we put $m^* = m$ in the terms proportional to β^2 .

In the weakly interacting regime the velocity of zero sound is close to the Fermi velocity and, hence, we have $(s - 1) \ll 1$ (see, e.g. [68]). Since $\beta \ll 1$, we first find coefficients η_j omitting the terms proportional to β and β^2 in Eqs. (2.96)-(2.98). For $j \gg 1$ equation (2.98) then becomes:

$$(s - 1)\eta_j - \frac{1}{2} \frac{d^2 \eta_j}{dj^2} = 0,$$

and searching for $s > 1$ we may write

$$\eta_j \simeq \exp\{-\sqrt{2(s-1)}j\}; \quad j \gg 1. \quad (2.100)$$

If $j \ll 1/\sqrt{s-1}$, then we may also omit the terms proportional to $(s-1)$ in the system of linear equations for η_j (2.96)-(2.98). The system then takes the form:

$$\begin{aligned}\eta_0 - \frac{1}{2}\eta_1 &= 0; \\ \eta_1 - \eta_0 - \frac{1}{2}\eta_2 &= 0; \\ \eta_j - \frac{1}{2}[\eta_{j-1} + \eta_{j+1}] &= 0; j \geq 2.\end{aligned}$$

Without loss of generality we may put $\eta_0 = 1/2$. This immediately gives $\eta_j = 1$ for $j \geq 1$, which is consistent with Eq. (2.100) at $j \ll 1/\sqrt{s-1}$. We thus have the zero order solution:

$$\begin{cases} \eta_0 = 1/2; \\ \eta_j = 1; 1 \leq j \ll 1/\sqrt{s-1}. \end{cases} \quad (2.101)$$

In order to find the coefficients η_j taking into account the terms linear in β , we consider j such that $\beta U_j \sim \beta/j^2 \gg (s-1)$, i.e. $j \ll \sqrt{\beta/(s-1)}$. Then we may omit the terms proportional to $(s-1)$ in equations (2.96)-(2.98). Omitting also the terms proportional to β^2 this system of equations becomes:

$$\eta_0 - \frac{1}{2}\eta_1 + \beta U_0 \eta_0 = 0; \quad (2.102)$$

$$\eta_1 - \eta_0 - \frac{1}{2}\eta_2 + \beta U_1 \eta_1 = 0; \quad (2.103)$$

$$\eta_j - \frac{1}{2}[\eta_{j-1} + \eta_{j+1}] + \beta U_j \eta_j = 0; j \geq 2. \quad (2.104)$$

Putting again $\eta_0 = 1/2$ the solution of these equations reads:

$$\eta_1 = 1 + \beta U_0;$$

$$\eta_j = 1 + \beta j U_0 + 2\beta \sum_{p=1}^{j-1} (j-p) U_p; j \geq 2.$$

Confining ourselves to terms linear in β we put $U_p = 1/(p^2 - 1/4)$ and, hence, $U_0 = -4$. Then, using the relation

$$\sum_{p=1}^{j-1} \frac{1}{p^2 - 1/4} = \frac{4(j-1)}{2j-1},$$

which is valid for $j \geq 2$, we obtain:

$$\left\{ \begin{array}{l} \eta_0 = \frac{1}{2}; \\ \eta_1 = 1 - 4\beta; \\ \eta_j = 1 - 2\beta \left\{ \frac{2j}{2j-1} + \sum_{p=1}^{j-1} \frac{p}{p^2-1/4} \right\}; \quad j \geq 2. \end{array} \right. \quad (2.105)$$

For $j \gtrsim \sqrt{\beta/(s-1)}$ we should include the terms proportional to $(s-1)$ in Eq. (2.104). This leads to the solution in the form of the decaying Bessel function:

$$\eta_j \simeq \sqrt{2(s-1)/\pi} K_{\sqrt{1/4+\beta}}(\sqrt{s-1}j),$$

which for small β is practically equivalent to Eq. (2.100).

We now make a summation of equations (2.96)-(2.98) from $j = 0$ to $j = j_* \ll 1/\sqrt{s-1}$. The summation of the second terms of these equations gives $\sqrt{(s-1)}/2$, whereas the contribution of the terms proportional to $(s-1)$ is much smaller and will be omitted. The sums $\sum_{j=0}^{j_*} U_j \eta_j$ and $\sum_{j=0}^{j_*} \bar{\Phi}_j$ converge at $j \ll 1/\sqrt{s-1}$, and the upper limit of summation in these terms can be formally replaced by infinity. We thus obtain a relation:

$$\sqrt{\frac{s-1}{2}} + \sum_{j=0}^{\infty} \beta \eta_j U_j - \frac{\beta^2}{2} \sum_{j=0}^{\infty} \bar{\Phi}_j = 0. \quad (2.106)$$

Confining ourselves to contributions up to β^2 , in the second term on the left hand side of Eq. (2.106) we use coefficients η_j given by Eqs. (2.105), and write $U_j = 1/(j^2 - 1/4) + \beta/(j^2 - 1/4)^2$. In the expressions for $\bar{\Phi}_j$ we use $C_0 = 1/2$ and $C_p = 1$ for $p \geq 1$. We then have:

$$\sum_{j=0}^{\infty} \beta \eta_j U_j = -2\beta + \sum_{j=1}^{\infty} \frac{\beta}{j^2 - 1/4} + \beta^2 \{8 + S_1 - 2S_2 - 2S_3\}. \quad (2.107)$$

The contribution linear in β vanishes because $\sum_{j=1}^{\infty} 1/(j^2 - 1/4) = 2$. The quantities

S_1 , S_2 , and S_3 are given by

$$\begin{aligned} S_1 &= \sum_{j=1}^{\infty} \frac{1}{(j^2 - 1/4)^2} = \pi^2 - 8; \\ S_2 &= \sum_{j=2}^{\infty} \frac{1}{j^2 - 1/4} \sum_{p=1}^{j-1} \frac{p}{p^2 - 1/4} = \sum_{j=1}^{\infty} \frac{j}{(j^2 - 1/4)(j + 1/2)}; \\ S_3 &= \sum_{j=1}^{\infty} \frac{j}{(j - 1/2)(j^2 - 1/4)}, \end{aligned}$$

so that

$$S_2 + S_3 = \sum_{j=1}^{\infty} \frac{2j^2}{(j^2 - 1/4)^2} = \frac{\pi^2}{2}.$$

We thus see that the contribution quadratic in β also vanishes because the term in the curly brackets in Eq. (2.107) is exactly equal to zero. Hence, we have $\sum_{j=0}^{\infty} \beta \eta_j U_j = 0$ up to terms proportional to β^2 .

The sum in the third term on the left hand side of Eq. (2.106), after putting $C_0 = 1/2$ and $C_p = 1$ for $p \geq 1$ in the relations for $\bar{\Phi}_j$, reduces to

$$\begin{aligned} \sum_{j=0}^{\infty} \bar{\Phi}_j &= \frac{1}{4\pi} \sum_{j=-\infty}^{\infty} \int_0^{2\pi} \cos \theta \cos j\theta d\theta \\ &\quad \times \sum_{p=-\infty}^{\infty} \int_0^{2\pi} \cos p\theta' \Phi(\theta - \theta') d\theta'. \end{aligned} \quad (2.108)$$

For θ in the interval $0 \leq \theta \leq 2\pi$ we have a relation:

$$\sum_{j=-\infty}^{\infty} \cos j\theta = \pi[\delta(\theta) + \delta(\theta - 2\pi)],$$

which transforms Eq. (2.108) to

$$\sum_{j=0}^{\infty} \bar{\Phi}_j = \frac{\pi}{4} [2\Phi(0) + \Phi(2\pi) + \Phi(-2\pi)] = 2\pi^2, \quad (2.109)$$

and equation (2.106) becomes:

$$\sqrt{\frac{s-1}{2}} - \beta^2 \pi^2 = 0.$$

This gives $s = 1 + 2(\beta\pi)^4$, and recalling that $\beta = k_F r^*/\pi$ (we put $m^* = m$) we obtain

for the velocity of zero sound:

$$u_0 = v_F[1 + 2(k_F r_*)^4]. \quad (2.110)$$

Note that in contrast to the 3D two-species Fermi gas with a weak repulsive contact interaction (scattering length a), where the correction $(u_0 - v_F)$ exponentially depends on $k_F a$, for our 2D dipolar gas we obtained a power law dependence. This is a consequence of dimensionality of the system.

It is important that confining ourselves to only the leading part of the interaction function \tilde{F} , which is proportional to $k_F r_*$ and is given by the first term of Eq. (3.20), we do not obtain undamped zero sound ($s > 1$)¹. This corresponds to omitting the terms $\beta^2 \tilde{\Phi}_j/2$ in equations (2.96)-(2.98) and is consistent with numerical calculations [54]. Only the many-body corrections to the interaction function of quasiparticles, given by equations (2.84) and (2.85), provide non-zero positive values of $\Phi(0)$ and $\Phi(\pm 2\pi)$, thus leading to a positive value of $(u_0 - v_F)$. One then sees that many-body effects are crucial for the propagation of zero sound.

In principle, we could obtain the result of Eq. (2.110) in a simpler way, similar to that used for the two-species Fermi gas with a weak repulsive interaction (see, e.g. [68]). Representing the function $\nu(\theta)$ as $\nu(\theta) = \cos \theta \tilde{\nu}(\theta)/(s - \cos \theta)$ we transform Eq. (2.92) to the form:

$$\tilde{\nu}(\theta) = \frac{m^*}{(2\pi\hbar)^2} \int_0^{2\pi} \frac{\tilde{F}(\theta - \theta') \tilde{\nu}(\theta') \cos \theta'}{s - \cos \theta'} d\theta'. \quad (2.111)$$

Since s is close to unity, it looks reasonable to assume that the main contribution to the integral in Eq. (2.111) comes from θ' close to zero and to 2π . Using the fact that $\tilde{F}(\theta) = \tilde{F}(2\pi - \theta)$ we then obtain:

$$\tilde{\nu}(\theta) = \frac{m^* \tilde{F}(\theta) \tilde{\nu}(0)}{4\pi\hbar^2} \sqrt{\frac{2}{s-1}}. \quad (2.112)$$

We now take the limit $\theta \rightarrow 0$ and substitute $\tilde{F}(0) = (4\pi\hbar^2/m)(k_F r_*)^2$ as follows from Eqs. (3.20), (2.84), and (2.85). Putting $m^* = m$ we then obtain $s = 1 + 2(k_F r_*)^4$ and arrive at Eq. (2.110).

Note, however, that for very small θ or θ very close to 2π the dependence $\tilde{F}(\theta)$ is very steep. For $\theta \rightarrow 0$ the leading part of the interaction function, which is linear in $k_F r_*$, vanishes, and only the quadratic part contributes to $\tilde{F}(0)$. Therefore, strictly speaking the employed procedure of calculating the integral in Eq. (2.111) is questionable for very small θ . This prompted us to make the analysis based on representing $\nu(\theta)$ in the form (2.95) and on solving the system of linear equations (2.96)-(2.98).

¹In fact, we arrived at this conclusion confining ourselves to the contributions up to β^2 . In stead of considering higher order contributions we checked numerically that the solution with $s > 1$ is absent if we omit the $(k_F r_*)^2$ -terms in the interaction function of quasiparticles.

Equation (2.111) is useful for understanding why undamped zero sound requires the condition $s > 1$ so that $u_0 > v_F$. For $s < 1$ there is a pole in the integrand of Eq. (2.111), which introduces an imaginary part of the integral. As a result, the zero sound frequency ω will also have an imaginary part at real momenta k , which means the presence of damping (see, e.g. [68]).

We could also consider an odd function $\nu(\theta)$, namely such that $\nu(2\pi - \theta) = -\nu(\theta)$ and $\nu(0) = \nu(2\pi) = 0$. In this case, however, we do not obtain an undamped zero sound.

2.5. Concluding remarks

We have shown that (single-component) fermionic polar molecules in two dimensions constitute a novel Fermi liquid, where many-body effects play an important role. For dipoles oriented perpendicularly to the plane of translational motion, the many-body effects provide significant corrections to thermodynamic functions. Revealing these effects is one of the interesting goals of up-coming experimental studies. The investigation of the full thermodynamics of 2D polar molecules, including many-body effects, can rely on the in-situ imaging technique as it has been done for two-component atomic Fermi gases [33, 34]. This method can also be extended to 2D systems for studying thermodynamic quantities [69, 70]. Direct imaging of a 3D pancake-shaped dipolar molecular system has been recently demonstrated at JILA [71]. For 2D polar molecules discussed in this chapter, according to equations (2.88)-(2.90), the contribution of many-body corrections proportional to $(k_F r_*)^2$ can be on the level of 10% or 20% for $k_F r_*$ close to 0.5. Thus, finding many-body effects in their thermodynamic properties looks feasible.

It is even more important that the many-body effects are responsible for the propagation of zero sound waves in the collisionless regime of the 2D Fermi liquid of polar molecules with dipoles perpendicular to the plane of translational motion. This is shown in Section IV of this sections, whereas mean-field calculations do not find undamped zero sound [54]. Both collisionless and hydrodynamic regimes are achievable in on-going experiments. This is seen from the dimensional estimate of the relaxation rate of quasiparticles. At temperatures $T \ll \epsilon_F$ the relaxation of a non-equilibrium distribution of quasiparticles occurs due to binary collisions of quasiparticles with energies in a narrow interval near the Fermi surface. The width of this interval is $\sim T$ and, hence, the relaxation rate contains a small factor $(T/\epsilon_F)^2$ (see, e.g. [68]). Then, using the Fermi Golden rule we may write the inverse relaxation time as $\tau^{-1} \sim (g_{eff}^2/\hbar)(m/\hbar^2)n(T/\epsilon)^2$, where n is the 2D particle density, the quantity $\sim m/\hbar^2$ represents the density of states on the Fermi surface, and the quantity g_{eff} is the effective interaction strength. Confining ourselves to the leading part of this quantity, from Eqs. (2.72) and (2.79) we have $g_{eff} \sim \hbar^2 k_F r_*/m$. We thus obtain:

$$\frac{1}{\tau} \sim \frac{\hbar n}{m} (k_F r_*)^2 \left(\frac{T}{\epsilon_F} \right)^2. \quad (2.113)$$

Note that as $\epsilon_F \approx \hbar^2 k_F^2 / 2m \approx 2\pi\hbar^2 n / m$, for considered temperatures $T \ll \epsilon_F$ the relaxation time τ is density independent. Excitations with frequencies $\omega \ll 1/\tau$ are in the hydrodynamic regime, where on the length scale smaller than the excitation wavelength and on the time scale smaller than $1/\omega$ the system reaches a local equilibrium. On the other hand, excitations with frequencies $\omega \gg 1/\tau$ are in the collisionless regime. Assuming $T \sim 10$ nK, for KRb molecules characterized by the dipole moment $d \simeq 0.25$ D in the electric field of 5kV/cm as obtained in the JILA experiments, we find τ on the level of tens of milliseconds. The required condition $T \ll \epsilon_F$ is satisfied for $\epsilon_F \gtrsim 70$ nK, which corresponds to $n \gtrsim 2 \cdot 10^8$ cm⁻². In such conditions excitations with frequencies of the order of a few Hertz or lower will be in the hydrodynamic regime, and excitations with larger frequencies in the collisionless regime.

The velocity of zero sound is practically equal to the Fermi velocity $v_F = \hbar k_F / m^*$. This is clearly seen from Eq. (2.110) omitting a small correction proportional to $(k_F r_*)^4$. Then, using Eq. (2.91) for the effective mass and retaining only corrections up to the first order in $k_F r_*$, we have:

$$u_0 \simeq \frac{\hbar k_F}{m} \left(1 + \frac{4}{3\pi} k_F r_* \right). \quad (2.114)$$

In the hydrodynamic regime the sound velocity is:

$$u = \sqrt{\frac{N}{m} \frac{\partial \mu}{\partial N}} \simeq \frac{\hbar k_F}{m} \left(1 + \frac{8}{3\pi} k_F r_* \right), \quad (2.115)$$

where we used Eq. (2.87) for $\partial \mu / \partial N$ and retained corrections up to the first order in $k_F r_*$. The hydrodynamic velocity u is slightly larger than the velocity of zero sound u_0 , and the difference is proportional to the interaction strength. This is in sharp contrast with the 3D two-component Fermi gas, where $u_0 \approx v_F > u \approx v_F / \sqrt{3}$.

We thus see that it is not easy to distinguish between the hydrodynamic and collisionless regimes from the measurement of the sound velocity. A promising way to do so can be the observation of damping of driven excitations, which in the hydrodynamic regime is expected to be slower. Another way is to achieve the values of $k_F r_*$ approaching unity and still discriminate between u_0 and u in the measurement of the sound velocity. For example, in the case of dipoles perpendicular to the plane of their translational motion the two velocities are different from each other by about 20% at $k_F r_* \simeq 0.5$. These values of $k_F r_*$ are possible if the 2D gas of dipoles still satisfies the Pomeranchuk criteria of stability. These criteria require that the energy of the ground state corresponding to the occupation of all quasiparticle states inside the Fermi sphere, remains the minimum energy under an arbitrarily small deformation of the Fermi sphere. The generalization of the Pomeranchuk stability criteria to the case of the 2D single-component Fermi liquid with dipoles perpendicular to the plane

of their translational motion reads:

$$1 + \frac{m^*}{(2\pi\hbar)^2} \int_0^{2\pi} \tilde{F}(\theta) \cos j\theta d\theta > 0, \quad (2.116)$$

and this inequality should be satisfied for any integer j . As has been found in Ref. [54], the Pomeranchuk stability criteria (2.116) are satisfied for $k_F r_*$ approaching unity from below if the interaction function of quasiparticles contains only the first term of Eq. (3.20), which is the leading mean field term. We have checked that the situation with the Pomeranchuk stability does not change when we include the full expression for the interaction function, $\tilde{F}(\theta) = \tilde{F}^{(1)}(\theta) + \tilde{F}_1^{(2)}(\theta) + \tilde{F}_2^{(2)}(\theta)$, following from Eqs. (3.20), (2.84), and (2.85). Thus, achieving $k_F r_*$ approaching unity looks feasible. For KRb molecules with the (oriented) dipole moment of 0.25 D the value $k_F r_* \approx 0.5$ requires densities $n \approx 2 \cdot 10^8 \text{ cm}^{-2}$.

Finally, we would like to emphasize once more that our results are applicable equally well for the quasi2D regime, where the dipole-dipole length r_* is of the order of or smaller than the confinement length $l_0 = (\hbar/m\omega_0)^{1/2}$, with ω_0 being the frequency of the tight confinement. The behavior at distances $r \lesssim l_0$ is contained in the coefficient A defined in Eq. (2.18). Therefore, the results for the velocity of zero sound which is independent of A , are universal in the sense that they remain unchanged when going from $r_* \gg l_0$ to $r_* \lesssim l_0$. The only requirement is the inequality $k_F l_0 \ll 1$. It is, however, instructive to examine the ratio r_*/l_0 that can be obtained in experiments with ultracold polar molecules. Already in the JILA experiments using the tight confinement of KRb molecules with frequency $\omega_0 \approx 30 \text{ kHz}$ and achieving the average dipole moment $d \simeq 0.25 \text{ D}$ in electric fields of 5 kV/cm , we have $r_* \simeq 100 \text{ nm}$ and $l_0 \simeq 50 \text{ nm}$ so that $r_*/l_0 \simeq 2$. A decrease of the confinement frequency to 5 kHz and a simultaneous decrease of the dipole moment by a factor of 2 leads to $r_*/l_0 \sim 0.2$. On the other hand, for d close to 0.5 Debye (which is feasible to obtain for other molecules) one can make the ratio r_*/l_0 close to 10 at the same confinement length.

Zero sound in a two-dimensional dipolar Fermi gas

In the previous chapter, we study Fermi liquid properties of a weakly interacting 2D gas of single-component fermionic dipoles (polar molecules or atoms with a large magnetic moment). In particular, we have predicted that the existence of zero sound is solely a many-body effect beyond mean-field theory in that system. In this chapter, we extend the theory to study zero sound in systems where the fermionic dipoles are tilted with respect to the plane of their translational motion. It is shown that the propagation of zero sound is provided by both mean field and many-body (beyond mean field) effects, and the anisotropy of the sound velocity is the same as the one of the Fermi velocity. The damping of zero sound modes can be much slower than that of quasiparticle excitations of the same energy. One thus has wide possibilities for the observation of zero sound modes in experiments with 2D fermionic dipoles, although the zero sound peak in the structure function is very close to the particle-hole continuum.

Note: This chapter is based on the publication: *Zero sound in a two-dimensional dipolar Fermi gas*, Phys. Rev. A **88**, 033625 (2013), which was written originally by myself (first authorship).

3.1. Introduction

The creation of quantum gases of atoms with large magnetic moments [72, 38, 19, 20] and ultracold clouds of ground state diatomic polar molecules [29, 26] strongly stimulated the work in the domain of dipolar cold gases, because the long-range anisotropic dipole-dipole interaction drastically changes the nature of quantum degenerate regimes. Presently, there is a growing number of proposals to study new classes of many-body states in these systems [21, 39]. A serious difficulty for studying many-body physics with polar molecules is related to ultracold chemical reactions, such as $\text{KRb} + \text{KRb} \Rightarrow \text{K}_2 + \text{Rb}_2$ observed in the JILA experiments [56, 30], which lead to a rapid decay of the system at required densities. Therefore, the attention is now shifted to non-reactive molecules, in particular RbCs, NaK, and KCs, for which the ultracold chemistry is expected to be energetically unfavorable [32]. Another route assumes the suppression of chemical reactions for reactive molecules by confining them to the (quasi)two-dimensional (2D) geometry and orienting their dipole mo-

ments (by a strong electric field) perpendicularly to the plane of the 2D translational motion [57, 58]. This induces a strong intermolecular repulsion, and the suppression of chemical reactions by two orders of magnitude has been already demonstrated [31].

Therefore, 2D gases of polar molecules attract a special attention, in particular when the molecules are fermionic and they are in the same internal state. One then has an additional reduction of chemical reactions. Various aspects have been discussed regarding this system in literature, in particular the emergence and beyond mean field description of the topological $p_x + ip_y$ phase for microwave-dressed polar molecules [43, 23], interlayer superfluids in bilayer and multilayer systems [44, 50, 46, 60], the emergence of density-wave phases [48, 49, 52, 53, 54, 73], and superfluid pairing for tilted dipoles [42, 54]. The Fermi liquid behavior of this system has been addressed by using the Fourier transform of the dipole-dipole interaction potential (see [54] and refs. therein). The many-body theory (beyond mean field) describing Fermi liquid properties of a weakly interacting 2D gas of identical fermionic dipoles with dipole moments d oriented perpendicularly to the plane of their translational motion, has been developed in Ref. [74]. The theory relies on the presence of a small parameter $p_F r_*$, where p_F is the Fermi momentum, and $r_* = md^2/\hbar^2$ is the dipole-dipole length, with m being the molecule mass. With the use of the low-momentum solution of the scattering problem up to terms $\sim (pr_*)^2$, thermodynamic quantities were obtained as a series of expansion up to the second order in $p_F r_*$. Recent Monte Carlo calculations [75] confirmed the findings of Ref. [74] in the low-density limit ($p_F r_* < 1$) and studied a quantum transition to the crystalline phase at high densities.

In some sense, the 2D gas of identical fermionic dipoles perpendicular to the plane of their translational motion, constitutes a novel Fermi liquid because the existence of zero sound in this system is provided only by many-body effects [74]. Zero sound modes represent collective oscillations related to deformations of the Fermi surface and are important characteristics of Fermi liquids and gases in the collisionless regime [76, 68]. This stimulates an interest to zero sound for tilted dipoles and to possibilities for the observation of zero sound modes in experiments. In the present chapter we show that in the 2D gas of identical fermionic tilted dipoles the propagation of zero sound is due to both mean field and many-body effects. The sound modes are anisotropic, and the anisotropy of the sound velocity is the same as the one of the Fermi velocity. Importantly, the damping rate of zero sound can be much lower compared to the damping rate of quasiparticle excitations with the same energy. This is different from the situation in ^3He [77], where these damping rates are of the same order of magnitude. The small damping rate of zero sound in the 2D dipolar Fermi gas opens wide possibilities for the observation of the sound modes in experiments, in spite of the fact that the zero sound peak is very close to the particle-hole continuum in the structure function.

The chapter is organized as follows. In Section 3.2 we give general relations for various quantities of the 2D gas of tilted fermionic dipoles and in Section 3.3 we derive the many-body contribution to the interaction function of quasiparticles in this

system. Section 3.4 is dedicated to the derivation of our results for the dynamical structure factor and zero sound velocity. It is in particular shown that for tilted dipoles the second order mean field contribution to this quantity and the many-body contribution are of the same order of magnitude. In Sections 3.5 and 3.6 we calculate the relaxation rate of quasiparticles and the damping rate of zero sound, showing that the latter can be much smaller at the same excitation energy. We conclude in Section 3.7, emphasizing that the slow damping of zero sound provides wide possibilities for the measurement of zero sound modes. Aside from the observation of the surface modes in trapped samples, which in the collisionless regime are analogous to zero sound and have been observed in the 2D atomic Fermi gas [78], one should be able to observe zero sound in the response to small modulations of the density in (quasi)uniform gases like those created in the recent experiment [79]. In contrast to experiments in liquid ^3He , where the observation of zero sound is based on the difference between the zero sound and Fermi velocities [80], in ultracold gases the zero sound can be observed through the measurement of the dynamical structure factor in two-photon Bragg spectroscopy experiments. This method was successfully developed for Bose-condensed gases [81, 82] and then used for ultracold fermions [83]. Although the zero sound peak in the structure function is located very close to the particle-hole continuum, it can be visible as it may be higher than the maximum of the continuum due to slow damping of the zero sound.

3.2. General relations. Anisotropy of the Fermi surface

We consider a 2D gas of single-component fermionic dipoles tilted by an angle θ_0 with respect to the plane of their translational motion (see Fig. 1). These dipolar particles interact with each other via the potential which at large separations r is

$$U(\mathbf{r}) = \frac{d^2}{r^3}(1 - 3\sin^2\theta_0\cos^2\theta), \quad (3.1)$$

where θ is the angle between the vector \mathbf{r} and the x axis in which the dipoles are tilted. The Hamiltonian of the system reads:

$$\hat{\mathcal{H}} = \sum_{\mathbf{p}} \xi_p \hat{a}_{\mathbf{p}}^\dagger \hat{a}_{\mathbf{p}} + \frac{1}{2S} \sum_{\mathbf{p}_1, \mathbf{p}_2, \mathbf{q}} U(\mathbf{q}) \hat{a}_{\mathbf{p}_1 + \mathbf{q}}^\dagger \hat{a}_{\mathbf{p}_2 - \mathbf{q}}^\dagger \hat{a}_{\mathbf{p}_2} \hat{a}_{\mathbf{p}_1}, \quad (3.2)$$

where S is the surface area, $\xi_p = \hbar^2 p^2 / 2m - \mu$ with μ being the chemical potential, $\hat{a}_{\mathbf{p}}^\dagger$ and $\hat{a}_{\mathbf{p}}$ are creation and annihilation operators of fermionic dipoles with momentum \mathbf{p} , and $U(\mathbf{q})$ is the Fourier transform of the interaction potential $U(\mathbf{r})$:

$$U(\mathbf{q}) = \int d^2\mathbf{r} U(\mathbf{r}) e^{-i\mathbf{q}\cdot\mathbf{r}}, \quad (3.3)$$

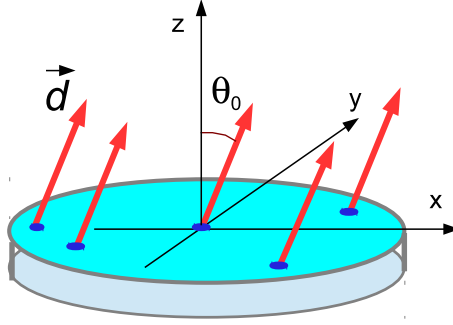


Figure 3.1. – 2D gas of dipoles tilted by an angle θ_0 in the x, z -plane.

We focus on the weakly interacting regime, where the interaction energy per particle is much smaller than the Fermi energy and the inequality

$$p_F r_* \ll 1 \quad (3.4)$$

is satisfied.

The potential $U(\mathbf{r})$ becomes partially attractive at sufficiently large tilting angles θ_0 , providing a possibility of superfluid pairing. This occurs at θ_0 exceeding a critical value 0.72 [54]. Assuming the absence of superfluid pairing the ground state of the system is a Fermi liquid and one may use the Landau theory relying on the existence of "dressed particles", or quasiparticles. At $T = 0$ the momentum distribution of free quasiparticles is the step function

$$n(\mathbf{p}) = \theta(p_F - p), \quad (3.5)$$

i.e. $n(\mathbf{p}) = 1$ for $p < p_F$ and zero otherwise. The chemical potential is equal to the boundary energy at the Fermi circle, $\mu = \epsilon_F \equiv \epsilon(p_F)$. The quasiparticle energy $\epsilon(\mathbf{p})$ is a variational derivative of the total energy with respect to the distribution function $n(\mathbf{p})$. Due to the interaction between quasiparticles, the deviation δn of this distribution from the step function (3.5) results in a change of the quasiparticle energy:

$$\delta\epsilon(\mathbf{p}) = \int F(\mathbf{p}, \mathbf{p}') \delta n(\mathbf{p}') \frac{d^2 p'}{(2\pi)^2}. \quad (3.6)$$

The interaction function of quasiparticles $F(\mathbf{p}, \mathbf{p}')$ is thus the second variational derivative of the total energy with regard to $n(\mathbf{p})$. The quantity $\delta n(\mathbf{p})$ is significantly different from zero only near the Fermi surface, so that one may put $\mathbf{p} = p_F \mathbf{n}$ and

$\mathbf{p}' = p_F \mathbf{n}'$ in the arguments of F in Eq. (3.6), where \mathbf{n} and \mathbf{n}' are unit vectors in the directions of \mathbf{p} and \mathbf{p}' .

The knowledge of the interaction function of quasiparticles allows one to calculate the compressibility relying only on the integration on the Fermi surface. One then obtains straightforwardly the chemical potential, ground state energy, and other thermodynamic quantities. This idea belongs to Landau [84] and it was pushed forward by Abrikosov and Khalatnikov [67] and implemented for a two-component 3D Fermi gas with a weak contact repulsion, revealing many-body (beyond mean field) effects and reproducing the results of an earlier (direct) calculation of Lee-Huang-Yang [66, 65]. The many-body theory relying on the Abrikosov-Khalatnikov approach has been developed in Ref. [74] for 2D fermionic single-component dipoles perpendicular to the plane of their translational motion ($\theta_0 = 0$). This theory accounts for the short-range physics in the scattering properties and represents thermodynamic quantities as a series of expansion in the small parameter $p_F r_*$ up to the second order. The construction of a similar theory for tilted dipoles requires extremely cumbersome calculations and is beyond the scope of the present chapter. Instead, we intend to reveal the properties of zero sound.

A distinguished feature of tilted 2D fermionic dipoles is a small anisotropy of the Fermi surface. The related corrections to the Fermi momentum, chemical potential, etc., are proportional to $p_F r_*$, and we omit higher order corrections. Relations for these quantities have been derived in Ref. [54], and we present them here for completeness without going into detailed calculations. In contrast to strongly interacting systems, in the weakly interacting regime the quasiparticle energy is well defined at any momenta, not only near the Fermi surface. One may write:

$$\epsilon(\mathbf{p}) = \frac{\hbar^2 p^2}{2m} - \mu + \int F(\mathbf{p}, \mathbf{p}') n(\mathbf{p}') \frac{d^2 p'}{(2\pi)^2}, \quad (3.7)$$

and take into account that exactly on the Fermi surface the quasiparticle energy is zero:

$$\epsilon(\mathbf{p}_F) = \frac{\hbar^2 p_F^2}{2m} - \mu + \int F(\mathbf{p}_F, \mathbf{p}') n(\mathbf{p}') \frac{d^2 p'}{(2\pi)^2} = 0. \quad (3.8)$$

In order to express the Fermi momentum through the density n and the interaction strength, one has to solve equations (3.7) and (3.8) selfconsistently with the particle number equation

$$n = \int \frac{d^2 p}{(2\pi)^2} n(\mathbf{p}). \quad (3.9)$$

Integrating the right-hand side of this equation one has

$$\int \frac{p_F^2(\phi) d\phi}{2\pi} = p_{F0}^2 = 4\pi n, \quad (3.10)$$

where ϕ is the angle between the vector \mathbf{p}_F and the x axis. Turning back to equation (3.8) we notice that to linear order in $p_F r_*$ one may use the distribution function of

a non-interacting Fermi gas $n(p') = \theta(p_{F0} - p')$ and put the interaction function of quasiparticles expressed through the Fourier transforms of the interaction potential $U(\mathbf{r})$ [54, 74]:

$$F_1(\mathbf{p}, \mathbf{p}') = [U(0) - U(\mathbf{p} - \mathbf{p}')] = 2\pi d^2 |\mathbf{p} - \mathbf{p}'| (\cos^2 \theta_0 - \sin^2 \theta_0 \cos^2 \phi_{\mathbf{p}-\mathbf{p}'}), \quad (3.11)$$

where $\phi_{\mathbf{p}-\mathbf{p}'}$ is the angle between the vector $\mathbf{p} - \mathbf{p}'$ and the x axis. Then, integrating Eq.(3.8) over $d\phi$ and using Eq.(3.10) we have:

$$\mu = \epsilon_{F0} \left(1 + \frac{32}{9\pi} p_{F0} r_* P_2(\cos \theta_0) \right), \quad (3.12)$$

with $\epsilon_{F0} = \hbar^2 p_{F0}^2 / 2m$, and $P_2(\cos \theta_0) = (3 \cos^2 \theta_0 - 1)/2$ being the second order Legendre polynomial. Eq.(3.8) immediately gives the anisotropic Fermi momentum:

$$p_F(\phi) = p_{F0} \left(1 + \frac{8}{15\pi} p_{F0} r_* \sin^2 \theta_0 \cos 2\phi \right). \quad (3.13)$$

For the quasiparticle energy near the Fermi surface, from Eq.(3.7) we have:

$$\epsilon(\mathbf{p}) = v_F(\phi)(p - p_F(\phi)), \quad (3.14)$$

where

$$v_F(\phi) = v_{F0} \left(1 + \frac{4}{3\pi} p_{F0} r_* P_2(\cos \theta_0) - \frac{2}{5\pi} p_{F0} r_* \sin^2 \theta_0 \cos 2\phi \right) \quad (3.15)$$

is the radial component of the Fermi velocity, and $v_{F0} = \hbar p_{F0} / m$.

3.3. Interaction function of quasiparticles

The interaction function of quasiparticles $F(\mathbf{p}, \mathbf{p}')$ consists of two parts: the mean field part and the many-body one, and we need to know this function on the Fermi surface ($|\mathbf{p}| = |\mathbf{p}'| = p_F$). The mean field term is expressed through the scattering amplitude [74], and the contribution linear in pr_* and $p'r_*$ is given by Eq.(3.11). The contribution $F_2(\mathbf{p}, \mathbf{p}')$ which is quadratic in pr_* and $p'r_*$, depends on the short-range physics. It is obtained from the solution of the 2D scattering problem, and we omit terms which are proportional to higher powers of pr_* and $p'r_*$ (see [74] for $\theta_0 = 0$). Thus, the mean field contribution to the interaction function can be written as

$$F_{mf}(\mathbf{p}, \mathbf{p}') = F_1(\mathbf{p}, \mathbf{p}') + F_2(\mathbf{p}, \mathbf{p}'), \quad (3.16)$$

with $F_1(\mathbf{p}, \mathbf{p}')$ from Eq.(3.11). We do not specify the expression for $F_2(\mathbf{p}, \mathbf{p}')$ and only mention that $F_2 = 0$ for $\mathbf{p} = \mathbf{p}'$.

The many-body part of the interaction function is obtained as the second variational derivative of the many-body (beyond mean field) contribution to the total

energy. This contribution is expressed in terms of the off-shell scattering amplitude $f(\mathbf{p}', \mathbf{p})$ [74]:

$$\tilde{E}_{mb} = -\frac{1}{2S^2} \sum_{\mathbf{p}_1, \mathbf{p}_2, \mathbf{p}'_1} \frac{2m|f(\mathbf{p}', \mathbf{p}) - f(\mathbf{p}', -\mathbf{p})|^2}{\hbar^2(\mathbf{p}_1^2 + \mathbf{p}_2^2 - \mathbf{p}'_1{}^2 - \mathbf{p}'_2{}^2)} \times n(\mathbf{p}_1)n(\mathbf{p}_2)n(\mathbf{p}'_1)\delta_{\mathbf{p}_1+\mathbf{p}_2-\mathbf{p}'_1-\mathbf{p}'_2}, \quad (3.17)$$

where $\mathbf{p} = (\mathbf{p}_1 - \mathbf{p}_2)/2$ and $\mathbf{p}' = (\mathbf{p}'_1 - \mathbf{p}'_2)/2$. As we are interested only in the powers of pr_* and $p'r_*$ not larger than two, the small anisotropy of the Fermi surface can be omitted. For the off-shell amplitudes in Eq.(3.17) we may take the result of the first Born approximation which is linear in pr_* and $p'r_*$:

$$f(\mathbf{p}', \mathbf{p}) - f(\mathbf{p}', -\mathbf{p}) = 2\pi d^2 |\mathbf{p}' + \mathbf{p}| (\cos^2 \theta_0 - \sin^2 \theta_0 \cos^2 \phi_{\mathbf{p}+\mathbf{p}'}) - 2\pi d^2 |\mathbf{p} - \mathbf{p}'| (\cos^2 \theta_0 - \sin^2 \theta_0 \cos^2 \phi_{\mathbf{p}-\mathbf{p}'}). \quad (3.18)$$

We then obtain the many-body contribution to the interaction function:

$$F_{mb}(\mathbf{p}, \mathbf{p}') = \tilde{F}_1(\mathbf{p}, \mathbf{p}') + \tilde{F}_2(\mathbf{p}, \mathbf{p}'); \quad (3.19)$$

$$\begin{aligned} \tilde{F}_1(\mathbf{p}, \mathbf{p}') &= -\frac{4\hbar^2}{m} (p_{F0} r_*)^2 \int_{p_1 < p_{F0}} \frac{d^2 p_1}{p_{F0}^2} \frac{\delta_{\mathbf{p}+\mathbf{p}_1-\mathbf{p}'-\mathbf{p}_2}}{p_1^2 - p_2^2} \left\{ \cos^2 \theta_0 (|\mathbf{p}' - \mathbf{p}| - |\mathbf{p}' - \mathbf{p}_1|) \right. \\ &\quad \left. + \sin^2 \theta_0 \left[\frac{(p' \cos \phi_{\mathbf{p}'} - p_1 \cos \phi_{\mathbf{p}_1})^2}{|\mathbf{p}' - \mathbf{p}_1|} - \frac{(p' \cos \phi_{\mathbf{p}'} - p \cos \phi_{\mathbf{p}})^2}{|\mathbf{p} - \mathbf{p}'|} \right] \right\}^2; \end{aligned} \quad (3.20)$$

$$\begin{aligned} \tilde{F}_2(\mathbf{p}, \mathbf{p}') &= -\frac{2\hbar^2}{m} (p_{F0} r_*)^2 \int_{p_1 < p_{F0}} \frac{d^2 p_1}{p_{F0}^2} \frac{\delta_{\mathbf{p}+\mathbf{p}'-\mathbf{p}_1-\mathbf{p}_2}}{2p_{F0}^2 - p_1^2 - p_2^2} \left\{ \cos^2 \theta_0 (|\mathbf{p}_1 - \mathbf{p}| - |\mathbf{p}' - \mathbf{p}_1|) \right. \\ &\quad \left. + \sin^2 \theta_0 \left[\frac{(p' \cos \phi_{\mathbf{p}'} - p_1 \cos \phi_{\mathbf{p}_1})^2}{|\mathbf{p}' - \mathbf{p}_1|} - \frac{(p_1 \cos \phi_{\mathbf{p}_1} - p \cos \phi_{\mathbf{p}})^2}{|\mathbf{p} - \mathbf{p}_1|} \right] \right\}^2, \end{aligned} \quad (3.21)$$

where we have used the step function (3.5) for the distribution function of quasiparticles when integrating over \mathbf{p}_1 , \mathbf{p}_2 , and \mathbf{p}'_1 .

For the analysis of the zero sound modes we will need the p^2 terms of the interaction function only at $\mathbf{p} = \mathbf{p}'$. One can easily check that in this case the integral in Eq.(3.21) is equal to zero. In the integral of Eq.(3.20) we use the notations:

$$\frac{\mathbf{p} + \mathbf{p}'}{2p_{F0}} = \mathbf{w}; \quad \frac{\mathbf{p} - \mathbf{p}'}{2p_{F0}} = \mathbf{b}; \quad \frac{\mathbf{p}_1 + \mathbf{p}_2}{2p_{F0}} = \mathbf{y}. \quad (3.22)$$

Then we have $\mathbf{p}_1/p_{F0} = \mathbf{y} - \mathbf{b}$; $(\mathbf{p}_1 - \mathbf{p}')/p_{F0} = \mathbf{y} - \mathbf{w}$, and equations (3.19-3.21) are reduced to:

$$\begin{aligned} F_{mb}(\mathbf{p}, \mathbf{p}') &= \tilde{F}_1(\mathbf{p}, \mathbf{p}') = \frac{\hbar^2}{m} (p_{F0} r_*)^2 \int_0^{y_{max}} \frac{d^2 y}{by \cos \phi_{yb}} \\ &\quad \times \left\{ \cos^2 \theta_0 (2b - |\mathbf{y} - \mathbf{w}|) + \sin^2 \theta_0 \left[\frac{(y \cos \phi_y - w \cos \phi_w)^2}{|\mathbf{y} - \mathbf{w}|} - 2b \cos^2 \phi_b \right] \right\}^2, \end{aligned} \quad (3.23)$$

where ϕ_y, ϕ_w, ϕ_b are the angles between the vectors $\mathbf{y}, \mathbf{w}, \mathbf{b}$ and the x axis, and ϕ_{yb} is the angle between \mathbf{y} and \mathbf{b} . The variable y changes from 0 to $y_{max} = b \cos \phi_{yb} + \sqrt{1 - b^2 \sin^2 \phi_{yb}}$. For $\mathbf{p}' \rightarrow \mathbf{p}$ we have $b \rightarrow 0$, and omitting the terms proportional to b^2 and higher powers of b , we may write $y_{max} = 1 + b \cos \phi_{yb}$. We now recall that $F(\mathbf{p}, \mathbf{p}') = F(\mathbf{p}', \mathbf{p})$. It is easy to check that $F(\mathbf{p}', \mathbf{p})$ is given by the same equation (3.23), but with a different sign and $y_{max} = 1 - b \cos \phi_{yb}$. Then, for $\mathbf{p}' \rightarrow \mathbf{p}$ ($b \rightarrow 0$) we have:

$$\begin{aligned} \frac{F(\mathbf{p}, \mathbf{p}') + F(\mathbf{p}', \mathbf{p})}{2} = F(\mathbf{p}, \mathbf{p}) &= \frac{2\hbar^2}{m} (p_{F0} r_*)^2 \int_{1-b \cos \phi_{yb}}^{1+b \cos \phi_{yb}} dy \int_0^{2\pi} \frac{d\phi_y}{4b \cos \phi_{yb}} \\ &\times \left\{ \cos^2 \theta_0 (2b - |\mathbf{y} - \mathbf{w}|) + \sin^2 \theta_0 \left[\frac{(y \cos \phi_y - w \cos \phi_w)^2}{|\mathbf{y} - \mathbf{w}|} - 2b \cos^2 \phi_b \right] \right\}^2. \end{aligned} \quad (3.24)$$

For $b \rightarrow 0$ the result of the integration over dy in Eq.(3.24) is simply obtained by putting $y = 1$ in the integrand and multiplying it by $2b \cos \phi_{yb}$. Then, omitting the terms proportional to b and putting $w = 1$ we obtain:

$$\begin{aligned} F(\mathbf{p}, \mathbf{p}) &= \frac{\hbar^2}{m} (p_{F0} r_*)^2 \int_0^{2\pi} d\phi_y \left\{ 2(1 - \cos \phi_{ys}) \cos^4 \theta_0 \right. \\ &\left. - 2 \sin^2 \theta_0 \cos^2 \theta_0 (\cos \phi_y - \cos \phi_s)^2 + \sin^4 \theta_0 \frac{(\cos \phi_y - \cos \phi_s)^4}{2(1 - \cos \phi_{ys})} \right\}. \end{aligned} \quad (3.25)$$

The integration in Eq.(3.25) is straightforward and it gives:

$$\begin{aligned} F(\mathbf{p}, \mathbf{p}) &= \frac{4\pi\hbar^2}{m} (p_{F0} r_*)^2 \left\{ \cos^4 \theta_0 - \sin^2 \theta_0 \cos^2 \theta_0 \left(\frac{1}{2} + \cos^2 \phi_p \right) \right. \\ &\left. + \sin^4 \theta_0 \left(\frac{1}{8} + \frac{1}{2} \cos^2 \phi_p \right) \right\}. \end{aligned} \quad (3.26)$$

For dipoles perpendicular to the plane of their translational motion ($\theta_0 = 0$) equation (3.26) reproduces the result of Ref. [74].

3.4. Dynamical structure factor and zero sound modes

We now calculate the dynamical structure factor and analyze zero sound modes. Consider a small scalar potential

$$\Phi(\mathbf{r}, t) = \Phi(\mathbf{k}, \omega) \exp(i\mathbf{k}\mathbf{r} - i\omega t) \quad (3.27)$$

acting on the system via the interaction Hamiltonian

$$\hat{H}_e = \int \hat{\rho}(\mathbf{r}, t) \Phi(\mathbf{r}, t) d^2 r, \quad (3.28)$$

where $\hat{\rho}(\mathbf{r}, t)$ is the operator of the particle density. The linear density response function of the system, which is the density-density correlation function, is defined as

$$\chi(\mathbf{k}, \omega) = \frac{d\langle \rho(\mathbf{k}, \omega) \rangle}{d\Phi(\mathbf{k}, \omega)} \Big|_{\Phi \rightarrow 0}, \quad (3.29)$$

with the symbol $\langle \dots \rangle$ standing for the statistical average. The dynamical structure factor $S(\mathbf{k}, \omega)$ is related to the imaginary part of the response function:

$$-\pi[S(\mathbf{k}, \omega) - S(\mathbf{k}, -\omega)] = \text{Im}\chi(\mathbf{k}, \omega). \quad (3.30)$$

In the collisionless regime, where the frequency ω of variations of the momentum distribution function greatly exceeds the relaxation rate, the distribution variations $\delta n(\mathbf{p}, \mathbf{r}, t)$ are related to deformations of the Fermi surface. Omitting the collisional integral, the kinetic equation in the presence of an external force reads [76]:

$$\frac{\partial \delta n}{\partial t} + \frac{\partial \epsilon(\mathbf{p})}{\partial \hbar \mathbf{p}} \cdot \frac{\partial \delta n}{\partial \mathbf{r}} - \frac{\partial n(\mathbf{p})}{\partial \hbar \mathbf{p}} \cdot \left\{ \frac{\partial \delta \epsilon(\mathbf{p})}{\partial \mathbf{r}} + \frac{\partial \Phi(\mathbf{r}, t)}{\partial \mathbf{r}} \right\} = 0, \quad (3.31)$$

where $n(\mathbf{p})$ is the equilibrium distribution function, $\epsilon(\mathbf{p})$ is the quasiparticle energy at equilibrium, and its variations $\delta \epsilon(\mathbf{p}, \mathbf{r}, t)$ are related to the variations of the distribution function through the interaction function of quasiparticles:

$$\frac{\partial \delta \epsilon(\mathbf{p}, \mathbf{r}, t)}{\partial \mathbf{r}} = \int F(\mathbf{p}, \mathbf{p}') \frac{\partial \delta n(\mathbf{p}', \mathbf{r}, t)}{\partial \mathbf{r}} \frac{d^2 p'}{(2\pi)^2}. \quad (3.32)$$

Relying on Eq.(3.27) we represent the variations of the distribution function in the form $\delta n(\mathbf{p}, \mathbf{r}, t) = \delta n(\mathbf{p}, \mathbf{k}, \omega) \exp(i\mathbf{k}\mathbf{r} - i\omega t)$ and transform equation (3.31) to

$$(\mathbf{k}\mathbf{v}_{\mathbf{p}} - \omega - i\eta) \delta n(\mathbf{p}, \mathbf{k}, \omega) - \mathbf{k}\mathbf{v}_{\mathbf{p}} \frac{\partial n(\mathbf{p})}{\partial \epsilon(\mathbf{p})} \left\{ \int F(\mathbf{p}, \mathbf{p}') \delta n(\mathbf{p}', \mathbf{k}, \omega) \frac{d^2 p'}{(2\pi)^2} + \Phi(\mathbf{k}, \omega) \right\} = 0, \quad (3.33)$$

with $\eta \rightarrow +0$ and $\mathbf{v}_{\mathbf{p}} = \partial \epsilon(\mathbf{p}) / \partial \hbar \mathbf{p}$, and we also took into account that $\partial n(\mathbf{p}) / \partial \hbar \mathbf{p} = \mathbf{v}_{\mathbf{p}} \partial n(\mathbf{p}) / \partial \epsilon(\mathbf{p})$.

The distribution variations $\delta n(\mathbf{p}, \mathbf{k}, \omega)$ are different from zero only for momenta \mathbf{p} near the Fermi surface, where $\mathbf{v}_{\mathbf{p}} = \mathbf{v}_F(\mathbf{p})$. Putting $\Phi(\mathbf{k}, \omega) = 0$ in Eq.(3.33) one finds a dispersion relation for the excitation modes. In the limit of interactions tending to zero ($F \rightarrow 0$) we immediately obtain particle-hole modes near the Fermi surface, $\omega = \mathbf{k}\mathbf{v}_F(\mathbf{p})$. Collective zero sound modes will be obtained below in this section.

We first note that the quantity $\langle \rho(\mathbf{k}, \omega) \rangle$ entering equation (3.29) for the density response function, is given by

$$\langle \rho(\mathbf{k}, \omega) \rangle = \int \delta n(\mathbf{p}, \mathbf{k}, \omega) \frac{d^2 p}{(2\pi)^2}, \quad (3.34)$$

and we calculate $\delta n(\mathbf{p}, \mathbf{k}, \omega)$. Introducing the function $\tilde{\nu}(\hat{\mathbf{p}})$:

$$\delta n(\mathbf{p}, \mathbf{k}, \omega) = -\frac{\mathbf{k}\mathbf{v}_F(\mathbf{p})}{\mathbf{k}\mathbf{v}_F(\mathbf{p}) - \omega - i\eta} \frac{\partial n(\mathbf{p})}{\partial \epsilon(\mathbf{p})} \tilde{\nu}(\hat{\mathbf{p}}), \quad (3.35)$$

equation (3.33) is reduced to

$$\tilde{\nu}(\hat{\mathbf{p}}) + \frac{1}{\hbar} \int_0^{2\pi} F(p_F(\phi_p)\mathbf{n}, p_F(\phi_{p'})\mathbf{n}') \frac{\mathbf{k}\mathbf{v}_F(\mathbf{p}')}{\mathbf{k}\mathbf{v}_F(\mathbf{p}') - \omega - i\eta} \frac{p_F(\phi_{p'})}{\hat{\mathbf{p}}'\mathbf{v}_F(\mathbf{p}')} \tilde{\nu}(\hat{\mathbf{p}}') \frac{d\phi_{p'}}{(2\pi)^2} + \Phi(\mathbf{k}, \omega) = 0, \quad (3.36)$$

where \mathbf{n} and \mathbf{n}' are unit vectors in the directions of \mathbf{p} and \mathbf{p}' , respectively.

Due to the anisotropy of the Fermi surface, the vectors \mathbf{p} and $\mathbf{v}_F(\mathbf{p})$ are not parallel to each other and both p_F and v_F depend on the angle ϕ_p between $\hat{\mathbf{p}}$ and the x axis. However, the anisotropy is small and it only leads to a small correction to the term $p_F(\phi_{p'})/\hat{\mathbf{p}}'\mathbf{v}_F(\mathbf{p}')$ in the integrand of Eq.(3.36), so that this term can be put equal to m/\hbar . We will also represent the scalar product $\mathbf{k}\mathbf{v}_F(\mathbf{p})$ as $kv_F(\phi_p) \cos(\phi_p - \phi_k)$. We thus write Eq.(3.36) as:

$$\nu(\phi_p) - \frac{m}{\hbar^2} \int_0^{2\pi} F(\phi_p, \phi_{p'}) \frac{\nu(\phi_{p'}) \cos(\phi_{p'} - \phi_k)}{s(\phi_{p'}) - \cos(\phi_{p'} - \phi_k) + i\eta} \frac{d\phi_{p'}}{4\pi^2} + \Phi(\mathbf{k}, \omega) = 0, \quad (3.37)$$

where $s(\phi_p) = \omega/kv_F(\phi_p)$. Assuming $|s - 1| \ll 1$ we integrate in Eq.(3.37) singling out the contribution from $\phi_{p'}$ near ϕ_k and denoting the rest of the integration as $C(\phi_p)$. This yields:

$$\tilde{\nu}(\phi_p) - C(\phi_p) + \Phi(\mathbf{k}, \omega) - \frac{mF(\phi_p, \phi_k)\tilde{\nu}(\phi_k)}{2\pi\hbar^2\sqrt{s^2(\phi_k) - 1}} = 0. \quad (3.38)$$

Substituting the obtained $\tilde{\nu}(\phi_p)$ into equation (3.37) we find a relation:

$$0 = \tilde{\nu}(\phi_p) - \frac{mF(\phi_p, \phi_k)[C(\phi_k) - \Phi(\mathbf{k}, \omega)]}{2\pi\hbar^2\sqrt{s^2(\phi_k) - 1}} - \frac{m^2}{8\pi^3\hbar^4} \int_0^{2\pi} \frac{F(\phi_p, \phi_{p'})F(\phi_{p'}, \phi_k) \cos(\phi_{p'} - \phi_k)\tilde{\nu}(\phi_k)}{\sqrt{s^2(\phi_k) - 1} [s(\phi_{p'}) - \cos(\phi_{p'} - \phi_k)]} d\phi_{p'} + \Phi(\mathbf{k}, \omega). \quad (3.39)$$

Here we omitted the unimportant contribution of $\phi_{p'}$ away from ϕ_k in the integral

$$\frac{m}{4\pi^2\hbar^2} \int_0^{2\pi} \frac{F(\phi_p, \phi_{p'})[C(\phi_{p'}) - \Phi(\mathbf{k}, \omega)] \cos(\phi_{p'} - \phi_k)}{s(\phi_{p'}) - \cos(\phi_{p'} - \phi_k)} d\phi_{p'}.$$

From equation (3.38) we immediately see that

$$C(\phi_k) - \Phi(\mathbf{k}, \omega) = \tilde{\nu}(\phi_k)[1 - mF(\phi_k, \phi_k)/(2\pi\hbar^2\sqrt{s^2(\phi_k) - 1})].$$

Then, putting $\phi_p = \phi_k$ in Eq.(3.39) gives:

$$\tilde{\nu}(\phi_k) = -\Phi(\mathbf{k}, \omega) \left\{ 1 - \frac{mF(\phi_k, \phi_k)}{2\pi\hbar^2\sqrt{s^2(\phi_k)-1}} + \left(\frac{mF(\phi_k, \phi_k)}{2\pi\hbar^2\sqrt{s^2(\phi_k)-1}} \right)^2 - \frac{m^2}{8\pi^3\hbar^4} \int_0^{2\pi} \frac{F^2(\phi_k, \phi_{p'}) \cos(\phi_{p'} - \phi_k) d\phi_{p'}}{\sqrt{s^2(\phi_k)-1} [s(\phi_{p'}) - \cos(\phi_{p'} - \phi_k)]} \right\}^{-1}. \quad (3.40)$$

The mean field contribution to $F(\phi_k, \phi_k)$ is equal to zero, and hence in the second and third terms in the square brackets in Eq.(3.40) we have to use the many-body interaction function $F(\phi_k, \phi_k)$ given by Eq.(3.26). The third term is exactly cancelled by the contribution of $\phi_{p'}$ near ϕ_k to the integral in fourth term. For $\phi_{p'}$ away from ϕ_k in this integral, we should use the mean field contribution to the interaction function given by Eq.(3.11), which is linear in $p_{F0}r_*$. This is because the use of quadratic contributions to the interaction function would lead to terms proportional to cubic or higher order powers of $p_{F0}r_*$, which are much smaller than the second term in the square brackets. Representing Eq.(3.11) on the Fermi surface in the form:

$$F_1(\phi_k, \phi_{p'}) = 4\pi d^2 p_{F0} \sin \frac{|\phi_k - \phi_{p'}|}{2} \left\{ P_2(\cos \theta_0) + \frac{1}{2} \sin^2 \theta_0 \cos(\phi_k + \phi_{p'}) \right\} \quad (3.41)$$

and putting $s(\phi_{p'}) = 1$, the integration of the fourth term in the square brackets in Eq.(3.40) yields:

$$\begin{aligned} & \frac{m^2}{8\pi^3\hbar^4} \int_0^{2\pi} \frac{F^2(\phi_k, \phi_{p'}) \cos(\phi_{p'} - \phi_k) d\phi_{p'}}{\sqrt{s^2(\phi_k)-1} [s(\phi_{p'}) - \cos(\phi_{p'} - \phi_k)]} \\ &= \frac{(p_{F0}r_*)^2 P_2(\cos \theta_0) \sin^2 \theta_0 (2 \cos^2 \phi_k - 1)}{\sqrt{s^2(\phi_k)-1}}. \end{aligned} \quad (3.42)$$

In Eqs. (3.41) and (3.42) we omitted the anisotropy of the Fermi surface as it leads to corrections which contain higher orders of $p_{F0}r_*$. As a result, equation (3.40) transforms to

$$\tilde{\nu}(\phi_k) = -\Phi(\mathbf{k}, \omega) \left[1 - \frac{2(p_{F0}r_*)^2 \left\{ P_2^2(\cos \theta_0) + \frac{1}{8} \sin^4 \theta_0 \right\}}{\sqrt{s^2(\phi_k)-1}} \right]^{-1}. \quad (3.43)$$

The pole of $\tilde{\nu}(\phi_k)$ corresponds to the solution of Eq.(3.37) with $\Phi(\mathbf{k}, \omega) = 0$, i.e. to the eigenmodes of zero sound. In the expression for $s_0(\phi_k)$ the anisotropy due to mean field effects and the anisotropy due to the many-body contribution cancel each other, and s_0 becomes independent of ϕ_k :

$$s_0 = 1 + 2(p_{F0}r_*)^4 \left\{ P_2^2(\cos \theta_0) + \frac{1}{8} \sin^4 \theta_0 \right\}^2. \quad (3.44)$$

For $\theta_0 = 0$ equation (3.44) reproduces the result of Ref. [74]. The zero sound velocity in the dispersion relation $\omega = v_0 k$ is:

$$v_0 = v_F(\phi_k) s_0. \quad (3.45)$$

Thus, the zero sound modes exist at any tilting angle θ_0 (for $\theta_0 > \theta_c \simeq 0.72$ this is true at temperatures exceeding the critical temperature of the superfluid transition). The anisotropy of the zero sound is practically the same as the anisotropy of the Fermi velocity (omitting corrections to v_F which are $\propto (p_{F0} r_*)^2$). Equation (3.42) clearly shows that in contrast to perpendicular dipoles ($\theta_0 = 0$), for tilted dipoles the mean field contribution is non-zero in the second order. This is related to the angular dependence of the interaction function $F(\mathbf{p}, \mathbf{p}')$ of quasiparticles, which in the tilted case depends on both angles ϕ_p and $\phi_{p'}$, not only on the difference between them. The mean field contribution for perpendicular dipoles appears only in higher orders of perturbation theory. It is proportional to higher powers of p_{F0} and therefore is omitted. Note that without the many-body contribution to the interaction function we would obtain that the propagation of zero sound is possible only when the result of Eq.(3.42) is positive. Namely, the zero sound exists for $\theta_0 < \arccos(1/\sqrt{3}) \simeq 0.96$ and is anisotropic requiring $\phi_k < \pi/4$, or it exists for $\theta_0 > 0.96$ and $\phi_k > \pi/4$. This is consistent with numerical calculations of Ref. [54]. As we see, the many-body contribution drastically changes the result.

We now return to Eq.(3.43) and use it for obtaining the linear response function on the basis of equations (3.29), (3.34), and (3.35). Integrating in Eq.(3.34) and dividing the result by $\Phi(\mathbf{k}, \omega)$ we obtain:

$$\begin{aligned} \chi(\mathbf{k}, \omega) &= \int \frac{d^2 p}{(2\pi)^2} \frac{\cos(\phi_p - \phi_k)}{s(\phi_p) - \cos(\phi_p - \phi_k) + i\eta} \frac{\partial n(\mathbf{p})}{\partial \epsilon(\mathbf{p})} \frac{\tilde{v}(\phi_p)}{\Phi(\mathbf{k}, \omega)} \\ &= -\frac{ms}{2\pi\hbar^2\sqrt{s^2-1}} \frac{\tilde{v}(\phi_k)}{\Phi(\mathbf{k}, \omega)} = \frac{m}{2\pi\hbar^2} \frac{s}{\sqrt{s^2-1} - \sqrt{s_0^2(\phi_k)-1}}, \end{aligned} \quad (3.46)$$

where $s \equiv s(\phi_k)$. Actually, we should have put $s = 1$ in the numerator of Eq.(3.46). However, keeping s in the numerator of the expression for $\chi(\mathbf{k}, \omega)$ makes it consistent with the result for a non-interacting 2D gas, which corresponds to $s_0 = 1$ and is valid for any $s < 1$. Thus, equation (3.46) becomes also valid for any s significantly smaller than unity, where the interaction between particles is not important. Relying on equations (3.30) and (3.46) we straightforwardly calculate the dynamical structure factor. For $s < 1$ we have:

$$S(\mathbf{k}, \omega) = \frac{m}{(2\pi\hbar)^2} \frac{s\sqrt{1-s^2}}{s_0^2-s^2}; \quad s < 1. \quad (3.47)$$

For $s > 1$ there is only a δ -functional contribution of the zero sound:

$$S(\mathbf{k}, \omega) = \frac{m}{(2\pi\hbar)^2} s\sqrt{s_0^2-1} \delta(s-s_0); \quad s > 1. \quad (3.48)$$

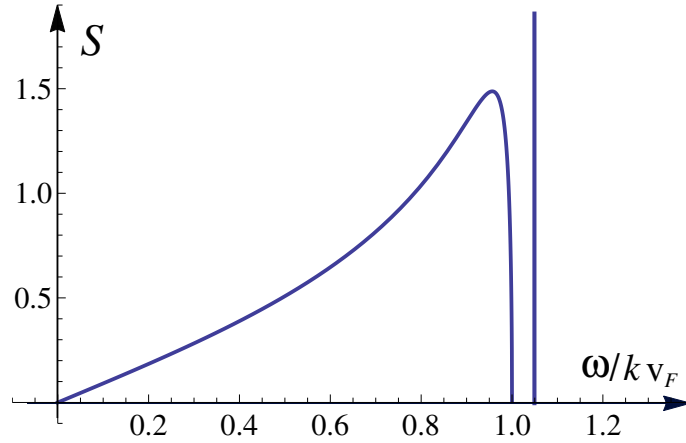


Figure 3.2. – (color online) Dynamical structure factor (in units of $m/(2\pi\hbar^2)^2$) as a function of ω/kv_F for $s_0 = 1.05$.

The obtained dynamical structure factor is shown in Fig.2. Note that for a non-interacting 2D Fermi gas one obtains a square root singularity in S for $\omega/kv_F \rightarrow 1$. The interaction between particles eliminates this singularity and we have S vanishing as $\sqrt{1 - (\omega/kv_F)^2}$ for $\omega/kv_F \rightarrow 1$, which is different from the 3D unpolarized interacting Fermi gas where S vanishes logarithmically for $\omega/kv_F \rightarrow 1$.

3.5. Relaxation rate of quasiparticles

The conditions of the collisionless regime, required for the existence of zero sound, are easily achievable in experiments with polar molecules or magnetic atoms. This is seen from the dimensional estimate of the relaxation rate of quasiparticles. At temperatures $T \ll \epsilon_F$ the relaxation of a non-equilibrium distribution of quasiparticles occurs due to binary collisions of quasiparticles which have energies in a narrow interval near the Fermi surface. The width of this interval is $\sim T$ and, hence, the relaxation rate contains a small factor $(T/\epsilon_F)^2$ (see, e.g. [68]). The rate is also proportional to the 2D density n and to the density of states on the Fermi surface, which is $\sim m/\hbar^2$. Using the Fermi golden rule we may write a dimensional estimate for the inverse relaxation time as $\tau^{-1} \sim (g_{eff}^2/\hbar)(m/\hbar^2)n(T/\epsilon_F)^2$, where the quantity g_{eff} is the effective interaction strength. Confining ourselves to the leading part of this quantity, from Eq. (3.11) we have $g_{eff} \sim p_F d^2 \sim \hbar^2 p_F r_*/m$. We thus obtain:

$$\frac{1}{\tau} \sim \frac{\hbar n}{m} (p_F r_*)^2 \left(\frac{T}{\epsilon_F} \right)^2 \sim \frac{m T^2 r_*^2}{\hbar^3}. \quad (3.49)$$

Interestingly, for considered temperatures $T \ll \epsilon_F$ the relaxation time τ is density independent. Excitations with frequencies $\omega \gg 1/\tau$ are in the collisionless regime.

Assuming $T \sim 10\text{nK}$, for dysprosium atoms which have magnetic moment $10\mu_B$ equivalent to the dipole moment $d \simeq 0.1 \text{ D}$, we find that τ is on the level of tenths of a second. The required condition $T \ll \epsilon_F$ is satisfied for $\epsilon_F \gtrsim 50 \text{ nK}$, which corresponds to $n \gtrsim 3 \cdot 10^8 \text{ cm}^{-2}$. In such conditions excitations with frequencies of the order of a Hertz or higher will be in the collisionless regime.

The occurrence of relaxation of excitations in the collisionless regime is important for understanding the visibility of zero sound. The dynamical structure factor $S(\mathbf{k}, \omega)$ characterizes the scattering process in which the momentum \mathbf{k} and energy $\hbar\omega$ are transferred to the system. The visibility of the zero sound peak in the structure factor can be smeared out by the fact that it is very close to the particle-hole continuum (see Fig.2). The related distance is $\sim (p_{F0}r_*)^4$ in units of $\omega/v_F k$. In order to make sure that this is not the case one has to find the actual height and width of the zero sound peak. Also, one can think of observing the oscillations of the cloud induced by small modulations of the density, with a time delay after switching off the driving force perturbing the density. In both cases the picture is determined by the damping of zero sound and quasiparticles excitations.

Thus, we should compare the relaxation rate of quasiparticles near the Fermi surface with the damping rate of zero sound. First, we calculate the rate of relaxation of a quasiparticle near the Fermi surface, with a given energy $\epsilon(\mathbf{p}) \ll \epsilon_{F0}$ at $T \rightarrow 0$. The relaxation mechanism involves the interaction of this quasiparticle with the filled Fermi sphere, which annihilates the quasiparticle, creates a hole with momentum \mathbf{p}_1 (annihilates a particle with momentum \mathbf{p}_1 inside the Fermi sphere), and creates quasiparticles with momenta \mathbf{p}_2 and \mathbf{p}_3 . As the relaxation rate τ^{-1} is small, we use the first order perturbation theory (Fermi golden rule) relying on the interaction Hamiltonian \hat{H}_{int} given by the second term of Eq.(4.1). We then have:

$$\frac{1}{\tau} = \frac{2\pi}{\hbar} \sum_{\mathbf{p}_1, \mathbf{p}_2, \mathbf{p}_3} |\langle \hat{a}_{\mathbf{p}_1}^\dagger \hat{a}_{\mathbf{p}_2} \hat{a}_{\mathbf{p}_3} \hat{H}_{int} \hat{a}_{\mathbf{p}}^\dagger \rangle|^2 \times \delta(\epsilon(\mathbf{p}) + \epsilon(\mathbf{p}_1) - \epsilon(\mathbf{p}_2) - \epsilon(\mathbf{p}_3)), \quad (3.50)$$

where the symbol $\langle \dots \rangle$ stands for the average over the equilibrium state, and

$$\hat{H}_{int} = \frac{1}{2S} \sum_{\mathbf{p}_1, \mathbf{p}_2, \mathbf{p}_3} U(\mathbf{p}_1 - \mathbf{p}_3) \hat{a}_{\mathbf{p}_3}^\dagger \hat{a}_{\mathbf{p}_4}^\dagger \hat{a}_{\mathbf{p}_2} \hat{a}_{\mathbf{p}_1}.$$

Using the Wick theorem and the relations

$$\langle \hat{a}_{\mathbf{p}_i}^\dagger \hat{a}_{\mathbf{p}_i'} \rangle = n(\mathbf{p}_i) \delta_{\mathbf{p}_i \mathbf{p}_i'}, \quad \langle \hat{a}_{\mathbf{p}_i} \hat{a}_{\mathbf{p}_i'}^\dagger \rangle = (1 - n(\mathbf{p}_i)) \delta_{\mathbf{p}_i \mathbf{p}_i'},$$

we reduce equation (3.50) to

$$\begin{aligned} \frac{1}{\tau} = & \frac{2\pi}{\hbar} \int_0^\infty \frac{p_1 dp_1}{(2\pi)^2} \int_0^\infty \frac{p_2 dp_2}{(2\pi)^2} \int_0^{2\pi} d\phi_1 \int_0^{2\pi} d\phi_2 n(\mathbf{p}_1)(1 - n(\mathbf{p}_2))(1 - n(\mathbf{p}_3)) \\ & \times [U(\mathbf{p} - \mathbf{p}_2) - U(\mathbf{p}_1 - \mathbf{p}_2)]^2 \delta(\epsilon(\mathbf{p}) + \epsilon(\mathbf{p}_1) - \epsilon(\mathbf{p}_2) - \epsilon(\mathbf{p}_3)) \delta_{\mathbf{p} + \mathbf{p}_1, \mathbf{p}_2 + \mathbf{p}_3}, \quad (3.51) \end{aligned}$$

where ϕ_1 (ϕ_2) are the angles between the vectors \mathbf{p}_1 (\mathbf{p}_2) and the x axis, and the presence of the Kronecker symbol $\delta_{\mathbf{p}+\mathbf{p}_1, \mathbf{p}_2+\mathbf{p}_3}$ reflects the momentum conservation law.

We omit the small anisotropy of the Fermi surface in the δ -function and occupation numbers. Since the anisotropy is omitted in all derivations below, we will use the notations v_F and p_F for the Fermi velocity v_F and Fermi momentum p_F . As all involved quasiparticle states are near the Fermi surface, we represent the energies of these states in the form $\epsilon(\mathbf{p}_i) = \hbar v_F q_i$, where $q_i = p_i - p_F$ and $|q_i| \ll p_F$. The particle that undergoes the relaxation is certainly above the Fermi surface, and $q = p - p_F > 0$. We first integrate in Eq.(3.51) over the angles ϕ_2 and ϕ_1 . The dependence of the integrand on these angles is contained in the δ -function and in the Fourier transforms $U(\mathbf{p} - \mathbf{p}_2)$ and $U(\mathbf{p}_1 - \mathbf{p}_2)$. From the energy and momentum conservation laws we have $p_3 = p + p_1 - p_2 = |\mathbf{p} + \mathbf{p}_1 - \mathbf{p}_2|$, which gives a relation:

$$pp_1[(1 - \cos(\phi_1 - \phi))] = pp_2[1 - \cos(\phi_2 - \phi)] + p_1p_2[1 - \cos(\phi_2 - \phi_1)], \quad (3.52)$$

with ϕ being an angle between the vector \mathbf{p} and x axis.

The calculation of the integral in Eq. (3.51) is presented in the Appendix and it gives the following result for the inverse relaxation time:

$$\frac{1}{\tau} = \frac{4\hbar}{\pi m} (p_F r_*)^2 q^2 \left\{ \left(\frac{3}{4} \ln \frac{p_F^2}{q^2} + \frac{3}{4} + \frac{3}{2} \ln 2 \right) (\cos^2 \theta_0 - \sin^2 \theta_0 \cos^2 \phi)^2 + \mathcal{F}(\theta_0, \phi) + \tilde{\mathcal{F}}(\theta_0, \phi) \right\}. \quad (3.53)$$

where

$$\mathcal{F}(\theta_0, \phi) = \sin^2 \theta_0 \cos^2 \theta_0 (2 \cos^2 \phi - 1) + \sin^4 \theta_0 \left(\frac{1}{4} + \cos^2 \phi - 2 \cos^4 \phi \right) \quad (3.54)$$

$$\tilde{\mathcal{F}}(\theta_0, \phi) = \mathcal{F}(\theta_0, \phi) - \frac{\pi}{2} \left(\cos^4 \theta_0 - \cos^2 \theta_0 \sin^2 \theta_0 + \frac{1}{8} \sin^4 \theta_0 \right). \quad (3.55)$$

Recalling that the quasiparticle energy is $\epsilon(q) = \hbar v_F q$ and $p_F^2 = 4\pi n$, we represent Eq.(3.53) in the form:

$$\frac{1}{\tau} = \frac{6\hbar}{m} n (p_F r_*)^2 \left(\frac{\epsilon(q)}{\epsilon_F} \right)^2 A(q, \theta_0, \phi), \quad (3.56)$$

where

$$A = (\cos^2 \theta_0 - \sin^2 \theta_0 \cos^2 \phi)^2 \ln \left[\frac{4e^{1/2} \epsilon_F}{\epsilon(q)} \right] + \frac{2}{3} \left(\mathcal{F}(\theta_0, \phi) + \tilde{\mathcal{F}}(\theta_0, \phi) \right). \quad (3.57)$$

The dependence $\tau^{-1} \propto q^2$ is generic for Fermi liquids [68], and the appearance of the logarithmic factor in Eq.(3.56) is due to the 2D geometry of the system.

The obtained relaxation rate strongly depends on the tilting angle θ_0 and on the angle ϕ of the quasiparticle wavevector \mathbf{p} with respect to the tilting direction. The rate reaches maximum when the dipoles are perpendicular to the plane of their translational motion ($\theta_0 = 0$). In this case

$$A_{max} = \ln \left[\frac{4e^{1/2}\epsilon_F}{\epsilon(q)} \right].$$

The minimum value of τ^{-1} is achieved for the dipoles lying in the plane of their translational motion ($\theta_0 = \pi/2$) at the angle ϕ equal to $\pi/2$. We then have

$$A_{min} = \frac{1}{3} - \frac{\pi}{24} \simeq 0.2.$$

The absolute value of the relaxation time of an excitation of a given frequency (in units of the Fermi energy) at a given density, strongly depends on a particular system. For example, in the case of dysprosium atoms ($d \simeq 0.1D$ and $r_* \simeq 25$ nm) at a density $n \sim 10^9$ cm⁻² we have the Fermi energy approaching 200 nK (5 kHz), and equation (3.56) gives the relaxation time τ of the order of a second or higher for the excitation energy of $10^{-2}\epsilon_F$ (50 Hz). At the same time for NaK molecules, selecting the electric field that provides $d \simeq 0.4D$ ($r_* \simeq 100$ nm), for $\epsilon(q) \simeq 10^{-2}\epsilon_F$ (which is 150 Hz as we now have $\epsilon_F \simeq 15$ kHz) we obtain $\tau \approx 20$ ms at the same density of 10^9 cm⁻² and $\theta_0 = 0$.

3.6. Damping of zero sound

The calculation of the damping rate of zero sound modes is more involved. It has to include the zero sound through the non-equilibrium character of the distribution function. The discussion of this topic has been initiated by Landau [85] who assumed that the transition probability for the scattering of quasiparticles with given momenta in the wave of zero sound is the same at temperatures $T \gg \hbar\omega$, where ω is the frequency of the zero sound, and at $T = 0$. He then established a relation between the damping of zero sound at $T \gg \hbar\omega$ and at zero temperature [85, 77]. In a later stage, theoretical studies of the attenuation of zero sound in liquid ³He were based on microscopic considerations [86, 87].

Following the idea of Landau we first consider the attenuation of zero sound at temperatures $T \gg \hbar\omega$ and start with the kinetic equation (3.31) in which we include the collisional integral $\mathcal{I}(n)$ and put the external potential $\Phi \rightarrow 0$:

$$\frac{\partial \delta n}{\partial t} + \frac{\partial \epsilon(\mathbf{p})}{\partial \hbar \mathbf{p}} \cdot \frac{\partial \delta n}{\partial \mathbf{r}} - \frac{\partial n(\mathbf{p})}{\partial \hbar \mathbf{p}} \cdot \frac{\partial \delta \epsilon(\mathbf{p})}{\partial \mathbf{r}} = \mathcal{I}(n), \quad (3.58)$$

where $n(\mathbf{p})$ is the equilibrium distribution function, $\delta n(\mathbf{p}, \mathbf{r}, t)$ is the deviation of the distribution function from the equilibrium value, and variations of the quasiparticle energy are expressed through δn by Eq.(3.32). In the presence of zero sound, variations of the distribution function follow from Eq.(3.35). Omitting the small anisotropy of the Fermi surface, δn can be written as (see Eq.(3.35)):

$$\delta n(\mathbf{p}, \mathbf{r}, t) = -\frac{\partial n(\mathbf{p})}{\partial \epsilon(\mathbf{p})} \nu(\phi) \exp\{i\mathbf{k}\mathbf{r} - i\omega t\}, \quad (3.59)$$

where the function $\nu(\phi)$ has a sharp peak for $\phi \rightarrow \phi_k$, with $\phi \equiv \phi_p$ and ϕ_k being the angle between the wave vector of the zero sound \mathbf{k} and the tilting direction.

At temperatures $T \gg \hbar\omega$ one may omit the frequency and momentum of the zero sound in the energy and momentum conservation laws. Then the collisional integral reduces to the form [88]:

$$\begin{aligned} \mathcal{I}(n) = & \frac{1}{T} \int W n(\epsilon(q)) n_1(1-n_2)(1-n_3)(\zeta_2 + \zeta_3 - \zeta_1 - \zeta) \\ & \times \delta(\epsilon(q) + \epsilon_1 - \epsilon_2 - \epsilon_3) \frac{d^2 p_1 d^2 p_2}{(2\pi)^4}, \end{aligned} \quad (3.60)$$

where $\epsilon_i = \epsilon(q_i)$, $n_i = n(\epsilon(q_i))$, and $\zeta_i = \nu(\phi_i) + (m/2\pi\hbar^2) \int \nu(\phi'_i) F(\phi_i, \phi'_i) d\phi'_i$. The momentum conservation law reads $\mathbf{p} + \mathbf{p}_1 = \mathbf{p}_2 + \mathbf{p}_3$. The quantity W is given by

$$W = \frac{2\pi}{\hbar} [U(\mathbf{p} - \mathbf{p}_2) - U(\mathbf{p}_1 - \mathbf{p}_2)]^2, \quad (3.61)$$

and the notations are the same as in Section V.

The functions ζ_i are taken on the Fermi surface, and we can do the same with respect to $U(\mathbf{p} - \mathbf{p}_2)$ and $U(\mathbf{p}_1 - \mathbf{p}_2)$. The only way to satisfy the momentum conservation on the Fermi surface and get a non-zero quantity $[\zeta(\phi) + \zeta(\phi_1) - \zeta(\phi_2) - \zeta(\phi_3)]$ is to put $\phi_1 = \phi + \pi$ (and, hence, $\phi_3 = \phi_2 + \pi$). We then have $W(\phi_2, \phi)$ following from equation (3.61) with $[U(\mathbf{p} - \mathbf{p}_2) - U(\mathbf{p}_1 - \mathbf{p}_2)]$ from Eq.(B.7), and the collisional integral becomes:

$$\begin{aligned} \mathcal{I}(n) = & \frac{m}{\hbar^2 T} \int_0^{2\pi} \frac{d\phi_2}{(2\pi)^4} \int_{-\infty}^{\infty} dq_1 \int_{-\infty}^{\infty} dq_2 \frac{W(\phi_2, \phi)}{|\sin(\phi_2 - \phi)|} \\ & \times [\zeta(\phi_2) + \zeta(\phi_2 + \pi) - \zeta(\phi) - \zeta(\phi + \pi)] n(\epsilon(q)) n_1(1-n_2)(1-n_3). \end{aligned} \quad (3.62)$$

Assuming $\epsilon_q \ll T$ and using the finite temperature Fermi-Dirac distribution for n_1 , n_2 , and n_3 we then obtain:

$$\mathcal{I}(n) = \frac{\pi^2 m T^2}{2(\hbar^2 v_F)^2} \int_0^{2\pi} \frac{d\phi_2}{(2\pi)^4} \frac{W(\phi_2, \phi)}{|\sin(\phi_2 - \phi)|} [\zeta(\phi) + \zeta(\phi + \pi) - \zeta(\phi_2) - \zeta(\phi_2 + \pi)] \frac{\partial n(\epsilon(q))}{\partial \epsilon(q)}. \quad (3.63)$$

We now set

$$\nu(\phi) = \frac{\bar{\nu}(\phi)}{s_0(\phi_k) - \cos(\phi - \phi_k)}, \quad (3.64)$$

where $\bar{\nu}(\phi)$ is a smooth function, and s_0 is given by Eq.(3.44). To zero order in p_{Fr*} we omit the second term in the expression for $\zeta(\phi_i)$ and then obtain:

$$\int_0^{2\pi} \frac{\pi^2 W(\phi_2, \phi)}{2|\sin(\phi_2 - \phi)|} \frac{d\phi_2}{(2\pi)^4} [\zeta(\phi) + \zeta(\phi + \pi) - \zeta(\phi_2) - \zeta(\phi_2 + \pi)] = \frac{\pi \hbar^3}{m^2} (p_{Fr*})^2 B(\phi), \quad (3.65)$$

where

$$\begin{aligned} B(\phi) = & \int_0^{2\pi} d\phi_2 \left\{ \frac{\bar{\nu}(\phi)}{s_0 - \cos(\phi - \phi_k)} + \frac{\bar{\nu}(\phi + \pi)}{s_0 + \cos(\phi - \phi_k)} - \frac{\bar{\nu}(\phi_2)}{s_0 - \cos(\phi_2 - \phi_k)} \right. \\ & \left. - \frac{\bar{\nu}(\phi_2 + \pi)}{s_0 + \cos(\phi_2 - \phi_k)} \right\} \times \left\{ \left| \sin\left(\frac{\phi_2 - \phi}{2}\right) \right| \left[\cos^2 \theta_0 - \sin^2 \theta_0 \sin^2\left(\frac{\phi_2 + \phi}{2}\right) \right] \right. \\ & \left. - \left| \cos\left(\frac{\phi_2 - \phi}{2}\right) \right| \left[\cos^2 \theta_0 - \sin^2 \theta_0 \cos^2\left(\frac{\phi_2 + \phi}{2}\right) \right] \right\}^2 \frac{d\phi_2}{|\sin(\phi_2 - \phi)|}. \quad (3.66) \end{aligned}$$

To zero order in p_{Fr*} we may put all $\bar{\nu}$ functions in Eq.(3.66) equal to $\bar{\nu}(\phi_k)$. This, in particular, yields:

$$B(\phi_k) = \frac{4\bar{\nu}(\phi_k)}{s_0^2 - 1} \left\{ (\cos^2 \theta_0 - \sin^2 \theta_0 \cos^2 \phi_k)^2 \ln \left[\frac{s_0 + 1}{s_0 - 1} \right] + 2\tilde{\mathcal{F}}(\theta_0, \phi_k) \right\}, \quad (3.67)$$

where the function $\tilde{\mathcal{F}}(\theta_0, \phi_k)$ has been introduced in Eq.(3.55). Using Eq.(3.65) the collisional integral (3.63) reduces to

$$\mathcal{I}(n) = \frac{1}{\tau_T} \frac{\partial n}{\partial \epsilon(q)} B(\phi), \quad (3.68)$$

with

$$\frac{1}{\tau_T} = \frac{\pi T^2}{2\hbar \epsilon_F} (p_{Fr*})^2, \quad (3.69)$$

and making use of Eqs. (3.59) and (3.68) the kinetic equation (3.58) takes the form:

$$[\omega - kv_F \cos(\phi - \phi_k)] \nu(\phi) - \frac{mkv_F}{4\pi^2 \hbar^2} \cos(\phi - \phi_k) \int_0^{2\pi} d\phi' F(\phi, \phi') \nu(\phi') = -\frac{iB(\phi)}{\tau_T}. \quad (3.70)$$

In the presence of damping the zero sound, frequency ω is complex for real k . We will use the notation $\omega/kv_F = s$, where the real part of s is equal to s_0 and the imaginary part is related to the attenuation of zero sound. We also assume that the damping rate is much smaller than the shift of the frequency ω from kv_F , given by $kv_F(s_0 - 1)$. This means that $(s_0 - 1)$ greatly exceeds the imaginary part of s . We

thus may first proceed with Eq.(3.70) in the same way as we did in Section IV (see equations (3.36) - (3.39)) and represent (3.70) in the form similar to Eq.(3.39). The difference is that now we replace $\Phi(\mathbf{k}, \omega)$ by the term $iB(\phi)/\tau_T$. We have:

$$\begin{aligned} \tilde{\nu}(\phi) - \frac{mF(\phi, \phi_k)\tilde{\nu}(\phi_k)}{2\pi\hbar^2\sqrt{s^2(\phi_k)-1}} + \frac{m^2F(\phi_k, \phi_k)F(\phi, \phi_k)\tilde{\nu}(\phi_k)}{4\pi^2\hbar^4(s^2(\phi_k)-1)} \\ - \frac{m^2}{8\pi^3\hbar^4} \int_0^{2\pi} \frac{F(\phi, \phi')F(\phi', \phi_k)\tilde{\nu}(\phi_k)\cos(\phi' - \phi_k)d\phi'}{\sqrt{s^2(\phi_k)-1}[s(\phi') - \cos(\phi' - \phi_k)]} = \frac{-iB(\phi)}{kv_F\tau_T}, \end{aligned} \quad (3.71)$$

where the function $\tilde{\nu}$ has been introduced in Eq.(3.35) and it is related to ν as $\nu(\phi) = \tilde{\nu}(\phi)\cos(\phi - \phi_k)/(s - \cos(\phi - \phi_k))$. The contribution of ϕ' close to ϕ_k in the integral over $d\phi'$ in the last term of the lhs of Eq.(3.71) and the third term of the lhs cancel each other, and Eq.(3.71) reduces to

$$\begin{aligned} \tilde{\nu}(\phi) - \frac{m^2}{8\pi^3\hbar^4} \int_0^{2\pi} \frac{F_1(\phi, \phi')F_1(\phi', \phi_k)\tilde{\nu}(\phi_k)\cos(\phi' - \phi_k)d\phi'}{\sqrt{s^2(\phi_k)-1}[s(\phi') - \cos(\phi' - \phi_k)]} \\ - \frac{mF(\phi, \phi_k)\tilde{\nu}(\phi_k)}{2\pi\hbar^2\sqrt{s^2(\phi_k)-1}} = \frac{-iB(\phi)}{kv_F\tau_T}, \end{aligned} \quad (3.72)$$

with the mean-field interaction function F_1 given by Eq.(3.41).

We now take the limit $\phi \rightarrow \phi_k$ and note that then the lhs of Eq.(3.72) can be conveniently expressed in terms of s_0 and s , which leads to the relation:

$$\tilde{\nu}(\phi_k) \left(1 - \sqrt{\frac{s_0^2 - 1}{s^2 - 1}} \right) = -\frac{iB(\phi_k)}{kv_F\tau_T}. \quad (3.73)$$

In equation (3.67) for $B(\phi_k)$ we may replace $\bar{\nu}(\phi_k)$ with $\tilde{\nu}(\phi_k)$ and thus obtain from Eq.(3.73):

$$\text{Im}s = -\frac{8}{kv_F\tau_T}D(\theta_0, \phi_k), \quad (3.74)$$

with

$$D(\theta_0, \phi_k) = \frac{1}{2}(\cos^2\theta_0 - \sin^2\theta_0\cos^2\phi_k)^2 \ln \left[\frac{s_0 + 1}{s_0 - 1} \right] + \tilde{\mathcal{F}}(\theta_0, \phi_k). \quad (3.75)$$

Writing the zero sound frequency as $\omega = s_0kv_F - i/2\tau_{0T}$, for the damping rate τ_{0T}^{-1} we find:

$$\frac{1}{\tau_{0T}} = \frac{16D(\theta_0, \phi_k)}{\tau_T}. \quad (3.76)$$

We now proceed in the same way as has been done in Ref. [87] for the attenuation of zero sound in ^3He and as described in [88]. In the regime where the zero sound frequency ω is comparable with T or exceeds it, the reduction of the number of the

zero sound quanta per unit time due to quasiparticle collisions is given by

$$\int \bar{W}(\{\mathbf{p}_i\}) [1n_2(1-n_3)(1-n_4) - n_3n_4(1-n_1)(1-n_2)] \\ \times \delta(\mathbf{p}_1 + \mathbf{p}_2 - \mathbf{p}_3 - \mathbf{p}_4 - \mathbf{p}) \times \delta(\epsilon_1 + \epsilon_2 - \epsilon_3 - \epsilon_4 - \hbar\omega) \prod d\mathbf{p}_i. \quad (3.77)$$

The quantity \bar{W} is not necessarily the same as W . However, assuming that the angular integrations are the same at an arbitrary ratio $\hbar\omega/T$ and in the classical limit $T \gg \hbar\omega$, we may proceed with the integration over the energies. This gives:

$$\int \prod d\epsilon_i [n_1n_2(1-n_3)(1-n_4) - n_3n_4(1-n_1)(1-n_2)] \\ \times \delta(\mathbf{p}_1 + \mathbf{p}_2 - \mathbf{p}_3 - \mathbf{p}_4 - \mathbf{p}) \times \delta(\epsilon_1 + \epsilon_2 - \epsilon_3 - \epsilon_4 - \hbar\omega) \propto T^2\omega \left[1 + \frac{\omega^2}{4\pi^2T^2} \right]. \quad (3.78)$$

The absorption coefficient is proportional to this integral, and the proportionality coefficient (which depends only on ω) can be found from the limiting case of $T \gg \hbar\omega$. So, the quantity in the square brackets in the rhs of Eq.(3.78) represents the ratio of the damping rate of zero sound at an arbitrary value of $\hbar\omega/T$ to the damping rate at $T \gg \hbar\omega$. Using Eq.(3.69) for τ_T we thus obtain the following damping rate at $T = 0$:

$$\frac{1}{\tau_0} = \frac{\omega^2}{8\pi T^2} \frac{1}{\tau_{0T}} = \frac{2\epsilon_F}{\pi\hbar} \left(\frac{\hbar\omega}{\epsilon_F} \right)^2 (p_F r_*)^2 D(\theta_0, \phi_k) = \frac{4\hbar}{m} n \left(\frac{\hbar\omega}{\epsilon_F} \right)^2 (p_F r_*)^2 D(\theta_0, \phi_k), \quad (3.79)$$

and using Eq.(3.44) for s_0 we rewrite $D(\theta_0, \phi_k)$ in the form:

$$D(\theta_0, \phi_k) = 2(\cos^2 \theta_0 - \sin^2 \theta_0 \cos^2 \phi_k)^2 \ln \left(\frac{1}{p_F r_*} \right) \\ + \tilde{\mathcal{F}}(\theta_0, \phi_k) - (\cos^2 \theta_0 - \sin^2 \theta_0 \cos^2 \phi_k)^2 \ln \left(P_2^2(\cos \theta_0) + \frac{1}{8} \sin^2 \theta_0 \right).$$

The condition that the damping rate is much smaller than $(s_0 - 1)\omega$ requires the inequality

$$\frac{\hbar\omega}{\epsilon_F} \ll (p_F r_*)^2, \quad (3.80)$$

which is important for the visibility of the zero sound in the dynamical structure factor.

The damping rate of zero sound is strongly anisotropic, and the anisotropy is similar to that of the relaxation rate of quasiparticles. The rate reaches maximum for dipoles perpendicular to the plane of their translational motion. We then have

$$D_{max} = 2 \ln \left(\frac{1}{p_F r_*} \right),$$

and for $p_{Fr_*} \approx 0.5$ and $\epsilon_F/\hbar\omega \sim 100$ the damping time τ_0 is by an order of magnitude larger than the relaxation time of quasiparticles with energy equal to $\hbar\omega$. The damping rate is minimal for dipoles lying in the plane of translational motion and the angle $\phi_k = \pi/2$. Then we obtain

$$D_{min} = \frac{4 - \pi}{16} \simeq 0.05.$$

3.7. Concluding remarks

The obtained results draw promising prospects for the observation of zero sound in 2D gases of polar molecules or magnetic atoms in the two-photon Bragg spectroscopy experiments by measuring the dynamical structure factor. This becomes especially feasible in view of the recent success in creating spatially uniform ultracold quantum gases [79]. The distance of the zero sound peak from the border of the particle-hole continuum (see Fig.2) is $\sim \omega(p_{Fr_*})^4$. Comparing it with the damping rate of the zero sound given by equation (3.79) we see that the latter is much smaller if the condition (3.80) is satisfied. This condition is easily fulfilled even for rather small p_{Fr_*} . For realistic systems one can think of the zero sound frequency of the order of a few tens or hundreds of Hertz, whereas the Fermi energy can easily be a few kiloHertz (a few hundreds of nanokelvins), so that the ratio $\epsilon_F/\hbar\omega$ exceeds 10. Under the condition (3.80) the height of the zero sound peak in the structure function $(2\pi\hbar)^2 S/m$ is $\sim \epsilon_F/\hbar\omega$, which is simply obtained replacing the δ -function in Eq.(3.47) by $\tau_0 k v_F$. The maximum of the particle-hole continuum following from equation (3.48) is $\sim (p_{Fr_*})^{-2}$ and it is much lower under the condition (3.80). Thus, the zero sound peak is not smeared out by the particle-hole continuum and can be visible in the dynamical structure factor. For example, if $p_{Fr_*} \approx 0.5$, then the separation between the border of the particle-hole continuum and the zero sound peak is $\sim \omega(p_{Fr_*})^4 \sim 20$ Hz for the sound frequency of a few hundred Hertz. It can be easily resolved as the relative frequency of the two Bragg beams can be controlled on the level of a Hertz.

Owing to a remarkable progress in experiments with ultracold quantum gases, it is also promising to directly observe the propagation of zero sound in the 2D dipolar Fermi gas. Using a tightly-focused and far detuned laser beam one can create a potential to introduce a localized density modulation in the gas, without heating it. This technique has been used to directly study the propagation of sound in Bose-Einstein condensates [89] and in resonantly interacting Fermi gases [90, 91, 92]. In our system, the far detuned laser can be focused to the center of the 2D sample, and one can choose a proper power and shape of the excitation pulse to resonantly drive the desired zero sound mode (see, e.g. [92]). After the zero sound mode is excited, one can observe the time evolution of the density profile and thus extract the information on the propagation of the mode.

Incoherent particle-hole excitations will also be excited during the pulse. However, as we have shown above, the decay of the zero sound is slower than that of particle-

hole excitation. After a time of the order of a fraction of the zero sound damping time τ_0 , let say $0.2\tau_0$ or $0.3\tau_0$, quasiparticle excitations are damped out and one is expected to see only the zero sound contribution to modulations of the density. The time τ_0 can be easily made on the level of a second. For example, this is the case for NaK molecules in the electric field providing $d \simeq 0.3D$ ($r_* \simeq 50\text{nm}$). Then, at the 2D density $n \sim 10^9 \text{ cm}^{-2}$ we have the Fermi energy approaching $1\mu\text{K}$ and $p_F r_* \approx 0.5$, and Eq.(3.79) gives $\tau_0 \sim 0.2\text{s}$ for dipoles perpendicular to the plane of their translational motion.

Stable dilute supersolid of two-dimensional dipolar bosons

We consider two-dimensional bosonic dipoles oriented perpendicularly to the plane. On top of the usual two-body contact and long-range dipolar interactions we add a contact three-body repulsion as expected, in particular, for dipoles in the bilayer geometry with tunneling. The three-body repulsion is crucial for stabilizing the system, and we show that our model allows for stable continuous space supersolid states in the dilute regime and calculate the zero-temperature phase diagram.

Note: This chapter is based on the publication: *Stable Dilute Supersolid of Two-Dimensional Dipolar Bosons*, Phys. Rev. Lett. **115**, 075303 (2015), which was written originally by myself (first authorship).

4.1. Introduction

Recent advances in the field of cold polar molecules [29, 26] and magnetic atoms [19, 20] interacting via long-range dipole-dipole forces make it realistic to create novel many-body quantum states in these systems. For polar molecules, ultracold chemical reactions observed at JILA [56, 30] and leading to a rapid decay of the system can be suppressed by tightly confining the molecules to a (quasi)two-dimensional (2D) geometry, orienting the dipoles perpendicularly to the plane of their translational motion, and thus inducing a strong intermolecular repulsion [57, 58, 31]. Therefore, 2D geometries are intensively discussed in the context of ultracold dipolar gases [21, 93, 94], together with possible experiments with non-reactive molecules, such as NaK[59, 95] and RbCs[96, 97].

The studies of ultracold dipolar gases may open perspectives for the observation of supersolidity. This remarkable quantum phenomenon combines superfluidity with a crystalline order [98, 99] (see [100] for review). It is still under debate as to what extent experimental results in solid helium prove the existence of this conceptually important phase [101]. On the other hand, supersolidity is rather well understood theoretically for soft-core two-body potentials [100, 102, 103, 104, 105] which can be realized, for example, in Rydberg-dressed atomic gases. However, such supersolids require a dense regime with at least several particles within the interaction range, which can be difficult to achieve. The same holds for supersolids discussed for 2D dipolar Bose gases [106] near the gas-solid phase transition [41, 107]. It is thus

an open question whether supersolids can exist in the dilute regime. The creation of such supersolids, especially if they are tunable regarding the lattice period, will allow for studies of non-conventional superfluid properties of supersolids and other aspects of supersolidity. Dilute 2D dipolar bosons may show the (helium-like) roton-maxon structure of the spectrum by fine-tuning the short-range part of the interaction potential and can be made unstable with respect to periodic modulations of the order parameter (roton instability) [108]. However, instead of forming a supersolid state when approaching such an instability, the gas collapses [109].

In this work we predict a stable supersolid state in a dilute two-dimensional dipolar system. In contrast to the earlier proposed soft-core supersolids, where the lattice period is of the order of the core radius, in our case it is tunable by varying the density and the dipole moment. In addition to the contact two-body term (g_2) and the dipole-dipole long-range tail characterized by the dipole moment d , we include a contact repulsive three-body term (g_3) which may prevent the collapse. Three-body forces are ubiquitous and arise naturally in effective field theories when one integrates out some of the high-energy degrees of freedom in the system [110]. In particular, our model can be realized for dipoles in the bilayer geometry with interlayer tunneling [111]. Tracing out the degree of freedom associated with the layer index one obtains an effective single-layer model in which g_2 and g_3 can be independently controlled by tuning the interlayer tunneling amplitude. Here we work out the phase diagram of this model and identify stable uniform and supersolid states.

4.2. Method

4.2.1. Hamiltonian

The Hamiltonian of the system reads

$$\begin{aligned} \mathcal{H} = & - \int d^2r \hat{\psi}^\dagger(\mathbf{r}) \frac{\hbar^2 \nabla^2}{2m} \hat{\psi}(\mathbf{r}) + \mathcal{H}_2 \\ & + \frac{g_3}{6} \int d^2r \hat{\psi}^\dagger(\mathbf{r}) \hat{\psi}^\dagger(\mathbf{r}) \hat{\psi}^\dagger(\mathbf{r}) \hat{\psi}(\mathbf{r}) \hat{\psi}(\mathbf{r}) \hat{\psi}(\mathbf{r}), \end{aligned} \quad (4.1)$$

where $\hat{\psi}(\mathbf{r})$ is the bosonic field operator, m is the particle mass, and the normalization volume is set equal to unity. The first term in Eq. (4.1) corresponds to the kinetic energy, the third one to the contact three-body repulsion ($g_3 > 0$), and the two-body interaction Hamiltonian \mathcal{H}_2 at low energies can be substituted by an effective momentum-dependent (pseudo)potential (see, e.g., [112])

$$\tilde{V}(\mathbf{k}, \mathbf{k}') = \tilde{V}(|\mathbf{k} - \mathbf{k}'|) = g_2 - 2\pi d^2 |\mathbf{k} - \mathbf{k}'|, \quad (4.2)$$

where \mathbf{k} and \mathbf{k}' are the incoming and outgoing relative momenta, g_2 is the contact term which depends on the short-range details of the two-body potential, and the momentum-dependent part corresponds to the long-range dipolar tail for dipoles

oriented perpendicularly to the plane of their translational motion. We thus have

$$\mathcal{H}_2 = \frac{1}{2} \int d^2r d^2r' \hat{\psi}^\dagger(\mathbf{r}) \hat{\psi}^\dagger(\mathbf{r}') \sum_{\mathbf{q}} \tilde{V}(\mathbf{q}) e^{i\mathbf{q}(\mathbf{r}'-\mathbf{r})} \hat{\psi}(\mathbf{r}) \hat{\psi}(\mathbf{r}'). \quad (4.3)$$

4.2.2. Bogoliubov excitation spectrum of a uniform BEC

The onset of supersolidity is frequently associated with the presence of a low-lying roton minimum in the excitation spectrum [113, 114, 115, 116, 102]. In our case the standard Bogoliubov approach for a uniform Bose condensate of density n gives the excitation spectrum

$$\epsilon(k) = \sqrt{E_k^2 + 2E_k(g_2n + g_3n^2 - 2\pi nd^2k)}, \quad (4.4)$$

where $E_k = \hbar^2 k^2 / 2m$, and we assume that $(g_2 + g_3n) > 0$. The validity conditions for the mean-field approach read

$$nr_*^2 \ll 1; \quad m(g_2 + g_3n) / \hbar^2 \ll 1, \quad (4.5)$$

where $r_* = md^2 / \hbar^2$ is a characteristic range of the dipole-dipole interaction. The structure of the spectrum is characterized by a dimensionless parameter β given by

$$\beta = \gamma / (1 + g_2 / g_3n); \quad \gamma = 4\pi^2 \hbar^2 r_*^2 / mg_3. \quad (4.6)$$

The excitation energy $\epsilon(k)$ shows a roton-maxon structure (local maximum and minimum at finite k) for β in the interval $8/9 < \beta < 1$, and at $\beta = 1$ the roton minimum touches zero. For $\beta > 1$ the excitation energies become imaginary, and the uniform superfluid (U) is dynamically unstable and is no longer the ground state.

4.2.3. Variational ansatz

A promising candidate for the new ground state is a supersolid state in which the condensate wavefunction is a superposition of a constant term and a lattice-type function of coordinates [98, 99, 113, 102]. We considered various lattice structures and found that the ground state can be either a triangular lattice supersolid (T) or a stripe supersolid (S). For T, the lattice is built up on three vectors in the x, y plane of the translational motion, with the angle of $2\pi/3$ between each pair: $\mathbf{k}_1 = (k, 0)$, $\mathbf{k}_2 = (-k/2, \sqrt{3}k/2)$, and $\mathbf{k}_3 = (-k/2, -\sqrt{3}k/2)$, while for the S phase the density modulation depends only on one wave vector $\mathbf{k} = (k, 0)$.

The variational ansatz for the condensate wavefunction of the T phase then takes the form:

$$\psi_T(\mathbf{r}) = \sqrt{n} \left(\cos \theta + \sqrt{2/3} \sin \theta e^{i\Phi} \sum_i \cos \mathbf{k}_i \mathbf{r} \right), \quad (4.7)$$

and for the S phase we have:

$$\psi_S(\mathbf{r}) = \sqrt{n} \left(\cos \theta + \sqrt{2} \sin \theta e^{i\Phi} \cos kx \right), \quad (4.8)$$

which satisfies the normalization condition $\int d\mathbf{r} |\psi_{T(S)}(\mathbf{r})|^2 = n$, with n being the mean density. The variational parameters of the wavefunctions are θ , Φ , and k . Density modulations appear at $\theta \neq 0$, and thus θ is the order parameter which exhibits the U to supersolid transition. We have checked that the lowest energy always corresponds to $\Phi = 0$ and for brevity we omit this parameter.

For obtaining the energy functionals of the T and S states, we replace the field operators in Eqs. (4.1) and (4.3) with $\psi_T(\mathbf{r})$ and with $\psi_S(\mathbf{r})$, respectively. This yields

$$\mathcal{E}_i = [E_k n - 4\pi n^2 d^2 k \mathcal{D}_i(\theta)] \sin^2 \theta + g_2 n^2 \mathcal{C}_i(\theta) + g_3 n^3 \mathcal{T}_i(\theta), \quad (4.9)$$

where the symbol i stands for T and S , and the functions $\mathcal{D}_{T(S)}(\theta)$, $\mathcal{C}_{T(S)}(\theta)$, and $\mathcal{T}_{T(S)}(\theta)$ are related to the two-body dipole-dipole, two-body contact, and three-body contact interactions, respectively.

4.2.4. Energy functionals

For calculating the energy functional we replace the field operators $\hat{\psi}(\mathbf{r})$ in the Hamiltonian (1) of the system with the condensate wavefunction $\psi_T(\mathbf{r})$ (7) for the triangular supersolid and with $\psi_S(\mathbf{r})$ (8) for the stripe phase. In both cases the kinetic energy term proves to be

$$\mathcal{K} = - \int d^2 r \psi_{T(S)}^*(\mathbf{r}) \frac{\hbar^2 \nabla^2}{2m} \psi_{T(S)}(\mathbf{r}) = \frac{\hbar^2 k^2 n}{2m} \sin^2 \theta. \quad (4.10)$$

In the calculation of the contribution of the two-body interaction we use the effective momentum-dependent interaction amplitude of Eq.(2). Substituting this amplitude into equation (3) in which the field operators $\hat{\psi}(\mathbf{r})$ are replaced with the condensate wavefunction $\psi_{T(S)}(\mathbf{r})$ we obtain:

$$\mathcal{H}_2^{T(S)} = \mathcal{H}_{2c}^{T(S)} + \mathcal{H}_{2d}^{T(S)}, \quad (4.11)$$

$$\mathcal{H}_{2c}^{T(S)} = \frac{g_2}{2} \int d^2 r |\psi_{T(S)}(\mathbf{r})|^4, \quad (4.12)$$

$$\mathcal{H}_{2d}^{T(S)} = \frac{1}{2} \int d^2 r |\psi_{T(S)}(\mathbf{r})|^2 f(|\mathbf{r} - \mathbf{r}'|) |\psi_{T(S)}(\mathbf{r}')|^2, \quad (4.13)$$

where Eqs. (4.12) and (4.13) represent the contributions of the contact and dipole-dipole interactions, respectively, and the function $f(|\mathbf{r} - \mathbf{r}'|)$ writes:

$$f(|\mathbf{r} - \mathbf{r}'|) = -\pi d^2 \int \frac{d^2 q}{(2\pi)^2} q \exp(i\mathbf{q}(\mathbf{r} - \mathbf{r}')). \quad (4.14)$$

The integration yields:

$$\mathcal{H}_{2c}^{T(S)} = g_2 n^2 \mathcal{C}_{T(S)}(\theta), \quad (4.15)$$

$$\mathcal{H}_{2d}^{T(S)} = -4\pi n^2 d^2 k \mathcal{D}_{T(S)}(\theta). \quad (4.16)$$

For the triangular phase the functions $\mathcal{C}_T(\theta)$ and $\mathcal{D}_T(\theta)$ are given by

$$\mathcal{C}_T(\theta) = \frac{1}{2} \left(\cos^4 \theta + 6 \cos^2 \theta \sin^2 \theta + 4\sqrt{\frac{2}{3}} \cos \theta \sin^3 \theta + \frac{5}{2} \sin^4 \theta \right), \quad (4.17)$$

$$\mathcal{D}_T(\theta) = \left[\cos^2 \theta + \sqrt{\frac{2}{3}} \cos \theta \sin \theta + \left(\frac{1}{4} + \frac{1}{2\sqrt{3}} \right) \sin^2 \theta \right], \quad (4.18)$$

and for the stripe phase we have:

$$\mathcal{C}_S(\theta) = \frac{1}{2} \left(1 + 4 \sin^2 \theta \cos^2 \theta + \frac{1}{2} \sin^4 \theta \right), \quad (4.19)$$

$$\mathcal{D}_S(\theta) = \left(1 - \frac{3}{4} \sin^2 \theta \right). \quad (4.20)$$

The integration of the third term of Eq.(1), representing the contribution of the three-body contact interaction,

$$\mathcal{H}_3^{T(S)} = \frac{g_3}{6} \int d^2 r |\psi_{T(S)}(\mathbf{r})|^6, \quad (4.21)$$

leads to

$$\mathcal{H}_3^{T(S)} = g_3 n^3 \mathcal{T}_{T(S)}(\theta). \quad (4.22)$$

The expressions for the functions \mathcal{T}_T and \mathcal{T}_S read:

$$\begin{aligned} \mathcal{T}_T(\theta) = \frac{1}{6} \left\{ \cos^6 \theta + 15 \cos^4 \theta \sin^2 \theta + 20\sqrt{\frac{2}{3}} \cos^3 \theta \sin^3 \theta + \frac{75}{2} \cos^2 \theta \sin^4 \theta \right. \\ \left. + 30\sqrt{\frac{2}{3}} \cos \theta \sin^5 \theta + \frac{85}{9} \sin^6 \theta \right\}. \end{aligned} \quad (4.23)$$

$$\mathcal{T}_S(\theta) = \frac{1}{6} \left(1 + 12 \sin^2 \theta - \frac{9}{2} \sin^4 \theta - 6 \sin^6 \theta \right). \quad (4.24)$$

The summation of \mathcal{K} (4.10), \mathcal{H}_{2c}^i (4.15), \mathcal{H}_{2d}^i (4.16), and \mathcal{H}_3^i (4.22), where the symbol i stands for T and S , leads to the energy functional in the form Eq. (4.9).

4.3. Results

By minimizing Eq. (4.9) with respect to k we obtain

$$\mathcal{E}_i(k_{mi}) = g_2 n^2 \mathcal{C}_i(\theta) + g_3 n^3 (\mathcal{T}_i(\theta) - 2\gamma \sin^2 \theta \mathcal{D}_i^2(\theta)), \quad (4.25)$$

where $k_{mi} = 4\pi n r_* \mathcal{D}_i(\theta)$. In the dilute limit of Eq. (4.5) the particle number per unit modulation volume is $n(2\pi/k_{mi})^2 \sim 1/nr_*^2 \gg 1$, which justifies the mean-field approach.

The energy functional $\mathcal{E}_{T(S)}$ can be expanded in powers of θ . The zero-order term $\mathcal{E}(\theta = 0) = g_2 n^2/2 + g_3 n^3/6$ gives the energy density of the uniform state. The expansion of \mathcal{E}_T contains terms $\propto \theta^3$, which is a consequence of the fact that the vectors \mathbf{k}_1 , \mathbf{k}_2 , and \mathbf{k}_3 form a closed triangle (“triad”, $\mathbf{k}_1 + \mathbf{k}_2 + \mathbf{k}_3 = 0$) [99]. In contrast, the expansion of \mathcal{E}_S contains only even powers of θ . According to the Ginzburg-Landau theory [68, 117], the U-supersolid transition should occur to the T phase and it is expected to be first order, so that θ jumps from 0 to a finite value. However, deeply in the supersolid regime the states with different structures are energetically competing and, in particular, the stripe phase can become the ground state of the system.

First-order transitions are convenient to analyse in the grand-canonical picture. We obtain the phase diagram by variationally minimizing the grand potential $\Omega = \mathcal{E}_{T(S)} - \mu n$ with respect to θ and n for given values of the chemical potential μ and the interaction parameters g_2 , g_3 and d . We have checked the phase diagram by employing the full numerical minimization of the grand potential density, which is equivalent to solving the corresponding Gross-Pitaevskii (GP) equation.

First, let us consider $g_2 = 0$. In this case the energy functional \mathcal{E} only contains terms $\propto n^3$, and the phase diagram is determined by a single dimensionless parameter γ defined in Eq. (4.6). The U to T transition occurs before the roton minimum touches zero (for $g_2 = 0$ we have $\beta = \gamma$), namely at $\gamma_0 \simeq 0.99$, where θ jumps from 0 to 0.0946. The inverse compressibility $\kappa^{-1} = \partial\mu/\partial n = 6\mathcal{E}/n^2$ is positive for γ smaller than approximately 1.4, indicating the existence of a stable supersolid state. However, our numerics predicts the collapse instability at about $\gamma_c \approx 0.88$ and indicates that for lower values of γ the ground state is a uniform superfluid. The discrepancy between the numerics and variational ansatz comes from the fact that the latter does not take into account higher order momentum harmonics.

For $g_2 \neq 0$, we turn to the rescaled dimensionless density $\tilde{n} = ng_3/|g_2|$, chemical potential $\tilde{\mu} = \mu g_3/g_2^2$, and grand potential $\tilde{\Omega}_{T(S)} = (g_3^2/|g_2|^3)\Omega_{T(S)} = \tilde{\mathcal{E}}_{T(S)} - \tilde{\mu}\tilde{n}$. The rescaled energy functional is given by

$$\tilde{\mathcal{E}}_i = [\mathcal{T}_i(\theta) - 2\gamma \sin^2 \theta \mathcal{D}_i^2(\theta)]\tilde{n}^3 + \text{sgn}(g_2)\tilde{n}^2 \mathcal{C}_i(\theta). \quad (4.26)$$

The phase diagram can be presented in the parameter space $(\tilde{\mu}, \gamma)$ and the phases are characterized by $\theta \in [-\pi/2, \pi/2]$ and \tilde{n} . One can easily see that in the high-density regime $\tilde{\Omega}_{T(S)}$ is dominated by the term $[\mathcal{T}_{T(S)}(\theta) - 2\gamma \sin^2 \theta \mathcal{D}_{T(S)}^2(\theta)]\tilde{n}^3$, whereas the

two-body contact interaction, i.e., the term containing $\mathcal{C}_{T(S)}(\theta)$, becomes irrelevant¹. In this case the T phase has a lower $\tilde{\Omega}$ than the S phase, and we obtain the same stability condition as in the case of $g_2 = 0$. Numerically we find that the phase diagram for $g_2 > 0$ contains only a stable U state at $\gamma < \gamma_c$ and the region of collapse for $\gamma > \gamma_c$.

The situation is quite different for $g_2 < 0$. The phase diagram is shown in Fig. 4.1 where all continuous curves correspond to the variational results and all symbols to the exact numerical solution of the GP equation. Let us first discuss the variational results. The dashed curves mark the U-T _{$\theta < 0$} and U-T _{$\theta > 0$} transitions, which occur for $\tilde{\mu} < 3/2$ and $\tilde{\mu} > 3/2$, respectively. These are first order transitions which weaken on approaching the point $\tilde{\mu} = 3/2$, $\gamma = 2/3$ (black dot). The same holds for the dotted curves, which correspond to the transitions from the T phases to the S phase. The black dot thus stands as a four-critical point and it is the only place in the phase diagram where the transitions are second order and occur when the roton minimum touches zero. In this case the grand potential $\tilde{\Omega} = \text{const} + O(\theta^4)$, i.e., the terms $\propto \theta^2$ and $\propto \theta^3$ are absent.

The region on the left of the black solid curve in Fig. 4.1 is the vacuum state: $\tilde{n} = 0$, $\Omega = 0$. Directly on the curve, vacuum can coexist with matter which has a finite density and zero pressure. We thus are dealing with a self-trapped droplet state²[118]. With increasing γ , the vacuum curve eventually bends towards negative $\tilde{\mu}$ and tends to the variational collapse line $\gamma \approx 1.4$ (not shown).

By solving the GP equation numerically we observe that the overall structure of the phase diagram is well captured by the variational ansätze (4.7) and (4.8). Close to the four-critical point the agreement is quantitative, which is generally expected in the regions where $\theta \ll 1$. Far from this point we see that the exact collapse line moves to $\gamma \approx 0.88$ (crosses in Fig. 4.1) and the vacuum curve (empty orange circles) bends towards negative $\tilde{\mu}$ faster than its variational version. The rest of the symbols in Fig. 4.1 are inside the U phase (filled circles), T _{$\theta < 0$} phase (down triangles), T _{$\theta > 0$} phase (up triangles), and S phase (squares). We see that the actual U-T _{$\theta < 0$} phase boundary is well described by the variational method, but one can notice a move of the S phase upwards and towards negative $\tilde{\mu}$. In fact, the vacuum-S-T _{$\theta > 0$} tri-critical point moves to $\tilde{\mu} \approx -1.27$, $\gamma = 0.78$ (outside of the plot).

In Fig. 4.1 we also show density profiles corresponding to the points enclosed by rectangular frames in the phase diagram. The blue and yellow colors stand for minima and maxima of the density. Without this rescaling the contrast, for instance, in the lowest rightmost picture would be very weak. However, one can clearly distinguish smooth density profiles, which can be described by a few harmonics in the spirit of Eqs. (4.7) and (4.8), and sharper profiles (as one moves further away from the four-critical point) requiring more harmonics or a different ansatz. The spatial coordinates

¹ In fact, one can think of the $g_2 = 0$ case as being represented by a vertical line in Fig.1 drawn at infinite $\tilde{\mu}$.

²Such droplets have been discussed for 3D Bose condensates with contact two- and three-body interactions by A. Bulgac.

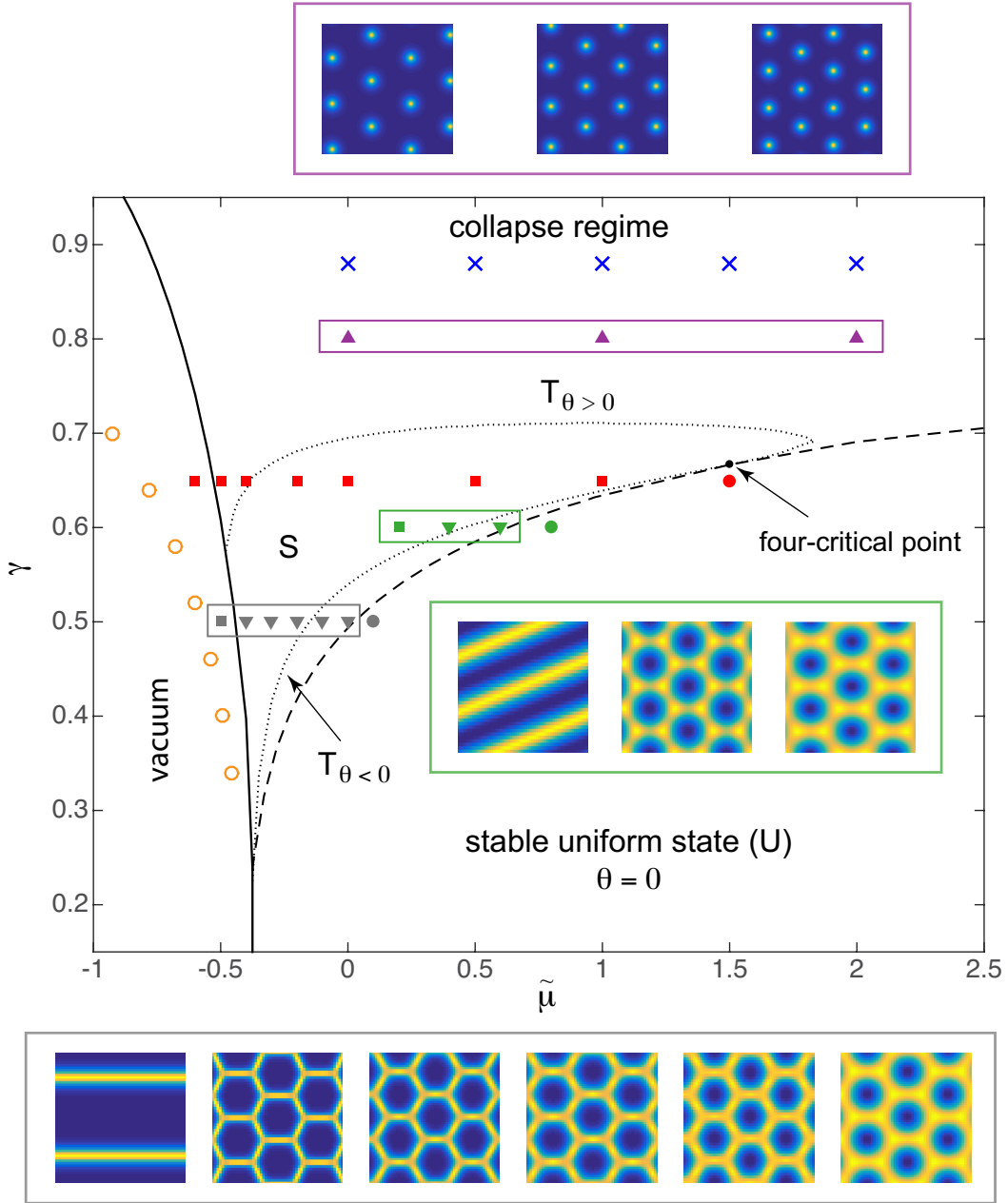


Figure 4.1. – (color online) Phase diagram for $g_2 < 0$. Continuous curves correspond to transitions between different phases obtained from the variational ansätze (4.7) and (4.8). Increasing γ one passes the U-T transition (dashed), then T-S (lower dotted curve), and S-T (upper dotted curve). To the left of the solid black curve the ground state of the system is vacuum. The black dot is the four-critical point for the U, S, and two T phases. The symbols indicate our numerical results: the filled circles are inside the U phase, the downward and upward pointing triangles are inside the $T_{\theta < 0}$ and $T_{\theta > 0}$ phases, respectively, and squares are in the stripe phase. The empty circles are on the vacuum-stripe line and crosses are at the collapse instability border. The color-coded pictures show density profiles corresponding to the symbols in the phase diagram put in frames: the upper set (violet frame) contains three points of the $T_{\theta > 0}$ phase at $\gamma = 0.8$, the middle set (green frame) shows one point in the S phase and two points in the hexagonal $T_{\theta < 0}$ phase at $\gamma = 0.6$, and the lower set (grey frame) corresponds to the six points at $\gamma = 0.5$.

have also been rescaled (except for the upper set in the violet frame) because the wave vector k_m changes very strongly from point to point.

To the right of the vacuum curve (empty circles in Fig. 4.1) the pressure is $P = -\Omega > 0$ and, therefore, this region of the phase diagram requires an external trapping. In Fig. 4.2 we present the exact GP result for an isotropically trapped gas with $g_2 < 0$, $\gamma = 0.575$, the global chemical potential $\tilde{\mu} = 0.6$, and trap frequency $\tilde{\omega} = 0.05$ (in units of $g_2^2/\hbar g_3$). The result is consistent with the local density approximation in which moving from the trap center towards its edge is equivalent to the trajectory along a horizontal line in Fig. 4.1 determined by the local chemical potential $\mu(r) = \mu - m\omega^2 r^2/2$. In Fig. 4.2 one can clearly distinguish the U phase in the trap center, the transition to the $T_{\theta < 0}$ phase, and eventually to the S phase. As the local chemical potential decreases, the contrast and the period of the density modulation increase, which is consistent with the free space results.

We should point out that first-order transitions involving density jumps are forbidden in 2D systems with dipolar interaction tails. The reason is that the surface tension in between two such phases can have a negative contribution which logarithmically diverges with the length of the interface and can thus overcome the positive local scale-independent contribution [119] (see also [100]). This means that the first-order transition curves that we describe here become (narrow) regions of intermediate “microemulsion” phases [119]. It is argued [100, 120] that the observation of these phases requires exponentially large system sizes which are likely much larger than the size of a typical ultracold sample. Nevertheless, we note that already the simplest vacuum-U interface that we predict in our dilute weakly-interacting system should be a good candidate for studying these interfacial effects. However, we leave this subject for future work.

4.4. Numerical methods

The numerical calculation is performed in the grand canonical ensemble, with a given chemical potential μ and fixed volume of the system $V = L_x L_y$. The field operator $\hat{\psi}$ is treated as a classical field, and is discretized on a two-dimensional grid with periodic boundary conditions in the coordinate and momentum space. The grand potential reads:

$$\begin{aligned} \Omega[\psi^*, \psi] = & \int d^2r \psi^*(\mathbf{r}) h_0 \psi(\mathbf{r}) + \frac{1}{2} \int d^2r d^2r' f(\mathbf{r} - \mathbf{r}') |\psi(\mathbf{r}')|^2 |\psi(\mathbf{r})|^2 \\ & + \frac{g_2}{2} \int d^2r |\psi(\mathbf{r})|^4 + \frac{g_3}{6} \int d^2r |\psi(\mathbf{r})|^6 - \mu \int d^2r |\psi(\mathbf{r})|^2, \end{aligned} \quad (4.27)$$

where the single-particle Hamiltonian h_0 includes a possible presence of the harmonic trapping potential:

$$h_0 = -\frac{\hbar^2}{2m} \nabla^2 + \frac{1}{2} m \omega^2 r^2. \quad (4.28)$$

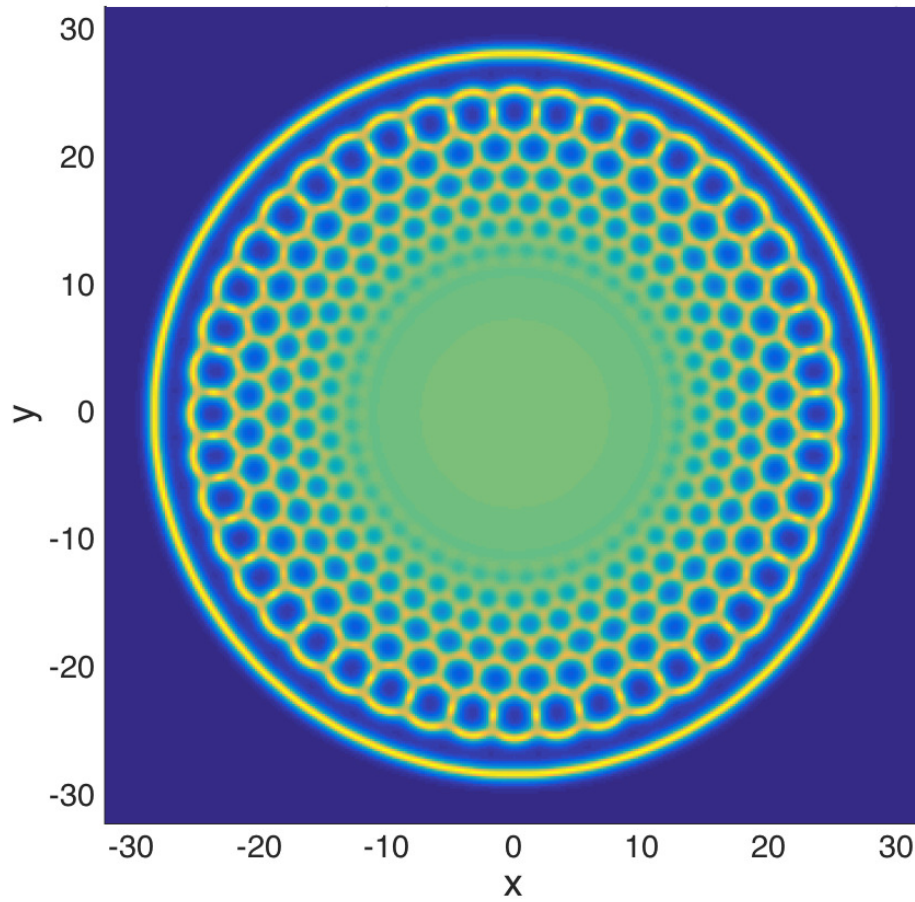


Figure 4.2. – (color online) The density profile for a harmonically trapped gas with $\tilde{\mu} = 0.6$, $\gamma = 0.575$, and trapping frequency $\tilde{\omega} = 0.05$. The coordinates x, y are in units of $\sqrt{\hbar^2 g_3 / m g_2^2}$.

The number of grid points that we use along each direction ranges from 64 to 128 in the absence of the trapping potential and from 512 to 1024 in presence of an isotropic harmonic trap.

The ground state is determined by minimizing the grand potential (4.27) with the use of the *conjugate gradient* algorithm. An ingredient of this method is the line minimization, that is in each iteration the wavefunction is changed as

$$\psi_{i+1}(\mathbf{r}) = \psi_i(\mathbf{r}) + \lambda \Delta \bar{\psi}_i(\mathbf{r}), \quad (4.29)$$

where $\psi_i(\mathbf{r})$ is the wavefunction in a current step, and λ is a real parameter chosen to minimize (4.27) along the proposed direction $\Delta \bar{\psi}_i(\mathbf{r})$. This procedure allows us to find the global minimum encountered when moving downhill in $\Omega[\psi^*, \psi]$ along a line. Consequently, it improves the efficiency of the calculation. The direction along which to move $\psi_i(\mathbf{r})$ is constructed as

$$\Delta \bar{\psi}_i(\mathbf{r}) = \Delta \psi_i(\mathbf{r}) + \frac{\int d^2r \Delta \psi_i^*(\mathbf{r}) [\Delta \psi_i(\mathbf{r}) - \Delta \psi_{i-1}(\mathbf{r})]}{\int d^2r |\Delta \psi_{i-1}(\mathbf{r})|^2} \Delta \bar{\psi}_{i-1}(\mathbf{r}), \quad (4.30)$$

in order to be *conjugate* with respect to the direction $\Delta \bar{\psi}_{i-1}(\mathbf{r})$ used in the previous step, and

$$\Delta \psi_i(\mathbf{r}) = -\frac{\delta \Omega}{\delta \psi^*} = -[\mathcal{H}_{\text{GP}}(\mathbf{r}) - \mu] \psi_i(\mathbf{r}), \quad (4.31)$$

is the gradient of the functional $\Omega[\psi^*, \psi]$ evaluated with $\psi_i(\mathbf{r})$, where

$$\mathcal{H}_{\text{GP}} = h_0 + \int d^2r' f(\mathbf{r} - \mathbf{r}') |\psi(\mathbf{r}')|^2 + g_2 |\psi(\mathbf{r})|^2 + \frac{g_3}{2} |\psi(\mathbf{r})|^4 \quad (4.32)$$

is the Gross-Pitaevskii Hamiltonian. The integral in the second term of Eq. (4.32) can be calculated by using the convolution theorem [121], namely

$$\int d^2r' f(\mathbf{r} - \mathbf{r}') |\psi(\mathbf{r}')|^2 = \mathcal{F}^{-1} \{ \mathcal{F}[f](\mathbf{q}) \mathcal{F}[|\psi|^2](\mathbf{q}) \} \quad (4.33)$$

where $\mathcal{F}[f](\mathbf{q})$ and $\mathcal{F}[|\psi|^2](\mathbf{q})$ are the Fourier transforms of $f(\mathbf{r})$ and $|\psi(\mathbf{r})|^2$ respectively, and \mathcal{F}^{-1} is the inverse transform. We set that the convergence is reached when the relative difference in the grand potential between the neighboring time steps is smaller than 5×10^{-9} .

In the absence of external trapping, the wave function can remain finite at the boundary. Due to the periodic boundary condition, the structure of the modulation for a non-uniform state is then limited by the size of the system imposed in the simulation. In order to overcome this constraint, for each given set of parameters (g_2, g_3, d, μ) we run the simulation several times with different L_x and L_y ranging from $4\pi/k_m$ to $9\pi/k_m$ respectively, where $k_m = 4\pi n r_* \mathcal{D}_{T(S)}(\theta)$ is fixed by the variational ansatz. In the end we choose the ground state as the one corresponding to the lowest grand potential density Ω/V .

Different trial wavefunctions are used in the simulation, including a uniform state, triangular (hexagonal) lattice state, square lattice state, stripe state, a combination of triangular (hexagonal) and stripe states. This is done in order to check whether the final result is biased by the initial conditions or not. We have also compared with each other the results obtained with a different number of grid points to make sure that they are not affected by the discretization of space.

4.5. Concluding remarks

In conclusion, we have found that a dilute 2D dipolar Bose gas can reside in a variety of supersolid phases stabilized by three-body repulsion. Our results represent a starting point for the analysis of collective modes of homogeneous, trapped or self-trapped supersolids. The developed approach can also be employed in the studies of novel vortex and soliton structures, and in the search for translationally nonperiodic phases, in particular density-disordered superfluid (superglass) phases.

Promising candidates for the creation of such dipolar Bose gases are (non-reactive) polar molecules in the bilayer geometry with interlayer tunneling. The validity of the Hamiltonian (4.1) requires the tunneling amplitude t be much larger than the interaction energy per particle (chemical potential). For the 2D confinement frequency ~ 50 kHz and interlayer spacing $\lambda \approx 200$ nm one has $t \sim 100$ nK for non-reactive NaK molecules. In the region of stability of supersolid states in the phase diagram in Fig.1 we have γ in between 0.3 and 0.85, so that for $r_* \sim \lambda$ one has the three-body coupling constant $g_3 \sim 2\pi^2\hbar^2\lambda^2/m$. The characteristic value of the chemical potential in the stability region is $|\mu| \sim g_2^2/g_3$ ($|\tilde{\mu}| \sim 1$) and it can be easily made about 10 nK, which is much smaller than t . The chemical potential is related to the 2D density as $\mu = g_2n + g_3n^2/2$, and for g_3 specified above the value $|\mu| \sim 10$ nK corresponds to $n \sim 5 \times 10^8$ cm⁻². Therefore, the Kosterlitz-Thouless critical temperature $T_{KT} = \pi\hbar^2n_s/2m$ (n_s is the superfluid density just below T_{KT} and in our conditions it is about a factor of 3 or 4 lower than the total density) will be ~ 20 nK. Then, in analogy with spinor Bose gases (see [122]) for the supersolid-uniform difference in the interaction energy per particle of a few nanokelvin the system should Bose-condense to the supersolid state in the region of its stability shown in Fig.1. We thus see that the observation of dilute supersolid states proposed here is feasible at temperatures of a few tens of nanokelvins.

The experimental setup and procedure

My major work during this PhD period was to construct an experimental setup for creating a sample of ultracold NaK polar molecules at their absolute ground state with my colleagues from scratch. In this chapter, I will first give an overview about the experimental setup and the experimental procedures. I then proceed to give some details about the individual steps for producing ultracold NaK ground state molecules. Further details about the experimental setup have been well presented in Dr. Nikolaus.W. Buchheim's thesis [123].

Note: This chapter summarizes my major experimental contribution during my PhD period. There is no result published from this experimental setup as the time of writing this thesis. Being the first generation of this experiment, Dr. Nikolaus W. Buchheim and I have constructed the setup together since 2011 to 2016. The similarities between the thesis of Dr. Buchheim [123] and this thesis are due to the great overlapping of our experimental works, which can not be identified individually. Dr. Buchheim has agreed the rights of citing and quoting the figures and texts appeared in this chapter from Dr. Buchheim's thesis [123].

5.1. Overview

In order to produce an ultracold sample of $^{23}\text{Na}^{40}\text{K}$ ground state molecules, the essential steps are summarized as follows,

1. Laser cooling and trapping ^{23}Na and ^{40}K atoms simultaneously in a magneto-optical trap (MOT).
2. Loading ^{23}Na and ^{40}K mixture into a magnetic trap and performing evaporative and sympathetic cooling of Na and K respectively.
3. Loading the mixture into an optical dipole trap for transporting to the glass cell and further evaporation to reach quantum degeneracy.
4. Preparing ^{23}Na and ^{40}K atoms into right spin states.
5. Using radio-frequency (rf) method to associate weakly bound state, Feshbach molecules.

6. Transferring adiabatically the Feshbach molecules to the deeply bounded ground state via Stimulated Raman Adiabatic Passage (STIRAP).
7. Loading the ground state molecules into one dimensional lattice and apply strong external electric field to polarize the molecules.

We designed and constructed the experimental apparatus deliberately to perform these steps. The experimental system architecture could be divided into the following parts:

1. An ultra high vacuum (UHV) environment with pressure ($p < 10^{-10}$ mbar) to suppress background gas collisions, together with atomic sources.
2. Separated laser systems for two different chemical elements are used for laser cooling and imaging atoms.
3. Plugged magnetic trap containing a pair of magnetic coils producing quadrupole magnetic field and a Coherent Verdi (532 nm, 10W) laser.
4. Trapping laser system for optically trapping and transporting atoms.
5. Feshbach coils system to generate and to stabilize magnetic field for associating Feshbach molecules.
6. Raman laser system, containing two separated lasers phase-locked into an ultra low expansion (ULE) cavity, to investigate molecular line structures and to perform STIRAP.
7. High resolution imaging system combined with one dimensional optical lattice system.
8. High voltage power system generating high electrical field to polarize the ground state molecules under the vacuum.
9. Various radio-frequency (rf) and microwave (MW) systems for manipulating hyperfine states and/or Zeeman sub levels.
10. Central real-time experiment control unit with a timing resolution of $1\mu s$, with a Python-based interface.

An overview of the main experimental setup (high vacuum part) is displayed in the Fig. 5.1 (The figure is taken from Fig. 2.2 of Ref.[123] with the permission of reproduction from Dr. Buchheim).

In the following sections, we provide some details about each sub systems and their application in the experimental procedures.

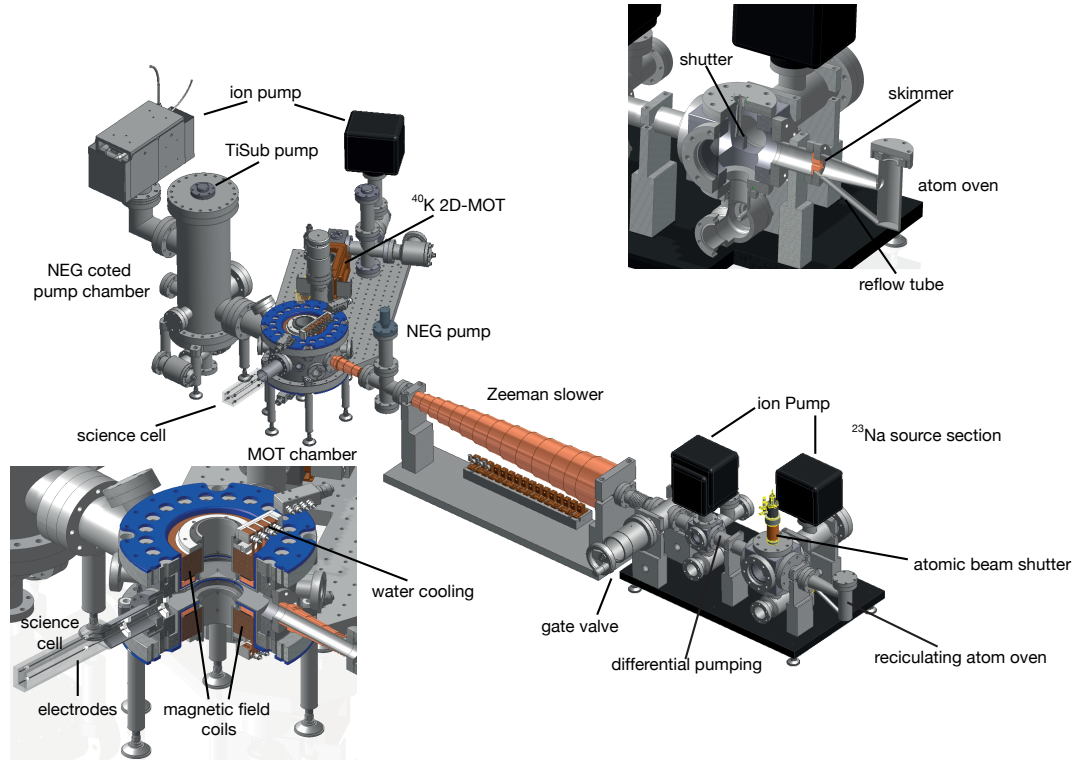


Figure 5.1. – CAD model of the current experimental setup. Right-up: Na oven section. Left-down: Magnetic trap section. This figure is taken from Fig. 2.2 of Ref.[123] with the permission of reproduction from Dr. Buchheim.

5.2. Creating a degenerate $^{23}\text{Na}^{40}\text{K}$ Bose-Fermi mixture

Making degenerated Bose or Fermi gas has been well established in the ultra cold atomic community [124, 125]. The experimental creation of various Bose-Fermi has also been achieved with $^{40}\text{K}^{87}\text{Rb}$ [126, 127] and $^{40}\text{K}^{23}\text{Na}$ [128]. We follow the standard experimental techniques to achieve quantum degenerate $^{23}\text{Na}^{40}\text{K}$ Bose-Fermi mixture.

Our cooling scheme contains three major steps. 1) A pre-cooling process with lasers in a dual species MOT. 2) Evaporative cooling of ^{23}Na in a plugged quadrupole magnetic trap and sympathetic cooling of ^{40}K . 3) Evaporative cooling of mixture in a optical dipole trap.

5.2.1. Na Zeeman slower and Na laser system

We use a spin-flip Zeeman slower to create a cold Na atomic beam. The Na oven is operating at of $330^\circ\text{C} = 603.15\text{K}$, corresponding to a vapor pressure of $\simeq 0.4\text{mbar}$, and the density is $\simeq 7.2 \cdot 10^{14} \frac{1}{\text{cm}^3}$ [123]. Na oven is separated from the main chamber

by a dual stage differential pumping section to maintain a low pressure of background gas at the main chamber.

The working principle of Zeeman slower has been well discussed in literatures[129], and the working parameters of our setup are presented in Ref. [123]. After passing the Zeeman slower, the fraction of ^{23}Na atoms with a velocity smaller than the MOT capture velocity is estimated to be $\sim 60\%$ [123].

All the light used for Na Zeeman slower, 3D MOT and imaging system are derived from a single second harmonic generation (SHG) modules. A commercial external cavity diode laser with wavelength 1178nm (Toptica DLPro) seeds a Raman fiber amplifier (MPB Communications). The Raman amplifier outputs 10W infrared light and pass a frequency-doubling module and results in 1.5W power at 589nm.

We use usual D2 line cooling technique for ^{23}Na . The laser frequency is stabilized to ^{23}Na $F = 2 \rightarrow F' = 3$ cycling transition via RF modulated Doppler-free saturated absorption spectroscopy technique [130]. To bring the atoms staying at $F = 1$ ground state back to the cycling transition, an additional ‘repumper’ laser which is on the resonant of $F = 1 \rightarrow F' = 2$ transition is required. The electronic hyperfine ground states splitting of ^{23}Na is 1771.6 MHz. For Zeeman slower light and 3D MOT light, we use Electro-optic modulators (EOMs) to generate frequency side bands which are ~ 1.7 GHz away from the carrier frequency. Therefore, the cooling light and repumping light are intrinsically overlapped, and no further alignment is required. However, for other purposes such as optical pumping and hyperfine resolved imaging, we use a special Acousto-optic modulator (AOM) with large modulation frequencies (up to ~ 2 GHz, Crystal Technology) and the frequency of the first order diffraction is away from the input by the microwave modulation frequency. In addition, we use various AOMs with the double-pass configurations to tune and control the frequencies of different laser ports.

All the laser ports are coupled to polarization maintaining optical fibers and then routed to the main setup to get better beam qualities and versatility.

5.2.2. K 2D-MOT and K laser system

We use a standard 2D-MOT as the atomic source of ^{40}K [131]. We do not apply on-axis cooling and pushing beams for the 2D-MOT. We use enriched of ^{40}K sample and the fraction of ^{40}K is $\sim 3\%$. The 2D-MOT is operating at temperature $\simeq 60^\circ\text{C}$. The 2D-MOT chamber is connected to the 3D-MOT chamber via a $\simeq 1\text{cm}$ differential pumping tube with $\simeq 3\text{mm}$ diameter, in order to keep 3D-MOT chamber under high vacuum during the operation. In addition, we use a camera to monitor the position of the ^{40}K atomic beam by its fluorescence. We tune the position of the atomic beam to the center region of differential pumping tube by 2D-MOT coils.

Saturated absorption spectroscopy technique is not feasible to lock the lasers to any transitions of ^{40}K due to the low abundance. Thus, we lock a home-built external cavity diode laser (master laser) to the D2 line of ^{39}K . All other lasers used for cooling, repumping and imaging are then locked to the master laser via master-slave configuration: the beat-note signals are detected by fast photodiodes and then pass

a digital phase-frequency discriminator (dPFD) to generate a rf signal. The error signal is generated by comparing rf signal from the dPFD and a local oscillator (it can be a voltage-controlled oscillator (VCO) or a direct digital synthesizer (DDS)). The error signal is then fed back to the slave laser and stabilize the frequency. By that, controllable large tuning range offset lock between master and slave lasers are achieved. The potassium laser system is versatile that can be used for both ^{39}K and ^{40}K isotopes.

For ^{40}K D2 line cooling scheme, the cycling transition is $F = 9/2 \rightarrow F' = 11/2$ and the repumping transition is $F = 7/2 \rightarrow F' = 9/2$. The hyperfine splitting of ^{40}K electronic excited states is small, therefore the repumping light needs equal amount power as the cooling light. We use four commercial tapered amplifier (TA) diode lasers (Toptica TA pro) in the current experiment, two for the 2D-MOT and two for the 3D-MOT. The pair that is used for the 2D-MOT is operated with a cooling to repumping power ratio of 1.0, the 3D-MOT pair with a ratio of 10.0. Since the cooling and the repumping light are from different lasers, we superimpose the beams and couple into a single mode polarization maintaining (SM/PM) fiber.

5.2.3. Dual species 3D MOT

It is crucial to start with a stable 3D MOT (atom number and temperature) in our experiments. For this purpose, we use an laser intensity stabilization setup to eliminate possible laser intensity fluctuation due to fiber polarization drift or vibration. We also use retro-reflected MOT configuration which is more compact and stable. We do not operate dark-spot MOT in our setup since we didn't see significant benefits of using it. With these experimental efforts, the long-term stability of the atom number for both species is $< \pm 5\%$.

At the end of 3D MOT loading, we employ the compressed MOT (cMOT) technique [123] to increase the density for better loading into the magnetic quadrupole trap.

5.2.4. Plugged magnetic trap and evaporative cooling

The temperature of $^{23}\text{Na}^{40}\text{K}$ clouds reach the Doppler limit after MOT. To cool down the clouds further, we need to perform evaporative cooling in a magnetic trap.

Therefore, we use circular polarized lasers with a $\simeq 1G$ guiding field to optically pump $^{23}\text{Na}^{40}\text{K}$ mixture to the stretched low field seeking hyperfine states ($|F = 2, m_F = 2\rangle$ for ^{23}Na and $|F = 9/2, m_F = 9/2\rangle$ for ^{40}K) after MOT to avoid spin-exchange collisions.. We then directly ramp up the magnetic field to $\simeq 250G/cm$ to catch most of atoms. To make sure we have a pure spin polarized mixture of $^{23}\text{Na}|F = 2, m_F = 2\rangle$ and $^{40}\text{K}|F = 9/2, m_F = 9/2\rangle$, we perform spin-purification techniques after loading into the magnetic trap: we keep the magnetic trap gradient at $8.25G/cm$ and wait for $\simeq 2s$ that all atoms at non-stretched states leave the trap due to the gravity.

We use a pair of coils at anti-Helmholtz configuration to create a quadrupole magnetic field. The center of the anti-Helmholtz coils has zero magnetic field and it

leads to the depolarization of atoms and losses (Majorana losses in literatures[132]). To avoid Majorana losses, we focus a high intensity laser beam ($\lambda = 532\text{nm}$, $P = 5\text{W}$, $w_0 = 50\mu\text{m}$) that is blue detuned with respect to the D1 and the D2-line in ^{23}Na and ^{40}K to the center of the magnetic trap. This laser beam is called *plug laser*.

We use forced microwave evaporation on $F = 2 \rightarrow F' = 1$ hyperfine transition of ^{23}Na in the plugged magnetic trap. Due to the large inter-species s-wave scattering length between ^{23}Na and ^{40}K , $\simeq -690a_0$, it is very efficient to sympathetically cool down fermionic ^{40}K in the trap.

Three-body loss appears at the end of the evaporation process when the density of the clouds becomes large [133]. To suppress three-body loss, we gradually decrease the magnetic field gradient at the end of the evaporation while keeping the re-thermalization still efficient [123].

To conclude, after the evaporative cooling in the plugged quadrupole trap, we can produce a spin polarized thermal ensemble of $\simeq 8 \cdot 10^7$ ^{23}Na $|F = 2, m_F = 2\rangle$ and $\simeq 5 \cdot 10^6$ ^{40}K $|F = 9/2, m_F = 9/2\rangle$ atoms at a temperature of $\simeq 6\mu\text{K}$. Shot to shot atom number fluctuations and long term atom number drift is below 10% of the average value. We then load the cold mixture into an optical dipole trap.

5.2.5. Optical dipole trap and transport

To associate Feshbach molecules, it requires a homogenous magnetic field with high stability. In addition, it is also required to have large optical access for future experiments. Therefore we load the cold mixture into an optical dipole trap and use this optical trap to transport the mixture from the main chamber to the glass cell. The glass cell is made of transparent windows and is immune to Eddy currents.

Optical dipole trap relies on the principle of AC Stark shift from far detuned laser lights, and has been widely used in ultracold experiments (see e.g. Ref. [134]). Spatially varying light shifts due to a focused high intensity laser form a trapping potential for the atoms:

$$U(r, z, \omega) = \frac{3\pi c^2}{2\omega_0^3} \left(\frac{\Gamma}{\omega_0 - \omega} + \frac{\Gamma}{\omega_0 + \omega} \right) \cdot I(r, z), \quad (5.1)$$

where ω_0 and Γ are the angular transition frequency and natural linewidth of the nearest atomic transition, $\omega = \frac{2\pi c}{\lambda}$ the angular frequency of the trapping laser and $I(\mathbf{r})$ the spatial intensity distribution of the trapping laser. We define *trap depth* U_0 of an optical dipole trap as $U_0 = U(r = 0, z = 0)$ [123].

Typically, Gaussian beams are used in experiments. The intensity distribution of a single Gaussian beam is given:

$$I(r, z) = \frac{2P}{\pi w(z)^2} \exp\left(-\frac{2r^2}{w(z)^2}\right), \quad (5.2)$$

with

$$w(z) = w_0 \sqrt{1 + \left(\frac{\lambda z}{\pi w_0}\right)^2}, \quad (5.3)$$

where P is the power, w_0 the beam waist and λ the wavelength of the laser. Within the harmonic approximation, the trapping potential can be expressed as,

$$U_h(r, z) = -U_0 + \frac{1}{2}m(\omega_r^2 r^2 + \omega_z^2 z^2) \quad (5.4)$$

The radial and axial trapping frequencies ω_r and ω_z are given by:

$$\omega_r = 2\sqrt{\frac{U_0}{mw_0^2}}, \omega_z = \sqrt{\frac{2U_0}{m(\pi w_0^2/\lambda)^2}}.$$

From Eq. (5.1), it can be seen that higher intensity results in larger energy shift. The atoms tend to locate at the focus of the dipole trap for red-detuned. The atoms are transported to the science glass cell by moving the focus of the dipole trap [136]. The details of our setup are presented in Ref. [123].

In our experiment, we load the cold mixture from the magnetic trap into a single beam dipole trap. The wavelength of the dipole trap is $\lambda = 1064\text{nm}$ which is far away from D1 and D2 transitions of ^{23}Na and ^{40}K . The maximum power of the dipole trap is $P = 7.5\text{W}$, and the the waist is of $w_0 = 40\mu\text{m}$.

At the end of the MW evaporation in the magnetic trap, we simultaneously ramp up the power of the dipole trap and switch off the quadrupole magnetic field and the plug beam. We optimize the loading efficiency by tuning the position the dipole trap beam with respect to the magnetic trap.

As reported in Ref.[135] and also observed in our experiment, the lifetime of ^{23}Na $|F = 2, m_F = 2\rangle + ^{40}\text{K}$ $|F = 9/2, m_F = 9/2\rangle$ mixture is short in the dipole trap ($\tau \lesssim 100\text{ms}$) due to inelastic hyperfine changing collisions. Therefore we transfer ^{23}Na from $F = 2, m_F = 2$ to $F = 1, m_F = 1$ (the lowest energy Zeeman substates) by applying a MW Landau-Zener sweep with a $B \simeq 1.35\text{G}$ guiding field. Currently, we could load $\sim 10\%$ ^{23}Na atoms and $\sim 60\%$ ^{40}K from the magnetic trap to the dipole trap.

We transport the ^{23}Na ^{40}K mixtures from the main chamber to the glass cell over $\sim 25\text{cm}$ within 750ms . The transport efficiency is $\simeq 65\%$ for ^{23}Na and $\simeq 90\%$ for ^{40}K . The temperatures of the mixture before/after transport stay the same, $\simeq 12\mu\text{K}$. The temperature increase from $\simeq 6\mu\text{K}$ to $\simeq 12\mu\text{K}$ during the dipole trap loading is due to adiabatic heating [137].

5.2.6. Degenerate Bose-Fermi mixture

After transporting into the glass cell, further evaporation is required for the mixture to reach quantum degeneracies. The single beam dipole trap does not provide sufficient confinement along the axial axis, therefore the density of the clouds and the

resulting thermalization rate is not high enough to reach efficient evaporation. To change that, we axially compress the trap by sending a second crossed laser beam ($\lambda = 1550\text{nm}$, $P = 5\text{W}$, $w_0 = 100\mu\text{m}$).

To evaporate the mixture further, we ramp down to transport dipole trap power from 90% down to few percent level (depending on the target temperature we would like to achieve) and ramp up the crossed dipole beam from 10% to 40% simultaneously. Experimentally we are able to change the initial MOT loading condition and control the endpoint of the evaporation to obtain a mixture with different atom number ratios and different temperatures. In Fig. 2.24 of Ref. [123], we show absorption images of degenerate Bose-Fermi mixtures of ^{23}Na and ^{40}K with various atom number ratios.

If we load ^{23}Na alone, we can produce a pure Bose-Einstein condensate with $\simeq 5 \cdot 10^6$ ^{23}Na atoms.

We can produce degenerate Bose-Fermi mixture of ^{40}K ^{23}Na at temperature as low as $\simeq 40\%$ of the Fermi temperature while $\simeq 95\%$ of ^{23}Na atoms are condensed [123]. It provides an ideal starting point for further experiments, such as association of weakly bound Feshbach molecules, molecular spectroscopy, Bose polarons, etc.

5.3. RF association of Feshbach molecules

5.3.1. Introduction

In this section, I present the experimental details of associating $^{23}\text{Na}^{40}\text{K}$ Feshbach molecules by using radio-frequency (rf) method. Theoretical details on Feshbach resonances and Feshbach molecules can be found in the next chapter.

Since the first creation of ultracold ^{85}Rb ^{87}Rb Feshbach molecules, heteronuclear Feshbach molecules have been produced in various systems, including Bose-Bose mixtures of ^{87}Rb ^{133}Cs [138], ^{87}Rb ^{41}K [139] and ^{87}Rb ^{23}Na [140], in Bose-Fermi mixtures of ^{87}Rb ^{40}K [141], ^{23}Na ^6Li [142] and ^{23}Na ^{40}K [128], and in Fermi-Fermi mixture of ^6Li ^{40}K [143].

There are two well established methods in the ultracold community to associate Feshbach molecules [144]: one is so called magneto-association by sweeping the magnetic fields across the Feshbach resonances [145, 144], and the second method is called radio frequency association by applying a rf pulse to an ultracold mixture [128, 146]. Currently, we use rf association method to associate Feshbach molecules in our setup. Compared to magneto-association, rf association is easier technical-wise and clearer way to produce molecules. The theoretical model of rf association has been discussed in Ref. [147, 148].

In Ref [135], 21 Feshbach resonances of $^{23}\text{Na}^{40}\text{K}$ have been identified and characterized. I list the 11 s-wave resonances in Table 5.1:

These low-field and wide Feshbach resonances are the ideal candidates for rf associations: it is easy to control magnetic fields at low fields with high stability, and

Collision channel	Position B_0 (G)	Width ΔB (G)
$ F = 1, m_F = 1\rangle_{Na} F = 9/2, m_F = -3/2\rangle_K$	116.9	0.5
$ F = 1, m_F = 1\rangle_{Na} F = 9/2, m_F = -3/2\rangle_K$	129.5	4.6
$ F = 1, m_F = 1\rangle_{Na} F = 9/2, m_F = -5/2\rangle_K$	175	20.0
$ F = 1, m_F = 1\rangle_{Na} F = 9/2, m_F = -5/2\rangle_K$	96.5	0.5
$ F = 1, m_F = 1\rangle_{Na} F = 9/2, m_F = -5/2\rangle_K$	106.9	1.8
$ F = 1, m_F = 1\rangle_{Na} F = 9/2, m_F = -5/2\rangle_K$	138	30
$ F = 1, m_F = 1\rangle_{Na} F = 9/2, m_F = -7/2\rangle_K$	81.6	0.2
$ F = 1, m_F = 1\rangle_{Na} F = 9/2, m_F = -7/2\rangle_K$	89.8	1.1 (2.5)
$ F = 1, m_F = 1\rangle_{Na} F = 9/2, m_F = -7/2\rangle_K$	108.6	6.6
$ F = 1, m_F = 1\rangle_{Na} F = 9/2, m_F = -9/2\rangle_K$	78.3	1.1
$ F = 1, m_F = 1\rangle_{Na} F = 9/2, m_F = -9/2\rangle_K$	88.2	4.3 (12)

Table 5.1. – 11 reported s-wave Feshbach resonances in Ref. [135]. Values in brackets are the results from our measurements.

the large widths indicate strong coupling between the open collisional channel and the closed molecular bound states [10]. We initially use the resonance at 138G with $|F = 1, m_F = 1\rangle_{Na}|F = 9/2, m_F = -5/2\rangle_K$ channel for association, and currently use the one at 88.2G with $|F = 1, m_F = 1\rangle_{Na}|F = 9/2, m_F = -9/2\rangle_K$ channel¹.

5.3.2. Experimental setup

We associate the Feshbach molecules at the center of the glass cell. We have built and installed essential hardware around the glass cell for the molecule association.

Feshbach magnetic coils

It is crucial to have a stable homogeneous magnetic field. We placed a pair of water-cooled Helmholtz coils on the top/bottom of the glass cell. The electrical current is controlled by a feed-back circuit : the current is measured with a high precision current transducer (LEM IT 700-SB ultrastab) and compared with a target value, the error signal is then fed back to the gate-source voltage of 4 identical high power MOSFETs (Semikron SKM111AR) which control the current of Feshbach coils.(see Sec. 3.2 of Ref.[123] for the design of this control circuit). We are able to get 10^{-5} stability with this control circuit.

RF components

We use custom built direct digital synthesizer (DDS) circuits to generate radio-frequency (rf) signal. DDS circuits can also generate continuous frequency sweeps.

¹The nuclear spin characters of this resonance has larger overlap to the ground state, thus better for STIRAP process.

The rf signal is amplified by a 25W power amplifier. We place a home-built rf antenna as close as possible to the glass cell in order to get larger Rabi frequencies.

5.3.3. Experimental steps

In Fig. 5.2, we illustrate the scheme of rf association. The experimental steps are summarized as follows,

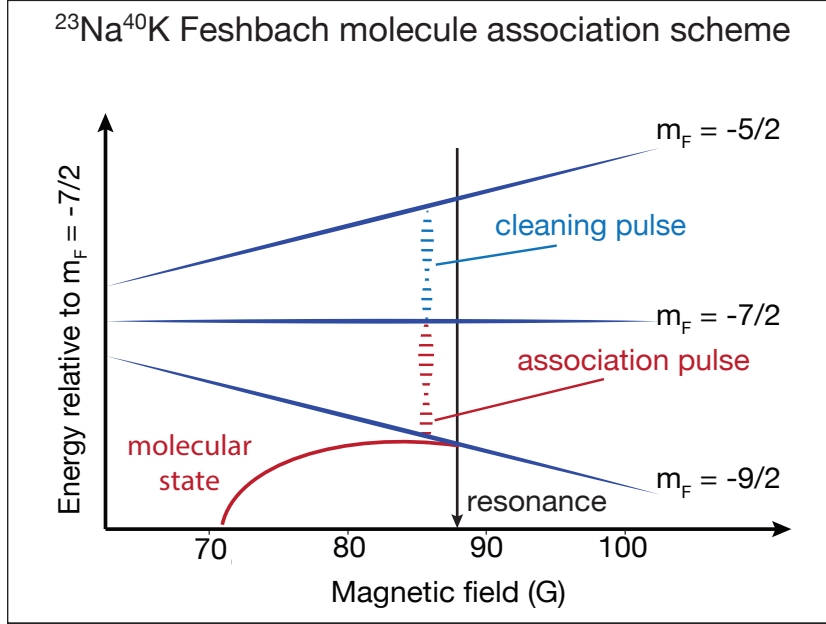


Figure 5.2. – rf association scheme of $^{23}\text{Na}^{40}\text{K}$ Feshbach molecules. We use the Feshbach resonance of $|F = 1, m_F = 1\rangle_{\text{Na}}|F = 9/2, m_F = -9/2\rangle_{\text{K}}$ channel (the resonance locates at 88.2G with $\sim 10\text{G}$ width) . The $^{23}\text{Na}^{40}\text{K}$ mixture is prepared in the non-resonant collision channel $|F = 1, m_F = 1\rangle_{\text{Na}}|F = 9/2, m_F = -7/2\rangle_{\text{K}}$ at 85.5G (slightly below the resonance) . A rf pulse drives the transition from the non-resonant channel to the resonant one. Depending on the frequency of the RF pulse either the hyperfine state of free ^{40}K atoms is changed or weakly bound molecules are associated. Two consecutive rf pulses transfer unassociated ^{40}K atoms to $F = 9/2, m_F = -3/2$ state in order to reduce the background signal during absorption imaging of Feshbach molecules. This figure is taken from Fig. 3.1 of Ref.[123] with the permission of reproduction from Dr. Buchheim.

1. We start from a near degenerated mixture of $^{23}\text{Na} |F = 1, m_F = 1\rangle ^{40}\text{K} |F = 9/2, m_F = 9/2\rangle$.
2. Perform a multi-level Landau-Zener sweep at a magnetic field 14.5G to transfer ^{40}K atoms from $|F = 9/2, m_F = 9/2\rangle$ to $|F = 9/2, m_F = -7/2\rangle$ state².

² We use Stern-Gerlach technique to check the fidelity of the state preparation: different Zeeman substates of ^{40}K atoms are spatially separated in the absorption imaging after applying a short magnetic field gradient pulse.

3. Ramp up the Feshbach coils to the 85.5G and hold the mixture until the magnetic field is stabilized. The mixture of ^{23}Na $|F = 1, m_F = 1\rangle$ ^{40}K $|F = 9/2, m_F = -7/2\rangle$ is not on resonant at 85.5G, so it gives sufficient time for field stabilization.
4. We apply a Blackman rf pulse with frequencies close to ^{40}K $|F = 9/2, m_F = -7/2\rangle \rightarrow |F = 9/2, m_F = -9/2\rangle$ hyperfine transition.
5. Apply two consecutive rf π pulses with resonant frequencies of ^{40}K $|F = 9/2, m_F = -7/2\rangle \rightarrow |F = 9/2, m_F = -5/2\rangle$ and ^{40}K $|F = 9/2, m_F = -5/2\rangle \rightarrow |F = 9/2, m_F = -3/2\rangle$ to bring unassociated ^{40}K atoms to $|F = 9/2, m_F = -3/2\rangle$ state.
6. Directly use absorption imaging technique to count the atom number of ^{40}K at $|F = 9/2, m_F = -9/2\rangle$ state³. The Zeeman splitting between $|F = 9/2, m_F = -3/2\rangle$ and $|F = 9/2, m_F = -9/2\rangle$ is $\simeq 3\Gamma$ at 85.5G, therefore we can selectively count atoms number of different hyperfine states by using different imaging light frequencies. In order to increase the reliability of Feshbach molecule counting, we use σ^- light with resonant frequency of $|F = 9/2, m_F = -9/2\rangle \rightarrow |F' = 11/2, m_F = -11/2\rangle$ cycling transition.

5.3.4. Experimental results

Fig.5.3 shows a typical rf spectrum when we scan the rf frequencies. Two features are clearly observed: an atomic peak near the unperturbed hyperfine transition (with resonant frequency 22.81kHz), and a molecular peak arising from ^{40}K atoms that have been rf associated into bound molecules. The distance between the atomic peak and the onset of the molecular feature yields the binding energy E_b of the molecules. At 85.5G, the binding energy of the Feshbach molecules is $\sim 85\text{kHz}$.

It worths mentioning that, the rf spectrum Fig.5.3 also shows an non-symmetric character. This tail is related to the universal Tan's contact (see Chap. 7 for details).

We use time of flight (TOF) technique to measure the temperature of the Feshbach molecules. The temperature ranges from 330nk to 800nk depending on the initial temperature of the mixture when we associate.

We optimize the rf pulse parameters systematically. We find it is needed to use maximum rf power (corresponding to a $\Omega \simeq 2\pi \cdot 14\text{kHz}$ Rabi frequency of atomic transition $|F = 9/2, m_F = -7/2\rangle \rightarrow |F = 9/2, m_F = -9/2\rangle$), and the optimal pulse duration is $\simeq 0.3\text{ms}$. Further increase of pulse duration does not increase the molecule number. We produce $\simeq 10^4$ Feshbach molecules with rf pulse, the corresponding association efficiency is $\simeq 10\%$.

We measure the lifetime of the Feshbach molecules, $\tau \sim 2\text{ms}$ ($1/e$ -lifetime). This short lifetime is due to two facts, there is a large amount of remaining unassociated

³the Feshbach molecules are weakly bounded, therefore this number equals to the molecules number we associated.

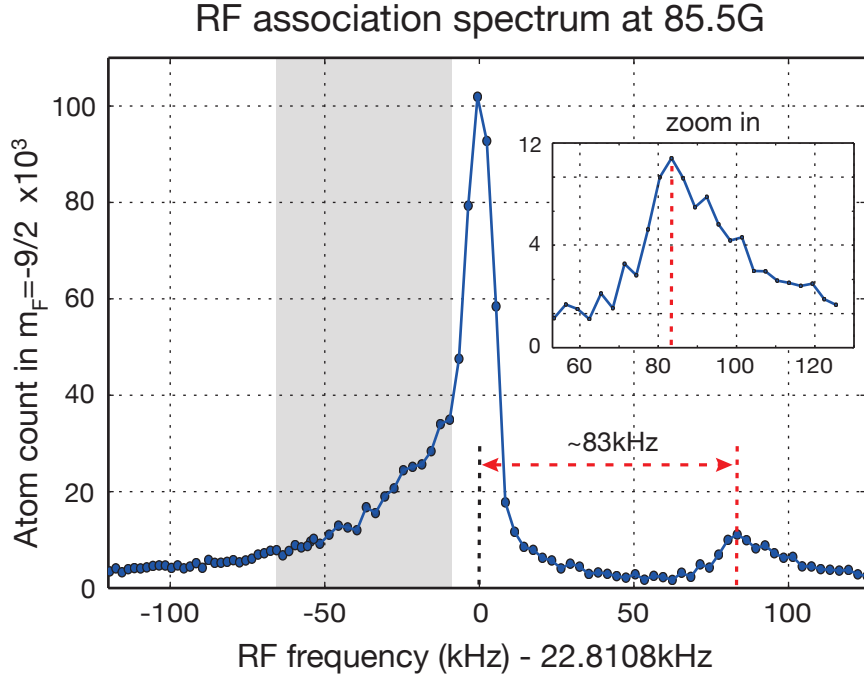


Figure 5.3. – rf spectrum of $^{23}\text{Na}^{40}\text{K}$ Feshbach molecules association at a magnetic field of $B = 85.5\text{G}$. The binding energy of the molecule is $\simeq +85\text{kHz}$. The grey shaded area indicates the effect of the inter-species interaction in the strongly interacting collision channel. This figure is taken from Fig. 3.4 of Ref. [123] with the permission of reproduction from Dr. Buchheim.

free atoms in the trap, and the atom-molecule and molecule-molecule collisions lead to the loss of Feshbach molecules. In Ref. [149], this collisional stability of different collisional partners has been studied in details for $^{40}\text{K}^{87}\text{Rb}$ systems. The universal laws should apply to $^{40}\text{K}^{23}\text{Na}$ as well, therefore the remaining ^{23}Na bosons dominate the loss.

To increase the lifetime, we follow the method developed in MIT [128] that ramping down the power of the transport dipole trap down to 0.5% right after the rf association. It immediately decrease the density of the sample, secondly ^{23}Na atoms leave the optical trap due to the gravity. With this technique, the lifetime of Feshbach molecules is $\sim 13.5\text{ms}(1/e\text{-lifetime})$ [123], which is enough for STIRAP transfer.

5.3.5. Summary

We produce $\simeq 10^4$ $^{23}\text{Na}^{40}\text{K}$ Feshbach molecule via rf association at 85.5G that is slightly below a broad s-wave Feshbach resonance in the $|F = 1m_F = 1\rangle_{\text{Na}}|F = 9/2m_F = -9/2\rangle_{\text{K}}$ collision channel at 88.2G. The temperature of the Feshbach molecules is $\simeq 300\text{nK}$ and the molecules live long enough to perform STIRAP transfer towards to the absolute hyperfine rovibronic ground states.

Collisional partners	loss rate for ($a > 0$)
X+ BF	$\beta(a) \propto a^{-1}$
B+ BF	$\beta(a) \propto P(a)a$
F+ BF	$\beta(a) \propto a^{-3.12}$
B+B+F	$K_3(a) \propto M(a)a^4$

Table 5.2. – “BF” refers to the Feshbach molecule, “B” to the boson, “F” to the fermion, and “X” to a distinguishable K atom. $P(a)$ and $M(a)$ are functions resulting from Efimovian states (see Ref.[149] and references therein).

The association efficiency is $\sim 10\%$ which is probably due to the limited overlapping between Bose-Fermi clouds in the trap. The efficiency might be improved by changing different trap geometry or by using magneto-association [146].

5.4. Creating rovibrational ground states of $^{23}\text{Na } ^{40}\text{K}$ molecules

During the period of this thesis writing, we have successfully transferred Feshbach molecules to rovibrational ground states with Stimulated Raman adiabatic passage (STIRAP) method. Compare to the previous successful ground state molecules experiments of $^{40}\text{K } ^{87}\text{K}$ [29], $^{87}\text{Rb } ^{133}\text{Cs}$ [96, 97] and $^{23}\text{Na } ^{40}\text{K}$ [95], we are the first experiment that using hyperfine-non-resolved intermediate states. We demonstrate that STIRAP method is still valid for transferring Feshbach molecules to rovibrational ground state via a generalized multi-level intermediate manifold. In this section, I summarize the first results of creating $^{23}\text{Na } ^{40}\text{K}$ ground state molecules.

The intermediate states are crucial for the success of STIRAP. We have investigated both theoretically and experimentally on the molecular structure of $d^3\Pi/D^1\Pi$ complex extensively. This part of study has been well presented in Chapter 4 of Ref.[123], therefore I skip this part in this section.

5.4.1. Theoretical background

The theory of stimulated Raman adiabatic passages has been developed over last two decades, and has applied to various systems including atomic systems, molecular systems and quantum dots[150]. We follow the classical reviews on this subject [151, 152, 153, 150].

In general, STIRAP works for a three level (lamda) system. We use our system as an example to illustrate the essential properties of STIRAP in Fig 5.4. The molecular three levels system consists of the initial Feshbach molecule state $|FB\rangle$, target rovibrational ground state $|X^1\Sigma, \nu = 0, J = 0\rangle$ and an intermediate state in $d^3\Pi/D^1\Pi$ complex, $|d^3\Pi, \nu = 5, J = 1\rangle$. The intermediate state is assumed to have short lifetime with a decay rate $2\pi \cdot \Gamma$ ($\Gamma \simeq 10\text{MHz}$), and the initial and the target states have longer lifetime. These three levels are coherently coupled by two lasers: the *pump* laser (with frequency ω_P) couples $|FB\rangle$ state and the intermediate state

with a single photon Rabi frequency $2\pi \cdot \Omega_P$ and a single photon detuning $2\pi \cdot \Delta_P = 2\pi(\omega_1 - \omega_P)$, and the *Stokes* laser (with frequency ω_S) couples the intermediate state and the target ground state with a single photon Rabi frequency $2\pi \cdot \Omega_S$ and a single photon detuning $2\pi \cdot \Delta_S = 2\pi(\omega_2 - \omega_S)$, where ω_1 and ω_2 are the resonant transition frequencies of $|FB\rangle \rightarrow |d^3\Pi, \nu = 5, J = 1\rangle$ and $|d^3\Pi, \nu = 5, J = 1\rangle \rightarrow |X^1\Sigma, \nu = 0, J = 0\rangle$, respectively. The two-photon resonant condition is defined as $\Delta_P = \Delta_S = \Delta$. For simplicity, we introduce $|1\rangle$ represents the initial state, $|2\rangle$ the intermediate state, and $|3\rangle$ the final state,

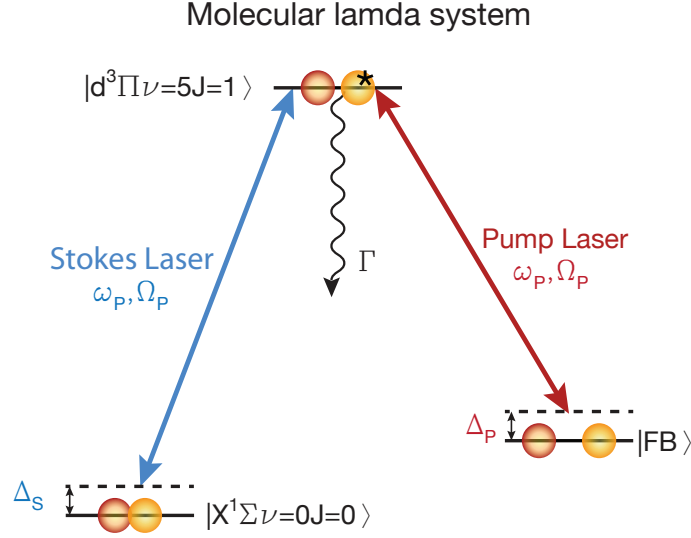


Figure 5.4. – Schematic of a three level lambda system. In this system, the three levels include the initial Feshbach molecule state $|FB\rangle$, target rovibrational ground state $|X^1\Sigma, \nu = 0, J = 0\rangle$ and an intermediate state in $d^3\Pi/D^1\Pi$ complex, $|d^3\Pi, \nu = 5, J = 1, \Omega = 1\rangle$. These three states are coherently coupled by a pair of lasers with frequencies $\omega_{P/S}$, Rabi frequencies $\Omega_{P/S}$ and single photon detunings with respect to the molecular transition frequencies $\Delta_{P/S}$, respectively. The two-photon resonant condition is $\Delta_P = \Delta_S = \Delta$. This figure is taken from Fig. 4.11 of Ref.[123] with the permission of reproduction from Dr. Buchheim.

In the rotating wave approximation [151], the non-Hermitian evolution matrix of the three-level system is given by:

$$W(t) = \frac{1}{2} \begin{pmatrix} 2\Delta_P & \Omega_P(t) & 0 \\ \Omega_P(t) & -i\Gamma & \Omega_S(t) \\ 0 & \Omega_S(t) & 2\Delta_S \end{pmatrix}, \quad (5.5)$$

where we assume that the Rabi frequencies are time-dependent (as the case for STIRAP) explicitly.

Under the two-photon resonant conditions, the eigenstates of the coupled system

Eq.(5.5) are [123]:

$$\begin{aligned} |\Phi_+\rangle &= \frac{\Omega_P(t)}{\Omega(t)}|1\rangle + \frac{\Omega_S(t)}{\Omega(t)}|3\rangle \\ |\Phi_2\rangle &= |2\rangle \\ |\Phi_-\rangle &= \frac{\Omega_S(t)}{\Omega(t)}|1\rangle - \frac{\Omega_P(t)}{\Omega(t)}|3\rangle, \end{aligned} \quad (5.6)$$

where the two-photon Rabi frequency is defined as $\bar{\Omega} = \sqrt{\Omega_P^2 + \Omega_S^2}$, and we use $|1\rangle$, $|2\rangle$, $|3\rangle$ to represent the initial state, the intermediate state and the target state for simplicity.

The eigenstates $|\Phi_+\rangle$ and $|\Phi_-\rangle$ do not contain $|2\rangle$ component, so they evolves freely without loss. In experiments, we start from a well defined quantum state $|FB\rangle$, corresponding to $|\Phi_-\rangle$ at $\Omega_P(0) \rightarrow 0$. By changing the ratio of $\Omega_S(t)/\Omega_P(t)$ in time, $|\Phi_-\rangle \rightarrow |3\rangle$ that Feshbach molecules are adiabatically transferred to the target states.

The adiabaticity criterium of STIRAP is given as [153]:

$$|\langle \frac{d}{dt}\Phi_- | \Phi_{+/2} \rangle| \ll \frac{1}{2} \sqrt{\Omega_P^2 + \Omega_S^2}, \quad \forall t \in [0, \tau]. \quad (5.7)$$

It leads to the following experimental requirements [153, 123]:

$$D \ll \frac{1}{\tau} \ll \frac{\Omega_0^2}{\pi^2 \Gamma}, \quad (5.8)$$

where D is the relative linewidth of the Raman lasers, Ω_0 is the Rabi frequency of the Raman lasers⁴, and τ is the pulse duration of the STIRAP.

5.4.2. Molecular structure of the intermediate manifold

A suitable intermediate state is crucial for the success of STIRAP transfer as mentioned in the previous section. To choose the intermediate state, we considered the following requirements:

1. The initial state $|FB\rangle$ is open-channel dominated therefore it is mainly a triplet state (see Chap. 6 for details). The rovibrational ground state $|X^1\Sigma, \nu = 0, J = 0\rangle$ is purely singlet character. Therefore the intermediate state must have both singlet and triplet characters. In diatomic alkali molecules, significant singlet-triplet mixing is primarily mediated by spin-orbit coupling of near degenerate vibrational levels of singlet and triplet potentials.
2. Besides the singlet-triplet mixing, the wave function of the initial Feshbach state and the ground state are significantly different. therefore the intermediate state

⁴We assume that the pump and the Stokes lasers have similar Rabi frequencies.

must have good Frank-Condon overlapping to both the Feshbach state and the ground state.

3. The relative linewidth of the Raman lasers need to be narrow for the STIRAP experiments. It's better to choose optically accessible transitions (the lasers for the corresponding transitions can be purchased from markets) for experimental feasibilities.

The molecular potential curves of $^{23}\text{Na}^{40}\text{K}$ is shown in Fig.5.5, where we only include the lowest electronic states. With the collaboration with the group of Prof. Olivier Dulieu and Dr. Nadia Bouloufa ⁵, we decided to use $|d^3\Pi, \nu = 5, J = 1\rangle$ state in $d^3\Pi/D^1\Pi$ complex while planning the experiment. This complex corresponds to the atomic $^{23}\text{Na}(3^2P) + ^{40}\text{K}(4^2S)$ asymptotes at large internuclear distance. The intermediate state used in previous experiments at MIT is in $c^3\Sigma^+/B^1\Pi$ complex corresponding to $^{23}\text{Na}(3^2S) + ^{40}\text{K}(4^2P)$ at large internuclear distance [95, 154].

LAC team predicted the transition dipole moments (TDM) of the initial Feshbach state to intermediate states and intermediate states to the ground state for different vibrational levels of $d^3\Pi/D^1\Pi$ complex, shown in Fig.5.6. The wavelength of the pump laser is $\simeq 652\text{nm}$ and the Stokes laser is $\simeq 487\text{nm}$

Experimentally, we have performed photo association spectroscopy [156] and have identified the vibrational levels $\nu = 0$ to $\nu = 6$ of $d^3\Pi$ potential (for experimental details, see Sec. 4.3 in Ref.[123, 161]), summarized in Table.5.3.

Vibrational level	Pump laser frequency (GHz)
$\nu = 0$	450177
$\nu = 1$	452129
$\nu = 2$	453574
$\nu = 3$	455926
$\nu = 4$	457773
$\nu = 5$	459340
$\nu = 6$	461371

Table 5.3. – Seven lowest vibrational levels of $d^3\Pi$ potential identified from photoassociation experiment. The value shown in the table are the experimental results. Theoretical predications are done by LAC team.

The vibrational level $\nu = 5$ of $d^3\Pi$ potential is expected to have large singlet-triplet mixing therefore it is chosen as the intermediate state for our STIRAP scheme that the TDMs of both transitions are balanced. We further perform high resolution spectroscopy on this vibrational level. The fine structure of $\nu = 5$ is shown in Fig.5.7. It contains three components and can be labelled with $\Omega = 0, \Omega = 1, \Omega = 2$, where

⁵ Laboratoire Aimé Cotton, CNRS, Université Paris-Sud, ENS Cachan, Université Paris-Saclay, 91405 Orsay, France.

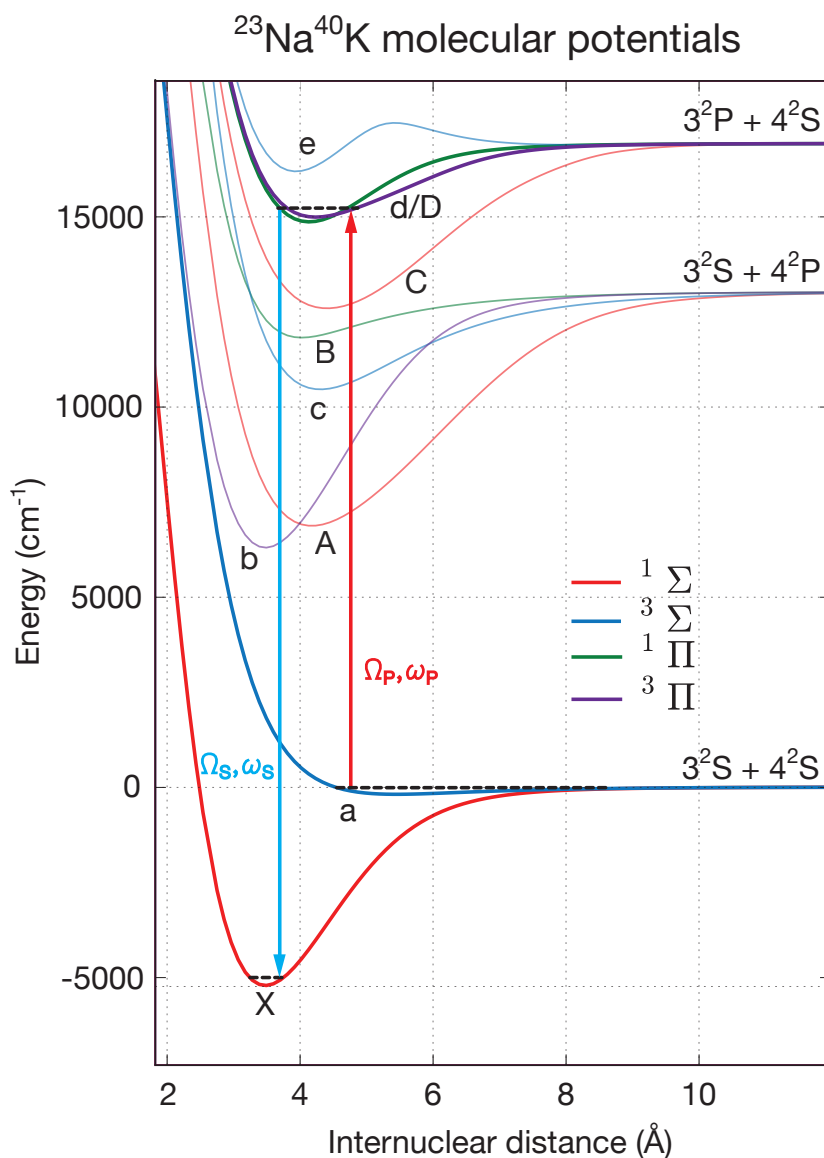


Figure 5.5. – Potential energy curves of the electronic ground state and the lower electronic excited states. Raman lasers (pump: $\sim 652\text{nm}$, Stokes: $\sim 487\text{nm}$) with frequencies $\omega_{P/S}$ and Rabi frequencies $\Omega_{P/S}$ couple a pair of vibrational states in the spin-orbit coupled $d^3\Pi/D^1\Pi$ complex to weakly bound $a^3\Sigma$ Feshbach molecules and the rovibronic groundstate in $X^1\Sigma$. Excited state molecular spectroscopy is performed on the pump transition. This figure was initially produced by Dr. Christoph Gohle, and has been included in both Ref. [123] as Fig. 4.1 and in this thesis.

Ω is the projection of the total electronic angular momentum along the internuclear

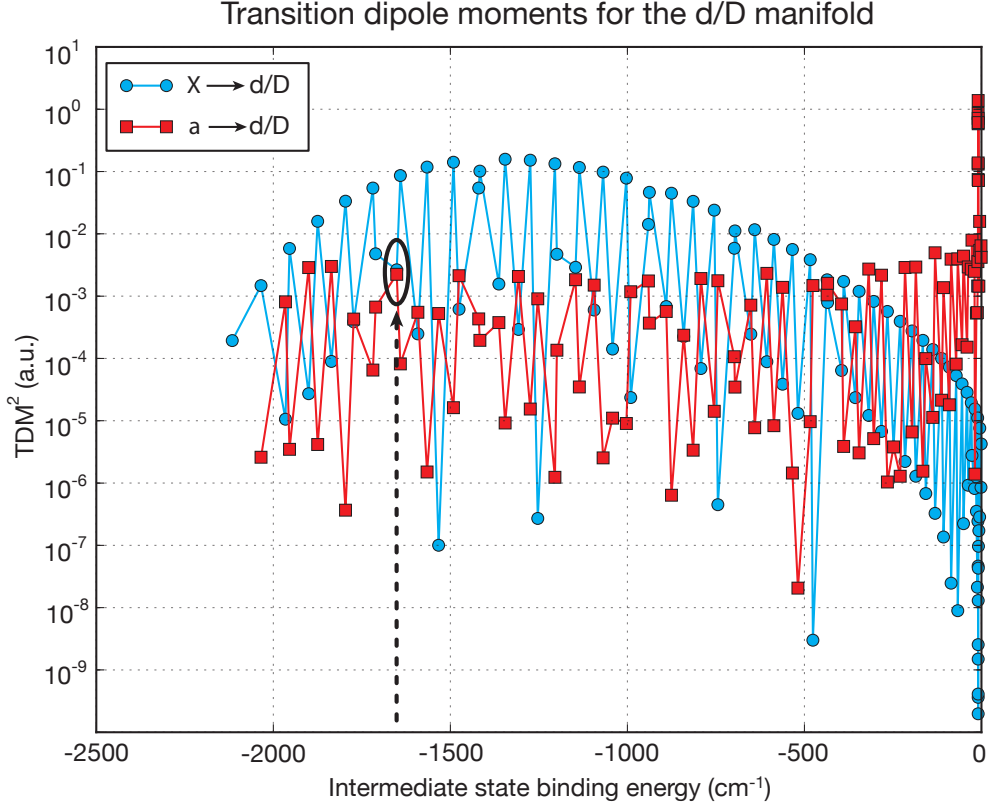


Figure 5.6. – Transition dipole moments of the Feshbach state and the $|X^1\Sigma, \nu = 0, J = 0\rangle$ ground state to the vibrational levels of the $d^3\Pi/D^1\Pi$ complex in atomic units, calculated in Ref.[155]. Binding energies are with respect to the atomic $^{23}\text{Na}(3^2P) + ^{40}\text{K}(4^2S)$ asymptote. The highlighted state is chosen for the candidate in our STIRAP experiment for its balanced TDMs of both transitions. This figure was initially produced by LAC team (see context), and has been included in both Ref. [123] as Fig. 4.2 and in this thesis.

axis⁶ [123, 157].

We further performed molecule excitation spectroscopy by driving the Feshbach molecule to intermediate state $|d^3\Pi, \nu = 5, J = 1, \Omega = 1\rangle$ transitions at 85.5G. We observe a Zeeman triplet feature and can be labelled as $m_J = -1, 0, +1$ states, see Fig.5.8.

However, in Fig.5.8 the molecular hyperfine structure is not resolved (In Sec. 4.4.3 of Ref. [123], we have presented a theoretical model to explain the reasons). Each Zeeman substates ($m_J = -1, 0, +1$) contains contributions from different nuclear

⁶We use *Hund's case a* to label the states in $d^3\Pi/D^1\Pi$ complex: the good “quantum number” in this case is Ω the projection of the total electronic angular momentum along the internuclear axis, J the total angular momentum [123, 157].

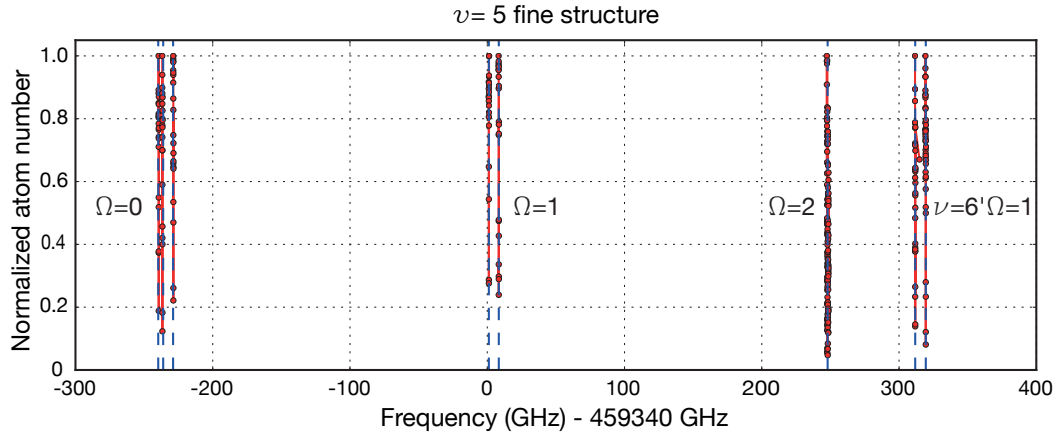


Figure 5.7. – Fine structure of the $^3d\Pi$ $\nu = 5$ vibrational level. This figure is taken from Fig. 4.6 of Ref.[123] with the permission of reproduction from Dr. Buchheim.

spin components (We have built a theoretical model to estimate the contribution of all hyperfine states to each Zeeman substates in Sec. 4.4.2 of Ref.[123]). Since the initial Feshbach molecule state is not a nuclear spin pure state either, the pump laser simultaneously couples to several intermediate states and the three-state picture of STIRAP fails. In the following section, I will discuss the method to overcome this multi-level coupling issue. It leads to a successful STIRAP transfer towards to the ground states.

5.4.3. Raman laser system

Narrow linewidth pump and Stokes lasers are critical for performing high resolution molecular spectroscopy, electromagnetically induced transparency and STIRAP experiments. For this purpose we have constructed a narrow linewidth Raman laser system. The details of this laser system is presented in the master thesis of Diana Amaro [158]. Some key modification and improvement of the system have been made afterwards, and is summarized as follows:

1. The wavelengths of the pump laser and the Stokes laser are 652nm and 487nm respectively. Commercial diode lasers of these two wavelengths are both available. We originally use diode lasers for both lasers.
2. We stabilize laser frequencies by using a dual wavelength high finesse ultra-low-expansion (ULE) cavity (Custom-made by Advanced thin films co.) via Pound-Drever-Hall technique [159, 160]. The finesse is $\simeq 200000$ for 652nm and $\simeq 37000$ for 487nm.
3. In order to have large frequency-tuning range for spectroscopy scanning, we have a master-slave configuration for each wavelength. The master and slave

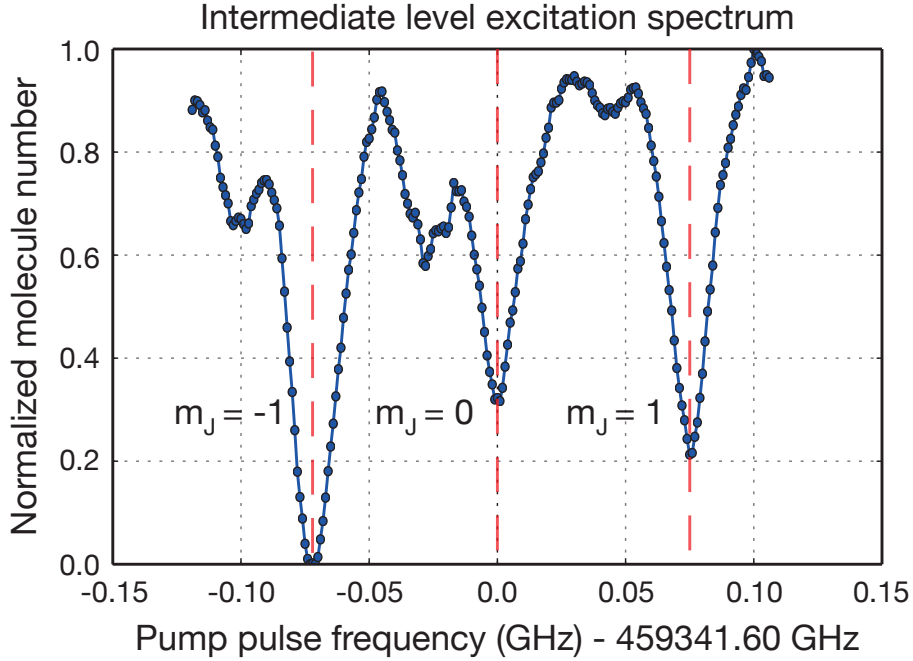


Figure 5.8. – Molecular excitation spectrum of Feshbach molecules to the $J = 1, \Omega = 1$ intermediate state at 85.5G. A Zeeman triplet $m_J = -1, 0, 1$ is clearly observable. The molecular hyperfine structure is not resolved. The data points are averaged over 12 measurements. The figure is taken from Fig. 4.9 in Ref.[123] with the permission of reproduction from Dr. Buchheim.

lasers are phase-locked via offset locking similar as in the K laser system. By controlling the local oscillator’s frequency (we use a DDS circuit), we have achieved $> 1\text{GHz}$ free tuning range.

4. The noise pedestal of the pump diode laser limits the coherence time [123] due to the short cavity length of laser diodes. We now lock a dye laser (Coherent 899)[161] directly to the ULE cavity via feeding back a fast inter-cavity EOM. The dye laser has longer cavity length and less noise pedestal, therefore it allows us to perform STIRAP transfer. Secondly, the Dye laser outputs $> 400\text{mW}$ power which can increase the Rabi frequency of the transition.

5.4.4. Identification of the rovibrational ground state $|X^1\Sigma, \nu = 0, J = 0\rangle$

To experimentally identify the rovibrational ground state $|X^1\Sigma, \nu = 0, J = 0\rangle$ of $^{23}\text{Na}^{40}\text{K}$ molecules, we use “dark-state resonance” technique [152]. We keep the pump laser frequency on the resonance, $\Delta_P = 0$, and scan the frequency of the Stokes laser. When the Stokes laser frequency is not on resonance, the pump laser depletes the initial Feshbach state. Once the Stokes laser frequency is on resonance, $\Delta_S = 0$, the three level lamda system is also on the two-photon resonant. Under

this condition, the system forms a dark state and the absorption of the pump laser is blocked, so the number of Feshbach molecules revives (see Sec. 4.5.2 of Ref.[123] for more experimental details).

We determine the binding energy of $|X^1\Sigma, \nu = 0, J = 0\rangle$ ground state by measuring the frequency of both lasers using a commercial wavemeter (Toptica, WS7) with 10 MHz resolution. Our result, $D_0 = 5212.045\text{cm}^{-1}$ agrees well with the result in MIT [95].

By taking into account of the nuclear spins of the atoms, there are $(2I_{\text{Na}} + 1)(2I_{\text{K}} + 1) = 36$ hyperfine states at $|X^1\Sigma, \nu = 0, J = 0\rangle$ level. The energy splitting between different hyperfine states is \sim hundreds kHz at 85.5G. By diagonalizing the following hyperfine Hamiltonian, we obtain the energy diagram of hyperfine states, shown in Fig.5.9. The absolute hyperfine ground state is $|X^1\Sigma, \nu = 0, J = 0\rangle \otimes |m_{\text{K}} = -4, m_{\text{Na}} = 3/2\rangle$.

$$H_{\text{HF}} = c_4 \cdot \mathbf{I}_{\text{K}} \cdot \mathbf{I}_{\text{Na}} + \mu_B(g_{I_{\text{K}}}\mathbf{I}_{\text{K}} + g_{I_{\text{Na}}}\mathbf{I}_{\text{Na}}) \cdot \mathbf{B} \quad (5.9)$$

where the scalar spin-spin coupling constant is given as $c_4 \simeq -466\text{Hz}$ [154, 95].

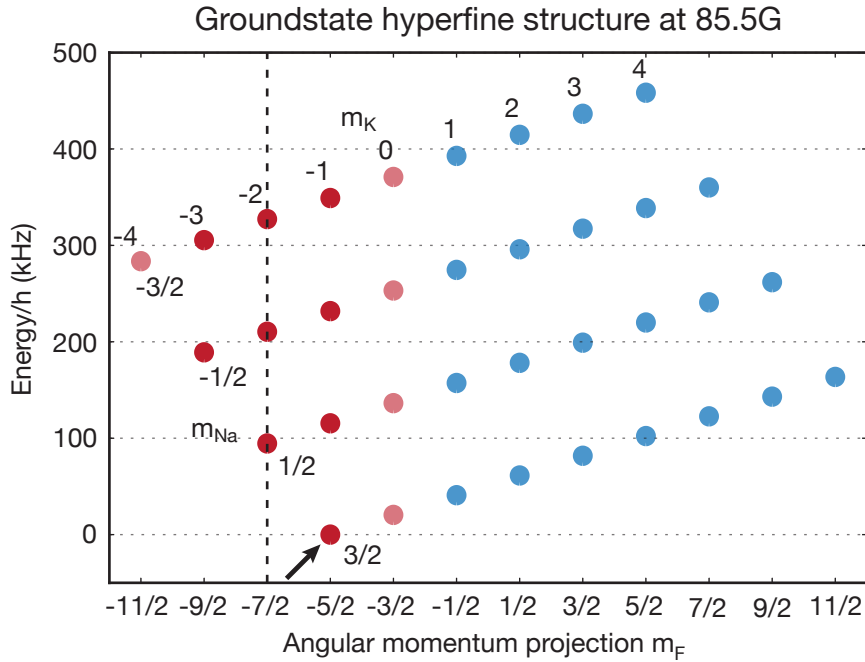


Figure 5.9. – Hyperfine structure of the rovibronic groundstate at 85.5G . The red dots indicate hyperfine components that can be accessed by STIRAP starting from Feshbach molecules ($m_F = -7/2$, dashed black line).The hyperfine component with total lowest energy is indicated by the back arrow. This figure is taken from Fig. 4.25 in Ref.[123] with the permission of reproduction from Dr. Buchheim.

5.4.5. Preliminary result of STIRAP transfer

It has been studied in Ref. [162, 163, 164], how STIRAP can still work for multiple level systems with magnetic substates. The STIRAP efficiency can be improved for a detuned scheme where $\Delta_P = \Delta_S \neq 0$. A numerical model of simulating multi-level STIRAP transfer has been developed in Ref.[123].

Fig.5.10 shows the current STIRAP scheme we use in the experiment: we use $\sigma^+ + \sigma^-$ polarization for the pump laser and π light for the Stokes laser. The initial Feshbach state has the total spin project of $m_F = -7/2$, therefore the pump laser can couple the Feshbach state to two intermediate states: $|m_{Na} = -1/2, m_K = -4\rangle$ and $|m_{Na} = -3/2, m_K = -3\rangle$. The Stokes laser has π polarization and it couples intermediate states to the hyperfine ground states with same nuclear spin characters.

We keep the two photon resonance and the single photon detuning to be 30MHz, that $\Delta_P = \Delta_S = -30\text{MHz}$. We use \cos^2 (in intensity) pulse shape, and the pulse duration is $\simeq 30\mu\text{s}$. To detect the efficiency of the STIRAP, we do inverse-STIRAP that brings the ground state molecules back to the Feshbach states and then use absorption imaging to count the number of Feshbach molecules.

By scanning the frequency of the Stokes laser, we have seen the signal of successful STIRAP transfer once the two photon resonance condition $\Delta_P = \Delta_S$ is satisfied. In Fig.5.11, we show the preliminary result of successful STIRAP transfer. The efficiency of the round trip is $\simeq 40\%$ corresponding to the efficiency of a single STIRAP $\simeq 60\%$.

However, the absolute hyperfine ground state has the nuclear spin characters $|m_{Na} = 3/2, m_K = -4\rangle$ and the ground state molecules we produced so far does not have this nuclear spin character.

5.4.6. Summary and Outlook

During writing this thesis, we have successfully transferred Feshbach molecules to the ground states via a multi-state STIRAP process. Our preliminary result shows the efficiency of one-way STIRAP is $\simeq 60\%$. However a modification of STIRAP scheme is required in order to reach the hyperfine ground state $|m_{Na} = 3/2, m_K = -4\rangle$. Furthermore, various properties of the ground state molecules (lifetime, dipole moment, etc.) need to be determined.

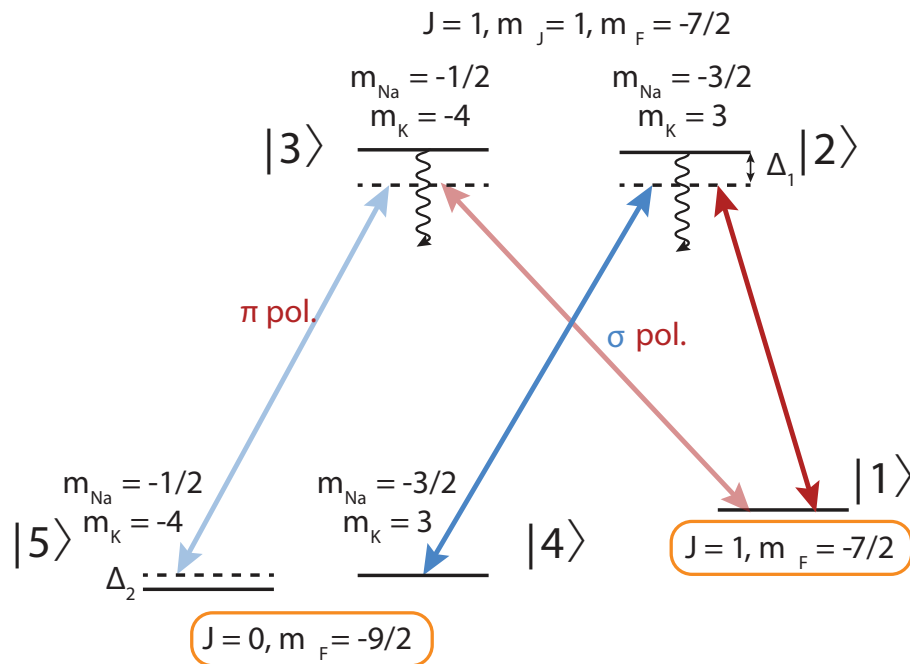


Figure 5.10. – Multilevel STIRAP scheme. We use $\sigma^+ + \sigma^-$ polarization for the pump laser and π light for the Stokes laser. The detuning of the lasers are $\Delta_P = \Delta_S = -30\text{MHz}$.

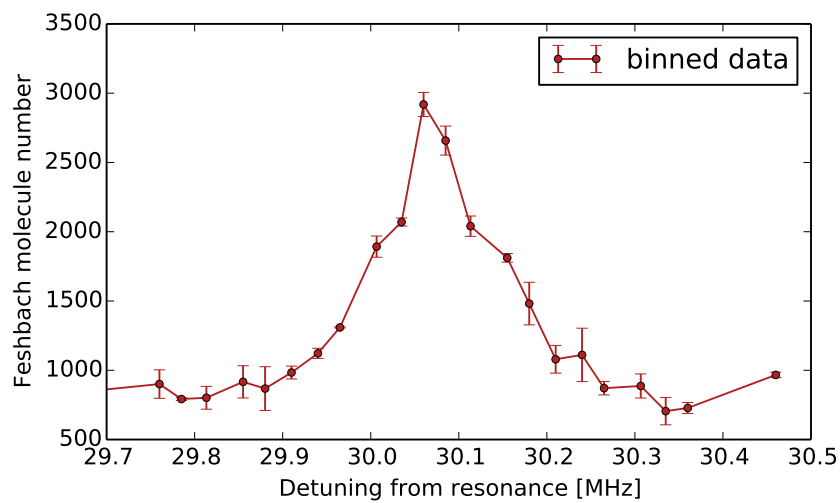


Figure 5.11. – Successful STIRAP transfer signal. We count the number of Feshbach molecules after a round trip of STIRAP. By keeping the pump laser frequency detuned -30MHz , we scan the frequency of the Stokes laser and see a peak of molecular number once the two phonon resonance condition is satisfied.

Asymptotic-bound-state model for Feshbach resonances

In order to analyze the spin character of the Feshbach resonances and predict their position and the width, the asymptotic-bound state model [166] has been proved to be powerful for these purpose. We have implemented ABM model to ^{23}Na - ^{40}K system. In this chapter, we use the ABM to analyze the spin characters of ^{23}Na - ^{40}K Feshbach resonances. Instead of giving a detailed theoretical derivation, the aim of this chapter is to provide a self consistent description and summarize the result we obtained.

Note: The theoretical background of this chapter is based on the publication [166], which was the first paper using the ABM to analyze LiK system.

6.1. Introduction

Feshbach resonances play an important role in the field of ultracold atomic gases (see Reviews [3, 10, 145]). With Feshbach resonances, an ultracold atomic system can be made repulsively interacting ($a > 0$), attractively interacting ($a < 0$), non interacting ($a = 0$) or strongly interacting ($|a| \rightarrow \infty$) in a continuous manner. The ability of tuning the two-body interaction over many orders of magnitude by varying external magnetic field allows the researchers to realize various quantum phases experimentally with atomic gases, such as fermionic superfluid states[7], superfluid-Mott insulator transition[165], and BEC-BCS crossover[8, 9], etc.

Feshbach resonances depend strongly on the internal atomic structures of the colliding atom pair, which can be controlled by external fields. For alkali-metal atoms, their internal structures are initiated by the hyperfine interaction which can be energetically modified by external magnetic field via the Zeeman interaction. Pairs of colliding atoms are prepared in a given spin channel, and its collision threshold and its two-body bound states depend in general differently on the external magnetic field. A resonance appears when the collision threshold is energetically degenerate with a bound state[10].

In addition, a detailed information about the spin characters of two body bound states (Feshbach molecules) for a given Feshbach resonance at certain magnetic fields, are crucial to determine the coupling strength between the Feshbach molecules and intermediate state of our STIRAP process[123].

Therefore, we need to build a theoretical model to describe the Feshbach resonances for ^{23}Na ^{40}K system, to predict the position and the width of the resonances, and to determine the spin characters of the corresponding bound states.

In principle, the two body scattering problem can be solved by a set of radially coupled Schrödinger equations in the spin basis. The set of equations is called ‘Coupled Channels’ equations and can be solved numerically[145]. However, this method requires certain modification of the ab-initio potentials and is sometimes time consuming. In this chapter, we use a simpler model called ‘asymptotic bound-state model’ (ABM model) which has been successfully used in ^6Li ^{40}K system[166]. The ABM neglects the mixing of singlet and triplet state due to the spin-orbital couplings, therefore allowing the use of uncoupled orbital and spin states. The radial singlet and triplet eigenstates can be determined directly from the corresponding Born-Oppenheimer potentials.

In this chapter, we first present the theoretical background of the model based on Ref.[166]. We then proceed to summarize the results from this model which give various properties of Feshbach resonances that we are currently using.

6.2. Basics of Asymptotic Bound-state Model

In ultracold atomic experiments, two colliding partners of atoms are typically both prepared in a hyperfine sublet $|F, m_F\rangle$, where F is the total spin and m_F is the projection along the quantization axis (normally along the magnetic field direction). We call the product state formed by the hyperfine substates of the two atoms the *entrance channel* or *open channel*. In a two-channel model picture of Feshbach resonances, there is coupled bound state which is called the *closed channel*. The energies of the entrance channel and the closed channel normally depend differently on the magnetic fields. Feshbach resonances appear at the magnetic field value where the entrance channel energy equals to the energy of the closed channel. The ABM is able to determine the energies of the two channels.

The effective Hamiltonian of the two-body system in the center of mass frame is a sum of two terms:

$$\mathcal{H} = \mathcal{H}^{rel} + \mathcal{H}^{int}. \quad (6.1)$$

\mathcal{H}^{rel} describes the relative motion of the atoms,

$$\mathcal{H}^{rel} = \frac{\mathbf{p}^2}{2\mu} + \mathcal{V}, \quad (6.2)$$

where $\frac{\mathbf{p}^2}{2\mu}$ is the relative kinetic energy with the reduced mass, μ , and \mathcal{V} is the effective interaction between the atoms resulting from all Coulomb interactions between the nuclei and electrons of both atoms. \mathcal{H}^{int} stands for the hyperfine and Zeeman interactions of the atoms.

The energy spectrum of \mathcal{H}^{rel} contains a set of discrete eigenstates, denoted as $|\psi_\nu^{Sl}\rangle|Y_{m_l}^l\rangle$ (the quantum number S , l , ν and m_l will be defined explicitly in the later

texts) with a binding energy ϵ_ν^{Sl} , and the continuum states of \mathcal{H}^{rel} corresponding to the scattering continuum. In a *standard* Asymptotic Bound state model, the scattering continuum states are not included.

The key idea of ABM is to solve the Schrödinger equation with Hamiltonian Eq. (6.1) by using the bound eigenstates of \mathcal{H}^{rel} as a basis, $\{|\psi_\nu^{Sl}\rangle|Y_{m_l}^l\rangle|\sigma\rangle\}$, where $|\sigma\rangle$ labels spin degrees of freedom:

$$(\mathcal{H}^{rel} + \mathcal{H}^{int})|\psi_\nu^{Sl}\rangle|Y_{m_l}^l\rangle|\sigma\rangle = E_b|\psi_\nu^{Sl}\rangle|Y_{m_l}^l\rangle|\sigma\rangle, \quad (6.3)$$

which leads to:

$$\epsilon_\nu^{Sl}\delta_{\sigma\sigma'}\delta_{\nu\nu'}\delta_{SS'}\delta_{ll'} + \langle\psi_{\nu'}^{Sl}|\psi_\nu^{Sl}\rangle\langle\sigma'| \mathcal{H}^{int} |\sigma\rangle = E_b\langle\psi_{\nu'}^{Sl}|\psi_\nu^{Sl}\rangle\delta_{\sigma\sigma'}\delta_{ll'}, \quad (6.4)$$

where we use the fact that \mathcal{H}^{rel} is diagonal in $\{|\sigma\rangle\}$ basis and spherical harmonics are orthonormal. The off-diagonal terms come from \mathcal{H}^{int} .

The binding energies ϵ_ν^{Sl} and the Franck-Condon factors are $\langle\psi_{\nu'}^{Sl}|\psi_\nu^{Sl}\rangle$ parameters in the secular equation Eq. (6.4) are the input parameters of the ABM model, which could be determined from Born-Oppenheimer potentials.

In general, the eigenvalues E_b depend on the value of external magnetic fields B . To determine the positions of Feshbach resonances, one needs to find the magnetic field value at which an eigenvalue E_b crosses the threshold energy of the entrance channel, E_{th} .

6.3. Spin basis and Hamiltonian

Spin characters are crucial in the ABM model, and different spin basis are used in the model. Therefore unitary transformations between different spin basis are required during the calculation. In this section, we summarize different sets of spin basis that we use in the model.

The colliding pair of atoms are labeled as α and β respectively. We denote the electron spins of the atoms as s_α, s_β , the corresponding quantum numbers projected along the magnetic field are $m_{s_\alpha}, m_{s_\beta}$, the nuclear spins are i_α, i_β , and their quantum numbers projected along the magnetic field are μ_α, μ_β . For given atomic species, s_α, s_β and i_α, i_β are constants.

We then have *product* spin basis of the two-body systems:

$$\{|m_{s_\alpha}, m_{s_\beta}, \mu_\alpha, \mu_\beta\rangle\}. \quad (6.5)$$

The total electron spin of the colliding atoms are $\mathbf{S} = \mathbf{s}_\alpha + \mathbf{s}_\beta$ (bold symbols correspond to vectors) and its projection along the magnetic field is M_s , we then define the *ABM* spin basis as:

$$\{|\sigma\rangle\} = \{|S, M_s, \mu_\alpha, \mu_\beta\rangle\}. \quad (6.6)$$

In addition, summing over the electron spin and the nuclear spin of individual atom, we have the total spin, $\mathbf{f}_\alpha = \mathbf{s}_\alpha + \mathbf{i}_\alpha$ and $\mathbf{f}_\beta = \mathbf{s}_\beta + \mathbf{i}_\beta$, and the corresponding

projections along the magnetic field are m_{f_α} and m_{f_β} , they result in the following basis:

$$\{|f_\alpha, m_{f_\alpha}, f_\beta, m_{f_\beta}\rangle\}. \quad (6.7)$$

6.3.1. Relative Hamiltonian

The Hamiltonian which governs the relative motions of the two particles reads, $\mathcal{H}^{rel} = \frac{\mathbf{P}^2}{2\mu} + \mathcal{V}$, and the central interaction depends only on the quantum number S associated with the magnitude of the total electron spin \mathbf{S} . Therefore the central interaction can be decomposed as: $\mathcal{V} = \sum_S |S\rangle V_S \langle S|$. For two-alkali-metal atomic systems, V_s is either the singlet ($S = 0$) or triplet ($S = 1$). Together with the nuclear spin parts, we can specify the ABM basis states as $|\psi_\nu^{Sl}\rangle |Y_{m_l}^l\rangle |S, M_S, \mu_\alpha, \mu_\beta\rangle$, where ν and l are the vibrational and orbital angular momentum quantum numbers of the relative motion, and m_l is the orbital projection quantum number along quantization axis. Importantly, the ABM basis are the eigenstate of the relative Hamiltonian and satisfy the projected eigenstate equations,

$$\left[-\frac{\hbar^2}{2\mu} \frac{d^2}{dr^2} + V_l^S(r) \right] \psi_\nu^{Sl}(r) Y_{m_l}^l(r) = \epsilon_\nu^{Sl} \psi_\nu^{Sl}(r) Y_{m_l}^l(r). \quad (6.8)$$

Here, $V_l^S(r) = l(l+1)\hbar^2/(2\mu r^2) + V^S(r)$.

In practice, starting from empirical Born-Oppenheimer potential [168], the wavefunctions and energies are determined numerically using the LEVEL program (developed by R. J. Le Roy's group, University of Waterloo, Canada¹).

6.3.2. Internal energy

The internal energy for a single atom, \mathcal{H}_α^{int} or \mathcal{H}_β^{int} reads,

$$\mathcal{H}^{int} = a_h f \mathbf{i} \cdot \mathbf{s} + (\gamma_e \mathbf{s} - \gamma_i \mathbf{i}) \cdot \mathbf{B} \quad (6.9)$$

where s and i are the electron and nuclear spins respectively. γ_e and γ_i are the corresponding electron and nuclear gyromagnetic ratios.

In the absence of an external magnetic field, \mathcal{H}^{int} is diagonal in the basis $|f_\alpha, m_{f_\alpha}, f_\beta, m_{f_\beta}\rangle$. With external magnetic field, the eigenstates of \mathcal{H}^{int} are the well-known *Breit-Rabi* states. Thus we call $|f_\alpha, m_{f_\alpha}, f_\beta, m_{f_\beta}\rangle$ *Breit-Rabi* basis and are labelled by their zero-field limit quantum numbers, $f_\alpha, m_{f_\alpha}, f_\beta, m_{f_\beta}$.

6.3.3. Angular momentum conservation

Experimentally, one prepares certain atomic mixture (the entrance channel) which corresponds to a state in the *Breit-Rabi* basis. To determine possible resonances, one

¹<http://scienide2.uwaterloo.ca/~rleroy/level/>

needs to work in a vector space spanned by all the states that can be coupled to the entrance channel.

In fact, \mathcal{H} conserves the orbital quantum number l because the effective potential in \mathcal{H}^{rel} is assumed to be isotropic. It means that the vector space can be divided into subspaces with different values of l . Furthermore, \mathcal{H} conserves

$$M_F = M_S + \mu_\alpha + \mu_\beta. \quad (6.10)$$

Hence, we only need to enumerate possible ABM states, $|\psi_\nu^{Sl}\rangle|Y_{m_l}^l\rangle|\sigma\rangle$, whose $M_S + \mu_\alpha + \mu_\beta$ equal to the M_F of the entrance channel. By that, the computation complexity is greatly reduced.

6.4. The standard ABM

In the standard ABM, one only needs to find a magnetic field at which the energy of the entrance channel is the same as the closed channel's.

6.4.1. Entrance channel energy

At large inter-particle distance (asymptotic limit), the effective interaction between the two atoms can be neglected, $\mathcal{V} = 0$. Furthermore, the kinetic energy approximates to zero at the ultra cold limit. Thus the energy of the entrance channel (threshold energy E_{th}) is the sum of the energies of the free atoms at given magnetic field,

$$\begin{aligned} E_{th} &= \langle \alpha\beta | \mathcal{H}^{int} | \alpha\beta \rangle = \langle \alpha\beta | \mathcal{H}_\alpha^{int} + \mathcal{H}_\beta^{int} | \alpha\beta \rangle \\ &= a_{hf,\alpha} \mathbf{i}_\alpha \cdot \mathbf{s}_\alpha + (\gamma_e \mathbf{s}_\alpha - \gamma_{i,\alpha} \mathbf{i}_\alpha) \cdot \mathbf{B} + a_{hf,\beta} \mathbf{i}_\beta \cdot \mathbf{s}_\beta + (\gamma_e \mathbf{s}_\beta - \gamma_{i,\beta} \mathbf{i}_\beta) \cdot \mathbf{B}. \end{aligned} \quad (6.11)$$

To simplify the calculation in the product basis, we express the hyperfine interaction terms with the ladder operators:

$$\mathbf{i}_\alpha \cdot \mathbf{s}_\alpha = \frac{1}{2} (s_\alpha^+ i_\alpha^- + s_\alpha^- i_\alpha^+) + s_z i_z \quad (6.12)$$

The eigenstates of \mathcal{H}^{int} (Breit-Rabi states) are labelled by the low field quantum number (f, m_f). E_{th} is the sum of two eigenstates' energies.

6.4.2. Closed channel energy

Having determined the threshold energy E_{th} , we need to determine the closed channel energy by solving Eq. (6.4) at given magnetic field. As mentioned previously, we use ABM states $\psi_\nu^{Sl}(r)Y_{m_l}^l(r)$ as the basis. \mathcal{H}^{rel} is diagonal in the ABM basis, and the off-diagonal terms come from \mathcal{H}^{int} .

Eq. (6.4) can be solved for subspaces of different l separately. In addition, we only include the ABM states which have the same value M_F as the entrance channel's due to the spin conservation.

Assuming that we take into account only one vibrational level and dealing only with alkali-metal atoms ($s_\alpha = s_\beta = \frac{1}{2}$) the number of unknown parameters in Eq. (6.4) is just three - the energies of singlet and triplet bound states for given l : $\epsilon_{\nu=0}^{S=0,l}$, $\epsilon_{\nu=0}^{S=1,l}$ and the non-trivial Frank-Condon factor $\langle \psi_{\nu=0}^{S=0,l} | \psi_{\nu=0}^{S=1,l} \rangle$. They can be obtained from molecular potentials.

The off-diagonal matrix elements $\langle \sigma' | \mathcal{H}^{int} | \sigma \rangle$ can be calculated for each magnetic field value, B . The eigenvalue E_b and the corresponding eigenvectors of Eq.(6.4) can be obtained by diagonalizing the Hamiltonian \mathcal{H} in the ABM basis.

We then compare E_{th} and E_b at different magnetic fields. The crossings of E_{th} and E_b are the Feshbach resonances in the system.

6.5. The dressed ABM

The standard ABM can predict the positions of Feshbach resonances, however the standard ABM can not estimate the width of Feshbach resonances. In order to determine the width of Feshbach resonances one needs to extend the ABM and include the coupling between the resonant level and the continuum states. The dressed ABM [166] uses the Mittag-Leffler expansion to approximate the contribution of continuum states by coupling of the resonant state with the entrance (open) channel. The inclusion of continuum states' contribution will shift the position of Feshbach resonances. This section reviews Sec. IV of Ref. [166] where dressed-ABM was originally developed.

6.5.1. The contribution of the continuum states

The first step is to partition the whole Hilbert space into orthogonal subspaces \mathcal{P} and \mathcal{Q} so that the states of the open channels are in \mathcal{P} , while \mathcal{Q} is spanned by states from the closed channels.

We thus define projector operators P and Q , which project onto the subspaces \mathcal{P} and \mathcal{Q} , respectively. Thus the two-body Schrödinger equation can be split into a set of coupled equations,

$$(E - \mathcal{H}_{PP})|\psi_P\rangle = \mathcal{H}_{PQ}|\psi_Q\rangle, \quad (6.13)$$

$$(E - \mathcal{H}_{QQ})|\psi_Q\rangle = \mathcal{H}_{QP}|\psi_P\rangle, \quad (6.14)$$

where $|\psi_P\rangle \equiv P|\psi\rangle$, $|\psi_Q\rangle \equiv Q|\psi\rangle$, $\mathcal{H}_{PP} \equiv P\mathcal{H}P$, $\mathcal{H}_{PQ} \equiv P\mathcal{H}Q$. The energy $E = \hbar^2 k^2 / 2\mu$ is defined with respect to the open channel dissociation threshold.

The S matrix in \mathcal{P} space reads:

$$S(k) = S_P(k) \left(1 - 2\pi i \frac{|\langle \phi_Q | \mathcal{H}_{QP} | \psi_P^+ \rangle|^2}{E - \epsilon_Q - \mathcal{A}(E)} \right), \quad (6.15)$$

where $H_{QP} = Q\mathcal{H}P$ describes the coupling between \mathcal{P} and \mathcal{Q} subspaces. ϕ_Q is the eigenstate of \mathcal{H}_{QQ} in \mathcal{Q} space, and ϵ_Q is the corresponding eigenvalue, the energy of

undressed bound state.

The complex energy shift, describing the dressing of the bare bound state by the coupling to the \mathcal{P} space, $\mathcal{A}(E)$, equals:

$$\mathcal{A}(E) = \left\langle \phi_Q | \mathcal{H}_{QP} \frac{1}{E + i\delta - \mathcal{H}_{PP}} \mathcal{H}_{PQ} | \phi_Q \right\rangle, \quad (6.16)$$

and can be calculated by the Mittag-Leffler expansion:

$$\frac{1}{E + i\delta - \mathcal{H}_{PP}} = \frac{\mu}{\hbar^2} \sum_n \frac{|\Omega_n\rangle \langle \Omega_n^D|}{k_n(k_n - 1)}. \quad (6.17)$$

where n runs over all poles of the S_P matrix, and the Gamow state $|\Omega_n\rangle$ is an eigenstate of \mathcal{H}_{PP} with eigenvalue $\epsilon_{P_n} = \hbar^2 k_n^2 / (2\mu)$. We then have:

$$\mathcal{A}(E) = \left\langle \phi_Q | \mathcal{H}_{QP} \left(\frac{\mu}{\hbar^2} \sum_n \frac{|\Omega_n\rangle \langle \Omega_n^D|}{k_n(k_n - 1)} \right) \mathcal{H}_{PQ} | \phi_Q \right\rangle \quad (6.18)$$

We could assume that the scattering in the open channel (\mathcal{P} space) is dominated by a single bound state with $k_n = i\kappa_P$. Thus the sum over all poles of the S_P matrix is then reduced to only one term which corresponds to the bound state in the open channel. The contribution from the rest of poles is assumed to be negligible, so

$$\mathcal{A}(E) \approx \frac{\mu}{\hbar^2} \frac{-i \langle \phi_Q | \mathcal{H}_{QP} | \Omega_P \rangle \langle \Omega_P^D | \mathcal{H}_{PQ} | \phi_Q \rangle}{\kappa_P(k - i\kappa_P)}. \quad (6.19)$$

The key point of dressed ABM model is that the dressed state can be considered as a (quasi-) bound state of the whole ($\mathcal{P} + \mathcal{Q}$) system, which corresponds to a pole of the S matrix, given in Eq. (6.15). Therefore, the energy of the dressed state is obtained by finding the poles of the S matrix:

$$E - \epsilon_Q - \mathcal{A}(E) = 0, \quad (6.20)$$

which is equivalent to a cubic equation for $x = \sqrt{E}$:

$$\sqrt{E_{th} - \epsilon_P} x^3 - i(E_{th} - \epsilon_P) x^2 - \sqrt{E_{th} - \epsilon_P} \epsilon_Q x + i(E_{th} - \epsilon_P) \epsilon_Q + \frac{i}{2} \mathcal{K}^2 = 0 \quad (6.21)$$

where we denote $\mathcal{K}^2 = |\langle \Omega_P | \mathcal{H}_{PQ} | \phi_Q \rangle|^2$, a positive constant characterizes the coupling between open-channel bound state and the closed channel one's.

6.5.2. Implementation the dressed ABM

The Breit-Rabi state $|\alpha\beta\rangle$ that corresponds to the entrance channel forms a one-dimensional subspace of \mathcal{P} . The rest of the states in the Breit-Rabi basis (with the total M_F the same as the entrance channel) span a subspace of \mathcal{Q} . The Breit-Rabi

basis partitions naturally the considered M_F subspace into open channel subspace (\mathcal{P}) and closed channel subspace (\mathcal{Q}). It is straightforward to distinguish subspace spanned by $|\alpha\beta\rangle$ and orthogonal subspace spanned by the rest of basis's vectors.

Therefore it is convenient to transform the \mathcal{H} matrix used in the standard ABM (ABM basis) to the Breit-Rabi basis. In the Breit-Rabi basis blocks \mathcal{H}_{PP} , \mathcal{H}_{QQ} , \mathcal{H}_{PQ} can be easily identified.

The bare binding energy of the least bound state in the entrance channel is the diagonal matrix element of \mathcal{H} :

$$\epsilon_P = \langle \alpha\beta | \mathcal{H} | \alpha\beta \rangle \quad (6.22)$$

(energies are defined so that the threshold energy $E_{th} = 0$). The bare binding energies of the states in the subspace of \mathcal{Q} are obtained by diagonalization of \mathcal{H}_{QQ} in the subspace of \mathcal{Q}

$$\mathcal{H}_{QQ} |\phi_Q\rangle = \epsilon_Q |\phi_Q\rangle, \quad (6.23)$$

while the basis in \mathcal{P} subspace remains unaltered. The resulting eigenvalues differ slightly from the eigenvalues obtained in the standard ABM because this time the eigenproblem is diagonalized in subspace orthogonal to $|\alpha\beta\rangle$, which is not an eigenstate of \mathcal{H} .

The next step is to consider each crossing of ϵ_Q and E_{th} and solve Eq. (6.21), in order to obtain the energies of the dressed states. Eq.(6.21) is a cubic equation with parameters ϵ_P , ϵ_Q and $\langle \Omega_P | H_{PQ} | \phi_Q \rangle$ which depend on the value of the magnetic field B . Eq. (6.21) has three real roots provided that the energy of the dressed state corresponding to $|\phi_Q\rangle$ is below threshold - one of the roots is then the dressed energy of $|\alpha\beta\rangle$ state, one is dressed energy of $|\phi_Q\rangle$ and the remaining one crosses the threshold energy in the same point as the previous one, but doesn't approach the bare energy ϵ_Q for B away from the threshold.

6.5.3. Transformation of spin basis in the dressed ABM

The transformation of \mathcal{H} between the ABM basis and the Breit-Rabi basis is quite involved since the Breit-Rabi states depend on the value of magnetic field B . While the single-specie Breit-Rabi states were obtained by diagonalizing the internal energy Hamiltonian \mathcal{H}^{int} , which read:

$$|f_\alpha m_{f_\alpha}\rangle = \sum_i d_i^\alpha(B) |m_\alpha \mu_\alpha\rangle, \quad (6.24)$$

$$|f_\beta m_{f_\beta}\rangle = \sum_i d_i^\beta(B) |m_\beta \mu_\beta\rangle, \quad (6.25)$$

where the summations take over all single-specie product states.

We denote $|br_i\rangle$, $|prod_i\rangle$ and $|\sigma_i\rangle$, the i th vector of Breit-Rabi, product and ABM basis respectively. To determine the matrix element of transformation between the

product state and Breit-Rabi states,

$$|br_i\rangle = \sum_j c_{ij}(B)|prod_j\rangle, \quad (6.26)$$

we include Breit-Rabi states $|br_i\rangle$ as the product of two single-specie states, $|br_i\rangle = |f_\alpha m_{f_\alpha}\rangle |f_\beta m_{f_\beta}\rangle$, where $m_{f_\alpha} + m_{f_\beta} = M_F$. While the product states $|prod_j\rangle = |m_\alpha \mu_\alpha\rangle |m_\beta \mu_\beta\rangle$ with $m_\alpha + \mu_\alpha + m_\beta + \mu_\beta = M_F$. Therefore the c_{ij} coefficients are simply the products of the corresponding d_k^α and d_k^β coefficients - the projections of single-specie Breit-Rabi states on the product basis.

To transform states from the product basis to the ABM basis, we use Clebsch-Gordan coefficients:

$$|br_i\rangle = \sum_j c_{ij}(B)|prod_j\rangle = \sum_{j,k} c_{ij}(B)CG(\sigma_k, prod_j)|\sigma_k\rangle \equiv \sum_k d_{ik}(B)|\sigma_k\rangle, \quad (6.27)$$

where the Clebsch-Gordan coefficient is denoted as $\langle \sigma_k | prod_j \rangle = CG(\sigma_k, prod_j)$.

Finally, the matrix element of the \mathcal{H} in the Breit-Rabi basis is given by:

$$\langle br_{i_1} | \mathcal{H} | br_{i_2} \rangle = \sum_{j_1, j_2} d_{i_1 j_1} \langle \sigma_{j_1} | \mathcal{H} | \sigma_{j_2} \rangle d_{i_2 j_2}. \quad (6.28)$$

The vector space of the closed channels, \mathcal{Q} is a $(N-1)$ dimensional space, whereas \mathcal{P} is a one-dimensional space. The resulting $\mathcal{H}_{\mathcal{Q}\mathcal{Q}}$ is thus a $(N-1) \times (N-1)$ matrix. To identify the $\mathcal{H}_{\mathcal{Q}\mathcal{Q}}$ matrix, it is straightforward in the Breit-Rabi basis - the whole \mathcal{H} matrix except the row and the column which correspond to the open channel state.

$\mathcal{H}_{\mathcal{Q}\mathcal{Q}}$ can be diagonalized, the eigenstates are the bare bound states in \mathcal{Q} space $\{|\phi_{Q1}\rangle, |\phi_{Q2}\rangle, \dots\}$, with eigenvalues (binding energies) $\{|\epsilon_{Q1}\rangle, |\epsilon_{Q2}\rangle, \dots\}$. We further transforms the full Hamiltonian \mathcal{H} in the \mathcal{Q} space $\{|\phi_{Q1}\rangle, |\phi_{Q2}\rangle, \dots\}$ basis, so that the $\mathcal{H}_{\mathcal{Q}\mathcal{Q}}$ block is diagonal and $H_{\mathcal{P}\mathcal{P}}$ is unaltered. The rest matrix elements corresponds to the coupling between the open channel space \mathcal{P} and the closed channel space \mathcal{Q} , $|\langle \Omega_P | \mathcal{H}_{\mathcal{P}\mathcal{Q}} | \phi_Q \rangle$, the term used for solving Eq. (6.21).

We could identify the bare bound states in \mathcal{Q} space responsible for the Feshbach resonances - the ones cross threshold energy. It allows us to calculate the corresponding coupling constant \mathcal{K}^2 . Therefore the Feshbach resonant positions in the dressed ABM model can be determined by solving Eq. (6.21) at threshold, which is for $E_{th} = 0$:

$$\epsilon_P(B)\epsilon_Q(B) - \frac{1}{2}\mathcal{K}^2(B) = 0. \quad (6.29)$$

Finally, for each detected crossing, we calculate the width of resonance ΔB which is proportional to the magnetic field difference between the crossings of the dressed B_0 and uncoupled \mathcal{Q} bound states \tilde{B}_0 with the threshold energy:

$$\Delta B = \frac{a_P}{a_P + a_{bg}^P}(B_0 - \tilde{B}_0), \quad (6.30)$$

where a_{bg}^P is calculated as

$$a_{bg}^P \approx r_0 = \frac{1}{2} \left(\frac{2\mu C_6}{\hbar^2} \right)^{\frac{1}{4}} \quad (6.31)$$

and

$$a_{bg} = \frac{1}{\kappa_P} = \sqrt{-\frac{\hbar^2}{2\mu} \frac{1}{\epsilon_P}}. \quad (6.32)$$

6.6. Open/Closed channel fraction

One application of ABM model is to determine the open/closed channel fraction of Feshbach molecule states at various magnetic fields. For the STIRAP process, we start from a Feshbach molecule state at certain magnetic field, and this ‘halo’ Feshbach state is a superposition state of open-channel scattering wavefunction and closed channel bound molecular state[10]

$$|FB\rangle = \sqrt{Z(B)}\phi_C(R)|close\rangle + \sqrt{1-Z(B)}\phi_{bg}(R)|open\rangle \quad (6.33)$$

where Z represents the fraction of the fraction of the closed channel, the unit normalization of $|FB\rangle$ ensures that the open channel fraction is $1 - Z$. The value of Z depends on the magnetic fields. Therefore the up-leg Rabi frequency of STIRAP process (Feshbach molecule to intermediate state transition) depends on the magnetic field where we associate Feshbach molecules. Since the coupling between intermediate molecule state and scattering state is negligible, increasing the close channel fraction will increase the Rabi frequency.

We denote $-E_b$, the binding energy of the Feshbach molecules, and E_c is the energy of the state $|close\rangle$ relative to the energy of the separated atoms (open channel). Then using Hellmann-Feynmann theorem

$$\frac{\partial(-E_b)}{\partial x} = \langle FB | \frac{\partial H}{\partial x} | FB \rangle, \quad (6.34)$$

it follows then, $Z = \partial(-E_b)/\partial E_c = \partial(-E_b)/(\delta\mu \cdot B)$, where $\delta\mu$ is the difference of the magnetic moments between the open channel and the closed channel. In order to get the fraction of the closed/open channel, one needs the information about the binding energy of the Feshbach molecule $E_b(B)$, and the difference of the magnetic moment $\delta\mu$.

In our situation, the magnetic field where we create the Feshbach molecules is very close to the resonance, therefore we could use the universal binding energy formula $E_b \sim \frac{\hbar^2}{2m(a-\bar{a})^2}$ with $a(B) \sim a_{bg}(1 + \frac{\Delta B}{B-B_0})$. We use ABM model to calculate the difference of the magnetic moments between the open and closed channels. In fact $\delta\mu$ is a function of the magnetic field B , however the variation of $\delta\mu$ is small within the width of the resonance. We set $\delta\mu$ as a constant.

6.7. Application in $^{23}\text{Na}^{40}\text{K}$ system

6.7.1. Modification of the model

In the previous section, we present the dressed ABM model with only one bound state in the open channel space \mathcal{P} . This approximation is fine for small background scattering length, however it turns out to be insufficient for large background scattering length. In $^{23}\text{Na}^{40}\text{K}$ system, the background scattering length is large and negative, and it indicates that a virtual scattering (quasi-bound) state is above and close to the threshold. Therefore, to amend the dressed ABM model for $^{23}\text{Na}^{40}\text{K}$, one needs to include this virtual state into the Mittag-Leffler expansion of $\frac{1}{E+i\delta-H_{PP}}$, which leads to a different value of $\mathcal{A}(E)$:

$$\mathcal{A}(E) \approx \frac{\mu}{\hbar^2} \frac{-i\langle\phi_Q|\mathcal{H}_{QP}|\Omega_P\rangle\langle\Omega_P^D|\mathcal{H}_{PQ}|\phi_Q\rangle}{\kappa_P(k-i\kappa_P)} - \frac{\mu}{\hbar^2} \frac{-i\langle\phi_Q|\mathcal{H}_{QP}|\Omega_{vs}\rangle\langle\Omega_{vs}^D|\mathcal{H}_{PQ}|\phi_Q\rangle}{\kappa_{vs}(k+i\kappa_{vs})}, \quad (6.35)$$

where $|\Omega_{vs}\rangle$ is Gamow state that corresponds to a virtual-state pole close to threshold, $\kappa_{vs} = ik_{vs}$ (k_{vs} is wave vector of the virtual state) and $-\langle\phi_Q|\mathcal{H}_{QP}|\Omega_{vs}\rangle\langle\Omega_{vs}^D|\mathcal{H}_{PQ}|\phi_Q\rangle$ is a real constant.

The presence of an additional term in Eq. (6.35) also leads to a modification of Eq. (6.29)[167]:

$$E_b(B) + \epsilon_Q(B) - \frac{\frac{1}{2}\Delta_{vs}^2}{E_{vs}(1 + \sqrt{\frac{E_b}{E_{vs}}})} = 0, \quad (6.36)$$

where E_b is actual binding energy, $\epsilon_Q(B)$ is the binding energy without open-close coupling and can be obtained from the dressed ABM models. Δ_{vs}^2 is the coupling constant of the virtual bound state in the open channel and the bound molecular state in the closed channel. E_{vs} can be obtained from the background scattering length $E_{vs} \sim \frac{\hbar^2}{2m(a_{bg}-\bar{a})^2}$. Thus the only undetermined parameter is Δ_{vs}^2 .

6.7.2. Free parameters of $^{23}\text{Na}^{40}\text{K}$ system

As mentioned in previous sections, there are few unknown parameters in ABM models:

1. the bound state energies of singlet/triplet potentials,
2. the Franck-Condon factors between singlet and triplet bound states,
3. the energy of virtual bound state in the open channel E_{vs} ,
4. the coupling constant Δ_{vs}^2 .

For an unknown system, one could in principle keep these parameters as free parameters, and determine them from fitting to experimental observed Feshbach resonances (positions and widths of the resonances). However, $^{23}\text{Na}^{40}\text{K}$ system is well studied in literatures, and it makes these parameters deterministic.

Binding energies

The electronic ground state potentials (both singlet and triplet potentials) are reported in Ref.[168]. The bound state energy can be obtained by using LEVEL program. We only include the least bound states: for the triplet potential $\epsilon_T = -1654$ MHz, and for the singlet potential $\epsilon_S = -210$ MHz.

LEVEL program can also calculate bound states' wavefunctions which allow us to calculate the Franck-Condon factors(FCF). The FCF of the two singlet and triplet bound states is 0.499.

Virtual bound states

The energy of the virtual bound state can be obtained from the background scattering length a_{bg} :

$$E_{vs} \sim \frac{\hbar^2}{2\mu(a_{bg} - \bar{a})^2}, \quad (6.37)$$

for $^{23}\text{Na}^{40}\text{K}$, $a_{bg} = -690a_0$, and the mean scattering length $\bar{a} = 51a_0$ [128]. It gives $E_{vs} = k_B \times 110\mu\text{K}$.

The coupling constant Δ_{vs}^2 was obtained by fitting the experimentally observed Feshbach resonance width for $^{23}\text{Na} |F = 1, m_F = 1\rangle + ^{40}\text{K} |F = 9/2, m_F = -5/2\rangle$ channel, $\Delta_{vs}^2 = (\hbar \times 5.26\text{MHz})^2$ in Ref.[128]. To calculate Δ_{vs}^2 for other open channels, we assume that the spatial overlapping between the virtual bound state in the open channel and the 'triplet' bound state in the closed channel is a constant for all the spin combinations. Therefore we only need to calculate the spin overlapping and rescale Δ_{vs}^2 for other open channels.

To check the correctness, we first apply our code to $^{23}\text{Na} |F = 1, m_F = 1\rangle + ^{40}\text{K} |F = 9/2, m_F = -5/2\rangle$ channel and compare the result with the one in Ref.[128]. The result from ABM model is also consistent with the experimental datas.

6.8. $^{23}\text{Na} |F = 1, m_F = 1\rangle + ^{40}\text{K} |F = 9/2, m_F = -9/2\rangle$ channel

Currently, we use the resonance around 88 Gauss to associate Feshbach molecules and the corresponding open channel is $^{23}\text{Na} |F = 1, m_F = 1\rangle + ^{40}\text{K} |F = 9/2, m_F = -9/2\rangle$. We present details of this Feshbach resonance from ABM calculation in this section.

6.8.1. Resonance position and width

Fig.6.1 shows two crossings between the entrance channel and bound molecular states around 76 Gauss and 79 Gauss². Fig.6.2 shows the crossing within dressed ABM model where the resonance position shifts towards to larger magnetic field value, and

²The magnetic field values of the resonances are smaller than the experimental datas. This is an artefact from standard ABM model which can amended by dressed ABM model.

the asymptotic behavior of the binding energy close to the resonance. The dressed ABM model gives the resonant position at **86.4 Gauss** and the width is **5.95 Gauss**.

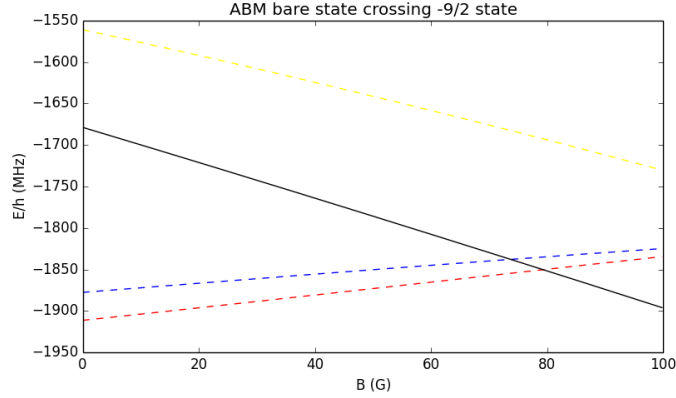


Figure 6.1. – The result from standard ABM model, $^{23}\text{Na} |F = 1, m_F = 1\rangle + ^{40}\text{K} |F = 9/2, m_F = -9/2\rangle$. Black solid line corresponds to the threshold energy. Blue and red dashed lines represent two bound states. The figure shows two crossings, therefore there are two Feshbach resonances expected for this collision channel.

6.8.2. Spin components of Feshbach molecules

We can also use ABM model to calculate the spin components of Feshbach molecules, both open channel and closed channel, shown in Table 6.1.

J	m_J	μ_{Na}	μ_K	closed channel (amplitude)	open channel (amplitude)
0	0	-3/2	-2	0.017	0.0
0	0	-1/2	-3	-0.036	0.0
0	0	1/2	-4	-0.045	0.0
1	-1	-3/2	-1	0.129	0.319
1	-1	-1/2	-2	-0.377	0.0
1	-1	1/2	-3	0.077	0.0
1	-1	3/2	-4	0.148	-0.893
1	0	-3/2	-2	0.151	0.0
1	0	-1/2	-3	0.323	0.0
1	0	1/2	-4	0.457	0.319
1	1	-3/2	-3	-0.632	0.0
1	1	-1/2	-4	-0.273	0.0

Table 6.1. – Spin components of the Feshbach molecular state at 85.5G calculated with the asymptotic bound state model.

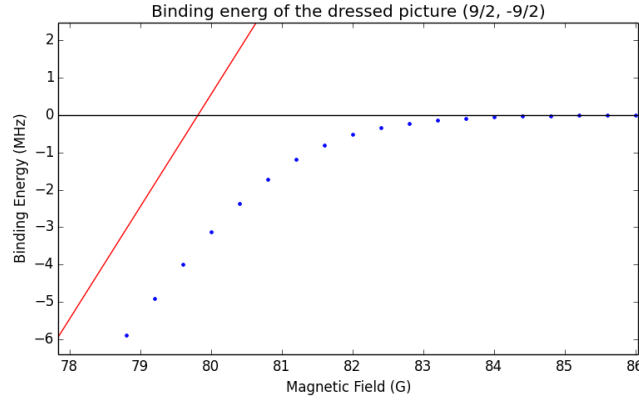


Figure 6.2. – The result from the dressed ABM model, $^{23}\text{Na } |F = 1, m_F = 1\rangle + ^{40}\text{K } |F = 9/2, m_F = -9/2\rangle$. We zoom in the region around the Feshbach resonance that we are using for molecule association. Black solid line corresponds to the threshold energy. Red solid line represents a bare bound state energy without open-close channel coupling. Blue dots represent the root of Eq. (6.36) at different magnetic fields which correspond to the real binding energies of the Feshbach molecules.

6.8.3. Close channel fraction

With dressed ABM model, we are able to get the difference of the magnetic moment $\delta\mu$ between open and closed channels. We use RF loss spectroscopy to determine the binding energies of Feshbach molecules at different magnetic fields experimentally (see Fig.6.3). We are then able to calculate the closed channel fraction. The result is shown in Fig. 6.4. For Feshbach molecules with $\sim 80\text{kHz}$ binding energy at 85.5 Gauss, the close channel fraction is $\sim 2\%$.

6.9. Discussion and outlook

Compare to the experimental datas from measuring the binding energies of the Feshbach molecules by RF loss spectroscopy, we find that the resonant position is ~ 88.9 Gauss, and the width is ~ 11 Gauss. So it shows discrepancy between the experimental datas and the ABM results. The possible reason that we use Δ_{vs}^2 from reported in Ref.[128], and we find that the widths of Feshbach resonances reported by Zwiernlein’s group [59] are systematically smaller than our experimental datas. Therefore we suspect that the value of Δ_{vs}^2 we use is underestimated.

In order to increase to Rabi frequency for the STIRAP process, it is better to increase the close channel fraction of the Feshbach molecules. It requires to associate the Feshbach molecules with large binding energies away from the resonances. RF association is not suitable for associating deeply bound Feshbach molecules due to the Franck-Condon arguments, however magnetic field sweeping association should in principle work. We will try to use magnetic field sweeping method in the future.

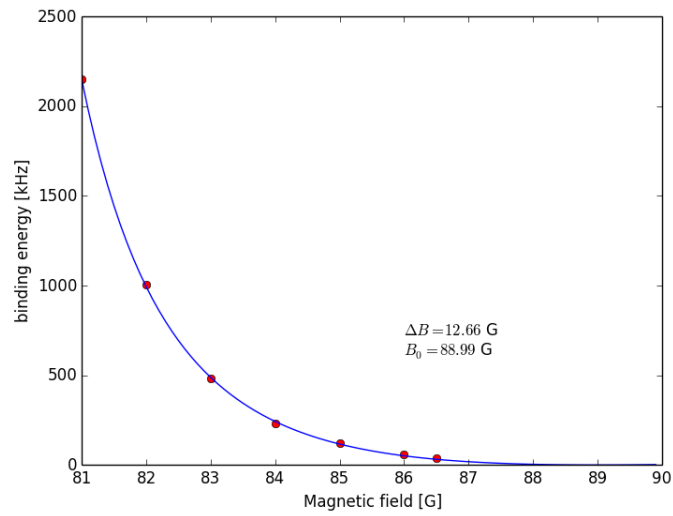


Figure 6.3. – Feshbach molecule binding energies at various magnetic fields. Red points are the experimental datas, Blue solid line fits the experimental datas to the universal binding energy formula, $E_b \sim \frac{\hbar^2}{2m(a-\bar{a})^2}$.

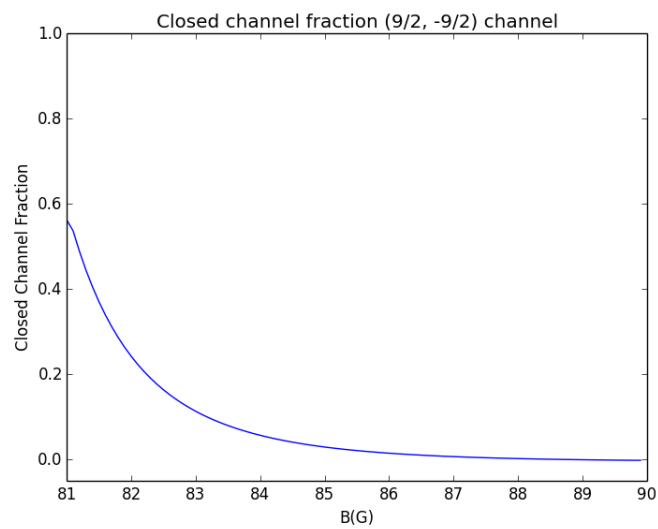


Figure 6.4. – Close channel fraction of Feshbach molecules vs. magnetic fields.

Bose polaron

In our experiments, we can successfully prepare a degenerate $^{23}\text{Na}^{40}\text{K}$ Bose-Fermi mixture with different atom number ratios under control. In addition, the inter-species interactions between ^{23}Na and ^{40}K , characterized by the *s-wave* scattering length, a , can be well controlled by tuning the external magnetic field. Thus it provides an ideal experimental platform for studying so called *Bose polaron* problems, where impurity atoms interact with a Bose-Einstein condensate. In this chapter, we present the physical background, the experimental method, and preliminary results towards Bose polaron physics.

7.1. Introduction

Quantum impurity problems are the building blocks of quantum many-body physics. As originally pointed out by Landau and Pekar[169, 170], a single moving electron in the ionic lattice can cause distortion of the underlying environment that is sufficient to change the electron's motion backwards, and the electron tends to localize at sufficiently strong interactions. The resulting 'dressed' electron is called *polaron* in literature. The properties of these 'phononic' dressed electrons are crucial to understand many solid state material. In fact, the concept of 'polaron' goes beyond conventional solid state system, and was also extensively studied in superfluid ^4He [171], polar semiconductors[172], and high temperature superconductors[173].

With the advanced development of ultracold atom community, new possibilities to study the properties of quantum impurities in the ultracold atomic systems have emerged. The experimental creation of various Bose-Fermi[126, 135, 127], Bose-Bose [174, 175, 140] or Fermi-Fermi [176] mixtures gives the chance to investigate different types of polarons, Fermi polaron (an impurity moving in a fermionic environment) or Bose polaron (an impurity moving in a bosonic environment). One powerful tool in the ultracold experiments is that the interactions between impurities and the environment can be tuned via Feshbach resonances[3, 10, 145]. It allows us to access different regimes, ranging from weakly interacting, medium interacting (Fröhlich regime) and strongly interacting [177].

The case of the Fermi polaron has received considerable experimental attention[178, 179]. In particular, Fermi polaron's spectral function has been studied via the technique of inverse radio-frequency (rf) spectroscopy both in two and three dimensions

[178, 179]. It has been shown that in the strongly interacting regime, an impurity in a Fermi sea can be treated as quasi-particle - the Fermi polaron- with a well-defined energy and effective mass.

However, the Bose polaron problem, which is more related to the original Landau-Pekar problem, has not yet been studied in any ultracold atom experiment. The Bose polaron in the strongly interacting regimes remains also a challenging problem in theoretical physics and various theoretical tools have been used to study, including Green function perturbation theories, self-consistent Born approximation, mean-field approach, Feynmann path integral approach, Monte Carlo simulations, renormalization group calculations, and Gaussian variational ansatz (see review [177]). However different methods lead to ambiguous results (see e.g. [177]).

Therefore an experimental realization of Bose polaron with ultracold atoms will serve as a testbed for studying the properties of Bose polaron and testing theoretical models. $^{23}\text{Na}^{40}\text{K}$ system have several wide Feshbach resonances at low magnetic field, is thus an ideal system for that purpose.

7.2. Inverse radio-frequency (rf) spectroscopy

In order to access Bose polaron physics in the strongly interacting regime where impurities resonantly interact with the background bosons, one has to consider the three-body process[133]. One impurity atom resonantly interacts with a neighboring boson and forms a weakly bound state. The released binding energy was taken by a third atom. The recombination rate scales as $\sim a^4$ [149, 180], where a is the s -wave scattering length between the impurity and the background boson. This process leads to heatings and losses which limits the lifetime of system to perform experimental measurements. To overcome this obstacle, it has been proposed in Refs. [181, 182] to use *inverse radio-frequency (rf) spectroscopy* for experimental detection: one first prepares a weakly interacting mixture which lives sufficiently long, and then uses radio frequency photon to spin-flip the impurity into a strongly interacting channel. The properties of the polarons can be extracted from the measured spectral response. This method has been successfully used in Fermi polaron experiments with $^6\text{Li}^{40}\text{K}$ system[178, 179].

7.2.1. Theoretical framework

The inverse rf spectral response of Bose polaron problem has been calculated within field theory method [182], second-quantization method [181], and variational ansatz method[183]. We follow the formulations in Ref. [181] to illustrate the essential theoretical background, and we summarize the theoretical predictions in the following subsection.

We assume the concentration of impurities is small that we could neglect the statistics and the interactions between the impurities. Thus we could consider a single impurity of mass M , which has two hyperfine states ($|\uparrow\rangle, |\downarrow\rangle$). The background en-

environment is a Bose-Einstein condensate (BEC) consists of a different bosonic species with mass m . The Hamiltonian of the system reads:

$$\mathcal{H} = \mathcal{H}_i + \mathcal{H}_b + |\uparrow\rangle \otimes \langle\uparrow| \mathcal{H}_{int\uparrow} + |\downarrow\rangle \otimes \langle\downarrow| \mathcal{H}_{int\downarrow} \quad (7.1)$$

where \mathcal{H}_b is the BEC Hamiltonian, $\mathcal{H}_i = \frac{\hat{\mathbf{p}}^2}{2M}$ is the impurity Hamiltonian with momentum \mathbf{p} , $\mathcal{H}_{int,\sigma}$ describes density-density interactions between the bosons and the impurity in state σ ,

$$\mathcal{H}_{int,\sigma} = g_{IB,\sigma} \cdot \rho_{BEC}, \quad (7.2)$$

where $g_{IB,\sigma}$ is the coupling constant between the impurity and boson. At the ultracold limit, the effective coupling constant is related to the s-wave scattering length $a_{IB,\sigma}$,

$$g_{IB,\sigma} = \frac{2\pi a_{IB,\sigma}}{\mu}, \quad (7.3)$$

where μ is the reduced mass $\mu = \frac{Mm}{M+m}$ and we also set $\hbar = 1$.

The background BEC is typically in the weakly interacting regime, therefore Bogoliubov approximation is valid to use. Therefore one can separate the Hamiltonian into two parts : the condensed part is treated as a ‘mean field’ background and a bath of free phonons for the excitation part:

$$\mathcal{H}_b = \sum_{\mathbf{k} \neq 0} \omega_{\mathbf{k}} b_{\mathbf{k}}^\dagger b_{\mathbf{k}}, \quad (7.4)$$

with the dispersion relationship:

$$\omega_{\mathbf{k}} = ck \sqrt{1 + \frac{(k\xi)^2}{2}}, \quad (7.5)$$

where $\xi = 1/(\sqrt{2}mc)$ is the healing length, c is the speed of sound in the BEC, and $k = |\mathbf{k}|$.

As a consequence, the interaction terms $\mathcal{H}_{int,\sigma}$ can be separated into two parts as well,

$$\mathcal{H}_{int,\sigma} = \frac{2\pi a_{IB,\sigma}}{\mu} n_0 + \sum_{\mathbf{k} \neq 0} V_{\mathbf{k}\sigma} e^{i\mathbf{k}\cdot\mathbf{x}} (\hat{b}_{-\mathbf{k}}^\dagger + \hat{b}_{\mathbf{k}}), \quad (7.6)$$

where n_0 is the BEC density and N_0 is the number of atoms in the condensate part, and the interaction matrix element is given by:

$$V_{\mathbf{k},\sigma} = \frac{2\pi a_{IB,\sigma} n_0}{\mu} \left(\frac{\xi k}{\sqrt{2 + (\xi k)^2}} \right)^{1/2}. \quad (7.7)$$

The effect of a rf phonon is to change the internal state of the impurity atom without changing its moment, we thus treat the rf spin flip as an instantaneous action. Experimentally, it requires that the rf pulse duration is shorter than any

relaxing process duration. Under this condition, the rf spectral response can be computed within Fermi's golden rule as follows,

$$I(p, \omega) = \sum_n |\langle n_{\uparrow, p} | \hat{V}_{rf} | i_{\downarrow, p} \rangle|^2 \delta(\omega - (E_{n\uparrow} - E_{i\downarrow})), \quad (7.8)$$

where $|i_{\downarrow, p}\rangle$ is the initial state that the impurity stays at $|\downarrow\rangle$ with momentum p and energy $E_{i\downarrow}$, $|n_{\uparrow, p}\rangle$ stands for a final state, and the sum is over all possible final states with momentum p . The rf transition operator $\hat{V}_{rf} = |\uparrow\rangle\langle\downarrow|$ instantaneously changes the internal state of the impurity without retardation. $I(p, \omega)$ can be rewritten as:

$$I(p, \omega) = \mathcal{R} \frac{1}{\pi} \int_0^\infty e^{i\omega t} A_p(t) dt, \quad (7.9)$$

$$A_p(t) = e^{iE_{i\downarrow}t} \langle i_{\uparrow p} | e^{-i(\mathcal{H}_b + \mathcal{H}_i + \mathcal{H}_{int\uparrow})t} | i_{\downarrow p} \rangle, \quad (7.10)$$

where ω corresponds to the rf photon frequency. The quantity $A_p(t)$ gives the rf spectra of Bose polarons.

It worths to mention that $A_p(t)$ given in Eq. (7.10) has the form of the amplitude of a real-time evolution propagator. The physical interpretation of this propagator is clear, that an eigenstate of the initial Hamiltonian $\mathcal{H}_b + \mathcal{H}_I + \mathcal{H}_{int\downarrow}$, $|i_{\downarrow p}\rangle$ evolves with the Hamiltonian $\mathcal{H}_b + \mathcal{H}_I + \mathcal{H}_{int\uparrow}$ in the real time domain. It leads to another theoretical method used in Ref. [182].

In Ref.[182], a two-field theory was constructed: one field $\phi_{x,\tau}$ represents the boson background and the second field $\psi_{x,\tau}$ is the impurity field. The corresponding euclidean action reads as follows,

$$\begin{aligned} \mathcal{S} = \int d\tau \int d^3x \left\{ \phi^* \left(\partial_\tau - \frac{1}{2m_\phi} \nabla^2 - \mu_\phi \right) \phi \right. \\ \left. + \psi^* \left(\partial_\tau - \frac{1}{2m_\psi} \nabla^2 - \mu_\psi \right) \psi + \frac{g_{\phi\phi}}{2} |\phi|^4 + g_{\phi\psi} |\phi|^2 |\psi|^2 \right\}, \end{aligned} \quad (7.11)$$

where $g_{\phi\phi}$ is the coupling constant between the bosons while $g_{\phi\psi}$ is the coupling constant between the impurity and the background. Therefore, this theory is identical as the previous theory formulated with Hamiltonian.

The two-field theory results in two propagators, the Bose propagator and the impurity propagator. The rf spectral response is the real part of the impurity propagator and the effective mass can also be extracted from the impurity propagator. The propagator can be estimated by $\mathcal{T} - Matrix$ approximation, as presented in Ref.[182].

7.2.2. Theoretical prediction

We summarize the theoretical predication from Ref.[182] and Ref.[181].

RF spectral response

The theoretical prediction of the rf spectral response at with different interaction strength is shown in the following figure, taken from Fig. 7 of Ref.[182] with permission.

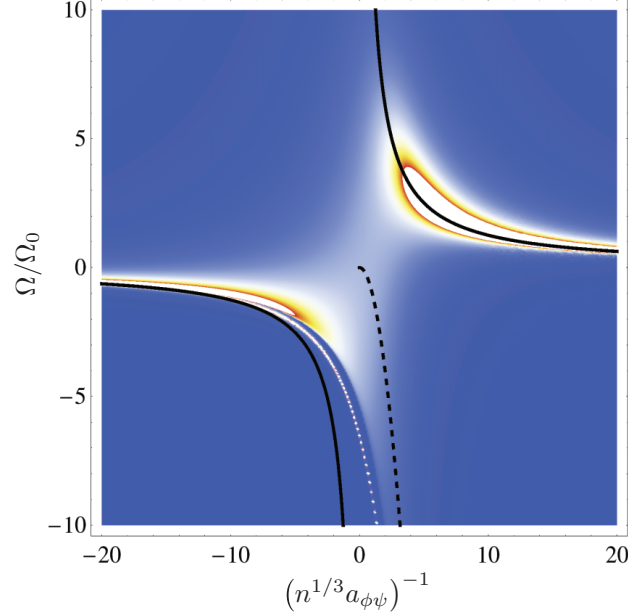


Figure 7.1. – Inverse rf spectra based on vanishing momentum ($\mathbf{p} = 0$) polarons with self-consistent \mathcal{T} -matrix approach, taken from Fig. 7 in Ref.[182] with permission. n is the density of the BEC, $a_{\phi\psi}$ is the interaction (s-wave scattering length) between the impurity and the Bose background, $\Omega_0 = n^{2/3}/m_\phi$.

The interaction parameter is defined as $(n^{1/3}a_{\phi\psi})^{-1}$, and the typical energy scale is set to $\Omega_0 = n^{2/3}/m_\phi$ in the calculation.

Theory predicts two dominating spectral features, one at positive Ω and one is at negative Ω . We call the low-energy features as attractive polarons because they mainly appear when the interaction is attractive ($a_{\phi\psi} < 0$). The high-energy features are called repulsive polarons mainly appearing at repulsive interaction ($a_{\phi\psi} > 0$).

In general, at the weakly interacting regime, $|(n^{1/3}a_{\phi\psi})^{-1}| \gg 1$, polarons are well defined quasi-particles, and the interaction shift approximates to the mean-field interaction shift. At strongly interacting regimes, $|(n^{1/3}a_{\phi\psi})^{-1}| \ll 1$, the spectral response becomes broad and the quasiparticle characters are smeared out.

Momentum dependence

Previous plot shows the rf spectral response for impurities with zero momentum $\mathbf{p}=0$. Experimentally, we use an ensemble of atoms in a trap as impurities which has certain momentum distribution depending on the statistics of the impurity atoms and the trap geometry. The momentum dependence of rf spectral response was also investigated in Ref.[182]. The following figure is taken from Fig. 8 in Ref. [182] with permission:

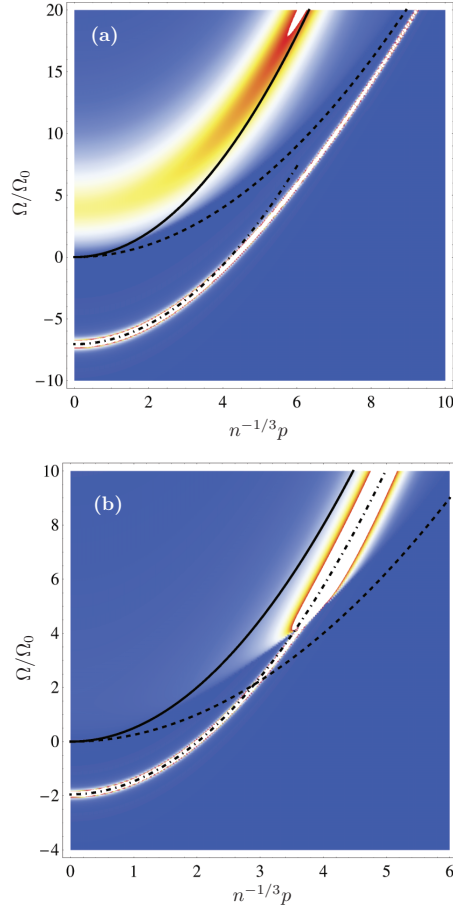


Figure 7.2. – Momentum dependence of polaron spectral response using self-consistent \mathcal{T} -matrix approach in Ref. [182]. Solid line: free impurity dispersion. (a) $(n^{1/3}a_{\phi\psi})^{-1} = 1$. (b) $(n^{1/3}a_{\phi\psi})^{-1} = -5$.

The essential point is that the rf spectral response touches the free impurity dispersion line at high momentum regions, $|n^{-1/3}p| \gtrsim 5$. It means that for fast moving impurities, the effect of interaction vanishes and the impurities become free particles. This effect can be understood by the simple argument that, the *s-wave* scattering

length $a_{\phi\psi}$ is the low-momentum limit of the *s-wave* phase shift' tangent, $\delta_0(k)$,

$$a_{\phi\psi} = -\lim_{k \rightarrow 0} \frac{1}{k} \tan \delta_0(k), \quad (7.12)$$

for sufficient large collisional momentum, $a_{\phi\psi}$ is not enough to characterizes the inter-particle interaction, thus higher order of the expansion should be included,

$$k \cot \delta_0(k) = -a_{\phi\psi}^{-1} + r_{eff} k^2/2, \quad (7.13)$$

so the phase shift goes to zero at high momentum limit.

Tan's contact tails

As pointed out in Ref. [181], the rf spectral signal should contain an incoherent part with a characteristic high frequency power-law tail which corresponds to the excitations of the background BEC. It is a manifestation of the universal "contact" physics studied by Shina Tan [184, 185, 186, 187].

7.3. Experimental details

7.3.1. Experimental sequence

We follow the theoretical proposals and perform inverse rf spectroscopy with $^{23}\text{Na}^{40}\text{K}$ mixtures. The experimental procedures are summarized as follows:

1. We prepare a large ^{23}Na cloud with a few ^{40}K in a crossed dipole trap. ^{23}Na is at $|F = 1, m_F = 1\rangle$ state and ^{40}K is at $|F = 9/2, m_F = -7/2\rangle$.
2. We perform combined evaporation, and the evaporation procedure was optimized to get a mixture with large atom ratio $N_{\text{Na}}/N_{\text{K}}$. After the evaporation, ^{23}Na is condensed with $\sim 3 \cdot 10^5$ atoms (this number is the 'condensed part', not including the thermal part; measured from long TOF images). The atom number of ^{40}K is fluctuating, a few 10^4 , corresponding to $< 10\%$ of the Na atom number.
3. We use a Feshbach resonance of $^{23}\text{Na} |F = 1, m_F = 1\rangle + ^{40}\text{K} |F = 9/2, m_F = -9/2\rangle$ at 78.1G with 1.1G width.
4. After evaporation in the crossed dipole trap, we ramp up the homogenous magnetic field to various values around the Feshbach resonance and stabilize it. Afterwards, we apply a rf pulse (π pulse) to spin flip the impurities ^{40}K from the $|m_F = -7/2\rangle$ to $|m_F = -9/2\rangle$ state.
5. For each magnetic field value, we first determine the bare atomic transition frequency of ^{40}K without ^{23}Na background. We then use the same pulse with

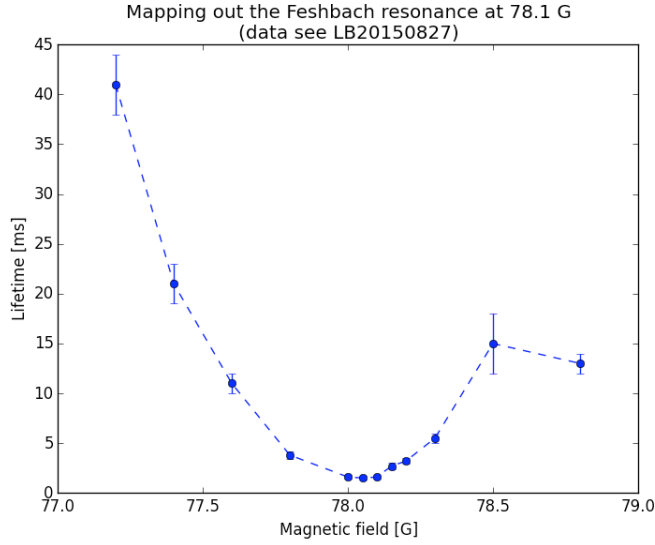


Figure 7.3. – Life time of the impurity vs magnetic field. The error bar indicates the fitting deviation to an exponential decay.

a ^{23}Na BEC to determine the frequency shift and broadening due to the interaction with the ^{23}Na background.

- To overcome the problem of ^{40}K atom number fluctuations from shot to shot, we use two-state imaging techniques: we transfer the remaining $|m_F = -7/2\rangle$ atoms from $|m_F = -7/2\rangle$ to $|m_F = -3/2\rangle$ by two consecutive rf π pulses and then we record the atom numbers at $|m_F = -9/2\rangle$ and at $|m_F = -3/2\rangle$ by spin-resolved high-field imaging method. For the data analysis, we can determine how many atoms get transferred, $N(m_F = -9/2)/[N(m_F = -3/2) + N(m_F = -9/2)]$.

7.3.2. Experimental calibration

Impurity lifetime

We measure the impurity lifetime coexisting with a ^{23}Na BEC at different magnetic field values around the Feshbach resonance, as shown in Fig.7.3. The lifetime was determined by fitting to an exponential decay curve in time. The lifetime of the impurity is $> 1\text{ms}$ for all magnetic fields ensures that the broadening of rf spectral response due to finite lifetime should be $< 1\text{kHz}$.

Trapping frequencies

We use parametric heating methods to measure the trapping frequencies of dipole trap at different laser power, and then extrapolate to the low power value to get the trapping frequencies ($\omega_x, \omega_y, \omega_z$) for both species.

Cloud size and density distribution

The cloud size of the ^{23}Na BEC and the ^{40}K Fermi cloud was estimated by assuming a Thomas-Fermi profile in a trap.

For bosons, the density profile is given by,

$$n(x, y, z) = n_0 \left(1 - \frac{x^2}{R_x^2} - \frac{y^2}{R_y^2} - \frac{z^2}{R_z^2} \right), \quad (7.14)$$

and the Thomas-Fermi radius ($i = x, y, z$) is given by [188]:

$$R_i = \left(\frac{15Na_{bg}}{l_i^h} \right)^{1/5} \cdot l_i^h, \quad (7.15)$$

where N is the atom number of BEC, a_{bg} is the scattering length of bosons ($a_{bg} \sim 60a_0$ for ^{23}Na), and l_i^h is the harmonic oscillator length along i axis.

For fermions, the density profile is [189],

$$n(x, y, z) = \frac{8}{\pi^2} \frac{N}{R_x R_y R_z} \left(1 - \frac{x^2}{R_x^2} - \frac{y^2}{R_y^2} - \frac{z^2}{R_z^2} \right)^{3/2}, \quad (7.16)$$

and the Thomas-Fermi radius ($i = x, y, z$) is given by:

$$R_i = l_i^h (48N)^{1/6}, \quad (7.17)$$

where N is the atom number of the Fermi gas, and l_i^h is the harmonic oscillator length along i axis.

Since we know the atom numbers of the two species and the trapping frequency, we are able to determine the cloud sizes and the densities. For the trap we use, the Thomas-Fermi radius of the ^{23}Na BEC is roughly the same as ^{40}K cloud's. The average density of ^{23}Na BEC is $\sim 10^{14} \text{ cm}^{-3}$, and the Fermi energy, $E_F = \frac{\hbar^2}{2m} (3\pi^2 n)^{2/3}$, is $\sim 10 \text{ kHz}$.

Scattering length

The initial state is $^{23}\text{Na} |F = 1, m_F = 1\rangle + ^{40}\text{K} |F = 9/2, m_F = -7/2\rangle$. There are two relevant Feshbach resonances around 78.1G in this scattering channel.

We extract the parameters for the two Feshbach resonances: One is at 81.5 G and is 1 G wide, the other is at 90.2 G and is 2.5 G wide [59, 123]. The background scattering length is about $-690a_0$ [128], where a_0 is the Bohr radius. Using the universal Feshbach resonance formula [10],

$$a(B) = a_{bg} \left(1 + \frac{\Delta B_1}{B - B_1} + \frac{\Delta B_2}{B - B_2} \right). \quad (7.18)$$

We plot the scattering length versus the magnetic field of the initial channel in Fig.7.4.

The scattering length of the final channel, $^{23}\text{Na} |F = 1, m_F = 1\rangle + ^{40}\text{K} |F = 9/2, m_F = -9/2\rangle$, is shown in Fig.7.5, where we include two Feshbach resonances in this channel: One is at 78.1 G and is 1.1 G wide, the other is at 89.2 G and is 12.85 G wide [123].

Since we perform our measurements around 78.1 G, the initial mixture is ‘weakly’ interacting with a scattering length about $-390a_0$.

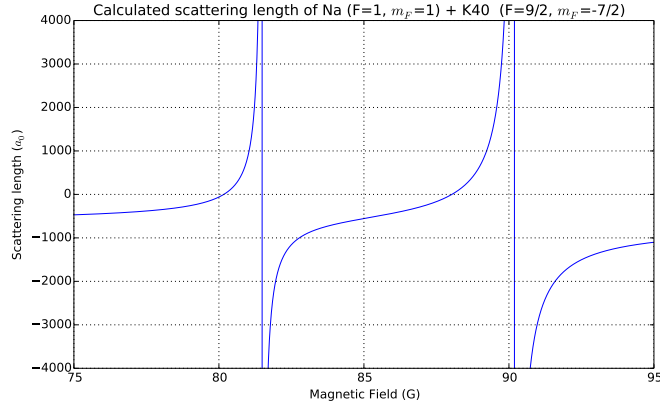


Figure 7.4. – The scattering length vs. magnetic field of the initial channel, $|F = 1, m_F = 1\rangle + ^{40}\text{K} |F = 9/2, m_F = -5/2\rangle$.

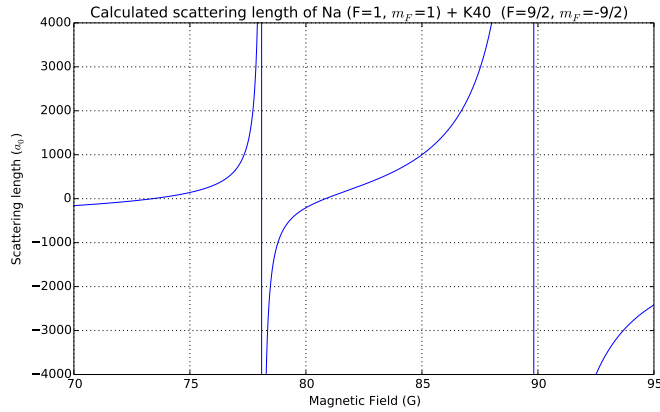


Figure 7.5. – The scattering length vs. magnetic field of the final channel, $|F = 1, m_F = 1\rangle + ^{40}\text{K} |F = 9/2, m_F = -9/2\rangle$.

7.4. Experimental results: rf spectral response across the FB resonance

We took rf spectral response at various magnetic fields around Feshbach resonances at 78.1G. The results are shown in Fig. 7.6. We convert the experimental data to a color scaled figure, Fig. 7.7. We fit the experimental data to Gaussian distribution curves phenomenologically, and extract the centers and the widths from the fitting.

We then calculate the frequency differences between the situations with or without ^{23}Na BEC. It shows how impurity atoms get dressed by the BEC. We plot the frequency shifts in Fig.7.8.

7.5. Discussion

Experimentally, we have seen following features which agree with theoretical predictions qualitatively:

1. We see frequency shifts when impurity atoms interact with ^{23}Na BEC. With repulsive interactions, the resonant rf frequencies shift towards lower values (corresponds to positive value of Ω/Ω_0 in Ref.[182]), and with attractive interactions, the resonant frequencies shift towards to higher values.
2. Close to the Feshbach resonance where the interaction becomes stronger, we see the rf spectra become broad ($\sim 10\text{kHz}$ level), simultaneously the transition amplitude decrease.
3. Away from the Feshbach resonance, the rf spectra are more localized and the transition amplitudes approach to the ones without ^{23}Na atoms.
4. Away from the RF resonance, the spectra develop tails that extend to very high energy.

7.5.1. Discrepancies between experiments and theory

The energy scale is given as $\Omega_0 = \hbar^2 n^{2/3}/m_B$ [182]. Under our experimental conditions, the peak density of ^{23}Na BEC is $\sim 10^{14} \text{ cm}^{-3}$, the frequency shifts should be tens of kHz when $1/(k_n a_{IB}) \sim 1$, where $k_n = (6\pi^2 n)^{1/3}$. However, the maximum frequency shifts is 2kHz in our experiments. In Fig.7.9, we compare the experimental results with theoretical predictions while keeping the boson density as a free parameters. It shows that the experimental results are smaller than theoretical predictions by one order of magnitude.

7.5.2. Possible reasons

To understand the discrepancies between the experimental datas and the theory, we have checked a few possible reasons.

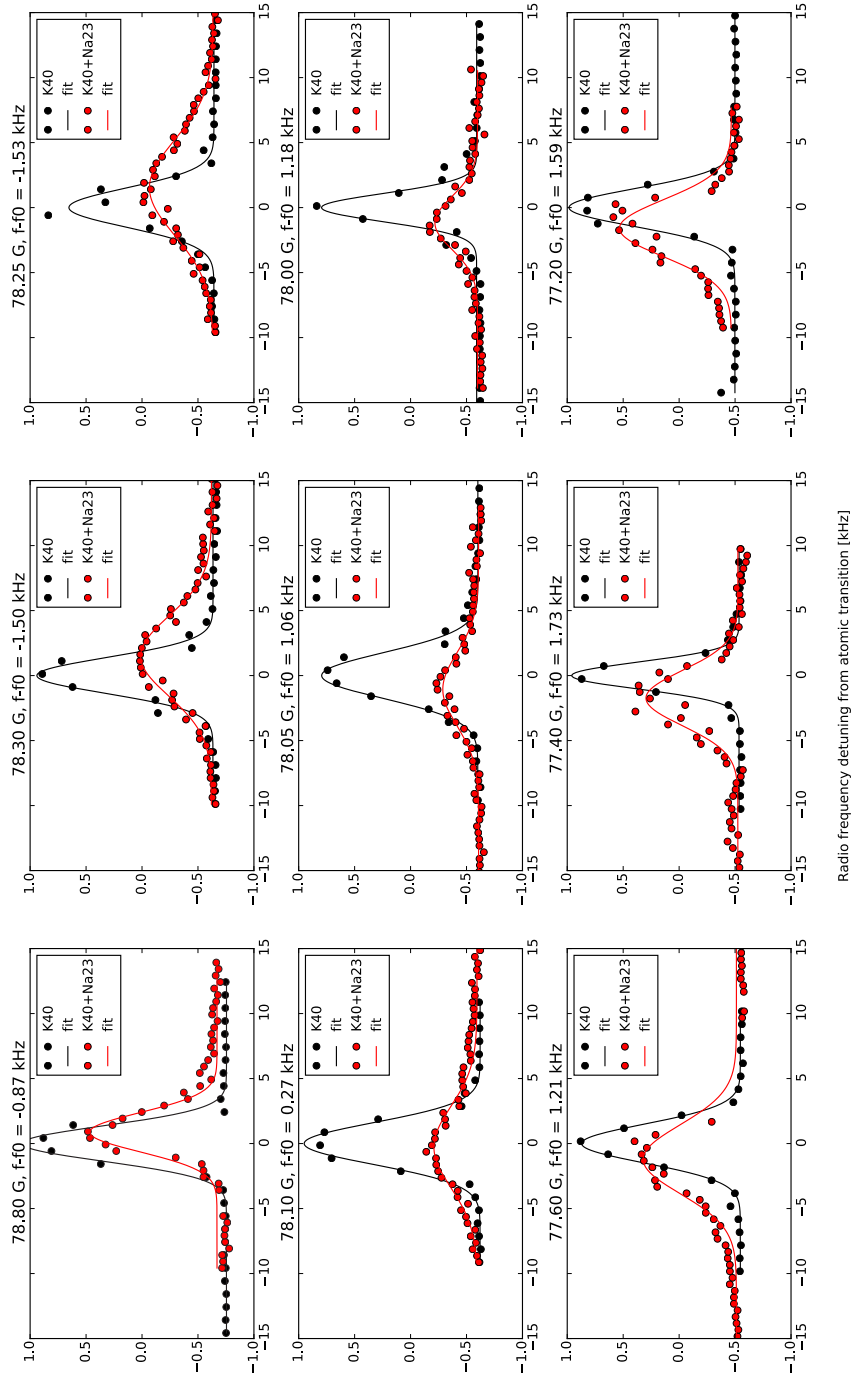


Figure 7.6. – rf spectral response of impurities at various magnetic fields. Black dots are the experimental data points of bare ^{40}K atomic transitions without ^{23}Na atoms. Red dots are the experimental data points while spin-flipping ^{40}K with ^{23}Na a Na BEC background. Solid lines show the results of fitting experimental datas to a Gaussian distribution.

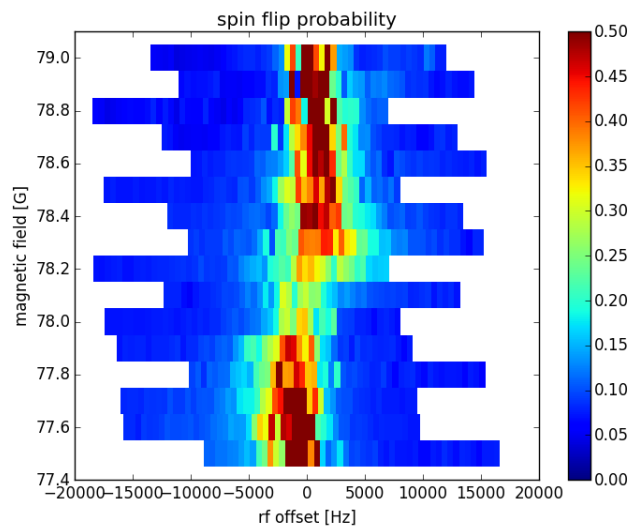


Figure 7.7. – Color scaled rf spectral response of impurities at various magnetic fields across the Feshbach resonance.

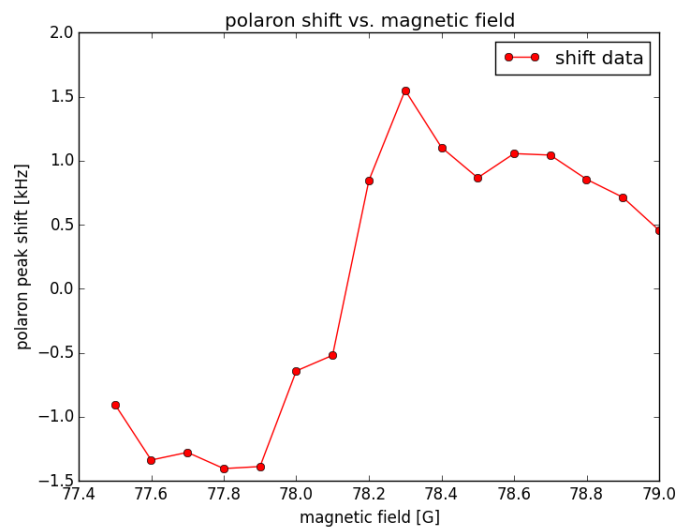


Figure 7.8. – Frequency shifts of impurity atoms due to ^{23}Na BEC at various magnetic fields across the Feshbach resonance.

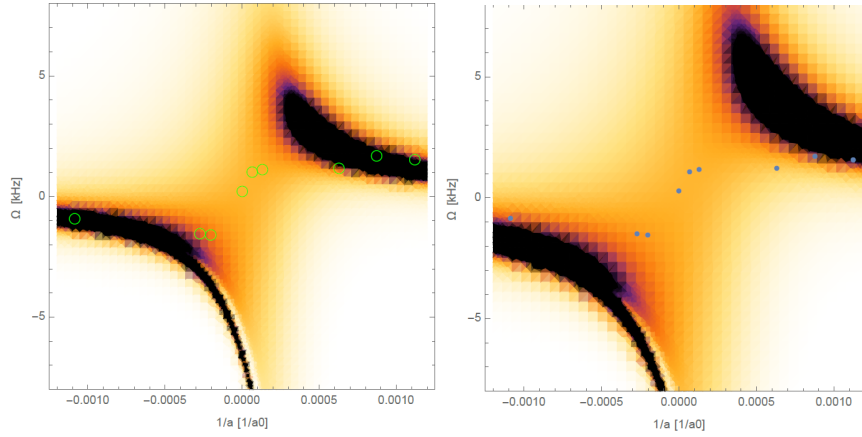


Figure 7.9. – Comparison between experimental data and theoretical prediction with various BEC density. Circles correspond to experimental data. Left figure: $n = 5 \cdot 10^{12} \text{cm}^{-3}$. Right figure: $n = 10^{13} \text{cm}^{-3}$. Private communication from Yulia E. Shchadilova, Richard Schmidt, Fabian Grusdt, and Eugene Demler.

One obvious reason could be that the overlapping between ^{23}Na and ^{40}K clouds is poor due to different trapping frequencies and gravitational sag. We have used *in-situ* imaging techniques to check the in-trap positions of the two clouds and they are well overlapped.

According to Ref.[182], the fermionic impurity atoms become ‘supersonic’ when the Fermi velocity ($v_F = \hbar k_F/M$) exceeds the critical velocity of the BEC ($c_S = \sqrt{ng/m}$). In our system, we estimate the Fermi velocity of ^{40}K is $\sim 10 \text{mm/s}$ while the critical velocity of ^{23}Na BEC is $\sim 6 \text{mm/s}$. It means that the majority of impurities are ‘supersonic’ and become ‘undressed’.

Up to date, we do not have a concrete idea of understanding the discrepancies in our experiments.

7.6. Outlook

As mentioned in introduction, Bose polaron is an interesting subject to study. It is feasible to investigate following properties in our experiments.

High frequency tails: The rf spectra of ^{40}K impurities with ^{23}Na BEC show an unsymmetrical behavior (see Fig. 7.10). The tails appear at the high frequency regions and range over tens of kHz and they might be related to universal ‘Tan’ contact physics.

Effective mass: The effective mass of Bose polarons at strongly interacting regimes is an ambiguous question in theoretical physics. The lifetime of impurities in our experiments is $> 1 \text{ms}$ and it enables us to observe low-frequency cloud oscillations ($f > 1 \text{kHz}$). We have prepared a new imaging system to observe clouds with higher resolution. By comparing the oscillation frequencies with and without Na atoms,

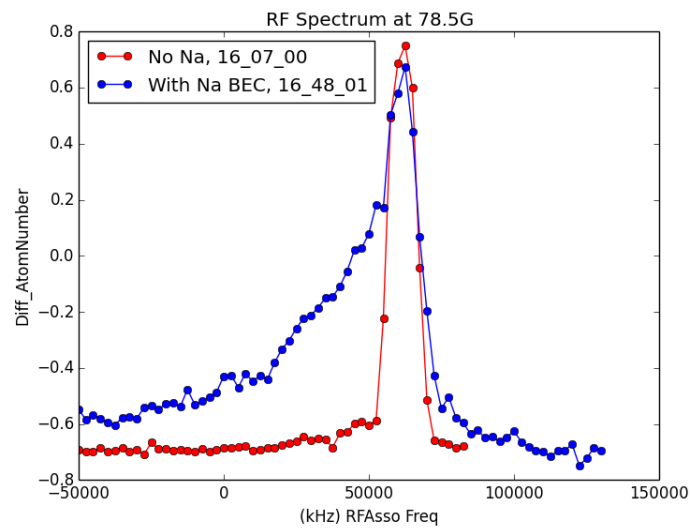


Figure 7.10. – RF spectra of impurity ^{40}K atoms at 78.5 Gauss. Red points show the spectrum without Na atoms. Blue points represent the spectrum with a Na BEC where a tail is clearly visible.

we should be able to extract the effective mass of Bose polaron at various interaction regimes.

Conclusion and outlook

In this thesis, I have presented in details a novel experimental apparatus designed for creating ultracold $^{23}\text{Na}^{40}\text{K}$ ground state molecules. Owing to its large dipole moment and chemical stability, this system should lead to a new generation of experiments to explore many-body physics with long range dipole-dipole interaction.

During the course of this PhD project, several crucial steps towards to the goal have been achieved experimentally:

- Creation of a degenerated Bose-Fermi $^{23}\text{Na}^{40}\text{K}$ mixture with controllable atomic ratios.
- Association of weakly bound Feshbach molecules with $^{23}\text{Na}|F = 1, m_F = 1\rangle + ^{40}\text{K}|F = 9/2, m_F = -9/2\rangle$ channel.
- Implementation of asymptotic-bound state model to $^{23}\text{Na}^{40}\text{K}$ system to obtain the spin characters of Feshbach molecules.
- Identification of a suitable intermediate state $|d^3\Pi, \nu = 5, J = 1, \Omega = 1\rangle$ in $d^3\Pi/D^1\Pi$ complex for STIRAP process.
- Demonstration of successful STIRAP transfer to the rovibrational ground state, $|X^1\Sigma, \nu = 0, J = 0\rangle$.

In addition, with the experimental apparatus, it is also feasible to study Bose polaron problems and preliminary experimental results of inverse rf spectroscopy is included in this thesis.

Some theoretical studies have been accomplished and they serve as the motivation and could be investigated in our experimental apparatus in future:

- Fermi liquid properties of a weakly-interacting two dimensional dipolar fermions.
- Stable supersolid states of two-dimensional dipolar bosons in the dilute limit.

Outlook

Current STIRAP scheme does not lead to the absolute hyperfine ground state $|X^1\Sigma, \nu = 0, J = 0\rangle \otimes |m_{Na} = 3/2, m_K = -4\rangle$, thus we have to investigate further. Properties of

the ground state molecules need to be characterized experimentally, such as lifetime, polarizability and collisional stability.

NaK ground state molecules are expected to be chemically stable at ultracold temperatures. This will allow us to perform further evaporative cooling to reach the quantum degeneracy at which quantum many body effects start to appear.

We have built a high resolution imaging system combined with a 1D optical lattice. The resolution obtained is $\simeq 0.8\mu\text{m}$ for 589nm. This high resolution imaging system will allow us to detect spatial correlation of the molecular sample. The molecular sample becomes a two-dimensional system after loading the molecule sample into the 1D optical lattice, and it will be suitable for testing theoretical proposals presented in this thesis.

We have designed and tested the in-vacuum high voltage electrodes [123]. The electric fields created by the electrodes can polarize the molecules being tilted with respect to the plane of their translational motion. It paves the way to study the anisotropy properties of dipole-dipole interaction.

Calculation of integrals for the thermodynamical quantities

A.1. Direct calculation of the first order contribution to the interaction energy

For directly calculating the first order (mean field) contribution to the interaction energy $\tilde{E}^{(1)}$ (2.74), we represent it as $\tilde{E}^{(1)} = \tilde{E}_1^{(1)} + \tilde{E}_2^{(1)}$ where

$$\tilde{E}_1^{(1)} = \int \bar{f}^{(1)} \left(\frac{|\mathbf{k}_1 - \mathbf{k}_2|}{2} \right) n_{\mathbf{k}_1} n_{\mathbf{k}_2} \frac{d^2 k_1 d^2 k_2}{(2\pi)^4}, \quad (\text{A.1})$$

$$\tilde{E}_2^{(1)} = \int \bar{f}^{(2)} \left(\frac{|\mathbf{k}_1 - \mathbf{k}_2|}{2} \right) n_{\mathbf{k}_1} n_{\mathbf{k}_2} \frac{d^2 k_1 d^2 k_2}{(2\pi)^4}, \quad (\text{A.2})$$

and the amplitudes $\bar{f}^{(1)}$ and $\bar{f}^{(2)}$ are given by Eqs. (2.79) and (2.80), respectively. In the calculation of the integrals for $\tilde{E}_1^{(1)}$ and $\tilde{E}_2^{(1)}$ we turn to the variables $\mathbf{x} = (\mathbf{k}_1 - \mathbf{k}_2)/2k_F$ and $\mathbf{y} = (\mathbf{k}_1 + \mathbf{k}_2)/2k_F$, so that $d^2 k_1 d^2 k_2 = 8\pi k_F^4 dx d^2 y d\varphi$, where φ is the angle between the vectors \mathbf{x} and \mathbf{y} , and the integration over $d\varphi$ should be performed from 0 to 2π . The distribution functions $n_{\mathbf{k}_1}$ and $n_{\mathbf{k}_2}$ are the step functions (3.5). The integration over dk_1 and dk_2 from 0 to k_F corresponds to the integration over dy from 0 to $y_0(x, \varphi) = -x|\cos \varphi| + \sqrt{1 - x^2 \sin^2 \varphi}$ and over dx from 0 to 1. Using Eq. (2.79) we reduce Eq. (A.1) to

$$\tilde{E}_1^{(1)} = \frac{S\hbar^2 k_F^4}{\pi^2 m} k_F r_* I_1, \quad (\text{A.3})$$

where

$$\begin{aligned} I_1 &= \int_0^{2\pi} d\varphi \int_0^1 x^2 dx \int_0^{y_0(x, \varphi)} y dy \\ &= \frac{1}{2} \int_0^{2\pi} d\varphi \int_0^1 x^2 dx \times [1 - 2|\cos \varphi| \sqrt{1 - x^2 \sin^2 \varphi} + x^2(\cos^2 \varphi - \sin^2 \varphi)]. \end{aligned}$$

The last term of the second line vanishes, and the integration of the first two terms over $d\varphi$ and dx gives:

$$I_1 = \int_0^1 x^2 \left(\pi - 2x\sqrt{1-x^2} - 2\arcsin x \right) dx = \frac{8}{45}.$$

Then Eq. (A.3) yields:

$$\tilde{E}_1^{(1)} = \frac{8S}{45\pi^2} \frac{\hbar^2 k_F^4}{m} k_{Fr*} = \frac{N^2}{S} \frac{128}{45} \frac{\hbar^2 k_F^2}{m} k_{Fr*}, \quad (\text{A.4})$$

which exactly coincides with the second term of the first line of Eq. (2.90).

Using Eq. (2.80) the contribution $\tilde{E}_2^{(1)}$ takes the form:

$$\tilde{E}_2^{(1)} = \frac{S\hbar^2 k_F^4}{2\pi^2 m} (k_{Fr*})^2 \left\{ \left[\ln(\xi k_{Fr*}) - \frac{25}{12} + 3 \ln 2 \right] I_2 + I_3 \right\}, \quad (\text{A.5})$$

where the integrals I_2 and I_3 are given by

$$\begin{aligned} I_2 &= \int_0^{2\pi} d\varphi \int_0^1 x^3 dx \int_0^{y_0(x,\varphi)} y dy \\ &= \frac{1}{2} \int_0^{2\pi} d\varphi \int_0^1 x^3 dx \times [1 - 2|\cos \varphi| x \sqrt{1 - x^2 \sin^2 \varphi} + x^2(\cos^2 \varphi - \sin^2 \varphi)] \\ &= \frac{1}{2} \int_0^1 x^3 [2\pi - 4x\sqrt{1-x^2} - 4\arcsin x] dx = \frac{\pi}{32}, \end{aligned}$$

and

$$\begin{aligned} I_3 &= \int_0^{2\pi} d\varphi \int_0^1 x^3 \ln x dx \int_0^{y_0(x,\varphi)} y dy \\ &= \frac{1}{2} \int_0^{2\pi} d\varphi \int_0^1 dx \times x^3 \ln x [1 - 2|\cos \varphi| x \sqrt{1 - x^2 \sin^2 \varphi} + x^2(\cos^2 \varphi - \sin^2 \varphi)] \\ &= \frac{1}{2} \int_0^1 x^3 \ln x [2\pi - 4x\sqrt{1-x^2} - 4\arcsin x] dx = \frac{\pi}{32} \left(\frac{1}{6} - \ln 2 \right). \end{aligned}$$

Substituting the calculated I_2 and I_3 into Eq. (A.5) we obtain:

$$\tilde{E}_2^{(1)} = \frac{S\hbar^2 k_F^4}{64\pi m} (k_{Fr*})^2 \left[\ln(4\xi k_{Fr*}) - \frac{23}{12} \right] = \frac{N^2}{S} \frac{\pi \hbar^2}{4m} (k_{Fr*})^2 \left[\ln(4\xi k_{Fr*}) - \frac{23}{12} \right]. \quad (\text{A.6})$$

This exactly reproduces the third term of the first line of Eq. (2.90).

A.2. Calculation of the interaction function $\tilde{F}_1^{(2)}$

The interaction function $\tilde{F}_1^{(2)}$ is the second variational derivative of the many-body contribution to the interaction energy, $\tilde{E}_1^{(2)}$ (2.82), with respect to the momentum distribution function. It can be expressed as

$$\tilde{F}_1^{(2)}(\mathbf{k}, \mathbf{k}') = -\frac{2\hbar^2}{m}(k_F r_*)^2(\tilde{I}_1 + \tilde{I}_2 + \tilde{I}_3), \quad (\text{A.7})$$

where

$$\tilde{I}_1 = 2 \int_{|\mathbf{k}_1| < k_F} \frac{d^2 k_1}{k_F^2} \frac{|\mathbf{k} - \mathbf{k}_1|^2}{\mathbf{k}^2 + \mathbf{k}'^2 - \mathbf{k}_1^2 - \mathbf{k}_2^2} \delta_{\mathbf{k} + \mathbf{k}' - \mathbf{k}_1 - \mathbf{k}_2}, \quad (\text{A.8})$$

$$\tilde{I}_2 = 2 \int_{|\mathbf{k}_1| < k_F} \frac{d^2 k_1}{k_F^2} \frac{|\mathbf{k} - \mathbf{k}'|^2}{\mathbf{k}^2 + \mathbf{k}_1^2 - \mathbf{k}'^2 - \mathbf{k}_2^2} \delta_{\mathbf{k} + \mathbf{k}_1 - \mathbf{k}' - \mathbf{k}_2}, \quad (\text{A.9})$$

$$\tilde{I}_3 = 2 \int_{|\mathbf{k}_1| < k_F} \frac{d^2 k_1}{k_F^2} \frac{|\mathbf{k}_1 - \mathbf{k}'|^2}{\mathbf{k}_1^2 + \mathbf{k}^2 - \mathbf{k}'^2 - \mathbf{k}_2^2} \delta_{\mathbf{k}_1 + \mathbf{k} - \mathbf{k}' - \mathbf{k}_2}, \quad (\text{A.10})$$

and the presence of the Kronecker symbols $\delta_{\mathbf{q}}$ reflects the momentum conservation law. On the Fermi surface we put $|\mathbf{k}| = |\mathbf{k}'| = k_F$ and denote the angle between \mathbf{k} and \mathbf{k}' as θ . Due to the symmetry property: $F(\mathbf{k}, \mathbf{k}') = F(\mathbf{k}', \mathbf{k})$ we have $F(\theta) = F(2\pi - \theta)$ and may consider θ in the interval from 0 to π .

In order to calculate the integral \tilde{I}_1 , we use the quantities $\mathbf{s} = (\mathbf{k} + \mathbf{k}')/2k_F$ and $\mathbf{m} = (\mathbf{k} - \mathbf{k}')/2k_F$ and turn to the variable $\mathbf{x} = (\mathbf{k}_1 - \mathbf{k}_2)/2k_F = (2\mathbf{k}_1 - \mathbf{s})/2k_F$. For given vectors \mathbf{k} and \mathbf{k}' , the vectors \mathbf{s} and \mathbf{m} are fixed and $|\mathbf{s}| = \cos(\theta/2)$, $|\mathbf{m}| = \sin(\theta/2)$. The integral can then be rewritten as:

$$\tilde{I}_1 = \int \frac{m^2 + x^2}{m^2 - x^2} d^2 x.$$

The integration region is shown in Fig.A.1, where the distance between the points O_1 and O_2 is $\mathbf{R}_{O_1 O_2} = \mathbf{s}$. The distance between the points O_1 and N is $\mathbf{R}_{O_1 N} = \mathbf{k}_1/2k_F$, and $\mathbf{R}_{N O_2} = \mathbf{k}_2/2k_F$, so that $\mathbf{R}_{ON} = \mathbf{x}/2$. The quantity $|\mathbf{x}|$ changes from 0 to $l_1(\varphi)$ where

$$l_1^2(\varphi) + \cos^2 \frac{\theta}{2} - 2l_1(\varphi) \cos \frac{\theta}{2} \cos \varphi = 1,$$

and $l_1(\varphi) \cdot l_1(\varphi + \pi) = \sin^2(\theta/2)$, with φ being an angle between \mathbf{m} and \mathbf{x} . In the polar coordinates the integral \tilde{I}_1 takes the form:

$$\tilde{I}_1 = \int_0^{2\pi} d\varphi \int_0^{l_1(\varphi)} \left(-1 + 2 \sin^2 \frac{\theta}{2} \frac{1}{\sin^2(\theta/2) - x^2} \right) x dx,$$

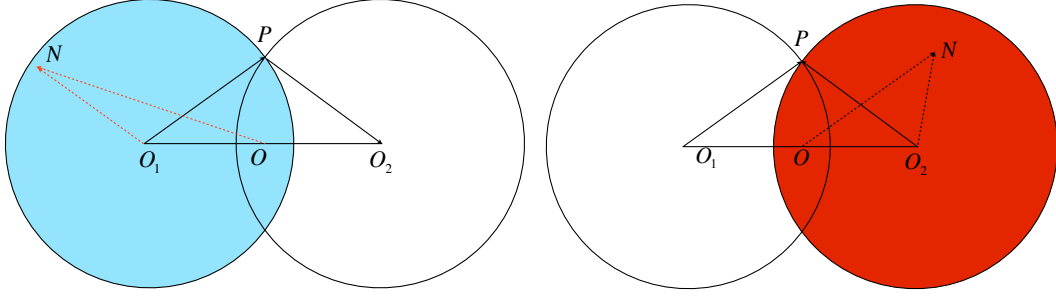


Figure A.1. – (color online). Left: The integration area for \tilde{I}_1 (in blue). The distance between the points O_1 and P is $\mathbf{R}_{O_1P} = \mathbf{k}/2k_F$, $\mathbf{R}_{PO_2} = \mathbf{k}'/2k_F$, and $\mathbf{R}_{O_1N} = \mathbf{k}_1/2k_F$. Right: The integration area for \tilde{I}_2 and \tilde{I}_3 (in red). The distance between the points O_2 and N is $\mathbf{R}_{O_2N} = \mathbf{k}_1/2k_F$, $\mathbf{R}_{O_1P} = \mathbf{k}/2k_F$, and $\mathbf{R}_{O_2P} = \mathbf{k}'/2k_F$.

and after a straightforward integration we obtain:

$$\tilde{I}_1 = \pi \left(2 \sin^2 \frac{\theta}{2} \ln \left| \tan \frac{\theta}{2} \right| - 1 \right). \quad (\text{A.11})$$

In the integral \tilde{I}_2 , using the variable $\mathbf{y} = (\mathbf{k}_1 + \mathbf{k}_2)/2k_F$ we observe that it changes from 0 to $l_2(\tilde{\varphi})$ where

$$l_2^2(\tilde{\varphi}) + \sin^2 \frac{\theta}{2} - 2l_2(\tilde{\varphi}) \sin \frac{\theta}{2} \cos(\tilde{\varphi}) = 1$$

and $l_2(\tilde{\varphi}) - l_2(\tilde{\varphi} + \pi) = 2 \sin \frac{\theta}{2} \cos \tilde{\varphi}$, with $\tilde{\varphi}$ being an angle between \mathbf{y} and \mathbf{m} . We then have:

$$\tilde{I}_2 = -2 \int \frac{m^2}{\mathbf{m} \cdot \mathbf{y}} d^2y = -2 \sin \frac{\theta}{2} \int_0^{2\pi} d\tilde{\varphi} \int_0^{l_2(\tilde{\varphi})} \frac{dy}{\cos \tilde{\varphi}} = -4\pi \sin^2 \frac{\theta}{2}. \quad (\text{A.12})$$

For the integral \tilde{I}_3 we have:

$$\begin{aligned} \tilde{I}_3 &= -\frac{1}{2} \int \frac{s^2 + y^2 - 2\mathbf{s} \cdot \mathbf{y}}{\mathbf{m} \cdot \mathbf{y}} \\ &= -\frac{1}{2 \sin \frac{\theta}{2}} \int_0^{2\pi} \frac{d\tilde{\varphi}}{\cos \tilde{\varphi}} \int_0^{l_2(\tilde{\varphi})} dy \left[y^2 + \cos^2 \frac{\theta}{2} - 2y \cos \frac{\theta}{2} \sin \tilde{\varphi} \right] \\ &= -2\pi \left(\cos^2 \frac{\theta}{2} + \frac{1}{3} \sin^2 \frac{\theta}{2} \right), \end{aligned} \quad (\text{A.13})$$

where we used the relation $l_2(\tilde{\varphi}) = l_2(-\tilde{\varphi})$.

Using integrals \tilde{I}_1 (A.11), \tilde{I}_2 (A.12), and \tilde{I}_3 (A.13) in Eq. (A.7), we obtain equation

(2.84):

$$\tilde{F}_1^{(2)}(\theta) = \frac{2\hbar^2 r_*^2 k_F^2}{m} \left[3\pi + 2\pi \sin^2 \frac{\theta}{2} \left(\frac{4}{3} - \ln \left| \tan \frac{\theta}{2} \right| \right) \right].$$

A.3. Calculation of the interaction function $\tilde{F}_2^{(2)}$

The interaction function $\tilde{F}_2^{(2)}$ is the second variational derivative of the many-body contribution to the interaction energy, $\tilde{E}_2^{(2)}$ (2.83), with respect to the momentum distribution. It reads:

$$\tilde{F}_2^{(2)}(\mathbf{k}, \mathbf{k}') = \frac{2\hbar^2}{m} (k_F r_*)^2 (I'_1 + I'_2), \quad (\text{A.14})$$

where

$$I'_1 = 2 \int_{|\mathbf{k}_1| < k_F} \frac{d^2 k_1}{k_F^2} \frac{|\mathbf{k} - \mathbf{k}_1| \cdot |\mathbf{k}' - \mathbf{k}_1|}{\mathbf{k}^2 + \mathbf{k}'^2 - \mathbf{k}_1^2 - \mathbf{k}_2^2} \delta_{\mathbf{k} + \mathbf{k}' - \mathbf{k}_1 - \mathbf{k}_2}, \quad (\text{A.15})$$

$$I'_2 = 4 \int_{|\mathbf{k}_1| < k_F} \frac{d^2 k_1}{k_F^2} \frac{|\mathbf{k} - \mathbf{k}'| \cdot |\mathbf{k}_1 - \mathbf{k}'|}{\mathbf{k}^2 + \mathbf{k}_1^2 - \mathbf{k}'^2 - \mathbf{k}_2^2} \delta_{\mathbf{k} + \mathbf{k}_1 - \mathbf{k}' - \mathbf{k}_2} \quad (\text{A.16})$$

The integration area for I'_1 is shown in Fig. A.2, where the distance between the points O_1 and P is $\mathbf{R}_{O_1 P} = \mathbf{k}/2k_F$, $\mathbf{R}_{P O_2} = \mathbf{k}'/2k_F$, $\mathbf{R}_{O_1 N} = \mathbf{k}_1/2k_F$, and $\mathbf{R}_{O N} = \mathbf{x}/2$. We thus have $\mathbf{R}_{NP} = (\mathbf{k} - \mathbf{k}_1)/2k_F$ and $\mathbf{R}_{NP'} = (\mathbf{k}' - \mathbf{k}_1)/2k_F$. In the region of integration we should have $|\mathbf{R}_{O_1 N}| = k_1/2k_F \leq 1/2$. This leads to

$$I'_1 = 4 \int \frac{|\mathbf{R}_{NP}| \cdot |\mathbf{R}_{NP'}|}{m^2 - x^2} d^2 n = - \int_0^{2\pi} d\varphi \int_0^{l_3(\varphi)} x dx \times \frac{\sqrt{[x^2 + \sin^2(\theta/2)]^2 - 4x^2 \sin^2(\theta/2) \cos^2 \varphi}}{x^2 - \sin^2(\theta/2)}, \quad (\text{A.17})$$

where φ is the angle between \mathbf{x} and \mathbf{m} (see Fig. A.2), and the quantity $l_3(\varphi)$ obeys the equation

$$l_3^2(\varphi) - 2 \cos \frac{\theta}{2} \sin \varphi \cdot l_3(\varphi) + \cos^2 \frac{\theta}{2} = 1.$$

Turning to the variable $z = r^2 - \sin^2(\theta/2)$ the integral I'_1 is reduced to

$$I'_1 = -\frac{1}{2} \int_0^{2\pi} d\varphi \int_{-\sin^2(\theta/2)}^{l_3^2(\varphi) - \sin^2(\theta/2)} \frac{\sqrt{R}}{z} dz, \quad (\text{A.18})$$

with

$$R = z^2 + 4z \sin^2 \frac{\theta}{2} \sin^2 \varphi + 4 \sin^4 \frac{\theta}{2} \sin^2 \varphi.$$

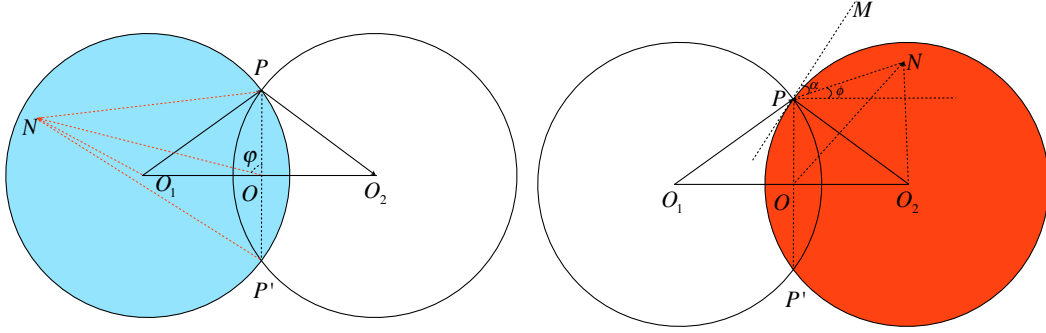


Figure A.2. – (color online). Left: The integration area for I'_1 (in blue): $\mathbf{R}_{O_1P} = \mathbf{k}/2k_F$, $\mathbf{R}_{PO_2} = \mathbf{k}'/2k_F$, $\mathbf{R}_{O_1N} = \mathbf{k}_1/2k_F$, and φ is the angle between the vectors \mathbf{R}_{OP} and \mathbf{R}_{ON} , which is the same as the angle between \mathbf{m} and \mathbf{x} . Right: The integration area for I'_2 (in red): $\mathbf{R}_{O_1P} = \mathbf{k}/2k_F$, $\mathbf{R}_{O_2P} = \mathbf{k}'/2k_F$, $\mathbf{R}_{O_2N} = \mathbf{k}_1/2k_F$, α is the angle between \mathbf{R}_{PM} and \mathbf{R}_{PN} , and ϕ is the angle between \mathbf{R}_{PN} and \mathbf{R}_{OO_2} .

It is easy to see that:

$$\begin{aligned}
 I_r &= \int_{-\sin^2(\theta/2)}^{l_3^2(\varphi) - \sin^2(\theta/2)} \frac{\sqrt{R}}{z} dz \\
 &= \left\{ \sqrt{R} - \sqrt{a} \ln \left(2a + bz + 2\sqrt{aR} \right) + \frac{b}{2} \ln \left(2\sqrt{R} + 2z + b \right) \right\} \Big|_{-\sin^2(\theta/2)}^{l_3^2(\varphi) - \sin^2(\theta/2)} \\
 &+ \sqrt{a} \cdot P \int_{-\sin^2(\theta/2)}^{l_3^2(\varphi) - \sin^2(\theta/2)} \frac{dz}{z} = I_{r\uparrow} - I_{r\downarrow},
 \end{aligned}$$

where $a = 4 \sin^4(\theta/2) \sin^2 \varphi$, $b = 4 \sin^2(\theta/2) \sin^2 \varphi$, and the symbol P stands for the principal value of the integral. The quantities $I_{r\uparrow}$ and $I_{r\downarrow}$ denote the values of the integral at the upper and lower bounds, respectively (in the last line we have to take the principal value of the integral and, hence, if the upper bound of the integral is positive we have to replace the lower bound with $\sin^2(\theta/2)$). Then $I_{r\uparrow}$ and $I_{r\downarrow}$ are given by:

$$\begin{aligned}
 I_{r\uparrow} &= 2 |\sin \varphi| \cdot l(\varphi) - 2 \sin^2 \frac{\theta}{2} |\sin \varphi| \cdot \ln \left(8 \sin^2 \frac{\theta}{2} \sin^2 \varphi \right) \\
 &- 2 \sin^2 \frac{\theta}{2} |\sin \varphi| \cdot \ln \left(\sin^2 \frac{\theta}{2} + \cos \frac{\theta}{2} \sin \varphi \cdot l(\varphi) + l(\varphi) \right) + 2 \sin^2 \frac{\theta}{2} |\sin \varphi| \cdot \ln |2 \cos \frac{\theta}{2} \sin \varphi \cdot l(\varphi)| \\
 &+ 2 \sin^2 \frac{\theta}{2} \sin^2 \varphi \left[\ln 4 + \ln \left(|\sin \varphi| \cdot l(\varphi) + \cos \frac{\theta}{2} \sin \varphi \cdot l(\varphi) + \sin^2 \frac{\theta}{2} \sin^2 \varphi \right) \right], \\
 I_{r\downarrow} &= \sin^2 \frac{\theta}{2} - 2 \sin^2 \frac{\theta}{2} |\sin \varphi| \cdot \left[\ln \left(4 \sin^4 \frac{\theta}{2} \right) + \ln (\sin^2 \varphi + |\sin \varphi|) \right] \\
 &+ 2 \sin^2 \frac{\theta}{2} |\sin \varphi| \cdot \ln \left(\sin^2 \frac{\theta}{2} \right) + 2 \sin^2 \frac{\theta}{2} \sin^2 \varphi \cdot \ln \left(4 \sin^2 \frac{\theta}{2} \sin^2 \varphi \right).
 \end{aligned}$$

The integral I'_1 can be expressed as:

$$I'_1 = -\frac{1}{2} \int_0^{2\pi} [I_{r\uparrow} - I_{r\downarrow}] d\varphi,$$

and for performing the calculations we notice that $l_3(\varphi) \cdot l_3(\varphi + \pi) = \sin^2 \frac{\theta}{2}$, $l_3(\varphi) - l_3(\varphi + \pi) = 2 \cos \frac{\theta}{2} \sin \varphi$, and $l_3(\varphi) + l_3(\varphi + \pi) = 2 \sqrt{\cos^2 \frac{\theta}{2} \sin^2 \varphi + \sin^2 \frac{\theta}{2}}$. We then obtain:

$$\begin{aligned} I'_1 = & -\sin^2 \frac{\theta}{2} \left(\pi \ln 2 + \pi/2 - \pi \ln \sin \frac{\theta}{2} + 4 \ln |\cos \frac{\theta}{2}| - 4 \ln(1 + \sin \frac{\theta}{2}) + \mathcal{G}(\theta) \right) \\ & + \sin^2 \frac{\theta}{2} \left(\frac{2\pi}{|\cos \frac{\theta}{2}|} + \frac{4 \arcsin(\sin \frac{\theta}{2})}{|\cos \frac{\theta}{2}|} \right) - \frac{k_F^2}{|\cos \frac{\theta}{2}|} \left(\pi - 2 \arcsin(\sin \frac{\theta}{2}) + |\sin \theta| \right), \end{aligned} \quad (\text{A.19})$$

with

$$\mathcal{G}(\theta) = \int_0^\pi 2 \sin^2 \varphi \ln \left(\sin \varphi + \sqrt{\sin^2 \frac{\theta}{2} + \cos^2 \frac{\theta}{2} \sin^2 \varphi} \right) d\varphi. \quad (\text{A.20})$$

The integration area for I'_2 is shown in Fig. A.2, and we get:

$$I'_2 = -4 \int \frac{|\mathbf{m}| \cdot |\mathbf{R}_{PN}|}{\mathbf{m} \cdot \mathbf{y}} d^2 y = -8 \int \frac{d^2 \rho}{\cos \phi}, \quad (\text{A.21})$$

where we denote $\mathbf{R}_{PN} = \boldsymbol{\rho}$, and $\phi = \alpha - \theta/2$ is the angle between the vectors \mathbf{m} and $\boldsymbol{\rho}$, with α being the angle between the vectors \mathbf{R}_{PM} and \mathbf{R}_{PN} (see Fig. A.2). We then have:

$$\begin{aligned} I'_2 = & -8 \int_0^\pi d\alpha \int_0^{\sin \alpha} \frac{\rho d\rho}{\cos(\alpha - \theta/2)} \\ = & -4 \left[\cos^2 \frac{\theta}{2} \ln \frac{1 + \sin(\theta/2)}{1 - \sin(\theta/2)} + 2 \sin \frac{\theta}{2} \right]. \end{aligned} \quad (\text{A.22})$$

Using I'_1 (A.19) and I'_2 (A.22) in Eq. (A.14) we get equation (2.85) for the interaction function $\tilde{F}_2^{(2)}(\theta)$.

Calculation of the integral for the relaxation rate of quasiparticles

It is convenient to represent Eq.(3.52) in the form:

$$\sin(\phi_2 - \phi_1 - \tilde{\phi}) = \frac{pp_1[1 - \cos(\phi_1 - \phi)] - (p_2p_1 + pp_2)}{\sqrt{[p_2p_1 + pp_2 \cos(\phi_1 - \phi)]^2 + p^2p_2^2 \sin^2(\phi_1 - \phi)}}, \quad (\text{B.1})$$

where

$$\begin{aligned} \sin \tilde{\phi} &= \frac{p_2p_1 + pp_2 \cos(\phi_1 - \phi)}{\sqrt{[p_2p_1 + pp_2 \cos(\phi_1 - \phi)]^2 + p^2p_2^2 \sin^2(\phi_1 - \phi)}}; \\ \cos \tilde{\phi} &= \frac{pp_2 \sin(\phi_1 - \phi)}{\sqrt{[p_2p_1 + pp_2 \cos(\phi_1 - \phi)]^2 + p^2p_2^2 \sin^2(\phi_1 - \phi)}}. \end{aligned}$$

For the derivative $dp_3/d\phi_2$ we have:

$$\begin{aligned} \left| \frac{dp_3}{d\phi_2} \right| &= \frac{\sqrt{[p_2p_1 + pp_2 \cos(\phi_1 - \phi)]^2 + p^2p_2^2 \sin^2(\phi_1 - \phi)}}{p_3} |\cos(\phi_2 - \phi_1 - \tilde{\phi})| \\ &= 2p_F \left| \sin\left(\frac{\phi_1 - \phi}{2}\right) \right| \sqrt{\cos^2\left(\frac{\phi_1 - \phi}{2}\right) + (q - q_2)(q_2 - q_1)/p_F^2}. \end{aligned}$$

In the Fourier transforms $U(\mathbf{p} - \mathbf{p}_2)$ and $U(\mathbf{p}_1 - \mathbf{p}_2)$ we may put $|\mathbf{p}| = |\mathbf{p}_1| = |\mathbf{p}_2| = p_F$. Then equation (3.52) gives either $\phi_2 = \phi_1$ or $\phi_2 = \phi$. In both cases, using Eq.(3.11) we obtain:

$$\begin{aligned} &U(\mathbf{p} - \mathbf{p}_2) - U(\mathbf{p}_1 - \mathbf{p}_2) \\ &= \pm 4\pi d^2 p_F \left| \sin\left(\frac{\phi_1 - \phi}{2}\right) \right| \left\{ \cos^2 \theta_0 - \sin^2 \theta_0 \sin^2\left(\frac{\phi_1 + \phi}{2}\right) \right\}. \quad (\text{B.2}) \end{aligned}$$

Integrating over ϕ_2 in Eq.(3.51) we then have:

$$\int_0^{2\pi} d\phi_1 \int_0^{2\pi} d\phi_2 [U(\mathbf{p} - \mathbf{p}_2) - U(\mathbf{p}_1 - \mathbf{p}_2)]^2 \delta(\epsilon(\mathbf{p}) + \epsilon(\mathbf{p}_1) - \epsilon(\mathbf{p}_2) - \epsilon(\mathbf{p}_3)) \delta_{\mathbf{p}+\mathbf{p}_1, \mathbf{p}_2+\mathbf{p}_3} = \frac{16\pi^2 m d^4}{\hbar^2} I(q_1, q_2), \quad (\text{B.3})$$

where the quantity $I(q_1, q_2)$ also depends on q , θ_0 , ϕ and is given by

$$I(q_1, q_2) = \int_0^{2\pi} d\phi_1 \frac{\left| \sin\left(\frac{\phi_1 - \phi}{2}\right) \right| \left[\cos^2 \theta_0 - \sin^2 \theta_0 \sin^2\left(\frac{\phi_1 + \phi}{2}\right) \right]^2}{\sqrt{\cos^2\left(\frac{\phi_1 - \phi}{2}\right) + (q - q_2)(q_2 - q_1)/p_F^2}}. \quad (\text{B.4})$$

Formally, when integrating over ϕ_1 one should put a constraint $\cos^2[(\phi_1 - \phi)/2] \geq (q_2 - q)(q_2 - q_1)/p_F^2$ in order to satisfy the inequality $\sin^2(\phi_2 - \phi_1 - \tilde{\phi}) \leq 1$. However, at $T = 0$ the created particles are above the Fermi surface, so that $q_2 > 0$ and $q_3 = q + q_1 - q_2 > 0$. The annihilated particle is below the Fermi surface and, hence, $q_1 < 0$. We thus have $q > q_2$ and $q_2 > q_1$, and the inequality $\cos^2[(\phi_1 - \phi)/2] \geq (q_2 - q)(q_2 - q_1)/p_F^2$ is satisfied for any ϕ_1 . Putting $n(\mathbf{p}_1) = 1$, $n(\mathbf{p}_2) = n(\mathbf{p}_3) = 0$ in Eq.(3.51) and writing $p_i dp_i = p_F dq_i$ we set the following limits of integration over q_1 and q_2 :

$$-q \leq q_1 \leq 0; \quad (\text{B.5})$$

$$0 \leq q_2 \leq q + q_1. \quad (\text{B.6})$$

Equations (B.3) and (B.4) describe the contributions which correspond to ϕ_2 close to ϕ_1 or to ϕ . Another contribution comes from ϕ_1 close to $\phi + \pi$. In this case we may put $\phi_1 = \phi + \pi$ in the Fourier transform $U(\mathbf{p}_1 - \mathbf{p}_2)$, which gives:

$$|U(\mathbf{p} - \mathbf{p}_2) - U(\mathbf{p}_1 - \mathbf{p}_2)| = 4\pi d^2 p_F \left[\left| \sin\left(\frac{\phi_1 - \phi}{2}\right) \right| \left\{ \cos^2 \theta_0 - \sin^2 \theta_0 \sin^2\left(\frac{\phi_1 + \phi}{2}\right) \right\} - \left| \cos\left(\frac{\phi_1 - \phi}{2}\right) \right| \left\{ \cos^2 \theta_0 - \sin^2 \theta_0 \cos^2\left(\frac{\phi_1 + \phi}{2}\right) \right\} \right]. \quad (\text{B.7})$$

Performing similar calculations as above we obtain Eq.(B.3) in which the function

$I(q_1, q_2)$ is replaced with $\tilde{I}(q_1, q_2)$ given by ¹:

$$\begin{aligned} \tilde{I}(q_1, q_2) = & \int_0^{2\pi} d\phi_2 \left\{ \frac{\left| \sin\left(\frac{\phi_2 - \phi}{2}\right) \right| \left[\cos^2 \theta_0 - \sin^2 \theta_0 \sin^2\left(\frac{\phi_2 + \phi}{2}\right) \right]^2}{2\sqrt{\cos^2\left(\frac{\phi_2 - \phi}{2}\right) - 2(q_2 - q_1)/p_F}} \right. \\ & - \left[\cos^2 \theta_0 - \sin^2 \theta_0 \sin^2\left(\frac{\phi_2 + \phi}{2}\right) \right] \times \left[\cos^2 \theta_0 - \sin^2 \theta_0 \cos^2\left(\frac{\phi_2 + \phi}{2}\right) \right] \\ & \left. + \frac{2 \left| \sin\left(\frac{\phi_2 - \phi}{2}\right) \right| \left| \cos\left(\frac{\phi_2 - \phi}{2}\right) \right|}{4 \sin^2\left(\frac{\phi_2 - \phi}{2}\right) + (q - q_2)^2/p_F^2} \left[\cos^2 \theta_0 - \sin^2 \theta_0 \cos^2\left(\frac{\phi_2 + \phi}{2}\right) \right]^2 \right\}, \end{aligned} \quad (\text{B.8})$$

where we keep only leading powers of q, q_1, q_2 . Note that when integrating the first term in the curly brackets we have a constraint that the argument of the square root in the denominator is positive.

With both contributions taken into account, equation (3.51) reduces to

$$\frac{1}{\tau} = \frac{2\hbar}{\pi m} (p_F r_*)^2 \int_{-q}^0 dq_1 \int_0^{q_1+q} dq_2 (I(q_1, q_2) + \tilde{I}(q_1, q_2)). \quad (\text{B.9})$$

The integrals (B.4) and (B.8) take the forms

$$\begin{aligned} I(q_1, q_2) &= 4 \int_0^1 \frac{dx}{\sqrt{x^2 + (q - q_2)(q_2 - q_1)/p_F^2}} \{ (\cos^2 \theta_0 - \sin^2 \theta_0 \cos^2 \phi)^2 \\ &+ \sin^4 \theta_0 [x^4 (\sin^4 \phi + \cos^4 \phi - 6 \sin^2 \phi \cos^2 \phi) + x^2 (6 \cos^2 \phi \sin^2 \phi - 2 \cos^4 \phi)] \\ &+ 2x^2 \sin^2 \theta_0 \cos^2 \theta_0 (2 \cos^2 \phi - 1) \} \\ &= 2(\cos^2 \theta_0 - \sin^2 \theta_0 \cos^2 \phi)^2 \ln \left(\frac{4p_F^2}{(q - q_2)(q_2 - q_1)} \right) + 4\mathcal{F}(\theta_0, \phi); \end{aligned} \quad (\text{B.10})$$

¹Strictly speaking, for ϕ_1 close to $\phi + \pi$ we have to use the relation $\epsilon(\mathbf{p}_i) = \hbar^2 p_i^2 / 2m$ for the quasiparticle energy. Regarding all the rest, the calculations are similar to those for the case where ϕ_2 is close to ϕ or to ϕ_1 .

$$\begin{aligned}
 \tilde{I}(q_1, q_2) &= 2 \int_0^1 dx \left[\frac{1}{\sqrt{x^2 + 2(q_2 - q_1)/p_F}} + \frac{4x}{4x^2 + (q - q_2)^2/p_F^2} \right] \\
 &\times \left\{ (\cos^2 \theta_0 - \sin^2 \theta_0 \cos^2 \phi)^2 + 2x^2 \sin^2 \theta_0 \cos^2 \theta_0 (2 \cos^2 \phi - 1) \right. \\
 &+ \sin^4 \theta_0 [x^4 (\sin^4 \phi + \cos^4 \phi - 6 \sin^2 \phi \cos^2 \phi) + x^2 (6 \cos^2 \phi \sin^2 \phi - 2 \cos^4 \phi)] \left. \right\} \\
 &- 2\pi \left(\cos^4 \theta_0 - \cos^2 \theta_0 \sin^2 \theta_0 + \frac{1}{8} \sin^4 \theta_0 \right) \\
 &= (\cos^2 \theta_0 - \sin^2 \theta_0 \cos^2 \phi)^2 \ln \left(\frac{8p_F^3}{(q - q_2)^2(q_2 - q_1)} \right) + 4\tilde{\mathcal{F}}(\theta_0, \phi), \quad (\text{B.11})
 \end{aligned}$$

where we omitted higher powers of q , q_1 , and q_2 and introduced the functions:

$$\begin{aligned}
 \mathcal{F}(\theta_0, \phi) &= \sin^2 \theta_0 \cos^2 \theta_0 (2 \cos^2 \phi - 1) + \sin^4 \theta_0 \left(\frac{1}{4} + \cos^2 \phi - 2 \cos^4 \phi \right), \\
 \tilde{\mathcal{F}}(\theta_0, \phi) &= \mathcal{F}(\theta_0, \phi) - \frac{\pi}{2} \left(\cos^4 \theta_0 - \cos^2 \theta_0 \sin^2 \theta_0 + \frac{1}{8} \sin^4 \theta_0 \right).
 \end{aligned}$$

Substituting the results of Eqs. (B.10) and (B.11) into equation (B.9) and integrating over q_1 and q_2 we obtain:

$$\frac{1}{\tau} = \frac{4\hbar}{\pi m} (p_F r_*)^2 q^2 \left\{ \left(\frac{3}{4} \ln \frac{p_F^2}{q^2} + \frac{3}{4} + \frac{3}{2} \ln 2 \right) (\cos^2 \theta_0 - \sin^2 \theta_0 \cos^2 \phi)^2 + \mathcal{F}(\theta_0, \phi) + \tilde{\mathcal{F}}(\theta_0, \phi) \right\}.$$

Bibliography

- [1] M. H. Anderson, J. R. Ensher, M. R. Matthews, C. E. Wieman, and E. A. Cornell. “Observation of Bose-Einstein Condensation in a Dilute Atomic Vapor”. In: *Science* 269.5221 (1995), pp. 198–201 (cit. on p. 1).
- [2] K. B. Davis, M. -O. Mewes, M. R. Andrews, N. J. van Druten, D. S. Durfee, D. M. Kurn, and W. Ketterle. “Bose-Einstein Condensation in a Gas of Sodium Atoms”. In: *Phys. Rev. Lett.* 75 (22 Nov. 1995), pp. 3969–3973 (cit. on p. 1).
- [3] Immanuel Bloch, Jean Dalibard, and Wilhelm Zwerger. “Many-body physics with ultracold gases”. In: *Rev. Mod. Phys.* 80 (3 July 2008), pp. 885–964 (cit. on pp. 1, 95, 111).
- [4] I. M. Georgescu, S. Ashhab, and Franco Nori. “Quantum simulation”. In: *Rev. Mod. Phys.* 86 (1 Mar. 2014), pp. 153–185 (cit. on p. 1).
- [5] Markus Greiner, Olaf Mandel, Tilman Esslinger, Theodor W. Haensch, and Immanuel Bloch. “Quantum phase transition from a superfluid to a Mott insulator in a gas of ultracold atoms”. In: *Nature* 415 (2002), pp. 39–40 (cit. on p. 1).
- [6] K. W. Madison, F. Chevy, W. Wohlleben, and J. Dalibard. “Vortex Formation in a Stirred Bose-Einstein Condensate”. In: *Phys. Rev. Lett.* 84 (5 Jan. 2000), pp. 806–809 (cit. on p. 1).
- [7] M. W. Zwierlein, J. R. Abo-Shaer, A. Schirotzek, C. H. Schunck, and W. Ketterle. “Vortices and superfluidity in a strongly interacting Fermi gas”. In: *Nature* 435 (June 2005), pp. 1047–1051 (cit. on pp. 1, 95).
- [8] T. Bourdel, L. Khaykovich, J. Cubizolles, J. Zhang, F. Chevy, M. Teichmann, L. Tarruell, S. J. J. M. F. Kokkelmans, and C. Salomon. “Experimental Study of the BEC-BCS Crossover Region in Lithium 6”. In: *Phys. Rev. Lett.* 93 (5 July 2004), p. 050401 (cit. on pp. 1, 95).
- [9] M. Bartenstein, A. Altmeyer, S. Riedl, S. Jochim, C. Chin, J. Hecker Denschlag, and R. Grimm. “Collective Excitations of a Degenerate Gas at the BEC-BCS Crossover”. In: *Phys. Rev. Lett.* 92 (20 May 2004), p. 203201 (cit. on pp. 1, 95).
- [10] Cheng Chin, Rudolf Grimm, Paul Julienne, and Eite Tiesinga. “Feshbach resonances in ultracold gases”. In: *Rev. Mod. Phys.* 82 (2 Apr. 2010), pp. 1225–1286 (cit. on pp. 1, 79, 95, 104, 111, 119).

- [11] Bloch Immanuel. *Ecole de Physique des Houches: Many-Body Physics with Ultracold Gases*. Oxford University Press, 2010 (cit. on p. 1).
- [12] J. Hubbard. “Electron Correlations in Narrow Energy Bands”. In: *Proceedings of the Royal Society of London A: Mathematical, Physical and Engineering Sciences* 276.1365 (1963), pp. 238–257 (cit. on p. 1).
- [13] D. Jaksch, C. Bruder, J. I. Cirac, C. W. Gardiner, and P. Zoller. “Cold Bosonic Atoms in Optical Lattices”. In: *Phys. Rev. Lett.* 81 (15 Oct. 1998), pp. 3108–3111 (cit. on p. 1).
- [14] D. Jaksch and P. Zoller. “The cold atom Hubbard toolbox”. In: *Annals of Physics* 315.1 (2005). Special Issue, pp. 52–79 (cit. on p. 1).
- [15] L.D. Landau and E.M. Lifshitz. “Quantum Mechanics, Non-Relativistic Theory”. In: *Butterworth-Heinemann, Oxford* (1999) (cit. on pp. 1, 10, 15, 18, 22).
- [16] Baxter. R. J. *Exactly solved models in statistical mechanics*. Academic Press, 1982 (cit. on p. 1).
- [17] David S. Betts and JH Jefferson. “LT-19 Derivation of the t-J model for high temperature superconductivity”. In: *Physica B: Condensed Matter* 165 (1990), pp. 1013–1014 (cit. on p. 1).
- [18] M. Saffman, T. G. Walker, and K. Mølmer. “Quantum information with Rydberg atoms”. In: *Rev. Mod. Phys.* 82 (3 Aug. 2010), pp. 2313–2363 (cit. on p. 1).
- [19] Mingwu Lu, Nathaniel Q. Burdick, Seo Ho Youn, and Benjamin L. Lev. “Strongly Dipolar Bose-Einstein Condensate of Dysprosium”. In: *Phys. Rev. Lett.* 107 (19 Oct. 2011), p. 190401 (cit. on pp. 1, 37, 59).
- [20] K. Aikawa, A. Frisch, M. Mark, S. Baier, A. Rietzler, R. Grimm, and F. Ferlaino. “Bose-Einstein Condensation of Erbium”. In: *Phys. Rev. Lett.* 108 (21 May 2012), p. 210401 (cit. on pp. 1, 37, 59).
- [21] M.A. Baranov. “Theoretical progress in many-body physics with ultracold dipolar gases”. In: *Physics Reports* 464.3 (2008), pp. 71–111 (cit. on pp. 2, 37, 59).
- [22] Alexey V. Gorshkov, Salvatore R. Manmana, Gang Chen, Jun Ye, Eugene Demler, Mikhail D. Lukin, and Ana Maria Rey. “Tunable Superfluidity and Quantum Magnetism with Ultracold Polar Molecules”. In: *Phys. Rev. Lett.* 107 (11 Sept. 2011), p. 115301 (cit. on p. 2).
- [23] J. Levinsen, N. R. Cooper, and G. V. Shlyapnikov. “Topological $p_x + ip_y$ superfluid phase of fermionic polar molecules”. In: *Phys. Rev. A* 84 (1 July 2011), p. 013603 (cit. on pp. 2, 7, 8, 10, 12, 38).

- [24] Andrew C. Potter, Erez Berg, Daw-Wei Wang, Bertrand I. Halperin, and Eugene Demler. “Superfluidity and Dimerization in a Multilayered System of Fermionic Polar Molecules”. In: *Phys. Rev. Lett.* 105 (22 Nov. 2010), p. 220406 (cit. on p. 2).
- [25] N. Y. Yao, C. R. Laumann, A. V. Gorshkov, S. D. Bennett, E. Demler, P. Zoller, and M. D. Lukin. “Topological Flat Bands from Dipolar Spin Systems”. In: *Phys. Rev. Lett.* 109 (26 Dec. 2012), p. 266804 (cit. on p. 2).
- [26] Lincoln D Carr, David DeMille, Roman V Krems, and Jun Ye. “Cold and ultracold molecules: science, technology and applications”. In: *New Journal of Physics* 11.5 (2009), p. 055049 (cit. on pp. 2, 7, 37, 59).
- [27] D. DeMille. “Quantum Computation with Trapped Polar Molecules”. In: *Phys. Rev. Lett.* 88 (6 Jan. 2002), p. 067901 (cit. on p. 2).
- [28] M. Ortner, Y. L. Zhou, P. Rabl, and P. Zoller. “Quantum information processing in self-assembled crystals of cold polar molecules”. In: *Quantum Information Processing* 10.6 (2011), pp. 793–819 (cit. on p. 2).
- [29] K.-K. Ni, S. Ospelkaus, M. H. G. de Miranda, A. Pe’er, B. Neyenhuis, J. J. Zirbel, S. Kotochigova, P. S. Julienne, D. S. Jin, and J. Ye. “A High Phase-Space-Density Gas of Polar Molecules”. In: *Science* 322.5899 (2008), pp. 231–235 (cit. on pp. 2, 7, 37, 59, 83).
- [30] K.-K. Ni, S. Ospelkaus, D. Wang, G. Quéméner, B. Neyenhuis, M. H. G. de Miranda, J. L. Bohn, J. Ye, and D. S. Jin. “Dipolar collisions of polar molecules in the quantum regime”. In: *Nature* 464 (2010), pp. 1327–1328 (cit. on pp. 2, 7, 37, 59).
- [31] M. H. G. de Miranda, A. Chotia, B. Neyenhuis, D. Wang, G. Quéméner, S. Ospelkaus, J. L. Bohn, J. Ye, and D. S. Jin. “Controlling the quantum stereodynamics of ultracold bimolecular reactions”. In: *Nature Physics* 7 (2011), pp. 502–507 (cit. on pp. 2, 8, 38, 59).
- [32] Piotr S. Żuchowski and Jeremy M. Hutson. “Reactions of ultracold alkali-metal dimers”. In: *Phys. Rev. A* 81 (6 June 2010), p. 060703 (cit. on pp. 2, 8, 37).
- [33] N. Navon, S. Nascimbène, F. Chevy, and C. Salomon. “The Equation of State of a Low-Temperature Fermi Gas with Tunable Interactions”. In: *Science* 328.5979 (2010), pp. 729–732 (cit. on pp. 2, 8, 34).
- [34] S. Nascimbène, N. Navon, K. J. Jiang, F. Chevy, and C. Salomon. “Exploring the thermodynamics of a universal Fermi gas”. In: *Nature* 463 (2010), pp. 1057–1060 (cit. on pp. 2, 8, 34).
- [35] J. Deiglmayr, A. Grochola, M. Repp, K. Mörtlbauer, C. Glück, J. Lange, O. Dulieu, R. Wester, and M. Weidemüller. “Formation of Ultracold Polar Molecules in the Rovibrational Ground State”. In: *Phys. Rev. Lett.* 101 (13 Sept. 2008), p. 133004 (cit. on p. 7).

- [36] K. Aikawa, D. Akamatsu, M. Hayashi, K. Oasa, J. Kobayashi, P. Naidon, T. Kishimoto, M. Ueda, and S. Inouye. “Coherent Transfer of Photoassociated Molecules into the Rovibrational Ground State”. In: *Phys. Rev. Lett.* 105 (20 Nov. 2010), p. 203001 (cit. on p. 7).
- [37] Markus Debatin, Tetsu Takekoshi, Raffael Rameshan, Lukas Reichsollner, Francesca Ferlaino, Rudolf Grimm, Romain Vexiau, Nadia Bouloufa, Olivier Dulieu, and Hanns-Christoph Nagerl. “Molecular spectroscopy for ground-state transfer of ultracold RbCs molecules”. In: *Phys. Chem. Chem. Phys.* 13 (42 2011), pp. 18926–18935 (cit. on pp. 7, 8).
- [38] T Lahaye, C Menotti, L Santos, M Lewenstein, and T Pfau. “The physics of dipolar bosonic quantum gases”. In: *Reports on Progress in Physics* 72.12 (2009), p. 126401 (cit. on pp. 7, 37).
- [39] B. Friedrich R.V. Krems and W.C. Stwalley. “Cold Molecules: Theory, Experiment, Applications”. In: *CRC Press, Taylor & Francis Group* (2009) (cit. on pp. 7, 37).
- [40] Daw-Wei Wang, Mikhail D. Lukin, and Eugene Demler. “Quantum Fluids of Self-Assembled Chains of Polar Molecules”. In: *Phys. Rev. Lett.* 97 (18 Nov. 2006), p. 180413 (cit. on p. 7).
- [41] H. P. Büchler, E. Demler, M. Lukin, A. Micheli, N. Prokof’ev, G. Pupillo, and P. Zoller. “Strongly Correlated 2D Quantum Phases with Cold Polar Molecules: Controlling the Shape of the Interaction Potential”. In: *Phys. Rev. Lett.* 98 (6 Feb. 2007), p. 060404 (cit. on pp. 7, 59).
- [42] G. M. Bruun and E. Taylor. “Quantum Phases of a Two-Dimensional Dipolar Fermi Gas”. In: *Phys. Rev. Lett.* 101 (24 Dec. 2008), p. 245301 (cit. on pp. 7, 8, 38).
- [43] N. R. Cooper and G. V. Shlyapnikov. “Stable Topological Superfluid Phase of Ultracold Polar Fermionic Molecules”. In: *Phys. Rev. Lett.* 103 (15 Oct. 2009), p. 155302 (cit. on pp. 7, 8, 38).
- [44] A. Pikovski, M. Klawunn, G. V. Shlyapnikov, and L. Santos. “Interlayer Superfluidity in Bilayer Systems of Fermionic Polar Molecules”. In: *Phys. Rev. Lett.* 105 (21 Nov. 2010), p. 215302 (cit. on pp. 7, 8, 38).
- [45] Roman M. Lutchyn, Enrico Rossi, and S. Das Sarma. “Spontaneous interlayer superfluidity in bilayer systems of cold polar molecules”. In: *Phys. Rev. A* 82 (6 Dec. 2010), p. 061604 (cit. on p. 7).
- [46] Andrew C. Potter, Erez Berg, Daw-Wei Wang, Bertrand I. Halperin, and Eugene Demler. “Superfluidity and Dimerization in a Multilayered System of Fermionic Polar Molecules”. In: *Phys. Rev. Lett.* 105 (22 Nov. 2010), p. 220406 (cit. on pp. 7, 8, 38).

- [47] B. Capogrosso-Sansone, C. Trefzger, M. Lewenstein, P. Zoller, and G. Pupillo. “Quantum Phases of Cold Polar Molecules in 2D Optical Lattices”. In: *Phys. Rev. Lett.* 104 (12 Mar. 2010), p. 125301 (cit. on p. 7).
- [48] Kai Sun, Congjun Wu, and S. Das Sarma. “Spontaneous inhomogeneous phases in ultracold dipolar Fermi gases”. In: *Phys. Rev. B* 82 (7 Aug. 2010), p. 075105 (cit. on pp. 7, 8, 38).
- [49] Yasuhiro Yamaguchi, Takaaki Sogo, Toru Ito, and Takahiko Miyakawa. “Density-wave instability in a two-dimensional dipolar Fermi gas”. In: *Phys. Rev. A* 82 (1 July 2010), p. 013643 (cit. on pp. 7, 8, 38).
- [50] M. A. Baranov, A. Micheli, S. Ronen, and P. Zoller. “Bilayer superfluidity of fermionic polar molecules: Many-body effects”. In: *Phys. Rev. A* 83 (4 Apr. 2011), p. 043602 (cit. on pp. 7, 8, 38).
- [51] N.T. Zinner and G.M. Bruun. “Density waves in layered systems with fermionic polar molecules”. In: *Eur. Phys. J. D* 65 (133 Sept. 2011), pp. 133–139 (cit. on p. 7).
- [52] M. M. Parish and F. M. Marchetti. “Density Instabilities in a Two-Dimensional Dipolar Fermi Gas”. In: *Phys. Rev. Lett.* 108 (14 Apr. 2012), p. 145304 (cit. on pp. 7, 8, 38).
- [53] Mehrtash Babadi and Eugene Demler. “Density ordering instabilities of quasi-two-dimensional fermionic polar molecules in single-layer and multilayer configurations: Exact treatment of exchange interactions”. In: *Phys. Rev. B* 84 (23 Dec. 2011), p. 235124 (cit. on pp. 7, 8, 38).
- [54] L. M. Sieberer and M. A. Baranov. “Collective modes, stability, and superfluid transition of a quasi-two-dimensional dipolar Fermi gas”. In: *Phys. Rev. A* 84 (6 Dec. 2011), p. 063633 (cit. on pp. 7, 8, 33, 34, 36, 38, 40–42, 48).
- [55] M. Abad, A. Recati, and S. Stringari. “Quadrupole oscillation in a dipolar Fermi gas: Hydrodynamic versus collisionless regime”. In: *Phys. Rev. A* 85 (3 Mar. 2012), p. 033639 (cit. on p. 7).
- [56] S. Ospelkaus, K.-K. Ni, D. Wang, M. H. G. de Miranda, B. Neyenhuis, G. Quéméner, P. S. Julienne, J. L. Bohn, D. S. Jin, and J. Ye. “Quantum-State Controlled Chemical Reactions of Ultracold Potassium-Rubidium Molecules”. In: *Science* 327.5967 (2010), pp. 853–857 (cit. on pp. 7, 37, 59).
- [57] Goulven Quéméner and John L. Bohn. “Electric field suppression of ultracold confined chemical reactions”. In: *Phys. Rev. A* 81 (6 June 2010), p. 060701 (cit. on pp. 8, 38, 59).
- [58] Andrea Micheli, Zbigniew Idziaszek, Guido Pupillo, Mikhail A. Baranov, Peter Zoller, and Paul S. Julienne. “Universal Rates for Reactive Ultracold Polar Molecules in Reduced Dimensions”. In: *Phys. Rev. Lett.* 105 (7 Aug. 2010), p. 073202 (cit. on pp. 8, 38, 59).

- [59] Jee Woo Park, Cheng-Hsun Wu, Ibon Santiago, Tobias G. Tiecke, Sebastian Will, Peyman Ahmadi, and Martin W. Zwierlein. “Quantum degenerate Bose-Fermi mixture of chemically different atomic species with widely tunable interactions”. In: *Phys. Rev. A* 85 (5 May 2012), p. 051602 (cit. on pp. 8, 59, 108, 119).
- [60] N. T. Zinner, B. Wunsch, D. Pekker, and D.-W. Wang. “BCS-BEC crossover in bilayers of cold fermionic polar molecules”. In: *Phys. Rev. A* 85 (1 Jan. 2012), p. 013603 (cit. on pp. 8, 38).
- [61] J. P. Kestner and S. Das Sarma. “Compressibility, zero sound, and effective mass of a fermionic dipolar gas at finite temperature”. In: *Phys. Rev. A* 82 (3 Sept. 2010), p. 033608 (cit. on p. 8).
- [62] Ching-Kit Chan, Congjun Wu, Wei-Cheng Lee, and S. Das Sarma. “Anisotropic-Fermi-liquid theory of ultracold fermionic polar molecules: Landau parameters and collective modes”. In: *Phys. Rev. A* 81 (2 Feb. 2010), p. 023602 (cit. on p. 8).
- [63] Takahiko Miyakawa, Takaaki Sogo, and Han Pu. “Phase-space deformation of a trapped dipolar Fermi gas”. In: *Phys. Rev. A* 77 (6 June 2008), p. 061603 (cit. on p. 8).
- [64] Qiuzi Li, E. H. Hwang, and S. Das Sarma. “Collective modes of monolayer, bilayer, and multilayer fermionic dipolar liquid”. In: *Phys. Rev. B* 82 (23 Dec. 2010), p. 235126 (cit. on p. 8).
- [65] Kerson Huang and C. N. Yang. “Quantum-Mechanical Many-Body Problem with Hard-Sphere Interaction”. In: *Phys. Rev.* 105 (3 Feb. 1957), pp. 767–775 (cit. on pp. 8, 20, 41).
- [66] T. D. Lee and C. N. Yang. “Many-Body Problem in Quantum Mechanics and Quantum Statistical Mechanics”. In: *Phys. Rev.* 105 (3 Feb. 1957), pp. 1119–1120 (cit. on pp. 8, 20, 41).
- [67] A. A. Abrikosov and I. M. Khalatnikov. “Concerning a Model for a Non-Ideal Fermi Gas”. In: *Sov. Phys. JETP* 6 (5 1958), p. 888 (cit. on pp. 8, 9, 20, 41).
- [68] E.M. Lifshitz and L.P. Pitaevskii. “Statistical Physics, Part 2”. In: *Pergamon Press, Oxford* (1980) (cit. on pp. 8, 18–20, 24, 28, 29, 33, 34, 38, 49, 52, 64).
- [69] Mark J. H. Ku, Ariel T. Sommer, Lawrence W. Cheuk, and Martin W. Zwierlein. “Revealing the Superfluid Lambda Transition in the Universal Thermodynamics of a Unitary Fermi Gas”. In: *Science* 335.6068 (2012), pp. 563–567 (cit. on p. 34).
- [70] Tarik Yefsah, Rémi Desbuquois, Lauriane Chomaz, Kenneth J. Günter, and Jean Dalibard. “Exploring the Thermodynamics of a Two-Dimensional Bose Gas”. In: *Phys. Rev. Lett.* 107 (13 Sept. 2011), p. 130401 (cit. on p. 34).

- [71] D. Wang, B. Neyenhuis, M. H. G. de Miranda, K.-K. Ni, S. Ospelkaus, D. S. Jin, and J. Ye. “Direct absorption imaging of ultracold polar molecules”. In: *Phys. Rev. A* 81 (6 June 2010), p. 061404 (cit. on p. 34).
- [72] Axel Griesmaier, Jörg Werner, Sven Hensler, Jürgen Stuhler, and Tilman Pfau. “Bose-Einstein Condensation of Chromium”. In: *Phys. Rev. Lett.* 94 (16 Apr. 2005), p. 160401 (cit. on p. 37).
- [73] J K Block, N T Zinner, and G M Bruun. “Density wave instabilities of tilted fermionic dipoles in a multilayer geometry”. In: *New Journal of Physics* 14.10 (2012), p. 105006 (cit. on p. 38).
- [74] Zhen-Kai Lu and G. V. Shlyapnikov. “Fermi liquid of two-dimensional polar molecules”. In: *Phys. Rev. A* 85 (2 Feb. 2012), p. 023614 (cit. on pp. 38, 41–44, 48).
- [75] N. Matveeva and S. Giorgini. “Liquid and Crystal Phases of Dipolar Fermions in Two Dimensions”. In: *Phys. Rev. Lett.* 109 (20 Nov. 2012), p. 200401 (cit. on p. 38).
- [76] D. Pines and P. Nosieres. “The Theory of Quantum Liquids”. In: *W.A. Benjamin, INC, New York, Amsterdam* (1966) (cit. on pp. 38, 45).
- [77] A. A. Abrikosov and I. M. Khalatnikov. In: *Sov. Phys. Uspekhi* 1 (1958), p. 68 (cit. on pp. 38, 52).
- [78] Enrico Vogt, Michael Feld, Bernd Fröhlich, Daniel Pertot, Marco Koschorreck, and Michael Köhl. “Scale Invariance and Viscosity of a Two-Dimensional Fermi Gas”. In: *Phys. Rev. Lett.* 108 (7 Feb. 2012), p. 070404 (cit. on p. 39).
- [79] Alexander L. Gaunt, Tobias F. Schmidutz, Igor Gotlibovych, Robert P. Smith, and Zoran Hadzibabic. “Bose-Einstein Condensation of Atoms in a Uniform Potential”. In: *Phys. Rev. Lett.* 110 (20 May 2013), p. 200406 (cit. on pp. 39, 57).
- [80] W. R. Abel, A. C. Anderson, and J. C. Wheatley. “Propagation of Zero Sound in Liquid He³ at Low Temperatures”. In: *Phys. Rev. Lett.* 17 (2 July 1966), pp. 74–78 (cit. on p. 39).
- [81] J. Stenger, S. Inouye, A. P. Chikkatur, D. M. Stamper-Kurn, D. E. Pritchard, and W. Ketterle. “Bragg Spectroscopy of a Bose-Einstein Condensate”. In: *Phys. Rev. Lett.* 82 (23 June 1999), pp. 4569–4573 (cit. on p. 39).
- [82] D. M. Stamper-Kurn, A. P. Chikkatur, A. Görlitz, S. Inouye, S. Gupta, D. E. Pritchard, and W. Ketterle. “Excitation of Phonons in a Bose-Einstein Condensate by Light Scattering”. In: *Phys. Rev. Lett.* 83 (15 Oct. 1999), pp. 2876–2879 (cit. on p. 39).
- [83] G. Veeravalli, E. Kuhnle, P. Dyke, and C. J. Vale. “Bragg Spectroscopy of a Strongly Interacting Fermi Gas”. In: *Phys. Rev. Lett.* 101 (25 Dec. 2008), p. 250403 (cit. on p. 39).

- [84] L. D. Landau. In: *Sov. Phys. JETP* 3 (1956), p. 920 (cit. on p. 41).
- [85] L. D. Landau. In: *Sov. Phys. JETP* 5 (1957), p. 101 (cit. on p. 52).
- [86] G. M. Eliashberg. In: *Sov. Phys. JETP* 15 (1962), p. 1151 (cit. on p. 52).
- [87] C. J. Pethick. “Attenuation of Zero Sound in a Normal Fermi Liquid”. In: *Phys. Rev.* 185 (1 Sept. 1969), pp. 384–392 (cit. on pp. 52, 55).
- [88] E.M. Lifshitz and L.P. Pitaevskii. “Physical Kinetics”. In: *Butterworth Heinemann, Oxford* (1999) (cit. on pp. 53, 55).
- [89] M. R. Andrews, D. M. Kurn, H.-J. Miesner, D. S. Durfee, C. G. Townsend, S. Inouye, and W. Ketterle. “Propagation of Sound in a Bose-Einstein Condensate”. In: *Phys. Rev. Lett.* 79 (4 July 1997), pp. 553–556 (cit. on p. 57).
- [90] J. Joseph, B. Clancy, L. Luo, J. Kinast, A. Turlapov, and J. E. Thomas. “Measurement of Sound Velocity in a Fermi Gas near a Feshbach Resonance”. In: *Phys. Rev. Lett.* 98 (17 Apr. 2007), p. 170401 (cit. on p. 57).
- [91] Meng Khoon Tey, Leonid A. Sidorenkov, Edmundo R. Sánchez Guajardo, Rudolf Grimm, Mark J. H. Ku, Martin W. Zwierlein, Yan-Hua Hou, Lev Pitaevskii, and Sandro Stringari. “Collective Modes in a Unitary Fermi Gas across the Superfluid Phase Transition”. In: *Phys. Rev. Lett.* 110 (5 Jan. 2013), p. 055303 (cit. on p. 57).
- [92] L. Sidorenkov, M. Tey, R. Grimm, Y. Hou, L. Pitaevskii, and S. Stringari. “Second sound and the superfluid fraction in a Fermi gas with resonant interactions”. In: *Nature* 498 (2013), pp. 78–81 (cit. on p. 57).
- [93] Ryan M. Wilson, Christopher Ticknor, John L. Bohn, and Eddy Timmermans. “Roton immiscibility in a two-component dipolar Bose gas”. In: *Phys. Rev. A* 86 (3 Sept. 2012), p. 033606 (cit. on p. 59).
- [94] Sarang Gopalakrishnan, Ivar Martin, and Eugene A. Demler. “Quantum Quasicrystals of Spin-Orbit-Coupled Dipolar Bosons”. In: *Phys. Rev. Lett.* 111 (18 Oct. 2013), p. 185304 (cit. on p. 59).
- [95] Jee Woo Park, Sebastian A. Will, and Martin W. Zwierlein. “Ultracold Dipolar Gas of Fermionic $^{23}\text{Na}^{40}\text{K}$ Molecules in Their Absolute Ground State”. In: *Phys. Rev. Lett.* 114 (20 May 2015), p. 205302 (cit. on pp. 59, 83, 86, 91).
- [96] Tetsu Takekoshi, Lukas Reichsöllner, Andreas Schindewolf, Jeremy M. Hutson, C. Ruth Le Sueur, Olivier Dulieu, Francesca Ferlaino, Rudolf Grimm, and Hanns-Christoph Nägerl. “Ultracold Dense Samples of Dipolar RbCs Molecules in the Rovibrational and Hyperfine Ground State”. In: *Phys. Rev. Lett.* 113 (20 Nov. 2014), p. 205301 (cit. on pp. 59, 83).
- [97] Peter K. Molony, Philip D. Gregory, Zhonghua Ji, Bo Lu, Michael P. Köppinger, C. Ruth Le Sueur, Caroline L. Blackley, Jeremy M. Hutson, and Simon L. Cornish. “Creation of Ultracold $^{87}\text{Rb}^{133}\text{Cs}$ Molecules in the Rovibrational Ground State”. In: *Phys. Rev. Lett.* 113 (25 Dec. 2014), p. 255301 (cit. on pp. 59, 83).

- [98] Eugene P. Gross. “Unified Theory of Interacting Bosons”. In: *Phys. Rev.* 106 (1 Apr. 1957), pp. 161–162 (cit. on pp. 59, 61).
- [99] D. A. Kirzhnits and Yu. A. Nepomnyashchii. “Supersolid”. In: *Sov. Phys. JETP* 32 (Apr. 1971), p. 1911 (cit. on pp. 59, 61, 64).
- [100] Massimo Boninsegni and Nikolay V. Prokof’ev. “Colloquium : Supersolids: What and where are they?” In: *Rev. Mod. Phys.* 84 (2 May 2012), pp. 759–776 (cit. on pp. 59, 67).
- [101] S. Balibar. “The enigma of supersolidity”. In: *Nature* 464 (Mar. 2010), pp. 176–182 (cit. on p. 59).
- [102] Yves Pomeau and Sergio Rica. “Dynamics of a model of supersolid”. In: *Phys. Rev. Lett.* 72 (15 Apr. 1994), pp. 2426–2429 (cit. on pp. 59, 61).
- [103] N. Henkel, R. Nath, and T. Pohl. “Three-Dimensional Roton Excitations and Supersolid Formation in Rydberg-Excited Bose-Einstein Condensates”. In: *Phys. Rev. Lett.* 104 (19 May 2010), p. 195302 (cit. on p. 59).
- [104] F. Cinti, P. Jain, M. Boninsegni, A. Micheli, P. Zoller, and G. Pupillo. “Supersolid Droplet Crystal in a Dipole-Blockaded Gas”. In: *Phys. Rev. Lett.* 105 (13 Sept. 2010), p. 135301 (cit. on p. 59).
- [105] S. Saccani, S. Moroni, and M. Boninsegni. “Phase diagram of soft-core bosons in two dimensions”. In: *Phys. Rev. B* 83 (9 Mar. 2011), p. 092506 (cit. on p. 59).
- [106] I. L. Kurbakov, Yu. E. Lozovik, G. E. Astrakharchik, and J. Boronat. “Quasiequilibrium supersolid phase of a two-dimensional dipolar crystal”. In: *Phys. Rev. B* 82 (1 July 2010), p. 014508 (cit. on p. 59).
- [107] G. E. Astrakharchik, J. Boronat, I. L. Kurbakov, and Yu. E. Lozovik. “Quantum Phase Transition in a Two-Dimensional System of Dipoles”. In: *Phys. Rev. Lett.* 98 (6 Feb. 2007), p. 060405 (cit. on p. 59).
- [108] L. Santos, G. V. Shlyapnikov, and M. Lewenstein. “Roton-Maxon Spectrum and Stability of Trapped Dipolar Bose-Einstein Condensates”. In: *Phys. Rev. Lett.* 90 (25 June 2003), p. 250403 (cit. on p. 60).
- [109] S. Komineas and N. R. Cooper. “Vortex lattices in Bose-Einstein condensates with dipolar interactions beyond the weak-interaction limit”. In: *Phys. Rev. A* 75 (2 Feb. 2007), p. 023623 (cit. on p. 60).
- [110] Hans-Werner Hammer, Andreas Nogga, and Achim Schwenk. “Colloquium : Three-body forces: From cold atoms to nuclei”. In: *Rev. Mod. Phys.* 85 (1 Jan. 2013), pp. 197–217 (cit. on p. 60).
- [111] D. S. Petrov. “Three-Body Interacting Bosons in Free Space”. In: *Phys. Rev. Lett.* 112 (10 Mar. 2014), p. 103201 (cit. on p. 60).
- [112] Abdelâali Boudjemâa and G. V. Shlyapnikov. “Two-dimensional dipolar Bose gas with the roton-maxon excitation spectrum”. In: *Phys. Rev. A* 87 (2 Feb. 2013), p. 025601 (cit. on p. 60).

- [113] L.P. Pitaevskii. “Supersolid1”. In: *JETP Lett.* 39 (Apr. 1984), p. 511 (cit. on p. 61).
- [114] P. Nozières. “Is the Roton in Superfluid 4He the Ghost of a Bragg Spot?” In: *Journal of Low Temperature Physics* 137.1 (), pp. 45–67 (cit. on p. 61).
- [115] P. Nozières. “More about Rotons in Superfluid Helium 4”. In: *Journal of Low Temperature Physics* 142.1 (), pp. 91–99 (cit. on p. 61).
- [116] P. Nozières. “Superfluidity, Crystallization and Localization”. In: *Journal of Low Temperature Physics* 156.1 (2009), pp. 9–21 (cit. on p. 61).
- [117] K. Binder. “Theory of first-order phase transitions”. In: *Reports on Progress in Physics* 50.7 (1987), p. 783 (cit. on p. 64).
- [118] Aurel Bulgac. “Dilute Quantum Droplets”. In: *Phys. Rev. Lett.* 89 (5 July 2002), p. 050402 (cit. on p. 65).
- [119] Boris Spivak and Steven A. Kivelson. “Phases intermediate between a two-dimensional electron liquid and Wigner crystal”. In: *Phys. Rev. B* 70 (15 Oct. 2004), p. 155114 (cit. on p. 67).
- [120] Saverio Moroni and Massimo Boninsegni. “Coexistence, Interfacial Energy, and the Fate of Microemulsions of 2D Dipolar Bosons”. In: *Phys. Rev. Lett.* 113 (24 Dec. 2014), p. 240407 (cit. on p. 67).
- [121] K. Góral and L. Santos. “Ground state and elementary excitations of single and binary Bose-Einstein condensates of trapped dipolar gases”. In: *Phys. Rev. A* 66 (2 Aug. 2002), p. 023613 (cit. on p. 69).
- [122] Dan M. Stamper-Kurn and Masahito Ueda. “Spinor Bose gases: Symmetries, magnetism, and quantum dynamics”. In: *Rev. Mod. Phys.* 85 (3 July 2013), pp. 1191–1244 (cit. on p. 70).
- [123] N. W. Buchheim. “Molecular spectroscopy for ground state transfer of ultracold NaK molecules”. PhD thesis. Ludwig-Maximilians-Universität München, 2015 (cit. on pp. 4, 71–80, 82–92, 95, 119, 120, 128).
- [124] W. Ketterle, D.S. Durfee, and D.M. Stamper-Kurn. “Making, probing and understanding Bose-Einstein condensates”. In: (1999), pp. 67–176 (cit. on p. 73).
- [125] Wolfgang Ketterle and Martin W. Zwierlein. “Making, probing and understanding ultracold Fermi gases”. In: (2008), pp. 247–422 (cit. on p. 73).
- [126] Z. Hadzibabic, C. A. Stan, K. Dieckmann, S. Gupta, M. W. Zwierlein, A. Görlitz, and W. Ketterle. “Two-Species Mixture of Quantum Degenerate Bose and Fermi Gases”. In: *Phys. Rev. Lett.* 88 (16 Apr. 2002), p. 160401 (cit. on pp. 73, 111).
- [127] G. Roati, F. Riboli, G. Modugno, and M. Inguscio. “Fermi-Bose Quantum Degenerate ^{40}K - ^{87}Rb Mixture with Attractive Interaction”. In: *Phys. Rev. Lett.* 89 (15 Sept. 2002), p. 150403 (cit. on pp. 73, 111).

- [128] Cheng-Hsun Wu, Jee Woo Park, Peyman Ahmadi, Sebastian Will, and Martin W. Zwierlein. “Ultracold Fermionic Feshbach Molecules of $^{23}\text{Na}^{40}\text{K}$ ”. In: *Phys. Rev. Lett.* 109 (8 Aug. 2012), p. 085301 (cit. on pp. 73, 78, 82, 106, 108, 119).
- [129] William D. Phillips and Harold Metcalf. “Laser Deceleration of an Atomic Beam”. In: *Phys. Rev. Lett.* 48 (9 Mar. 1982), pp. 596–599 (cit. on p. 74).
- [130] T. W. Hänsch, I. S. Shahin, and A. L. Schawlow. “High-Resolution Saturation Spectroscopy of the Sodium *D* Lines with a Pulsed Tunable Dye Laser”. In: *Phys. Rev. Lett.* 27 (11 Sept. 1971), pp. 707–710 (cit. on p. 74).
- [131] K. Dieckmann, R. J. C. Spreeuw, M. Weidemüller, and J. T. M. Walraven. “Two-dimensional magneto-optical trap as a source of slow atoms”. In: *Phys. Rev. A* 58 (5 Nov. 1998), pp. 3891–3895 (cit. on p. 74).
- [132] D. M. Brink and C. V. Sukumar. “Majorana spin-flip transitions in a magnetic trap”. In: *Phys. Rev. A* 74 (3 Sept. 2006), p. 035401 (cit. on p. 76).
- [133] P. O. Fedichev, M. W. Reynolds, and G. V. Shlyapnikov. “Three-Body Recombination of Ultracold Atoms to a Weakly Bound *s* Level”. In: *Phys. Rev. Lett.* 77 (14 Sept. 1996), pp. 2921–2924 (cit. on pp. 76, 112).
- [134] Rudolf Grimm, Matthias Weidemüller, and Yurii B. Ovchinnikov. “Optical Dipole Traps for Neutral Atoms”. In: ed. by Benjamin Bederson and Herbert Walther. Vol. 42. *Advances In Atomic, Molecular, and Optical Physics*. Academic Press, 2000, pp. 95–170 (cit. on p. 76).
- [135] Cheng-Hsun Wu, Ibon Santiago, Jee Woo Park, Peyman Ahmadi, and Martin W. Zwierlein. “Strongly interacting isotopic Bose-Fermi mixture immersed in a Fermi sea”. In: *Phys. Rev. A* 84 (1 July 2011), p. 011601 (cit. on pp. 77–79, 111).
- [136] T. L. Gustavson, A. P. Chikkatur, A. E. Leanhardt, A. Görlitz, S. Gupta, D. E. Pritchard, and W. Ketterle. “Transport of Bose-Einstein Condensates with Optical Tweezers”. In: *Phys. Rev. Lett.* 88 (2 Dec. 2001), p. 020401 (cit. on p. 77).
- [137] J.T.M Walraven. *Elements of Quantum Gases: Thermodynamic and Collisional Properties of Trapped Atomic Gases*. 2010 (cit. on p. 77).
- [138] Tetsu Takekoshi, Markus Debatin, Raffael Rameshan, Francesca Ferlaino, Rudolf Grimm, Hanns-Christoph Nägerl, C. Ruth Le Sueur, Jeremy M. Hutson, Paul S. Julienne, Svetlana Kotochigova, and Eberhard Tiemann. “Towards the production of ultracold ground-state RbCs molecules: Feshbach resonances, weakly bound states, and the coupled-channel model”. In: *Phys. Rev. A* 85 (3 Mar. 2012), p. 032506 (cit. on p. 78).
- [139] C. Weber, G. Barontini, J. Catani, G. Thalhammer, M. Inguscio, and F. Minardi. “Association of ultracold double-species bosonic molecules”. In: *Phys. Rev. A* 78 (6 Dec. 2008), p. 061601 (cit. on p. 78).

- [140] Fudong Wang, Xiaodong He, Xiaoke Li, Bing Zhu, Jun Chen, and Dajun Wang. “Formation of ultracold NaRb Feshbach molecules”. In: *New Journal of Physics* 17.3 (2015), p. 035003 (cit. on pp. 78, 111).
- [141] C. Ospelkaus, S. Ospelkaus, L. Humbert, P. Ernst, K. Sengstock, and K. Bongs. “Ultracold Heteronuclear Molecules in a 3D Optical Lattice”. In: *Phys. Rev. Lett.* 97 (12 Sept. 2006), p. 120402 (cit. on p. 78).
- [142] Myoung-Sun Heo, Tout T. Wang, Caleb A. Christensen, Timur M. Rvachov, Dylan A. Cotta, Jae-Hoon Choi, Ye-Ryoung Lee, and Wolfgang Ketterle. “Formation of ultracold fermionic NaLi Feshbach molecules”. In: *Phys. Rev. A* 86 (2 Aug. 2012), p. 021602 (cit. on p. 78).
- [143] A.-C. Voigt, M. Taglieber, L. Costa, T. Aoki, W. Wieser, T. W. Hänsch, and K. Dieckmann. “Ultracold Heteronuclear Fermi-Fermi Molecules”. In: *Phys. Rev. Lett.* 102 (2 Jan. 2009), p. 020405 (cit. on p. 78).
- [144] Francesca Ferlaino, Steven Knoop, and Rudolf Grimm. “Ultracold Feshbach molecules”. In: *Cold Molecules: Theory, Experiment, Applications*. Ed. by R. Krems, B. Friedrich, and W.C. Stwalley. CRC Press, 2009, pp. 319–354 (cit. on p. 78).
- [145] Thorsten Köhler, Krzysztof Góral, and Paul S. Julienne. “Production of cold molecules via magnetically tunable Feshbach resonances”. In: *Rev. Mod. Phys.* 78 (4 Dec. 2006), pp. 1311–1361 (cit. on pp. 78, 95, 96, 111).
- [146] J. J. Zirbel, K.-K. Ni, S. Ospelkaus, T. L. Nicholson, M. L. Olsen, P. S. Julienne, C. E. Wieman, J. Ye, and D. S. Jin. “Heteronuclear molecules in an optical dipole trap”. In: *Phys. Rev. A* 78 (1 July 2008), p. 013416 (cit. on pp. 78, 83).
- [147] C. Klempt, T. Henninger, O. Topic, M. Scherer, L. Kattner, E. Tiemann, W. Ertmer, and J. J. Arlt. “Radio-frequency association of heteronuclear Feshbach molecules”. In: *Phys. Rev. A* 78 (6 Dec. 2008), p. 061602 (cit. on p. 78).
- [148] Q. Beaufils, A. Crubellier, T. Zanon, B. Laburthe-Tolra, É. Maréchal, L. Vernac, and O. Gorceix. “Radio-frequency association of molecules: an assisted Feshbach resonance”. In: *The European Physical Journal D* 56.1 (2009), pp. 99–104 (cit. on p. 78).
- [149] J. J. Zirbel, K.-K. Ni, S. Ospelkaus, J. P. D’Incao, C. E. Wieman, J. Ye, and D. S. Jin. “Collisional Stability of Fermionic Feshbach Molecules”. In: *Phys. Rev. Lett.* 100 (14 Apr. 2008), p. 143201 (cit. on pp. 82, 83, 112).
- [150] Klaas Bergmann, Nikolay V. Vitanov, and Bruce W. Shore. “Perspective: Stimulated Raman adiabatic passage: The status after 25 years”. In: *The Journal of Chemical Physics* 142.17, 170901 (2015) (cit. on p. 83).
- [151] Bruce W. Shore. *The Theory Of Coherent Atomic Excitation*. 1990 (cit. on pp. 83, 84).

- [152] Michael Fleischhauer, Atac Imamoglu, and Jonathan P. Marangos. “Electromagnetically induced transparency: Optics in coherent media”. In: *Rev. Mod. Phys.* 77 (2 July 2005), pp. 633–673 (cit. on pp. 83, 90).
- [153] K. Bergmann, H. Theuer, and B. W. Shore. “Coherent population transfer among quantum states of atoms and molecules”. In: *Rev. Mod. Phys.* 70 (3 July 1998), pp. 1003–1025 (cit. on pp. 83, 85).
- [154] Jee Woo Park, Sebastian A Will, and Martin W Zwierlein. “Two-photon pathway to ultracold ground state molecules of $^{23}\text{Na } ^{40}\text{K}$ ”. In: *New Journal of Physics* 17.7 (2015), p. 075016 (cit. on pp. 86, 91).
- [155] Nadia Bouloufa, Romain Vexieu, and Olivier Dulieu. *Private communication* (cit. on p. 88).
- [156] Kevin M. Jones, Eite Tiesinga, Paul D. Lett, and Paul S. Julienne. “Ultracold photoassociation spectroscopy: Long-range molecules and atomic scattering”. In: *Rev. Mod. Phys.* 78 (2 May 2006), pp. 483–535 (cit. on p. 86).
- [157] Gerhard Herzberg. *Molecular Spectra and Molecular Structure. Volume 1 - Spectra of Diatomic Molecules*. 1950 (cit. on p. 88).
- [158] Diana Amaro. “A Raman Laser System for Groundstate transfer of NaK”. Master thesis. Universidade de Coimbra, 2013 (cit. on p. 89).
- [159] R. W. P. Drever, J. L. Hall, F. V. Kowalski, J. Hough, G. M. Ford, A. J. Munley, and H. Ward. “Laser phase and frequency stabilization using an optical resonator”. In: *Applied Physics B* 31.2 (), pp. 97–105 (cit. on p. 89).
- [160] Eric D. Black. “An introduction to Pound-Drever-Hall laser frequency stabilization”. In: *American Journal of Physics* 69.1 (2001), pp. 79–87 (cit. on p. 89).
- [161] Frauke Seeßelberg. “A Dye Laser System for NaK Photoassociation Spectroscopy”. Master thesis. Ludwig-Maximilians-Universität München, 2013 (cit. on pp. 86, 90).
- [162] B. W. Shore, J. Martin, M. P. Fewell, and K. Bergmann. “Coherent population transfer in multilevel systems with magnetic sublevels. I. Numerical studies”. In: *Phys. Rev. A* 52 (1 July 1995), pp. 566–582 (cit. on p. 92).
- [163] J. Martin, B. W. Shore, and K. Bergmann. “Coherent population transfer in multilevel systems with magnetic sublevels. II. Algebraic analysis”. In: *Phys. Rev. A* 52 (1 July 1995), pp. 583–593 (cit. on p. 92).
- [164] J. Martin, B. W. Shore, and K. Bergmann. “Coherent population transfer in multilevel systems with magnetic sublevels. III. Experimental results”. In: *Phys. Rev. A* 54 (2 Aug. 1996), pp. 1556–1569 (cit. on p. 92).
- [165] R. Jördens, N. Strohmaier, K. Günter, H. Moritz, and T. Esslinger. “A Mott insulator of fermionic atoms in an optical lattice”. In: *Nature* 455 (July 2008), pp. 204–207 (cit. on p. 95).

- [166] T. G. Tiecke, M. R. Goosen, J. T. M. Walraven, and S. J. J. M. F. Kokkelmans. “Asymptotic-bound-state model for Feshbach resonances”. In: *Phys. Rev. A* 82 (4 Oct. 2010), p. 042712 (cit. on pp. 95, 96, 100).
- [167] B. Marcelis, E. G. M. van Kempen, B. J. Verhaar, and S. J. J. M. F. Kokkelmans. “Feshbach resonances with large background scattering length: Interplay with open-channel resonances”. In: *Phys. Rev. A* 70 (1 July 2004), p. 012701 (cit. on p. 105).
- [168] A. Gerdes, M. Hobein, H. Knöckel, and E. Tiemann. “Ground state potentials of the NaK molecule”. In: *The European Physical Journal D* 49.1 (2008), pp. 67–73 (cit. on pp. 98, 106).
- [169] S. I. Pekar. In: *Zh. Eksp. Teor. Fiz.* 16.1 (1946), p. 341 (cit. on p. 111).
- [170] L.D. Landau and S. I. Pekar. In: *Zh. Eksp. Teor. Fiz.* 18.1 (1948), p. 419 (cit. on p. 111).
- [171] M. Girardeau. “Motion of an Impurity Particle in a Boson Superfluid”. In: *Physics of Fluids* 4.3 (1961), pp. 279–291 (cit. on p. 111).
- [172] A. S. Alexandrov and J. T. Devreese. “Advances in Polaron Physics”. In: *Springer Series in Solid-State Sciences* 159 (2009) (cit. on p. 111).
- [173] Elbio Dagotto. “Correlated electrons in high-temperature superconductors”. In: *Rev. Mod. Phys.* 66 (3 July 1994), pp. 763–840 (cit. on p. 111).
- [174] J. Catani, L. De Sarlo, G. Barontini, F. Minardi, and M. Inguscio. “Degenerate Bose-Bose mixture in a three-dimensional optical lattice”. In: *Phys. Rev. A* 77 (1 Jan. 2008), p. 011603 (cit. on p. 111).
- [175] G. Thalhammer, G. Barontini, L. De Sarlo, J. Catani, F. Minardi, and M. Inguscio. “Double Species Bose-Einstein Condensate with Tunable Interspecies Interactions”. In: *Phys. Rev. Lett.* 100 (21 May 2008), p. 210402 (cit. on p. 111).
- [176] M. Taglieber, A.-C. Voigt, T. Aoki, T. W. Hänsch, and K. Dieckmann. “Quantum Degenerate Two-Species Fermi-Fermi Mixture Coexisting with a Bose-Einstein Condensate”. In: *Phys. Rev. Lett.* 100 (1 Jan. 2008), p. 010401 (cit. on p. 111).
- [177] Fabian Grusdt and Eugene Demler. “New theoretical approaches to Bose polarons”. In: *arXiv:1510.04934* (2015) (cit. on pp. 111, 112).
- [178] C. Kohstall, M. Zaccanti, A. Jag M. and Trenkwalder, P. Massignan, G. M. Bruun, F. Schreck, and R. Grimm. “Metastability and Coherence of Repulsive Polarons in a Strongly Interacting Fermi Mixture”. In: *Nature* 485 (May 2012), pp. 615–618 (cit. on pp. 111, 112).
- [179] Marko Cetina, Michael Jag, Rianne S. Lous, Jook T. M. Walraven, Rudolf Grimm, Rasmus S. Christensen, and Georg M. Bruun. “Decoherence of Impurities in a Fermi Sea of Ultracold Atoms”. In: *Phys. Rev. Lett.* 115 (13 Sept. 2015), p. 135302 (cit. on pp. 111, 112).

- [180] J. P. D’Incao and B. D. Esry. “Scattering Length Scaling Laws for Ultracold Three-Body Collisions”. In: *Phys. Rev. Lett.* 94 (21 June 2005), p. 213201 (cit. on p. 112).
- [181] Aditya Shashi, Fabian Grusdt, Dmitry A. Abanin, and Eugene Demler. “Radio-frequency spectroscopy of polarons in ultracold Bose gases”. In: *Phys. Rev. A* 89 (5 May 2014), p. 053617 (cit. on pp. 112, 114, 117).
- [182] Steffen Patrick Rath and Richard Schmidt. “Field-theoretical study of the Bose polaron”. In: *Phys. Rev. A* 88 (5 Nov. 2013), p. 053632 (cit. on pp. 112, 114–116, 121, 124).
- [183] Weiran Li and S. Das Sarma. “Variational study of polarons in Bose-Einstein condensates”. In: *Phys. Rev. A* 90 (1 July 2014), p. 013618 (cit. on p. 112).
- [184] Shina Tan. “Energetics of a strongly correlated Fermi gas”. In: *Annals of Physics* 323.12 (2008), pp. 2952–2970 (cit. on p. 117).
- [185] Shina Tan. “Large momentum part of a strongly correlated Fermi gas”. In: *Annals of Physics* 323.12 (2008), pp. 2971–2986 (cit. on p. 117).
- [186] Shina Tan. “Generalized virial theorem and pressure relation for a strongly correlated Fermi gas”. In: *Annals of Physics* 323.12 (2008), pp. 2987–2990 (cit. on p. 117).
- [187] R. J. Wild, P. Makotyn, J. M. Pino, E. A. Cornell, and D. S. Jin. “Measurements of Tan’s Contact in an Atomic Bose-Einstein Condensate”. In: *Phys. Rev. Lett.* 108 (14 Apr. 2012), p. 145305 (cit. on p. 117).
- [188] Franco Dalfovo, Stefano Giorgini, Lev P. Pitaevskii, and Sandro Stringari. “Theory of Bose-Einstein condensation in trapped gases”. In: *Rev. Mod. Phys.* 71 (3 Apr. 1999), pp. 463–512 (cit. on p. 119).
- [189] Stefano Giorgini, Lev P. Pitaevskii, and Sandro Stringari. “Theory of ultracold atomic Fermi gases”. In: *Rev. Mod. Phys.* 80 (4 Oct. 2008), pp. 1215–1274 (cit. on p. 119).

List of Figures

3.1.	2D gas of dipoles tilted by an angle θ_0 in the x, z -plane.	40
3.2.	(color online) Dynamical structure factor (in units of $m/(2\pi\hbar^2)^2$) as a function of ω/kv_F for $s_0 = 1.05$	49
4.1.	(color online) Phase diagram for $g_2 < 0$. Continuous curves correspond to transitions between different phases obtained from the variational ansätze (4.7) and (4.8). Increasing γ one passes the U-T transition (dashed), then T-S (lower dotted curve), and S-T (upper dotted curve). To the left of the solid black curve the ground state of the system is vacuum. The black dot is the four-critical point for the U, S, and two T phases. The symbols indicate our numerical results: the filled circles are inside the U phase, the downward and upward pointing triangles are inside the $T_{\theta < 0}$ and $T_{\theta > 0}$ phases, respectively, and squares are in the stripe phase. The empty circles are on the vacuum-stripe line and crosses are at the collapse instability border. The color-coded pictures show density profiles corresponding to the symbols in the phase diagram put in frames: the upper set (violet frame) contains three points of the $T_{\theta > 0}$ phase at $\gamma = 0.8$, the middle set (green frame) shows one point in the S phase and two points in the hexagonal $T_{\theta < 0}$ phase at $\gamma = 0.6$, and the lower set (grey frame) corresponds to the six points at $\gamma = 0.5$	66
4.2.	(color online) The density profile for a harmonically trapped gas with $\tilde{\mu} = 0.6$, $\gamma = 0.575$, and trapping frequency $\tilde{\omega} = 0.05$. The coordinates x, y are in units of $\sqrt{\hbar^2 g_3 / mg_2^2}$	68
5.1.	CAD model of the current experimental setup. Right-up: Na oven section. Left-down: Magnetic trap section. This figure is taken from Fig. 2.2 of Ref.[123] with the permission of reproduction from Dr. Buchheim.	73

- 5.2. rf association scheme of $^{23}\text{Na}^{40}\text{K}$ Feshbach molecules. We use the Feshbach resonance of $|F = 1, m_F = 1\rangle_{\text{Na}}|F = 9/2, m_F = -9/2\rangle_{\text{K}}$ channel (the resonance locates at 88.2G with $\sim 10\text{G}$ width) . The $^{23}\text{Na}^{40}\text{K}$ mixture is prepared in the non-resonant collision channel $|F = 1, m_F = 1\rangle_{\text{Na}}|F = 9/2, m_F = -7/2\rangle_{\text{K}}$ at 85.5G (slightly below the resonance) . A rf pulse drives the transition from the non-resonant channel to the resonant one. Depending on the frequency of the RF pulse either the hyperfine state of free ^{40}K atoms is changed or weakly bound molecules are associated. Two consecutive rf pulses transfer unassociated ^{40}K atoms to $F = 9/2, m_F = -3/2$ state in order to reduce the background signal during absorption imaging of Feshbach molecules. This figure is taken from Fig. 3.1 of Ref.[123] with the permission of reproduction from Dr. Buchheim. 80
- 5.3. rf spectrum of $^{23}\text{Na}^{40}\text{K}$ Feshbach molecules association at a magnetic field of $B = 85.5\text{G}$. The binding energy of the molecule is $\simeq +85\text{kHz}$. The grey shaded area indicates the effect of the inter-species interaction in the strongly interacting collision channel. This figure is taken from Fig. 3.4 of Ref. [123] with the permission of reproduction from Dr. Buchheim. 82
- 5.4. Schematic of a three level lamda system. In this system, the three levels include the initial Feshbach molecule state $|FB\rangle$, target rovibrational ground state $|X^1\Sigma, \nu = 0, J = 0\rangle$ and an intermediate state in $d^3\Pi/D^1\Pi$ complex, $|d^3\Pi, \nu = 5, J = 1, \Omega = 1\rangle$. These three states are coherently coupled by a pair of lasers with frequencies $\omega_{P/S}$, Rabi frequencies $\Omega_{P/S}$ and single photon detunings with respect to the molecular transition frequencies $\Delta_{P/S}$, respectively. The two-photon resonant condition is $\Delta_P = \Delta_S = \Delta$. This figure is taken from Fig. 4.11 of Ref.[123] with the permission of reproduction from Dr. Buchheim. . . . 84
- 5.5. Potential energy curves of the electronic ground state and the lower electronic excited states. Raman lasers (pump: $\sim 652\text{nm}$, Stokes: $\sim 487\text{nm}$) with frequencies $\omega_{P/S}$ and Rabi frequencies $\Omega_{P/S}$ couple a pair of vibrational states in the spin-orbit coupled $d^3\Pi/D^1\Pi$ complex to weakly bound $a^3\Sigma$ Feshbach molecules and the rovibronic groundstate in $X^1\Sigma$. Excited state molecular spectroscopy is performed on the pump transition. This figure was initially produced by Dr. Christoph Gohle, and has been included in both Ref. [123] as Fig. 4.1 and in this thesis. 87

- 5.6. Transition dipole moments of the Feshbach state and the $|X^1\Sigma, \nu = 0, J = 0\rangle$ ground state to the vibrational levels of the $d^3\Pi/D^1\Pi$ complex in atomic units, calculated in Ref.[155]. Binding energies are with respect to the atomic $^{23}\text{Na}(3^2P)+^{40}\text{K}(4^2S)$ asymptote. The highlighted state is chosen for the candidate in our STIRAP experiment for its balanced TDMs of both transitions. This figure was initially produced by LAC team (see context), and has been included in both Ref. [123] as Fig. 4.2 and in this thesis. 88
- 5.7. Fine structure of the $^3d\Pi \nu = 5$ vibrational level. This figure is taken from Fig. 4.6 of Ref.[123] with the permission of reproduction from Dr. Buchheim. 89
- 5.8. Molecular excitation spectrum of Feshbach molecules to the $J = 1, \Omega = 1$ intermediate state at 85.5G. A Zeeman triplet $m_J = -1, 0, 1$ is clearly observable. The molecular hyperfine structure is not resolved. The data points are averaged over 12 measurements. The figure is taken from Fig. 4.9 in Ref.[123] with the permission of reproduction from Dr. Buchheim. 90
- 5.9. Hyperfine structure of the rovibronic groundstate at 85.5G. The red dots indicate hyperfine components that can be accessed by STIRAP starting from Feshbach molecules ($m_F = -7/2$, dashed black line). The hyperfine component with total lowest energy is indicated by the back arrow. This figure is taken from Fig. 4.25 in Ref.[123] with the permission of reproduction from Dr. Buchheim. 91
- 5.10. Multilevel STIRAP scheme. We use $\sigma^+ + \sigma^-$ polarization for the pump laser and π light for the Stokes laser. The detuning of the lasers are $\Delta_P = \Delta_S = -30\text{MHz}$ 93
- 5.11. Successful STIRAP transfer signal. We count the number of Feshbach molecules after a round trip of STIRAP. By keeping the pump laser frequency detuned -30MHz , we scan the frequency of the Stokes laser and see a peak of molecular number once the two phonon resonance condition is satisfied. 93
- 6.1. The result from standard ABM model, $^{23}\text{Na} |F = 1, m_F = 1\rangle + ^{40}\text{K} |F = 9/2, m_F = -9/2\rangle$. Black solid line corresponds to the threshold energy. Blue and red dashed lines represent two bound states. The figure shows two crossings, therefore there are two Feshbach resonances expected for this collision channel. 107

- 6.2. The result from the dressed ABM model, $^{23}\text{Na} |F = 1, m_F = 1\rangle + ^{40}\text{K} |F = 9/2, m_F = -9/2\rangle$. We zoom in the region around the Feshbach resonance that we are using for molecule association. Black solid line corresponds to the threshold energy. Red solid line represents a bare bound state energy without open-close channel coupling. Blue dots represent the root of Eq. (6.36) at different magnetic fields which correspond to the real binding energies of the Feshbach molecules. . . . 108
- 6.3. Feshbach molecule binding energies at various magnetic fields. Red points are the experimental datas, Blue solid line fits the experimental datas to the universal binding energy formula, $E_b \sim \frac{\hbar^2}{2m(a-\bar{a})^2}$ 109
- 6.4. Close channel fraction of Feshbach molecules vs. magnetic fields. . . . 109
- 7.1. Inverse rf spectra based of vanishing momentum ($\mathbf{p} = 0$) polarons with self-consistent \mathcal{T} -matrix approach, taken from Fig. 7 in Ref.[182] with permission. n is the density of the BEC, $a_{\phi\psi}$ is the interaction (s-wave scattering length) between the impurity and the Bose background, $\Omega_0 = n^{2/3}/m_\phi$ 115
- 7.2. Momentum dependence of polaron spectral response using self-consistent \mathcal{T} -matrix approach in Ref. [182]. Solid line: free impurity dispersion. (a) $(n^{1/3}a_{\phi\psi})^{-1} = 1$. (b) $(n^{1/3}a_{\phi\psi})^{-1} = -5$ 116
- 7.3. Life time of the impurity vs magnetic field. The error bar indicates the fitting deviation to an exponential decay. 118
- 7.4. The scattering length vs. magnetic field of the initial channel, $|F = 1, m_F = 1\rangle + ^{40}\text{K} |F = 9/2, m_F = -5/2\rangle$ 120
- 7.5. The scattering length vs. magnetic field of the final channel, $|F = 1, m_F = 1\rangle + ^{40}\text{K} |F = 9/2, m_F = -9/2\rangle$ 120
- 7.6. rf spectral response of impurities at various magnetic fields. Black dots are the experimental data points of bare ^{40}K atomic transitions without ^{23}Na atoms. Red dots are the experimental data points while spin-flipping ^{40}K with ^{23}Na a Na BEC background. Solid lines show the results of fitting experimental datas to a Gaussian distribution. 122
- 7.7. Color scaled rf spectral response of impurities at various magnetic fields across the Feshbach resonance. 123
- 7.8. Frequency shifts of impurity atoms due to ^{23}Na BEC at various magnetic fields across the Feshbach resonance. 123
- 7.9. Comparison between experimental datas and theoretical prediction with various BEC density. Circles correspond to experimental datas. Left figure: $n = 5 \cdot 10^{12}\text{cm}^{-3}$. Right figure: $n = 10^{13}\text{cm}^{-3}$. Private communication from Yulia E. Shchadilova, Richard Schmidt, Fabian Grusdt, and Eugene Demler. 124
- 7.10. RF spectra of impurity ^{40}K atoms at 78.5 Gauss. Red points show the spectrum without Na atoms. Blue points represent the spectrum with a Na BEC where a tail is clearly visible. 125

- A.1. (color online). Left: The integration area for \tilde{I}_1 (in blue). The distance between the points O_1 and P is $\mathbf{R}_{O_1P} = \mathbf{k}/2k_F$, $\mathbf{R}_{PO_2} = \mathbf{k}'/2k_F$, and $\mathbf{R}_{O_1N} = \mathbf{k}_1/2k_F$. Right: The integration area for \tilde{I}_2 and \tilde{I}_3 (in red). The distance between the points O_2 and N is $\mathbf{R}_{O_2N} = \mathbf{k}_1/2k_F$, $\mathbf{R}_{O_1P} = \mathbf{k}/2k_F$, and $\mathbf{R}_{O_2P} = \mathbf{k}'/2k_F$ 132
- A.2. (color online). Left: The integration area for I'_1 (in blue): $\mathbf{R}_{O_1P} = \mathbf{k}/2k_F$, $\mathbf{R}_{PO_2} = \mathbf{k}'/2k_F$, $\mathbf{R}_{O_1N} = \mathbf{k}_1/2k_F$, and φ is the angle between the vectors \mathbf{R}_{OP} and \mathbf{R}_{ON} , which is the same as the angle between \mathbf{m} and \mathbf{x} . Right: The integration area for I'_2 (in red): $\mathbf{R}_{O_1P} = \mathbf{k}/2k_F$, $\mathbf{R}_{O_2P} = \mathbf{k}'/2k_F$, $\mathbf{R}_{O_2N} = \mathbf{k}_1/2k_F$, α is the angle between \mathbf{R}_{PM} and \mathbf{R}_{PN} , and ϕ is the angle between \mathbf{R}_{PN} and \mathbf{R}_{OO_2} 134

List of Tables

5.1.	11 reported s-wave Feshbach resonances in Ref. [135]. Values in brackets are the results from our measurements.	79
5.2.	“BF” refers to the Feshbach molecule, “B” to the boson, “F” to the fermion, and “X” to a distinguishable K atom. $P(a)$ and $M(a)$ are functions resulting from Efimovian states (see Ref.[149] and references therein).	83
5.3.	Seven lowest vibrational levels of $d^3\Pi$ potential identified from photoassociation experiment. The value shown in the table are the experimental results. Theoretical predications are done by LAC team. . . .	86
6.1.	Spin components of the Feshbach molecular state at 85.5G calculated with the asymptotic bound state model.	107

Acknowledgements

First of all, I am greatly indebted to my supervisor Prof. Immanuel Bloch, for giving me the opportunity to work in his research group. It is a great privilege and honor to spend my PhD time in this famous group, especially for a foreigner. I admire his optimistic attitude towards experiments and his intuition to any physics problem. I thank him for his encouragement and appreciate his support during the whole PhD period. His advices during the group meetings or during the telephone calls are always useful for our experiments and stimulate new ideas.

Secondly, I would like to thank Prof. Georgy V. Shlyapnikov for his continuous concern about my PhD study and his kindness of being my “Zweitgutachter”. Even though my overlapping with Gora is small in time and in geography, he is always available on phone. Gora educates me how to study theoretical physics in a Russian style which I appreciate very much now. I admire his rigorousness towards the work - checking every formula repeatedly himself, his matchless mathematical ability - calculating nasty integrals in an amazing speed, and his humors. I thank him for his invitations to visit his group from time to time and his endless offers of coffee.

I would like to thank Prof. T. W. Hänsch, Prof. V. F. Mukhanov, Prof. U. Schollwöck, and Prof. J. von Delft for their kindness of being the committee members of my PhD exam.

I want to thank my “daily” supervisor, Dr. Christoph Gohle, for his guidance of experimental techniques, for his care about my daily life and for his invitations of wonderful birthday parties and BBQs in his house. Whenever we have troubles in experiments, he always has a solution and explains in a clear way. His optimism gives me the confidence to continue the experiments. His intuition on general physics and his knowledge about atomic physics impress me all the time. I remembered clearly the time that I went hiking with your family, you encouraged me to overcome fears. Thanks Christoph!

I would like to give a big thank to my colleague and good friend, Dr. Nikolaus Buchheim and his fiancé Judith. He treats me as his own brother or even more. As a local Bavarian, he takes me to enjoy the beautiful Alps, he introduces his friends to me and drives me to Austria for the mushroom hunting. With him, we experienced together the happiness from the progress of experiments and the sadness from the failure of the machine. It is the time we need to start the next chapter of our life, but I believe our friendship will last for long. I wish you and your family all the very best!

I am grateful to my former and current colleagues of polar molecule team Dr. Tobias Schneider, Diana Amaro, Frauke Seeßelberg, Roman Bause and our interns

who spent few months with us: Christian Hanauer, Ingo Laut, Yannick Seis, Andréas Tresmontant and Nathan Evetts. I wish the next generation of the team, Frauke and Roman, have great success and achieve outstanding results from this experimental apparatus.

I am grateful to my co-authors from the theory side : Dr. Dmitry Petrov, for his practical advice towards a publication and his theoretical proposals for our experimental setup. Dr. Yun Li, for her support of numerical methods and discussions, and Dr. Sergey Matveenko for his guidance on zero sound studies.

I want to thank my fellow colleagues in LMU and MPQ: Martin B., Timon H., Ahmed O., Guillaume S., Christian G., Katharina K., Sebastian H., Manuel E., Peter S., Johannes Z., Tarik Y., Jaeyoon C., Tony R., Tracy L., Lucia D., Martin R., Moritz H., Francesco S., Monika A., Monika S.-S. Pau K., Sean H. . . . for a nice chat, or a cold beer, or a fast meal, or a funny party time, that we spent together.

I would like to thank all the staff members working in the group who constantly support our work on mechanics, electronics, and administration. To our secretaries Marianne Kargl, Kristina Schuldt and Ildiko Kesckesi, to our electronic engineers Karsten Förster, Oliver Mödl and Bodo Hecker, to our mechanical engineer Anton Mayer. I believe that our experimental apparatus can not be built without their helps and knowledges.

Thanks to all my old and new friends all over the world for their non-physics advice, help and assistance.

Finally I want to thank my parents for their constant support over the distance.

This thesis is dedicated to my parents.